A GEOPHYSICAL INVESTIGATION OF THE LITHOSPHERE OF THE CAPE VERDE RISE

by

R. Young

A thesis submitted for the degree of

Doctor of Philosophy

at the University of Leicester

April, 1986.

A GEOPHYSICAL INVESTIGATION OF THE LITHOSPHERE OF THE CAPE VERDE RISE

by

R. Young

ABSTRACT

The Cape Verde Rise and Islands are considered to be the result of 'Hot Spot' activity. The results of reheating can be observed by changes in the physical properties of the lithosphere. The purpose of this work is to study the relationship of the islands to the rise and relate any changes in the physical properties of the lithosphere to its thermal structure.

A geophysical investigation of the lithosphere of the Cape Verde Rise has been carried out using measurements of total magnetic field, seismic reflection profiles, sonobuoy wide angle reflection/refraction experiments, free air gravity and bathymetry from surface ships. Geoid height data from the GEOS3 and SEASAT satellite missions have also been used.

Total magnetic field anomalies are attributed to sea floor spreading during the Mesozoic and used to show that 4 fracture zone traces exist in the vicinity of the archipelago. The history of spreading is comparable to corresponding studies in the Western North Atlantic.

Seismic stratigraphy from continuous reflection profiles and velocities from wide angle reflection/refraction studies are consistent with uplift during the Early Miocene followed by a period of island building volcanism.

Depths to oceanic layer 2, after correction for sediment loading, show that the rise is ~2 km shallower than expected for Mesozoic crust. The present depth is equivalent to only 25 Ma oceanic crust.

A 1-dimensional examination of the relationship between free air gravity anomalies and bathymetry using linear transfer function techniques indicates that the lithosphere of the Cape Verde Rise has an effective elastic thickness (EET) of only 15±3 km when compared with a thin plate flexure model. This value of EET is less than expected for Mesozoic crust from a global compilation of EET against age of crust at the time of loading.

Using geoid height data the above analysis has been extended to 2-dimensions and a value of 18±3 km has been observed for the EET. The same thin plate flexure model was used for the geoid response as was used for the gravity.

The Cape Verde Rise is associated with both a reduction in EET and a considerable depth anomaly. This is considered to be evidence for thermal rejuvenation. Hawaii, however, is only associated with a depth anomaly and no substantial reduction in EET is observed. This difference between the effect of 'Hot Spot' activity on Hawaii and on the Cape Verde Rise is considered to be due to the motion of the oceanic plate over the mantle heat source.

CONTENTS

CHAPTER 1

CHAPTER 2

CHAPTER 3

CHAPTER 8

CHAPTER 9

APPENDIX I

LIST OF FIGURES

CHAPTER 1

CHAPTER 2

CHAPTER 3

CHAPTER 4

CHAPTER 5

CHAPTER 6

CHAPTER 7

CHAPTER 8

APPENDIX I

CHAPTER 1 (INTRODUCTION TO THESIS)

1.1 INTRODUCTION

The Cape Verde Rise is an anomalous bathymetric swell in the Eastern North Atlantic. The swell rises to depths of only ~3 km and contrasts with oceanic depths of ~5 km to the north and south. Sitting to the south-west of the rise crest, the Cape Verde Archipelago consists of 10 volcanic islands forming a horseshoe shape, opening to the west, ~500 km from the Senegalese coast of Africa. Figure 1.1 shows the relative positions of the islands and the inset shows the position of the archipelago relative to the African continent.

Both the Cape Verde Islands and Rise are thought to be the result of a mantle 'hotspot' plume. The present study is a geophysical investigation of the lithosphere of the Cape Verde Rise. Total field magnetic anomalies have been interpreted in terms of a magnetic reversal sequence and used to establish the oceanic nature of the crust, its age and structural fabric. Seismic profiles and sonobuoy wide angle reflection/refraction measurements define the sediment thickness, seismic stratigraphy and constrain estimates of oceanic layer 2 depths, after accounting for sediment loading effects.

Shipborne gravity and satellite altimetry are interpreted within the constraints supplied by the other geophysical data to yield an estimate of the elastic rigidity of the lithosphere of the Cape Verde Rise and consequently its state of thermal reheating.

This introductory chapter outlines the research carried out, by the author, by devoting a section to each of the following chapters. Each chapter of this thesis is written as a self-contained section and each part has its own introduction.

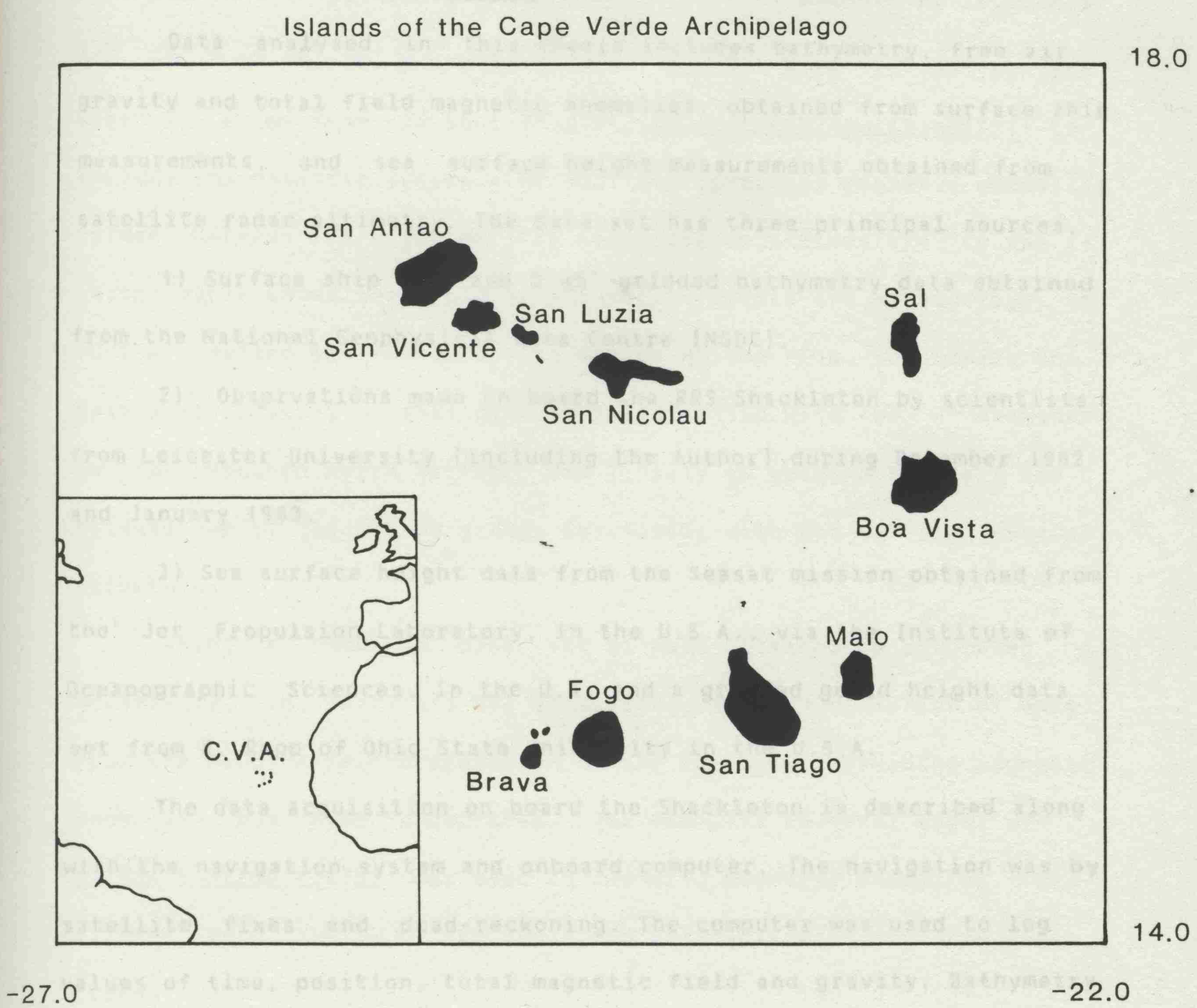

Figure 1.1 Chart of the Cape Verde Archipelago showing the relative positions of the islands. Inset shows the position of the archipelago relative to the African mainland.

1.2 DATA COLLECTION (CHAPTER 2)

Data analysed in this thesis includes bathymetry, free air gravity and total field magnetic anomalies, obtained from surface ship measurements, and sea surface height measurements obtained from satellite radar altimetry. The data set has three principal sources.

1) Surface ship data and 5'x5' gridded bathymetry data obtained from the National Geophysical Data Centre (NGDC).

2) Observations made on board the RRS Shackleton by scientists from Leicester University (including the Author) during December 1982 and January 1983.

3) Sea surface height data from the Seasat mission obtained from the Jet Propulsion Laboratory, in the U.S.A., via the Institute of Oceanographic Sciences, in the U.K. and a gridded geoid height data set from R. Rapp of Ohio State University in the U.S.A.

The data acquisition on board the Shackleton is described along with the navigation system and onboard computer. The navigation was by satellite fixes and dead-reckoning. The computer was used to log values of time, position, total magnetic field and gravity. Bathymetry was not interfaced to the computer and had to be added later by hand.

Seismic reflection and refraction experiments were also carried out. Recording of this data was by anologue magnetic tape but difficulties were encountered when trying to replay this data back at Leicester University.

The acquisition of sea surface heights from satellite radar altimetry is briefly described along with the sources of the data held on computer file at Leicester University.

1.3 MAGNETIC INVESTIGATION (CHAPTER 3)

The regional structure of the oceanic crust comprising the Cape Verde Rise can be investigated by examining total field magnetic anomalies. The area considered by this study is bounded by latitudes 13^{o} 00' N to 18^{o} 30' N and longitudes -26^{o} 00' W to -20^{o} 00' W. This area is known from previous studies (Hayes & Rabinowitz (1975)) to include the Mesozoic sequence of seafloor spreading magnetic anomalies formed between 108 & 155 Ma. The principal objectives are, to see if recognisable anomalies could be identified within the archipelago, to further define the fracture zone traces on the rise, to compare the spreading history of this part of the Atlantic with the 'M' sequence in the Western North Atlantic and finally to examine how well the orientation of the island groups correlates with pre-existing oceanic structures.

Using a combined data set of data obtained by Leicester University, on board the RRS Shackleton, and a compilation of data from the NGDC, a reinterpretation of the sea floor spreading magnetic anomalies has been undertaken. The magnetic reversal model of Larson & Hilde (1975) was used to identify magnetic anomalies. This allowed both dating of the crust and delineation of fracture zone traces.

The major conclusions of this study of the magnetic anomalies over the Cape Verde Rise are that:-

1) Seafloor spreading magnetic anomalies can be identified within the archipelago. These anomalies can be correlated with the Mesozoic reversal sequence of Larson & Hilde (1975).

2) The single fracture zone identified by Hayes & Rabinowitz 1975 has been refined to 4 fracture zones by this study. Offsets are variable with time, being zero at M25 and a maximum (~30 km) at M0.

3) The 'M' sequence observed here compares very well, in terms of both spreading rate and spreading direction changes, with the western Atlantic described by Schouten & Klitgord 1982.

4) The disposition of the islands with respect to the fracture zone traces suggests only the northern limb of the archipelago can be constrained to lie along a fracture zone trace.

These conclusions suggest that the crust comprising the Cape Verde Rise is 'normal' in respect of the magnetic anomalies. The heating event that must have accompanied island formation was not sufficiently strong that it obliterated the magnetic anomalies within the archipelago. Little difference can be seen between the crust of the Cape Verde Rise and its Western Atlantic counterpart as regards spreading history. The formation of the rise must certainly have occurred after the crust had migrated away from the Mid Atlantic Ridge.

1.4 SEISMIC INVESTIGATION (CHAPTER 4)

Seismic reflection profiling was carried out to study the distribution of sediments and the depth to volcanic basement around the Cape Verde Islands. In addition, several seismic refraction experiments were carried out to collect velocity information not available from single channel seismic profiling.

Despite problems with the seismic reflection recording equipment 6 separate profiles of data were collected. These varied in quality but were roughly evenly distributed around the archpeligo. A seismic stratigraphy analysis resulted in the division of the sediments into 4 groups.

1) The lowermost reflector was characterised by diffraction hyperbolae and no coherent reflectors could be seen beneath it. This is considered to be volcanic basement and it is easiest identified >50 km away from the islands.

2) The next unit is a series of horizontally layered reflectors

which infill the topography of the basement beneath. This is most likely a series of marine sediments. It is bounded above by an erosional unconformity. The extent to which this unit is identifiable depends on the transmitting properties of the overlying layers.

3) Above the unconformity is a unit characterised by its scattering reflective nature. This is also bounded above by an unconformity. This is probably a volcaniclastic horizon and its thickness appears to decrease with distance away from the islands.

4) The uppermost unit is relatively acoustically transparent. It is bounded above by the seabed and below by an unconformity. This is considered to be a series of recent pelagic sediments.

Seismic wide angle reflection and refraction experiments were carried out to supplement the reflection interpretation by examining the velocity structure of the upper crust around the Cape Verde Islands. Velocities were obtained for the sediments which suggest that their total thickness is approximately 1 km and that they overlay oceanic layer 2 with p-wave velocities of around 5.0 km/s. These results are consistent with previous work in the area by Hoskins et al (1974).

1.5 THEORETICAL FLEXURE MODELS (CHAPTER 5)

The relationship between free air gravity, geoid height and bathymetry can be described in the spatial frequency (or wavenumber) domain by relatively simple models. The simplest is one where the bathymetry is uncompensated and the resulting gravity or geoid anomaly is due to the density contrast between seawater and the bathymetric feature. A more complex model involves the regional compensation of the bathymetry by assuming that it represents a load on an elastic plate. The plate flexes under the load by an amount dependent on its elastic properties.

The relationship between the gravity, or geoid, anomaly and the bathymetry is termed the admittance, or response. The response of a thin plate flexure model can be calculated for a variety of different rigidities. A very rigid plate will support the bathymetry and the resulting response will be similar to the uncompensated model. A less rigid plate will bend easily and will result in the developement of negative side lobes to the gravity, or geoid, anomaly which reflect the compensation.

A useful parameter to descibe the rigidity of the model is termed the effective elastic thickness (EET). Large values (>40 km) indicate a rigid plate and low values (<5 km) indicate a plate that is easily bent.

The effective elastic thickness has been shown to vary with age of the lithosphere, at the time the bathymetric load was applied, in a similar manner to the cooling of a simple thermal model. This fact can be used to relate the EET to thermal properties of the lithosphere.

1.6 OBSERVED ADMITTANCE ESTIMATES (CHAPTER 6)

The observed admittance, or response, can be calculated using the measured variation of free air gravity or geoid height. The general observed relationship is wavelength dependent with the signals of bathymetry and gravity, or geoid, appearing similar at short wavelengths (<50 km) but dissimilar at long wavelengths (>100 km). The signals are therefore examined in the spatial frequency domain and the variation of the dependence of gravity, or geoid, on bathymetry calculated as a function of wavenumber.

The Fast Fourier Transform (FFT) algorithm is used and this requires some preprocessing of the data series. The data series must be an integer power of 2 or be padded out, usually by the addition of zeros, to an integer power of 2. The data must also have a mean and trend removed to prevent any discontinuities causing aliasing in the spatial frequency domain. A cosine taper is applied to further aid this requirement.

The free air gravity data are examined along ship's track profiles and as such can only be considered as 1-dimensional. The tracks were selected to approach the inter-island ridges in as near a perpendicular direction as possible. The load is then treated as having infinite strike length.

The geoid height data are examined as 2-dimensional gridded values and therefore the constraint of selecting appropriate tracks is removed. 2-dimensional bathymetric data are also used in this analysis.

A certain amount of averaging must be carried out in the spatial frequency domain to obtain noise free estimates of the observed admittance. For the 1-dimensional gravity data the averaging was acomplished by summing the results from 10 separate profiles and then applying a logarithmically varying bandwidth average to the result. The 2-dimensional data are averaged azimuthaly and then the same bandwidth average is applied to the result.

1.7 GRAVITY/BATHYMETRY RELATIONSHIP (CHAPTER 7)

The relationship between free air gravity and bathymetry is examined over the Cape Verde Rise. The model proposed is a thin plate model whereby the lithosphere of the rise flexes under the load of the islands. The best fitting model to the observed admittance data has an effective elastic thickness of only 15±3 km. The simplifying assumption of 1-dimensionality is tested by applying the thin plate model admittance to the 2-dimensional bathymetry to produce the calculated or expected gravity. The results confirm that the effective elastic thickness found from the inversion is still the best value.

A global compilation of oceanic swell heights plotted against age of the lithosphere shows that the Cape Verde Rise has risen to a depth equivalent to 25 Ma crust. This is compared to a cooling plate model.

A global compilation of effective elastic thickness against age of the lithosphere at the time of loading shows a similar variation to the thin plate cooling model. The effective elastic thickness generally increases with the age of the lithosphere at the time it was loaded. Using this relationship it is expected that the lithosphere of the Cape Verde Rise should have an EET of ~30 km. The observed value is considerably less than this and this is considered to be evidence of thermal rejuvenation.

The lithosphere of the Cape Verde Rise now has a thermal age equivalent to 25 Ma crust and this is expressed as both a depth anomaly and as a reduction in the effective elastic thickness. Comparison of this result with studies carried out over the Hawaiian Ridge, another swell with a large depth anomaly, show that the two swells are not exactly analoguous. The Hawaiian swell does not have a significantly reduced EET. This, it is thought, is due to the rate of motion of the Pacific plate over the mantle heat source not allowing time for the heat anomaly to perturbate completely through the crust and lower the EET. The Cape Verde Rise, however, is near the pole of rotation of the African plate and has been stationary over its heat source for approximately the last 30 Ma and thus the heat has been tranmitted sufficiently through the crust to result in reduction of the EET.

1.8 GEOID/BATHYMETRY RELATIONSHIP (CHAPTER 8)

Geoid height data provide an opportunity to extend the analysis of the previous chapter to 2-dimensions. The ship's track coverage of the Cape Verde Rise is insufficient to grid the gravity data on anything other than a regional basis. A combination of SEASAT and GEOS3 data gives a suitable sub-satellite track density that the geoid heights can be interpolated onto a 7.5'x7.5' grid. This data can be combined with gridded bathymetry data to analyse the relationship between geoid heights and bathymetry in 2-dimensions. The geoid is dependent on $1/r$, whereas gravity is dependent on $1/r^2$, and should define the compensation anomaly, occurring at some depth, better than the gravity.

The same thin plate flexure model used for the gravity will be used here to model the geoid anomaly. A simple transfer function is used to get the geoid response from the gravity response. The observed response compares favourably with a thin plate model with an EET of ~15 km.

The gridded geoid data have undergone some amount of lowpass filtering which will be dependent on the between track spacing. This is evident when comparing the original SEASAT tracks with the gridded data. The thin plate model was therefore used to predict the expected geoid anomaly due to the 2-dimensional bathymetry and this was compared with SEASAT sub-satellite tracks crossing the Cape Verde Archipelago. The models were produced at 1 km intervals of EET from 10 km to 27 km, inclusive. The goodness of fit between the expected geoid and observed geoid was computed by taking the r.m.s. difference between the two. A minimum in the r.m.s. difference was taken to indicate the best fitting model. Using this method a best fitting model, averaged over 8 sub-satellite tracks, was calculated to be with an EET of 18 ± 3 km. This supports the previous result.

The major conclusion of this study is that it confirms the earlier result that the effective elastic thickness of the Cape Verde

Rise, calculated using a thin plate model, is less than that predicted from a global compilation. This is considered to be evidence for lithospheric thermal rejuvenation.

1.9 SUMMARY OF CONCLUSIONS (CHAPTER 9)

The major conclusions from the different aspects of the work carried out in this thesis are brought together in the final chapter. The sea floor spreading magnetic anomalies suggest the lithosphere has had a formation and early history typical of oceanic crust. The fracture zone traces identified here are relatively insignificant in terms of offset size. Anomalies can be identified within the archipelago.

The evidence from interpretation of continuous seismic profiling is compatable with uplift sometime in the Early Miocene. Seismic velocities can be interpreted in terms of the same simple seismic stratigraphy.

The state of compensation of the bathymetric load of the islands from an examination of free air gravity and geoid height anomalies compares well with a thin plate flexure model. The rigidity of the best fitting model, expressed as an effective elastic thickness, is less than expected from global studies. This can be explained by thermal rejuvenation.

CHAPTER 2 (DATA COLLECTION & REDUCTION)

2.1 INTRODUCTION

Marine geophysical data were obtained from the National Geophysical Data Centre (NGDC) at Boulder, Colorado in the United States. The data was selected within latitude and longitude limits centred about the Cape Verde Rise.

In addition, during December 1982 and January 1983 the RRS Shackleton conducted 24 days of scientific observation in and around the Cape Verde Archipelago. Figure 2.1 shows the ship's tracks for the RRS Shackleton superimposed in the area of the Cape Verde Rise. The scientific crew (of which the Author was a member) were principally from Leicester University with technical support from NERC Research Vessel Services in Barry, Wales. The data collected at this time provide the principal data set on which the bulk of the work presented here is based.

Data were also made available from a cruise to the Cape Verde Islands by Cambridge University on board the RRS Discovery during December 1983 and January 1984. The total ship's track coverage available for analysis here at Leicester is shown on Map 1 contained at the back of this volume.

Data collection on board the RRS Shackleton consisted principally of logging the output from a total field magnetometer, a gravimeter and the satellite-navigation system and recording these values against ship's time. A PDP11/34 computer was used to both log and process the data values. Bathymetric data from a precision echo sounder was not logged automatically but added later after digitising by hand. Data values were also logged every 5 minutes by a watchkeeper throughout the time the ship was within the survey area. In addition seismic refraction experiments were undertaken using disposable radio sonobuoys and continuous seismic reflection profiles were shot.

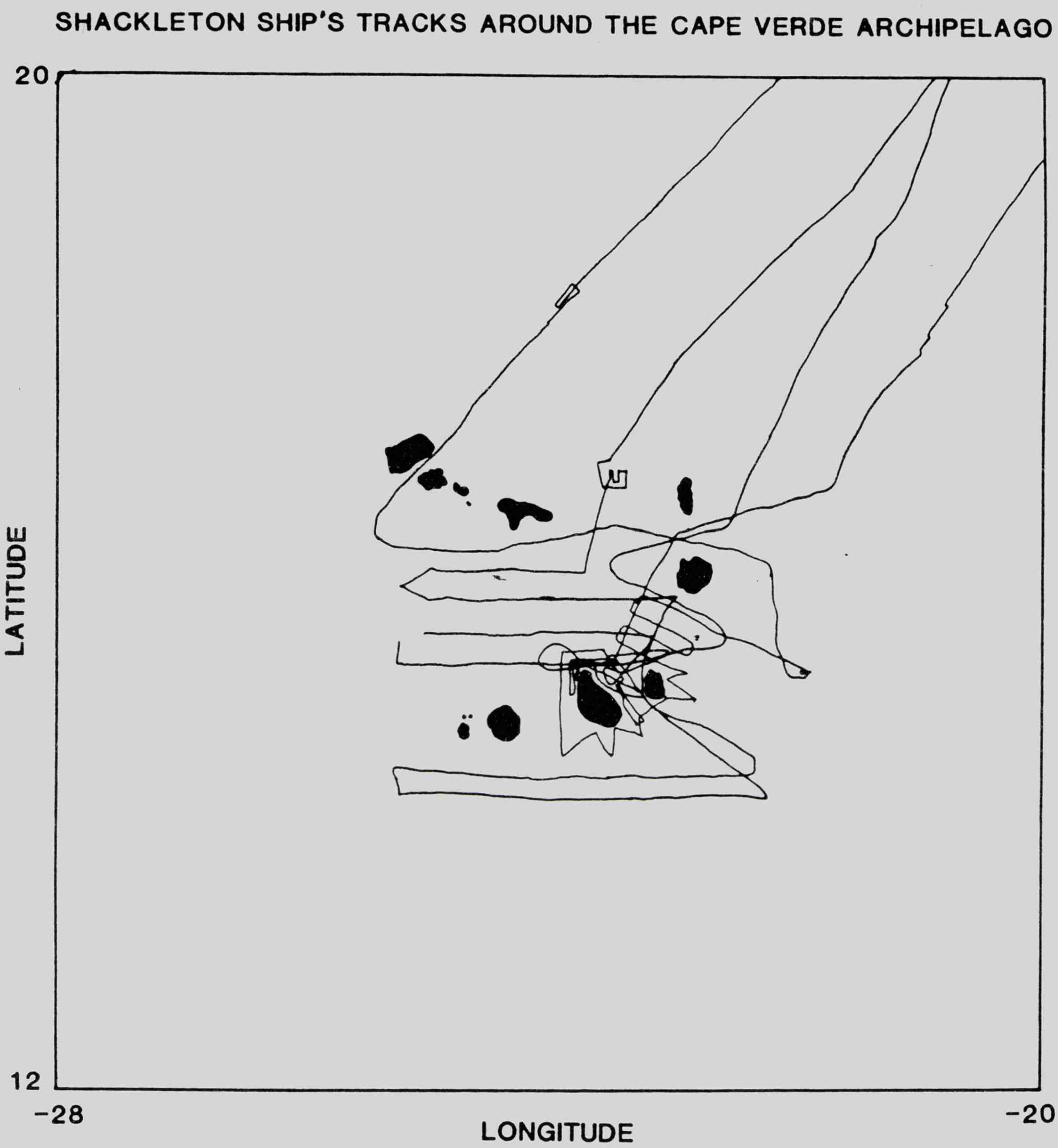

Figure 2.1 Chart of the area of the Cape Verde Rise showing the ship's tracks of the RRS Shackleton. Marine geophysical experiments were carried out by scientists from Leicester University during December 1982 and January 1983. The Cape Verde Islands are shown shaded.

Data processing involved the reduction of the observed total magnetic field to give anomaly values relative to the appropriate International Geomagnetic Reference Field, reduction of the observed gravity to give free air gravity anomalies and the correction of the ship's position with time to correct for dead reckoning inaccuracies between satellite fixes. All this was carried out by the data logging computer on board and position (latitude and longitude), time and data values were written to magnetic tape for transfer to the mainframe computer at Leicester University. The original chart records and navigation information were also kept as a back up. The rest of this chapter describes in more detail the collection and reduction of the data.

2.2 NAVIGATION

It is logical to first describe the navigation system since all the data points are related to ship's position by the ship's clock. Knowing the variation of position with time and also the variation of any geophysical quantity measured on board with time the data points can be easily related to position. Navigation on the Shackleton is based on the Navy Navigation Satellite System (NNSS) and uses a twin channel Magnavox Satellite receiver. The accuracy of this system for a 'good' fix, the criteria for which are laid out below, can be of the order of ± 25m. However, the computation of the position of the ship requires the input of an estimate of course and speed. Dead reckoning, using a gyrocompass for direction and an E.M. log for speed, both port-starboard and fore-aft, was used in-between satellite fixes. The D.R. instruments were also linked to the computer making the whole system automatic. Examination of the satellite records shows the frequency of satellite passes at the latitude of the Cape Verde

Archipelago is around 90 minutes, but not all the passes are 'good'. The criteria for a satellite pass to be 'good', according to the NNSS is that:

a) Elevation must be within the range 8^{o}-70^{o}

b) Sufficient duration of received signal

c) Doppler counts symmetric about the perigee

d) Constant message throughout the fix

e) As few iterations as possible

f) Relatively constant course and speed during fix

g) Good estimate of course and speed at start of calculation

The selection or rejection of passes was accomplished by the sofware of the system and it was possible that periods of as much as 4 hours could pass without an accurate assessment of the ship's position.

Once several 'good' satellite fixes have been received it is necessary to correct the dead reckoning, which will have been affected by wind, currents and tides. This is achieved by assuming a current existed, of constant speed and direction, between the satellite positions. This is somewhat complicated by the necessity to know the course and speed before the satellite position can be found. The final computed positions are logged against time and are shown on the track chart of Figure 2.1.

The main source of error in this method of navigation is the dead reckoning between satellite fixes. If many course and speed changes are made the error associated with any position on that portion of track will be correspondingly greater. It is, however, possible to check the accuracy of positions provided there are many track intersections and cross-over analysis for measurements, such as bathymetry, can be made.

The net result of the D.R. and the satellite positioning is that the position of the Shackleton is assumed to be known to within ±100m. The main source of error being the uncertain course and speed for the fix calculation.

The navigation system onboard the RRS Discovery is very similar to that just described for the RRS Shackleton and hence the positional accuracy is considered to be comparable.

The navigation for the data from the World Data Centre was highly variable, from satellite navigation similar to that outlined above to astro-geodetic. Information as to what techniques were used is given in the header preceeding the data block. The Shackleton data is considered to be sufficiently accurate that it can be used as a control and any major differences between this and the NGDC data are attributed to the NGDC data.

2.3 TOTAL MAGNETIC FIELD

Values of total magnetic field were obtained whenever the ship was underway within the survey area. The instrument used was a Varian Marine Proton Precession Magnetometer. The accuracy of this type of instrument is ±1 nT (gamma) when measuring a steady magnetic field. This represents a negligible error in the context of this kind of work where the magnetic anomalies are expected to have amplitudes of around 50-100 nT.

The reading cycle is 6 seconds and the total magnetic field value is shown on a digital display. The output from the detector is also fed into the computer logger, via an interface, and plotted on a servoscribe chart recorder. The chart is annotated, with time and data values, at regular time intervals. The magnetometer may have to be tuned occasionally as the mean value of the earth's total magnetic field varies but this was only really necessary during passage to and from the survey area.

To isolate the sensor from the magnetic field induced in the ship's metal hull and from any spurious electromagnetic noise from the ship's generators the bottle is towed some distance behind the ship. In this case the distance was ~150m. The magnetic field associated with the ship depends very much on the course being steered. The effect of this field on the sensor is therefore known as the 'heading error' and will have a constant value between course changes. The maximum value for Shackleton was ~20 nT. The cable carrying the signal back to the detector on the ship is susceptible to picking up transient signals. These show up as spikes on the chart record and can be removed later, by an averaging process.

Natural short term variations in the earth's magnetic field can be divided into diurnal variation and magnetic storms. The diurnal variation has an amplitude of ~50 nT but is spread over a period of 24 hours. This corresponds to a track length of ~220 km (@ 5 knts). This is of such long wavelength that it is not considered to interfere with detection of the geologically generated magnetic anomalies, which typically have amplitudes of 50-200nT and wavelengths of 10-50 km. Magnetic storms are generally more difficult to detect and deal with. The field can change 100 nT in a short period(0.5-2 hours) and can thus be confused with seafloor spreading magnetic anomalies. However, records affected by magnetic storms are generally noisier than normal and this can aid in their identification. An observatory at M'Bour on the African mainland, 500 km to the East, was used to check the natural magnetic field activity. As is stated in Chapter 3 corrections were not considered necessary.

Once the total magnetic field data have been collected the anomaly relative to a regional field must be calculated.

The regional geomagnetic field is calculated from spherical harmonic coefficients derived from global analysis and published as the International Geomagnetic Reference Field (IGRF). The changing nature of the earth's magnetic field is accomodated by periodic updates and time varying factors. The coefficients used for the Shackleton and Discovery data were those of IGRF 1975.0. Appropriate coefficients were used for the NGDC magnetic data. The calculated field is subtracted from the observed values to give an anomaly relative to the IGRF. The calculated field is of very long wavelength (>500 km) compared to the magnetic anomalies associated with seafloor spreading which have amplitudes of 50-200 nT and wavelengths of 10-50 km. The use of an IGRF as a regional field is not strictly necessary but is useful if the data are to be contoured at some stage. The IGRF was used in this study to be consistent with the majority of the existing data, although the data are only examined as profiles along track in this study.

2.4 GRAVITY

A LaCoste and Romberg Air/Sea gravimeter was utilised on board the RRS Shackleton to record values of gravity relative to a base station at Gibraltar. The measurement of gravity at sea is well explained in McQuillin & Ardus (1977) and will not be described here.

The gravimeter only measures gravity relative to a base station and by repeated measurements at that base station over a period of time the drift of the instrument can be determined. The drift is expected to be very low and only contribute a small amplitude, very long wavelength component to the gravity signal. This can be important in network, or grid, type surveys where it may add to gravity mis-ties at track intersections. The gravimeter on board the RRS Shackleton was linked to base 016.01 on the South Mole at Gibraltar using a Worden gravimeter at the start, finish and mid-cruise port calls. Over 28 days of the first leg the drift was -0.116 ±0.004 mgal/day and over the 26 days of the second leg the drift was -0.041 ±0.002 mgal/day.

A correction must also be made for the eastward component of the ship's velocity. This is known as the 'Eotvos' correction and is the vertical component of the Coriolis acceleration. An example of its importance is a comparison of 2 ships traveling East-West in opposite directions at 10 knts at the equator. The difference in gravity measured at the same point by both ships is 150 mgals. To apply the correction the ship's heading and speed should be known to an accuracy of ~5.0° and ~0.1 knts respectively. The effect is a maximum at the equator and zero at the poles. This correction is applied retrospectively by the shipboard computer system using the corrected navigation data. Any errors in the navigation will contribute to errors in the gravity via the Eotvos correction. At the latitude of the Cape Verde's the Eotvos correction will be accurate to ± 1 mgal for east-west tracks, at 5 knots, and ± 3 mgal for north-south tracks assuming the ship's heading is known to within 5° and the speed to within 0.1 knots. The free air gravity anomaly is finally calculated from the observed variation of gravity, relative to the base station, by subtracting the theoretical variation of gravity with latitude according to the International Gravity Formula (1967).

Analysis of track cross-overs gives an rms difference of 2.2 mgals.

2.5 BATHYMETRY

Values of bathymetry were obtained using an Institute of Oceanographic Sciences (I.O.S.) precision echo sounder (P.E.S.) mark III. The system uses a high frequency (12kHz) signal pulsed at 2 second intervals to record reflections from the seabed. The

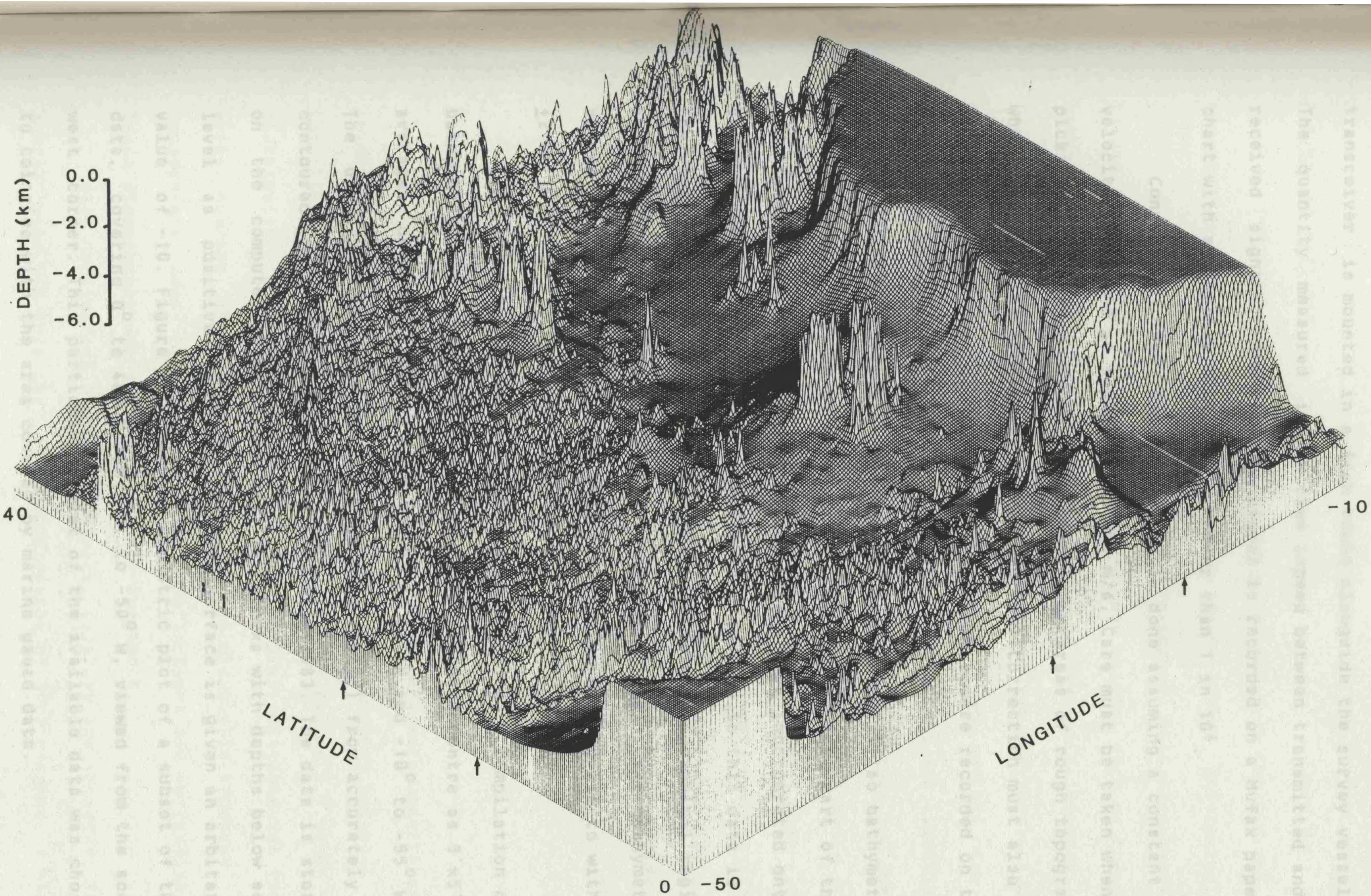

Figure 2.2 Isometric plot of bathymetric data available at Leicester University from the NGDC using the Synbaps program, <u>Van Wyckhouse (1973)</u>. The plot is viewed from the south-west. The African mainland and the eastern tip of South America are easily picked out. The original 5'x5' data set has been linearly interpolated onto a 7.5'x7.5' grid to coincide with the geoid height data over the same area. A subset of this data used in the analysis in Chapter 8 is indicated by the arrows.

transceiver is mounted in a fish towed alongside the survey vessel. The quantity measured is the time lapsed between transmitted and received signals. The received signal is recorded on a Mufax paper chart with a timebase accurate to better than 1 in 10^4.

Conversion from time to depth is done assuming a constant velocity for sound in seawater of 1500 m/s. Care must be taken when picking the returned signal, particularly in areas of rough topography where diffraction hyperbolae may be present. Correction must also be made for the depth of the towed fish. Time marks were recorded on the chart from the ship's clock.

No computer interface is available for the P.E.S. so bathymetry values were digitised by hand at 5 minute intervals as part of the watchkeeping duties. Later, 10 minute values were incorporated onto the computer database. The only correction applied to this data is for the variation of sound velocity in sea water with geographical region and depth. Carter's tables were used (Carter (1980)). The bathymetry values collected by RRS Shackleton are considered accurate to within ± 2 m.

In addition to the data along ship's tracks, a compilation of bathymetric data was obtained from the World Data Centre as 5'x5' averages over a total area covering 0° to 50° N and -10° to -55° W. The data is interpolated (van Wyckhouse (1973)) from accurately contoured maps compiled up to and including 1983. The data is stored on the computer at Leicester as 5°x5° blocks with depths below sea level as positive values and any land surface is given an arbitary value of -10. Figure 2.2 shows an isometric plot of a subset of this data, covering 0° to 40° N and -10° to -50° W, viewed from the south west corner. This particular subset of the available data was chosen to coincide with the area covered by marine geoid data.

2.6 MARINE DATA SET

A PDP11/34 computer monitored the output from the E-M log, gyrocompass, satellite navigation system, magnetometer, gravimeter and ship's clock at a frequency of one value/second. This represents rather an overkill in data density since values, such as the magnetometer, will not change with such a high frequency. However, the high sample rate does allow identification of spikes and spurious data points. The data were then averaged over 2 minute periods. The bathymetry data were entered at 10 minute intervals and linearly interpolated to 2 minutes to fit the density of the rest of the data.

The final data set was transfered to magnetic tape in merged-merged format (National Academy of Sciences (1972)) with cruise identifiers SHA1A/83 for the first leg, December 1982, and SHA1B/83 for the second leg, January 1983. The PDP11/34 data logger system worked very well through both legs of the cruise. The only section of data lost, due to logging malfunction, was from 0948 to 1250 on the 10th of December.

2.7 SEISMIC DATA

Seismic reflection and refraction experiments were undertaken to investigate the nature of the sediments and igneous basement comprising the upper part of the oceanic crust. Figure 2.3 shows the distribution of single channel seismic profiles available for this area; numbers indicate the locations of disposable sonobuoy deployments used to record wide angle reflections and refractions. These experiments are reported fully in Chapter 4.

Data collection required a source, receiver and recorder. The source used in this case was a combination of BOLT airguns, a high repetition pneumatic sound source giving a high density of shots/line

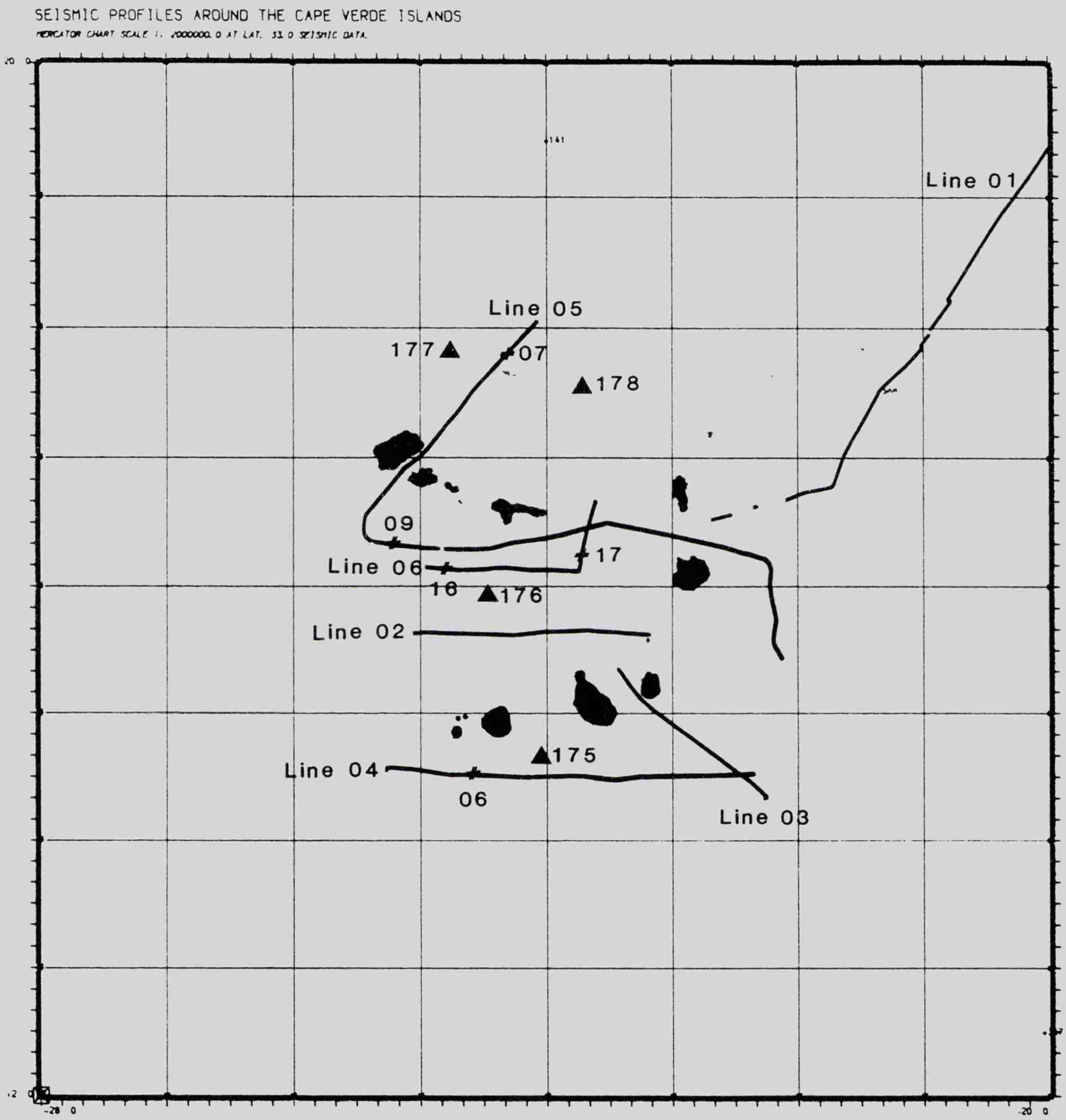

Figure 2.3 Chart of the distribution of seismic profile records over the Cape Verde Rise. Numbers correspond to positions of disposable radio sonobuoy deployments.

km. The receiver used for the continuous reflection profiling was a 30m array of hydrophones summed in series to give a single channel signal. A multichannel array was also used for part of the survey but due to a malfunction of the tape recorders this data could not be successfully replayed. Hard copy records of the received signal were plotted, after filtering, on electro sensitive paper chart recorders (EPC's). The records were annotated by hand at 30 minute intervals as part of the watchkeepers duties. Attempts to record the seismic signals on analogue magnetic tape failed due to hardware faults with the tape decks. The only records, therefore, available for analysis are the hard copies taken onboard ship.

Seimic refraction studies in deep water (>2 km) require source to receiver separations greater than the critical distance and to acheive this disposable radio sonobuoys were utilised. A single hydrophone detects the seismic energy and radios the signal back to a receiver on the shooting vessel. The sonobuoy is designed to sink after a preset interval and thus recovery is not necessary. The signal was recorded on an EPC and also on magnetic tape. The magnetic tape records were essential since the data was to be digitised at Leicester and replotted using scales more suitable for velocity analysis.

The sonobuoy type used in this experiment was Ultra Electronics SB6E4 transmitting on any one of 16 channnels between 162.25 MHz and 173.125 MHz. The hydrophone was suspended on a long wire to isolate it from wave generated noise and the wire incorporated a spring section to isolate the hydrophone from the motion of the sonobuoy. The sonobuoy is battery operated and self-scuttling after ≈8 hours.

The seismic energy was usually a 300 cu.in. BOLT airgun firing at 16 second intervals. The dominant frequency of this source is 14 hertz. This same source was also used for concurrent CSP. The frequency response of the hydrophone, according to the manufacturers specifications, is flat from 8Hz-200Hz.

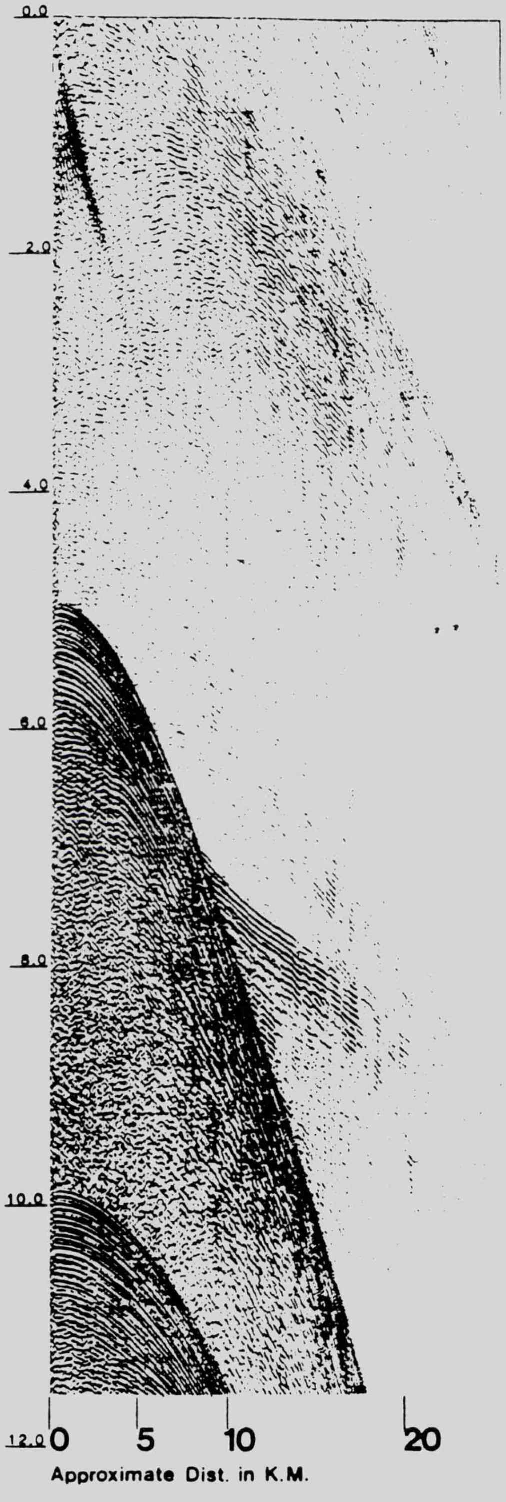

Figure 2.4 Electro-sensitive Paper Chart (EPC) record for sonobouy 07 taken on board ship during the experiment. This type of record does not lend itself to easy or accurate interpretation, serving only as a monitor during data acquisition. The vertical scale is seconds of two way travel time.

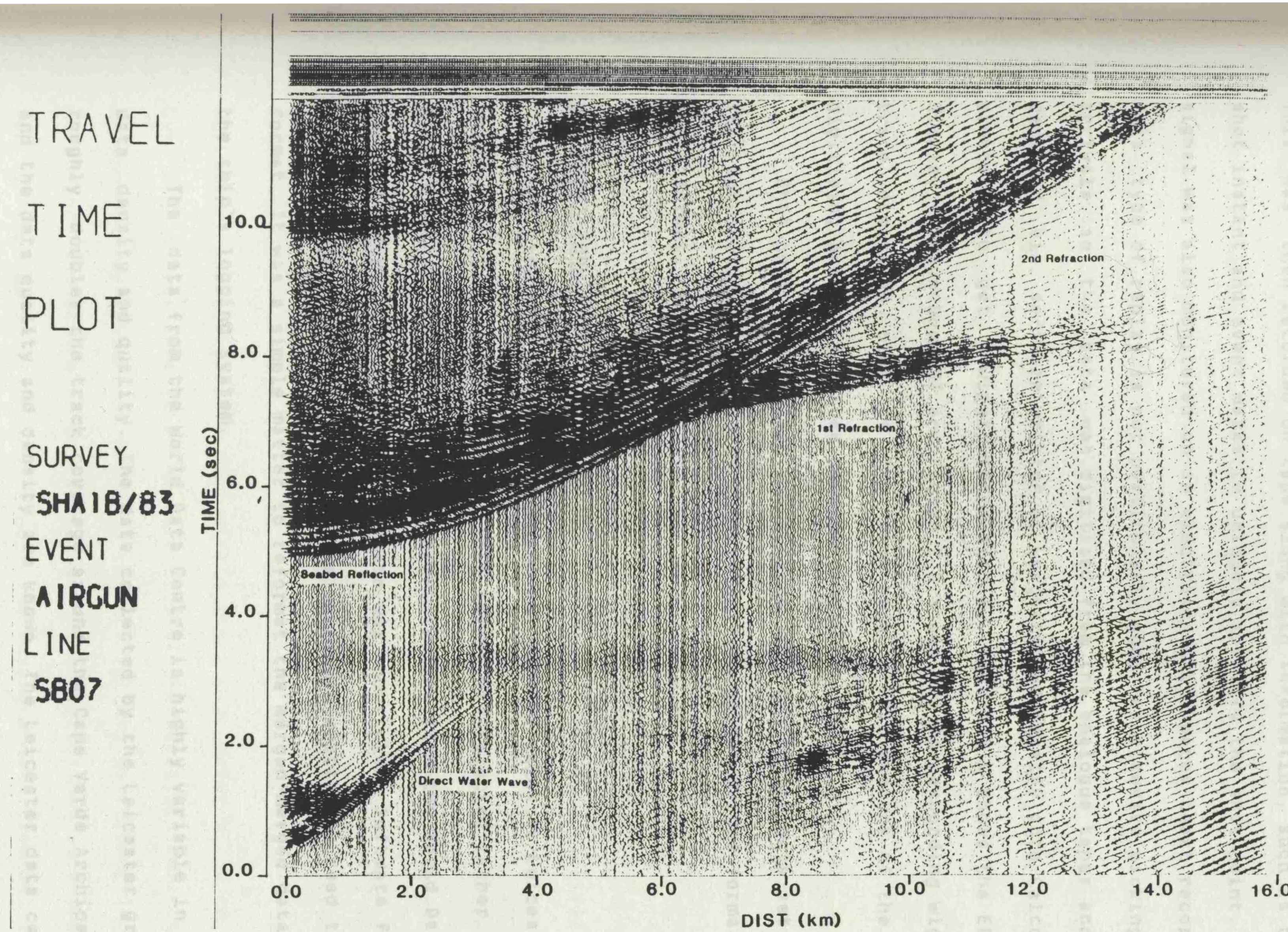

Figure 2.5 Wiggly trace plot of the same data shown in Figure 2.4 after digitisation. This type of plot is easier and more accurate to interpret. A considerable amount of data handling is, however, necessary to produce these plots.

A tunable receiver with variable output gain converted the frequency modulated sonobuoy radio signal back into a seismic signal. This was then recorded on tape along with information, such as the shot instant and event marks to uniquely identify the shot point. The signal was also monitored on an electrosensitive paper chart recorder. This type of replay is not particularly good for accurate picking of arrivals so the data was digitised from the analogue tapes and replayed via software written at Leicester University onto Calcomp plotters to get a wiggly trace display. Figure 2.4 shows the EPC display for sonobuoy 07 and Figure 2.5 shows the corresponding wiggly trace digitised plot of the same data. A full account of the digitising process is given in Appendix I.

Shot point information was entered into the marine data set, in the appropriate field, after conversion from Merged-Merged format to MGD77 format.

2.8 MGD77 FORMAT

All the ship's track data held on computer files at Leicester University is in MGD77 format. This format was selected rather by default since the data in this format arrived from the World Data Centre before the Shackleton cruise was undertaken. Software for plotting and analysing the data was therefore written to read this format. It was a simple matter to reformat the merged-merged data from the ship's logging system.

The data from the World Data Centre is highly variable in both data density and quality. The data collected by the Leicester group roughly doubles the track coverage around the Cape Verde Archipelago and the data quality and density are known. The Leicester data can be used as a quality check for the World Data Centre tracks.

2.9 SEASAT GEOID HEIGHT DATA

The SEASAT satellite, launched in June 1978, was equipped with, amongst other instruments, a radar altimeter (ALT), with which it was hoped to measure the height of the sea surface, relative to a reference ellipsoid, with an r.m.s. (root mean square) error of only 10 cm. Using the fact that the average sea surface height is an equipotential surface, undulations in the geoid can thus be mapped to a high degree of accuracy. The satellite and mode of operation are shown diagramatically in Figure 2.6.

The radar altimeter had 3 separate functions:

1) Measure the altitude from the satellite to the sea surface.

2) Estimate the Significant Wave Height (SWH), a measure of the sea surface roughness.

3) Measure the radar backscatter coefficient.

The third function does not concern us here, but the first and second are linked, in that the rougher the sea surface the less accurate the measurement of the altitude. The altimeter reflected a short duration (3 nS) pulse off the sea surface and timed the returned energy. The instrument operated at 13.5 GHz and the 'footprint', that area of the ocean that contributes to the reflection, had a diameter that varied from 2.4 to 12 km depending on the sea state. The altimeter was designed to stay within its r.m.s. error of 10 cm for SWH values less than 20 m. The attitude of the satellite vehicle was determined by sensors on board to correct for any deficiency in the direction the altimeter was pointing. These corrections were applied during the data processing stage. The analogue data from all the sensors on board was converted to digital form prior to transmission. Altimeter readings were taken at a rate of 10 Hz.

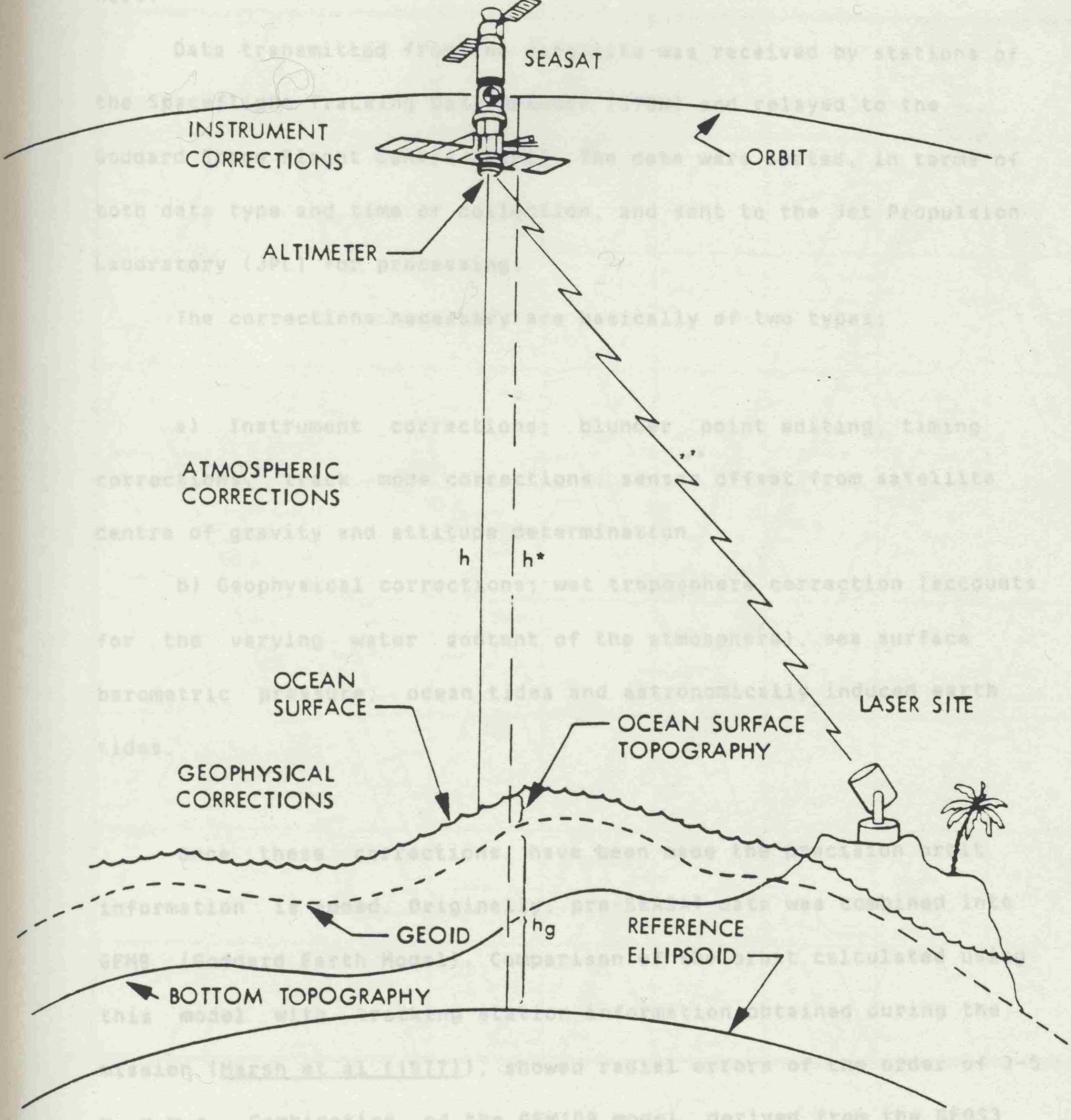

Figure 2.6 Diagram of the elements necessary to get the height of the marine geoid from satellite radar altimeter measurements. The corrections and mode of operation are outlined in the text.

Data collection and processing are complex and have been well described by Tapley et al (1982) so only a brief summary will be given here.

Data transmitted from the satellite was received by stations of the Spaceflight Tracking Data Network (STDN) and relayed to the Goddard Space Flight Centre (GSFC). The data were sorted, in terms of both data type and time of collection, and sent to the Jet Propulsion Laboratory (JPL) for processing.

The corrections necessary are basically of two types:

a) Instrument corrections; blunder point editing, timing corrections, track mode corrections, sensor offset from satellite centre of gravity and attitude determination.

b) Geophysical corrections; wet troposphere correction (accounts for the varying water content of the atmosphere), sea surface barometric pressure, ocean tides and astronomically induced earth tides.

Once these corrections have been made the precision orbit information is added. Originally, pre-SEASAT data was combined into GEM9 (Goddard Earth Model). Comparison of the orbit calculated using this model with tracking station information obtained during the mission (Marsh et al (1977)), showed radial errors of the order of 3-5 m r.m.s. Combination of the GEM10B model, derived from the GEOS3 satellite mission, with the PGS-S2 model, derived from tracking SEASAT, gave an improvement in radial orbit error; reducing it to 1.2 m r.m.s. This is still an order of magnitude larger than the required accuracy of 10 cm. Comparison of SEASAT geoid heights over the same area during the 3-day repeat orbit part of the mission shows that this

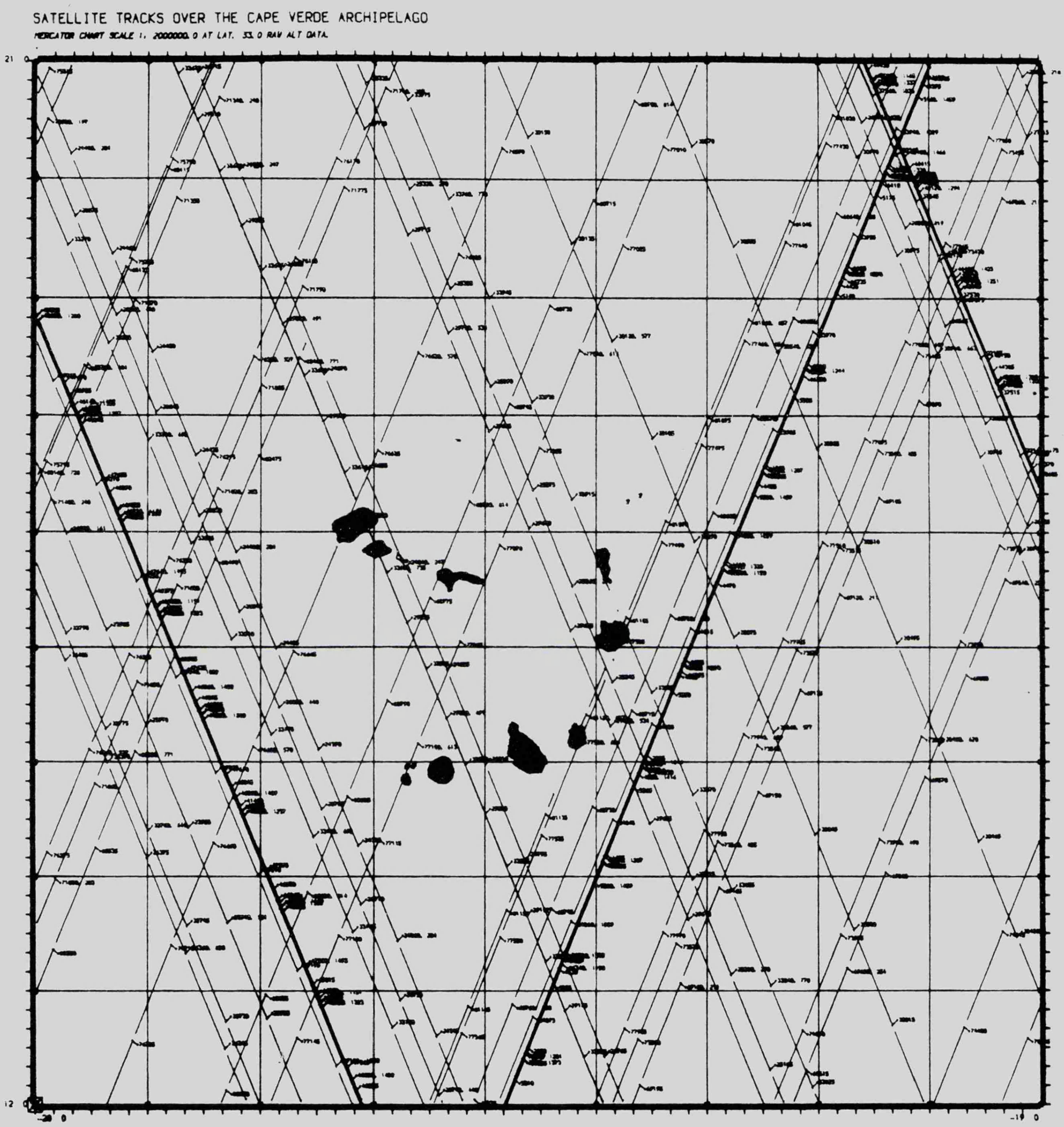

Figure 2.7 Seasat subsatellite tracks over the Cape Verde Rise. Thick lines indicate the tracks produced during the 3-day repeat orbit. Large gaps do exist in the track coverage. The satellite 'footprint', the diameter of the area illuminated by the radar, varied, according to the sea state, between 2.4 km and 12 km.

radial error results in a misfit of repeated tracks that can be approximated by a constant offset and a linear trend.

The SEASAT satellite lasted from 3rd of July 1978 to 10th October 1978 when a power failure cut short the mission. The satellite orbit was near-circular at an altitude of ~800 km. The orbit period was 101 minutes and SEASAT circled the earth 14 times/day.

The coverage in normal mode, from launch until 17th August 1978 gave an equatorial track spacing of ~165 km. After this period the satellite was manoeuvred into an orbit that repeated every 3 days (3-Day Repeat Orbit). Repeat tracks at an equatorial spacing of ~900 km were completed, up to a repeat coverage of 8, until the spacecraft failed. The total track coverage in the vicinity of the Cape Verde Rise is shown in Figure 2.7; heavy lines denote repeat tracks. Data was made available from JPL via the Institute of Oceanographic Sciences (IOS) in the form of a Geophysical Data Record (GDR) Lorrel et al (1980). The GDR and accompanying Algorithm Specifications, Lorrel (1980), contain sufficient information to reconstruct any of the corrections applied to get the final altimeter height, relative to a reference ellipsoid with semi-major axis of 6378137 m and flattening of 1/298.257 .

The along track density, in the GDR, corresponds to ~7 km/data point. During the processing sequence the original 10 Hz sample rate was averaged to give a reading every 1 second. The satellite was designed to turn itself off over land areas and occasionally failed to turn back on immediately. The instruments were also turned off during manoeuvring. These facts, plus blunder point editing, account for any gaps in the tracks shown in Figure 2.7.

An additional geoid data set was made available by R. Rapp from Ohio State University in the U.S.A. This data set consisted of

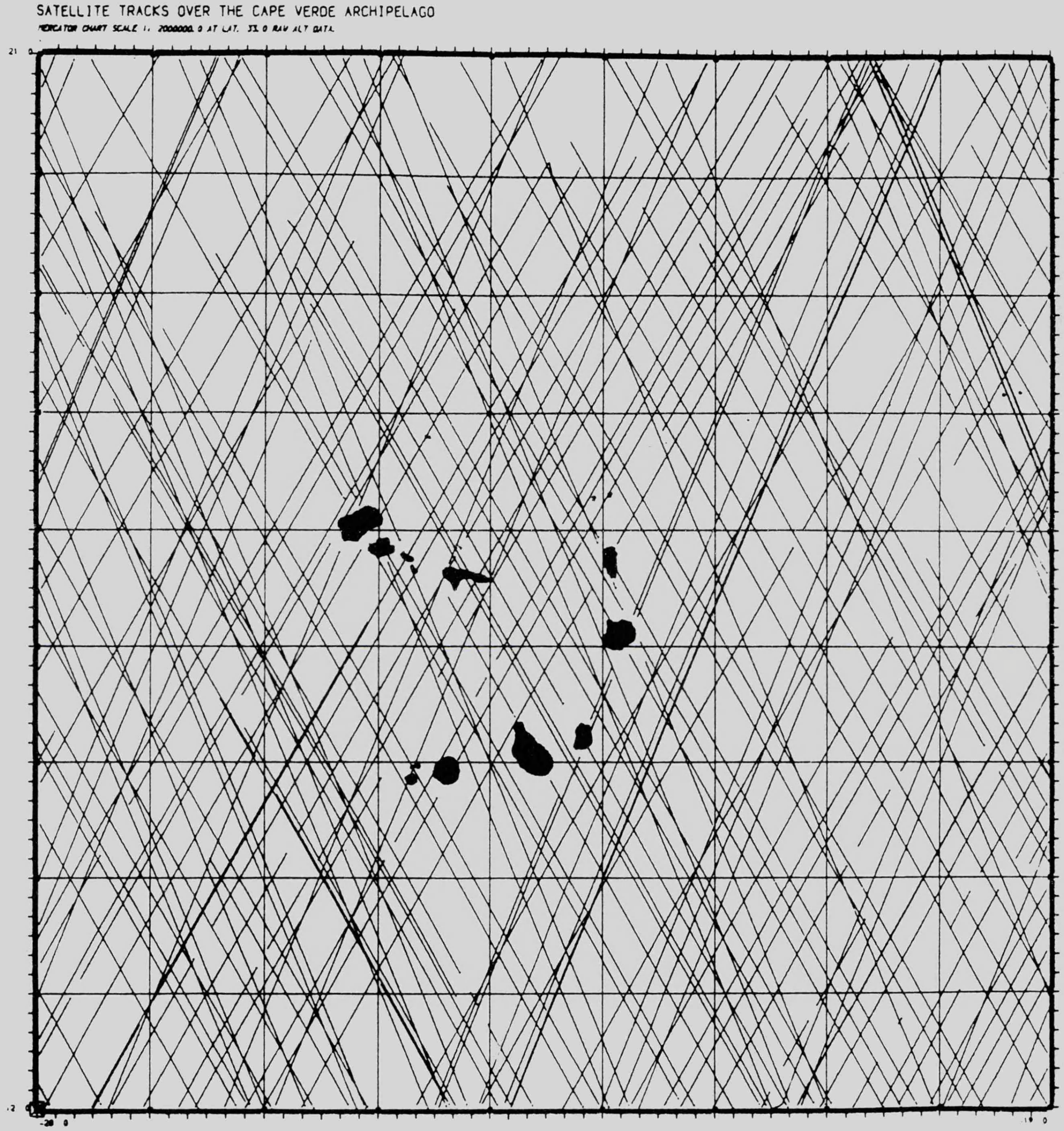

Figure 2.8 Combined SEASAT and GEOS3 track coverage over the Cape Verde Rise. The increase in track density is sufficient to interpolate the geoid heights on to a 7.5'x7.5' grid.

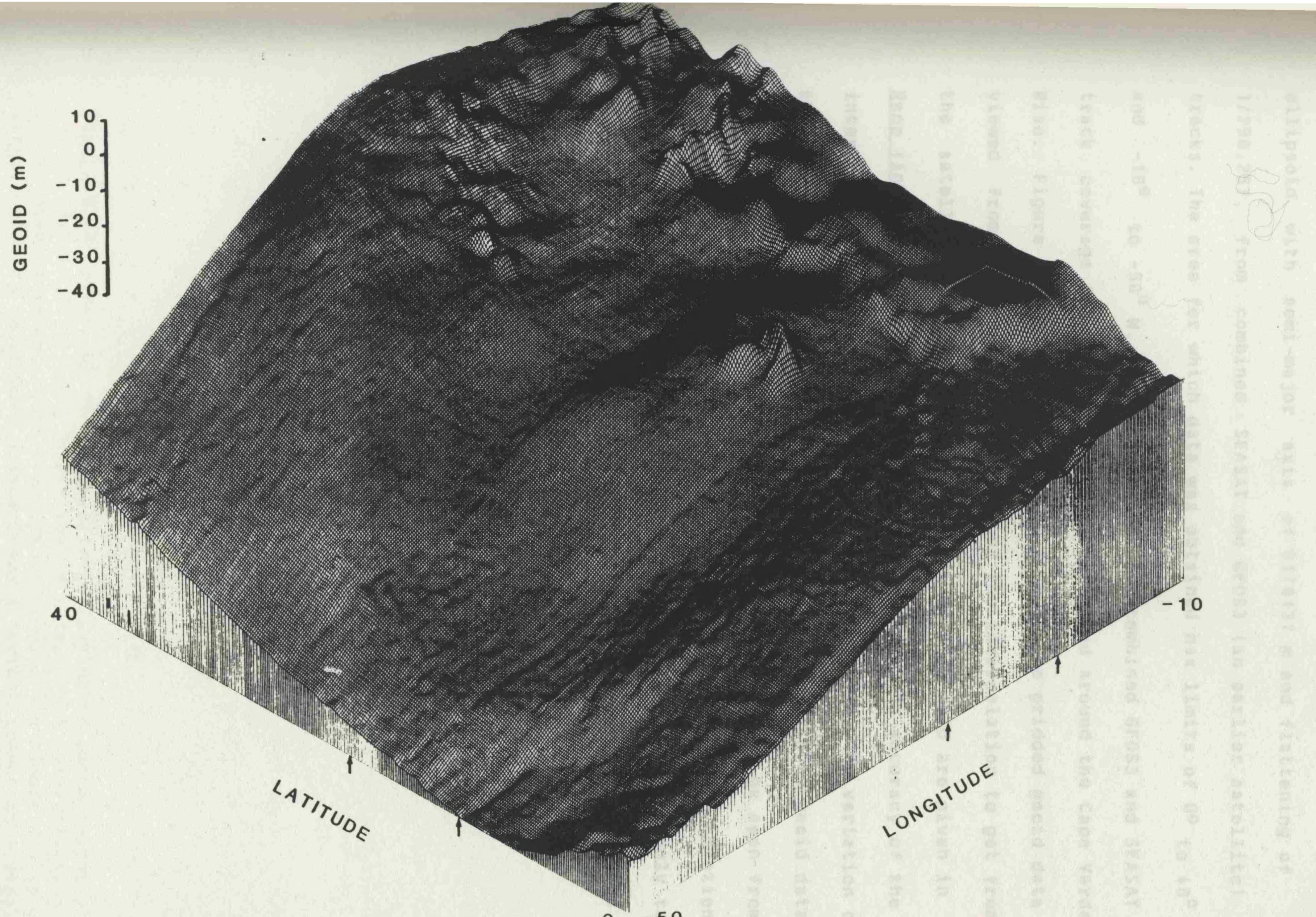

Figure 2.9 Isometric plot, viewed from the south-west, of the gridded geoid height data. The data covers the same area as Figure 2.2. The land areas corresponding to Africa and South America have highly variable geoid heights. The Cape Verde Rise and the Cape Verde Islands stand out quite well in this isometric view. The subset of the data used in the analysis in Chapter 8 is shown by the arrows.

7.5'x7.5' gridded values of geoid height, with respect to a reference ellipsoid with semi-major axis of 6378137 m and flattening of 1/298.257, from combined SEASAT and GEOS3 (an earlier satellite) tracks. The area for which data was obtained has limits of 0^{o} to 40^{o} N and -10^{o} to -50^{o} W. Figure 2.8 shows the combined GEOS3 and SEASAT track coverage for a smaller area concentrated around the Cape Verde Rise. Figure 2.9 shows an isometric plot of the gridded geoid data viewed from the south west. Details of the interpolation to get from the satellite track measurements onto a regular grid are given in Rapp (in press). A simple check can be made on the accuracy of the interpolation by examining a sub-satellite profile of the variation of the sea surface height and comparing this with the gridded geoid data set. Figure 2.10 shows just such a comparison and it can be seen from this that the gridded data set is a somewhat smoothed representation of the data contained on the sub-satellite profiles. This is only to be expected since the degree of smoothing will be determined by the satellite track spacing rather than the along track data density.

COMPARISON OF GRIDDED GEOID HEIGHTS WITH SEASAT GEOID HEIGHTS

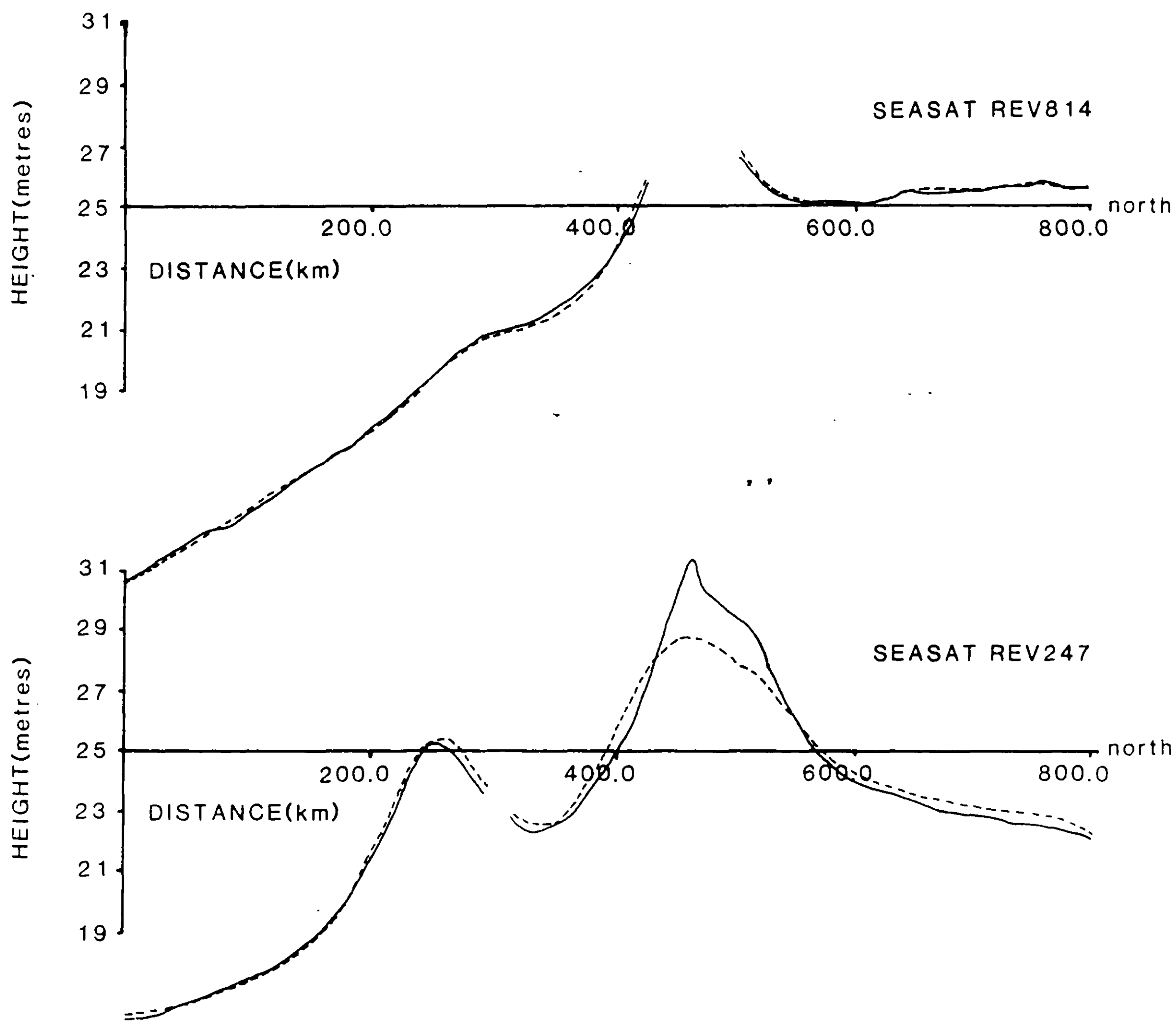

Figure 2.10 Comparison of the observed variation of geoid height along Seasat tracks REV814 and REV247 (solid lines) with interpolations of the gridded geoid height values (dashed lines). The comparison is good except at very short wavelengths where a certain amount of averaging has taken place to get the interpolated gridded values. This is discussed in greater detail in Chapter 8.

CHAPTER 3 (MAGNETIC STUDY)

3.1 INTRODUCTION

The Cape Verde Islands form a horseshoe shaped archipelago, opening to the west, that lies on the Cape Verde Rise, ~500 km, from the Senegalese coast of West Africa. The islands and the western part of the rise lie within the 'M' sequence of magnetic reversals formed between 108 & 155 Ma. These sea floor spreading anomalies provide an excellent means of determining the structure of the oceanic crust which now constitutes the rise. The eastern sequence of Mesozoic magnetic anomalies has been studied by Rona et al (1970) and Hayes & Rabinowitz (1975). The latter study in particular included the 'M' sequence to the north and south of the Cape Verde Islands and inferred the existence of a fracture zone passing through the archipelago between latitudes 15° 30' N and 16° 10' N. This was later confirmed and refined to a fracture zone at ~16° 00' N by van der Linden (1981), who studied the the older end of the sequence from the African coast to ~M20.

The islands are orientated along 2 prominent ridges as shown in Figure 3.1. This has lead previous workers (King (1974), Dash et al (1976)) to suggest that the islands formed along pre-existing zones of weakness in the oceanic crust. Bebiano (1932) proposed that the islands formed at the intersection of a series of major fractures. Robertson (1984) also inferred, from sedimentological evidence, the existence of a fracture zone passing through the island of Maio.

Using the theory of sea floor spreading first postulated by Hess (1962) and the observations of Vine (1966) that magnetic anomalies measured at sea can be related to reversal sequences, the regional structure of the oceanic crust can be determined by examining total magnetic field anomalies. In the absence of fracture zones, peaks and troughs in the anomalous magnetic field should form linear patterns perpendicular to the spreading direction. Any offsets in the linear pattern can be attributed to fracture zones and the accuracy with which these can be defined is dependent on the track coverage.

The heating event which must have accompanied the formation of the volcanic islands may have partialy masked or even obliterated the anomaly sequence nearby, since preservation of the magnetic remanence is dependent on the rocks being cooled through their Curie point and remaining below this temperature for the rest of their geological history. Hayes & Rabinowitz (1975) did not identify any anomalies within the archipelago itself and Dash et al (1976), although including a track crossing the archipelago, did not relate it to any reversal sequence, but simply correlated it with tracks to the north and south. Until the present study it was unknown whether anomalies correlatable with a recognised reversal sequence existed within the archipelago.

If it is assumed that seafloor spreading was a symmetric process during creation of the Mesozoic oceanic crust then the 'M' sequence should be directly related to its western counterparts. Studies near Bermuda have been carried out by Vogt et al (1971) and Schouten & Klitgord (1982) and they show that several small offset (<20 km.) fracture zones exist. Work by Le Pichon & Fox (1971) proposed that a fracture zone existed to the north of the Cape Verde Islands that coincided with the Cape Fear fracture zone when the North American and African plates were juxtaposed in their pre-rifted configuration. The current evidence, from the western Atlantic, (Schouten & Klitgord pers.comm.), would suggest that palaeogeographical reconstructions place the Blake Spur fracture zone in close proximity to the Cape Verde Archipelago during creation of the 'M' sequence.

New data have been collected around the Cape Verde Archipelago in an attempt to further define the fracture zones identified by Hayes & Rabinowitz (1975). In addition it is hoped to clarify the question of whether the islands are related to pre-existing features of the oceanic crust.

3.2 PRESENT STUDY

The principal data source for this study is Leicester University's investigation of the Cape Verde's hotspot. Total magnetic field data were collected on board the RRS Shackleton during a marine geophysical project to study the archipelago. Additional data were made available from the National Geophysical Data Centre (NGDC) in MGD77 format (Hittleman et al (1981)) computer files and Table 3.1 lists the data used in this study by the cruise identifier. Figure 3.1 shows the track coverage superimposed on a bathymetric map of the Cape Verde Rise. All the data are total magnetic field values, collected underway, after removal of the appropriate International Geomagnetic Reference Field (IGRF), or in the case of the Discoverer (DICPVERD) after removal of a regional trend. The IGRF leaves a residual positive anomaly of ~250 nT as was noted by van der Linden (1981). This does not affect the interpretation of the anomalies since the wavelengths of the reversal anomalies are ~50 km. and the residual magnetic high appears to have wavelengths greater than the dimensions of the rise (~500 km).

The density of the data along track depends on the ship's speed and the sampling rate of the instrumentation and varies from an average of ~2.98 samples/km. for the Shackleton to an average of ~0.42 samples/km. for the Vema. Where large gaps exist (>20 km), such as on the Atlantis II tracks, no interpolation has been attempted. The orientation of the tracks is generally east-west and data were so

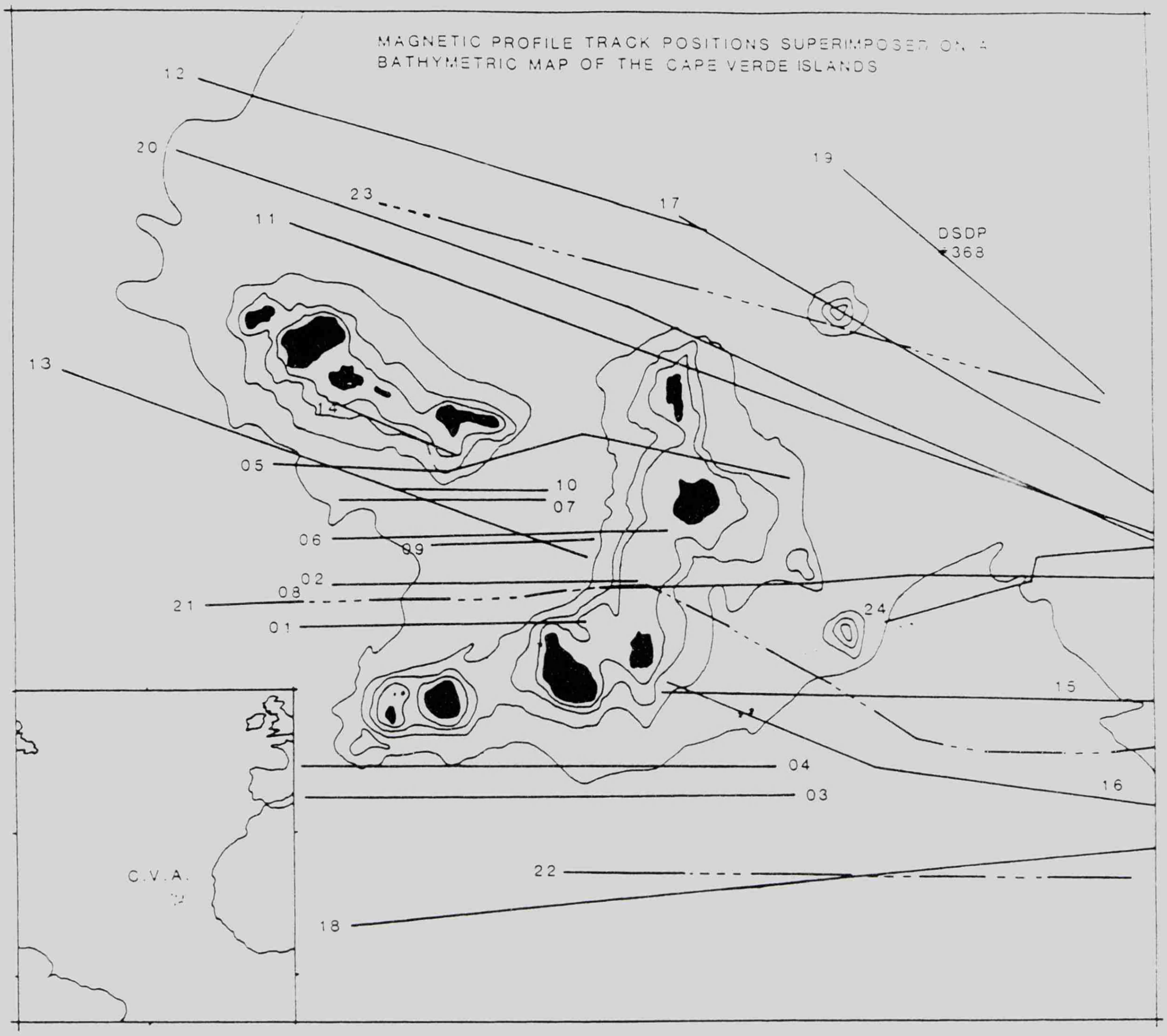

Figure 3.1 Track chart superimposed on a bathymetric contour map of the Cape Verde Archipelago. Contour interval is 1000 m. Numbers refer to profiles in Table 3.1. Inset shows the relation of the archipelago to the African mainland.

Table 3.1 Details of track portions used in this analysis. Profile numbers correspond to track chart of Figure 3.1. Cruise names and times correspond to MGD77 format, Hittleman et al (1977).

PROFILE NUMBER	CRUISE NAME	START TIME	END TIME	SOURCE OF DATA
01	SHA1A/83	82120922	82121009	Leicester University
02	SHA1A/83	82121012	82121108	" "
03	SHA1A/83	82121314	82121407	" "
04	SHA1A/83	82121409	82121515	" "
05	SHA1B/83	83010620	83010804	" "
06	SHA1B/83	83011222	83011314	" "
07	SHA1B/83	83011314	83011403	" "
08	DISC/143	83122300	83122502	Cambridge University
09	DISC/143	83122817	83122904	" "
10	DISC/143	83123107	83123114	" "
11	DICPVERD	70072903	70073101	World Data Centre
12	DICPVERD	70080104	70080116	" " "
13	DICPVERD	70080201	70080306	" " "
14	DICPVERD	70080414	70080419	" " "
15	DICPVERD	70080612	70080702	" " "
16	V2207	66052608	66052712	" " "
17	V2603	68101905	68102006	" " "
18	V3101	74010400	74010506	" " "
19	V3206	75021917	75022010	" " "
20	A2067L01	72013120	72020202	" " "
21	A2075L01	73020408	73020610	" " "
22	A2075L04	73042612	73042718	" " "
23	A2075L04	73042908	73043012	" " "
24	KA68F	68072900	68073010	" " "

collected, by the RRS Shackleton, as to not cross possible fracture zones. Figure 3.2 shows a compilation of all the magnetic anomaly data projected onto tracks with a 100^{o}-280^{o} orientation. The magnetic lineations are roughly normal to this direction (Hayes & Rabinowitz (1975)). The data have been roughly aligned on the trough corresponding to M22 using the Larson & Hilde (1975) reversal sequence to facilitate correlations from profile to profile. Where tracks do not extend as far east as M22 the data have been roughly aligned on the trough corresponding to M0.

Also shown in Figure 3.2 is a profile computed for a model using the magnetic reversal sequence of Larson & Hilde (1975). The Palaeopole, for the early Cretaceous, was taken from Smith et al (1981) which gives a declination of -35^{o} and an inclination of $+30^{o}$ for the remanent field. The present field

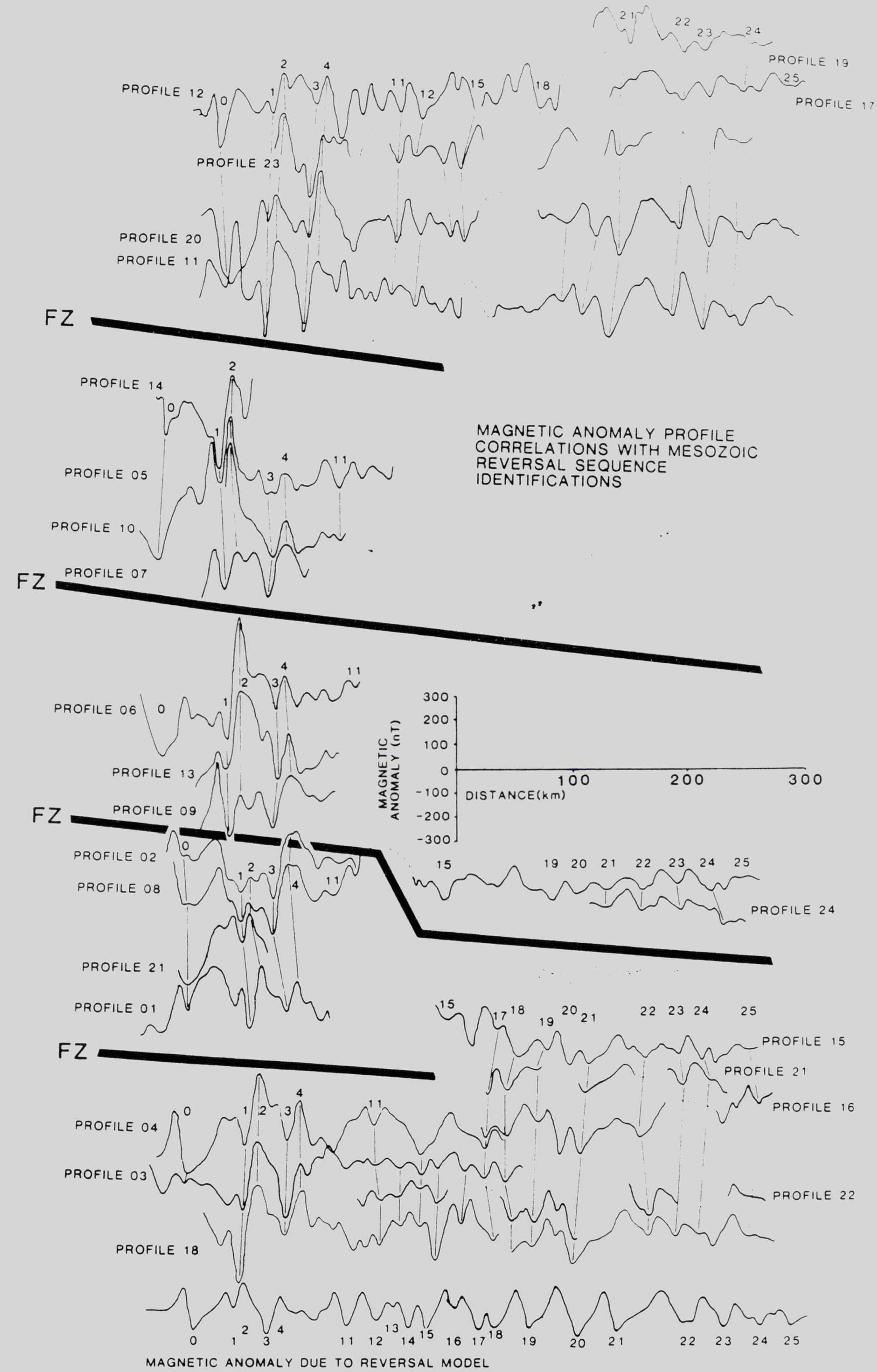

Figure 3.2 A compilation of the magnetic anomaly profiles shown in Figure 3.1 Profiles have been aligned on the trough corresponding to M22 but where tracks do not extend sufficiently far east, The trough corresponding to M0 has been used. A model magnetic anomaly profile is shown at the bottom for comparison. The parameters of the model are given in Table 3.2. The scales are as shown and are the same for both the observed and the model. Positions of the fracture zone traces are indicated. The profiles are roughly aligned on anomaly M22.

orientation has a declination of -17° and an inclination of $+20^{\circ}$. The depth to the source layer is assumed to vary with age according to the normal age/depth relationship of Parsons & Sclater (1977) and the source layer is assumed to be a constant 0.4 km. thick. This thickness is similar to values used by both Larson & Hilde (1975) and Hayes & Rabinowitz (1975). Table 3.2 lists the model parameters that best fit the majority of the observed profiles. Periods of normal polarity correspond to peaks in the anomalous field and reversals correspond to troughs. These have been numbered according to the system of Larson & Hilde (1975) and compared with the observed profiles. A decrease in anomaly amplitude occurs at the older part of the 'M' sequence, as was discussed by Hayes & Rabinowitz (1975), and has been modelled in this study by a ~30% decrease in remanent magnetisation intensity at 140 Ma. Recent studies by van der Linden (1981), off the African coast, and Barret & Keen (1976), in the Northwest Atlantic, suggest that reversals occur that are older than M25 within the Jurassic quiet zone. These have not been included in the model used here since they would occur far to the east of the archipelago and within the zone of low amplitude anomalies.

Table 3.2 Parameters of model. Uses reversal time scale of Larson & Hilde (1975). Assumes the normal age/depth relationship. The magnetised layer is assumed to be 0.4 km thick.

AGE	ANOMALY	SPREADING RATE
108	M0	0.80 cm/yr
120	M8	0.60 "
126	M11	0.95 "
141	M19	1.86 "

3.3 RESULTS

Correlations from profile to profile are generally very good. A distinctive large (125 nT peak to trough) anomaly can be seen, corresponding to the reversed period at anomaly M22, that persists throughout the survey area. Similarily a peak representing anomaly M2, a normal interval, is well developed throughout the area. Anomaly identifications, by comparison with the model curves, are good for the section from M16 to M23; possibly because the model is a better approximation, in terms of the depth to the source layer, in this region than closer to the islands. Identification of M24 and M25 is not always possible due to a decrease in amplitude of the observed anomalies. M25 has been recognised throughout this study as a trough (reversed interval) rather than the peak (normal interval) identified by both Van der Linden (1981) and Hayes & Rabinowitz (1975). High amplitude (500 nT), intermediate wavelength (20 km) magnetic anomalies are associated with shallow (<1500 m) bathymetric features such as inter-island ridges and isolated seamounts. The proximity of the source layer and the possibility that the remanent magnetisation is due to later, island-forming, igneous activity means that these anomalies have been ignored when comparing observed profiles with model anomalies.

The part of the sequence between M4 & M11 has very indistinct anomalies, characterised by many short wavelength, low amplitude variations. The remainder of the 'M' sequence compares well with the model profiles; see Figure 3.2.

Figure 3.3 shows the identified anomalies plotted on a chart of the Cape Verde Archipelago. Positive identifications are indicated by dots, linear trends are shown as thin lines, projected trends are shown as dashed thin lines and inferred fracture zones are indicated by heavy lines. Where a fracture zone is inferred from changes in the magnetic character the trace of the fracture zone is shown as a dashed heavy line. A total of 4 fracture zone traces have been identified; a northern trace at ~16° 40' N, southern trace at ~15° 00' N and a pair of traces passing through the centre of the archipelago. The central

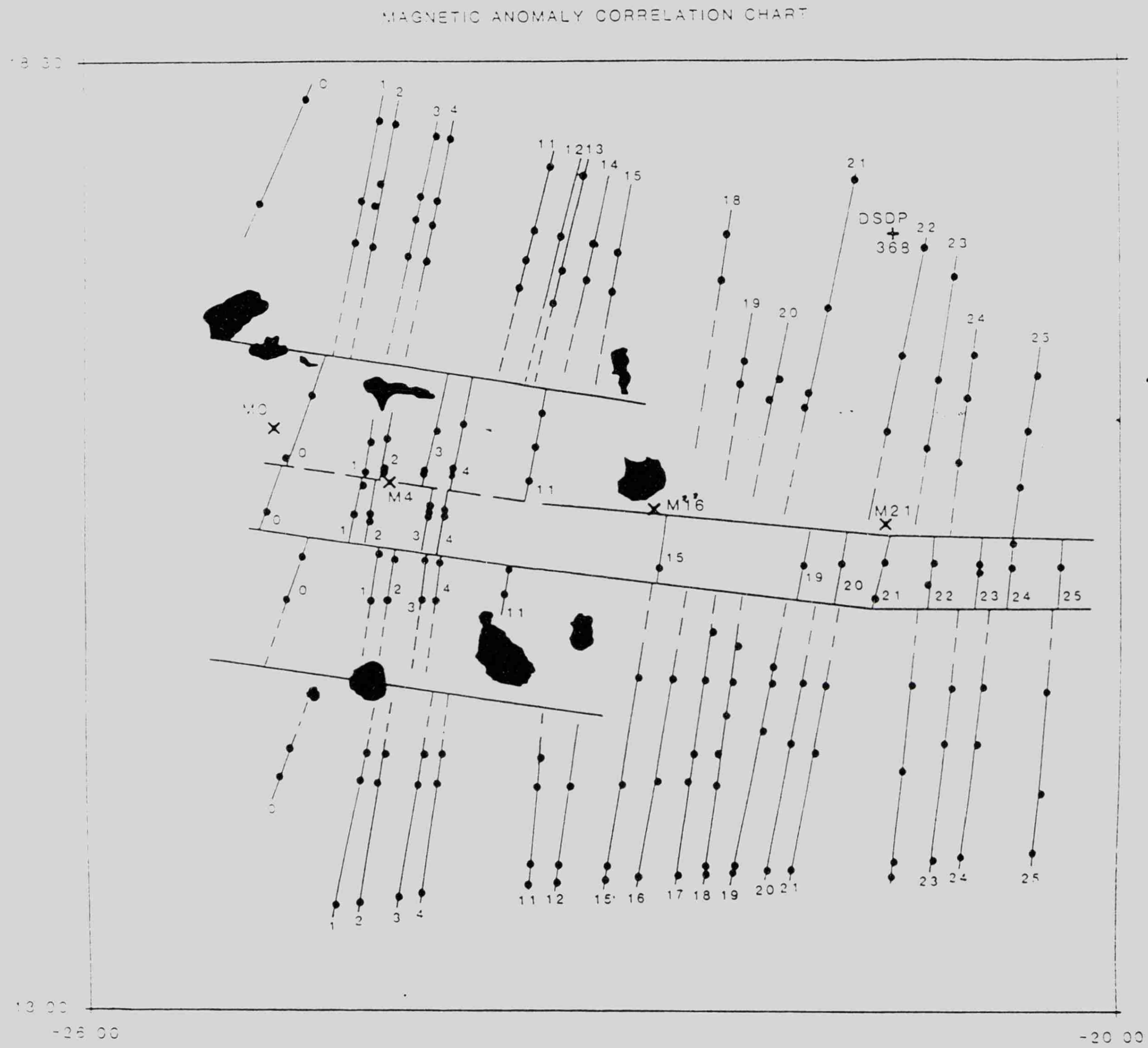

Figure 3.3 Identified anomalies are plotted on a chart of the cape verde islands. Dots indicate actual identifications, lines show anomaly correlations and dotted lines are projected identifications. Fracture zones are shown by heavy lines. The rotated positions of the anomalies from the Western Atlantic are shown as crosses.

fracture zone has been delimited, not only by offsets in the lineation pattern, but by changes in the magnetic signature. The displacement along the fracture zones is not constant and reaches a maximum of ~30 km at M0, the youngest end of the 'M' sequence, on the northern fracture zone trace. Both the northern and southern fracture zone traces do not become apparent until after M15 times.

The orientation of the spreading lineations appears to change from ~004° N at M25 to ~018° N at M0, with a significant proportion of the change taking place around M22 times. This change can also be seen in figure 3 of Hayes & Rabinowitz (1975). It is considered that this reorientation is real but variations due to the nature of the source layer make any systematic analysis of the spreading direction difficult.

3.4 DISCUSSION

Many of the observed variations can be accounted for by the theory of Schouten & White (1980) that sea floor spreading occurs in discrete cells that are independent of their neighbours. Offsets may be either spatial or temporal, although in general individual cells may have approximately the same spreading history. In detail, however, the cells may have different magnetic signatures. This can be seen, to some extent, in Figure 3.2 where anomalies such as M2 and M22 have quite different shapes and amplitudes in each of the spreading cells, delimited by the inferred fracture zones. The offsets recorded by this study are only small, relative to contemporary transform faults, with a maximum age-offset of only 3 Ma, at the central fracture zone during M0 times, corresponding to a spatial offset of only 30 km. This contrasts with age-offsets of 10-20 Ma for the Kane and Vema fracture zones at the Mid-Atlantic ridge.

Figure 3.4 shows the variation of distance, relative to M22, for

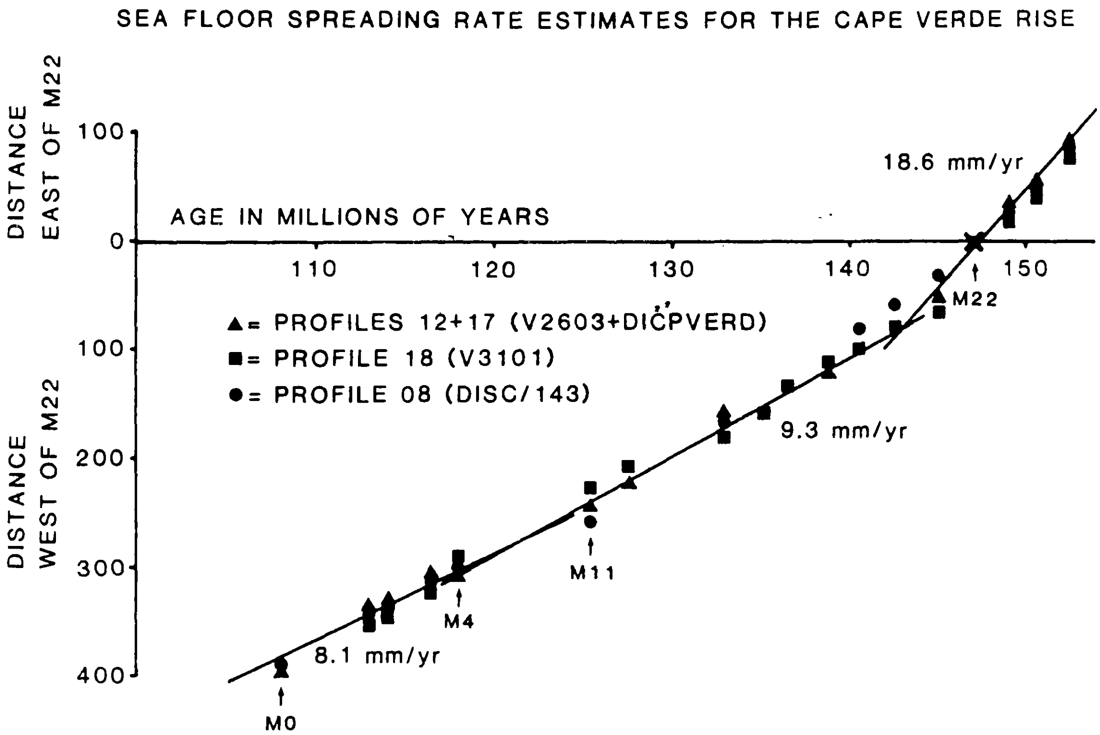

Figure 3.4 Identified anomalies for 3 selected track portions, V3101, DISC/143 and DICPVERD+V2603, are plotted with respect to M22 against age, in Ma. The lines are taken from Schouten & Klitgord (1982) and constrained to pass through M22 assuming the Hawaiian lineations have a constant spreading rate of 3.0 cm/yr. The excellent fit of the spreading rates, calculated for the Western Atlantic, to the data obtained here for the Eastern Atlantic suggest that spreading was symmetric during the Mesozoic. The arrows indicate particular anomalies refered to in the text.

3 tracks spanning a large proportion of the 'M' sequence. Each track is taken from a separate spreading cell, defined as being between two fracture zones. The gap between M4-M11 is due to lack of identifiable anomalies on the observed profiles. The exact shape of the anomalous magnetic field generated for the model is very sensitive, in this part of the sequence, to variations in spreading rate since the inferred spreading rate is low and magnetised blocks are correspondingly narrow. Also shown in Figure 3.4 are spreading rate estimates made by Schouten & Klitgord (1982) for the Western Atlantic counterparts of the 'M' sequence. The spreading rate curves from the Western Atlantic have been constrained to pass through M22 and have been calculated assuming a constant spreading rate for the Hawaiian lineations of 3.0 cm/yr. The excellent fit of spreading rates from the western counterparts of the 'M' sequence observed here suggests that spreading was symmetric during this part of the Mesozoic. The uncertainty between M4-M11 means that no estimate of the spreading rate can be made for this interval. The observation, here, that 3 distinct changes in spreading rate took place, at ~M22 times and M11-M4 times (2 changes) is the same as that made by Schouten & Klitgord (1982) in the Western Atlantic. The same workers also state that the period of slow spreading, between M11 and M4, is characteristic of the Mesozoic central North Altantic regime.

Little direct evidence is available about the age of the oceanic crust around the Cape Verde Islands. The D.S.D.P. hole 368 drilled on leg 41 of the ocean drilling program did not penetrate basement and gives an age of ~100 Ma (Albian-Turonian) for the lowermost sediments encountered, Lancelot & Seibold et al (1977). The position of hole 368 is shown on Figure 3.1. The magnetic anomaly data would suggest an age for basement of ~144 Ma (M21-M22) which does not contradict the borehole evidence. Geological mapping on the island of Maio by

Stillman et al (1982) identified lavas of Mid-Ocean Ridge pillow basalts. Dating of these rocks by K-Ar and $^{40}Ar/^{39}Ar$ methods, by Mitchell et al (1983), yields a minimum age of ~113±8 Ma. Magnetic anomalies constrain the age of the ocean crust to lie between 128-131 Ma. The agreement between the dates from completely different methods is reasonable, despite the possibility of thermal overprinting of the rocks exposed on Maio.

A recent study by Tucholke & Ludwig (1982) suggests that the younger end of the 'M' sequence is associated with an increase in basement topography between M0-M4. This is so well developed in places that a ridge is formed protruding above the blanketing sediments. This has been called the J-Anomaly ridge in the North Western Atlantic and the Madeira Torre rise in the Eastern North Atlantic. Similarily, a study by Purdy & Rohr (1979) observed a basement ridge associated with M0. During the present study a number of continuous single channel seismic profiles, see Chapter 4, were shot while collecting the magnetic data. Oceanic basement cannot always be identified but Figure 3.5 shows the interpreted basement topography and corresponding magnetic anomalies for profile 04. The formation of the basement ridge, arrowed, is considered to be strong support for the correct identification of M0. Variations in source layer topography may also account for the differences in the magnetic signature of M0.

Using the absolute poles of rotation, determined by Klitgord & Schouten, taken from Schult & Gordon (1984), the position of anomalies M0, M4, M16 and M21 to the north of the Blake Spur fracture zone, from Mutter & Detrick (1984), can be rotated to their equivalent positions in the eastern 'M' sequence. Table 3.3 lists the poles, rotations and times used to plot the rotated anomalies, shown as crosses, in Figure 3.3. The rotated anomalies are sufficiently close to the central fracture zone to suggest that this fracture zone is the eastern counterpart of the Blake Spur fracture zone.

COMPARISON OF MAGNETIC PROFILE LINE 04
WITH BASEMENT STRUCTURES FROM SEISMIC REFLECTION

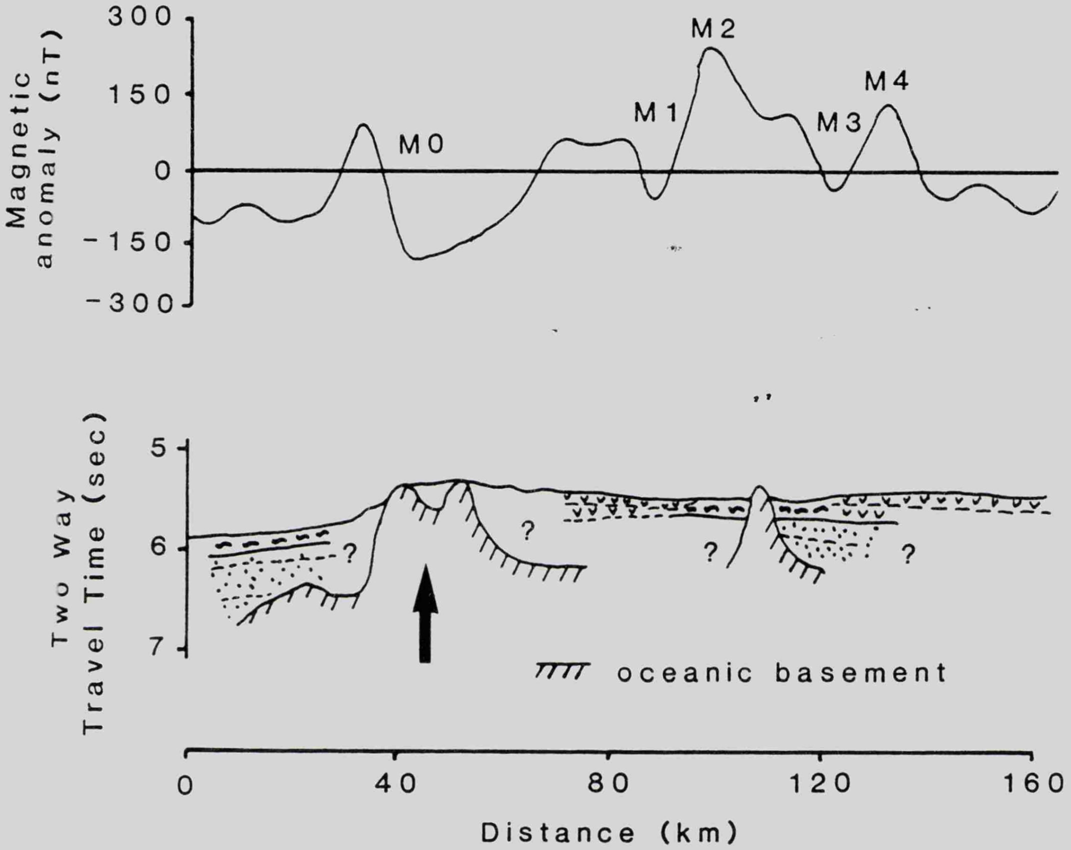

Figure 3.5 Magnetic anomalies for track 04 with the basement structures interpreted from seismic profiling shown beneath. The arrowed basement ridge is thought to correspond to the J-Anomaly ridge at M0 times.

Table 3.3 Poles of rotation used to rotate the trace of the Blake Spur fracture zone in the Western Atlantic, relative to the American continent. Ages are in Ma. The errors on each determination are unknown.

AGE	ANOMALY	LATITUDE	LONGITUDE	ANGLE
108	M0	66.30	340.10	-54.3
114	M4	66.10	341.00	-56.4
135	M16	66.10	341.60	-59.8
145	M21	66.10	341.60	-63.2

Changes in orientation of the spreading direction may have resulted in the introduction of the northern and southern fracture zones. Using the model of Menard & Atwater (1968) whereby reorientation is accomplished by the introduction of adjustment fractures; the offsets across the fracture zones can be related to the times of changes in spreading direction. Thus the reorientation at M4 times resulted in the commencement of spatial offsets on all the fracture zones observed here. Offsets are observed at a maximum at M0. The larger reorientation at M21 times does not appear to have influenced the fracture zone offsets to the same degree and it is not known at present why this should be so.

The relationship of the islands to the fracture zones is not clear. The northern fracture zone can be made to pass through S. Antao to S. Nicolau without contradicting the magnetic evidence. The southern fracture zone, however, is better defined and does not appear to pass through the island of Maio as was suggested by Robertson (1984). The question is then raised as to why the islands should form as they have done and not along the Blake Spur fracture zone which may have been a major structural feature and zone of weakness in this area during the Mesozoic.

3.5 CONCLUSIONS

1) Seafloor spreading magnetic anomalies can be identified within the Cape Verde Archipelago. These anomalies can be correlated with the Mesozoic reversal sequence of Larson & Hilde (1975).

2) The single fracture zone identified by Hayes & Rabinowitz (1975) has been refined to 4 fracture zones by this study. Offsets are variable with time, being a minimum at M25, less than 5 km, and a maximum at M0, ~30 km. The 2 fracture zones inferred passing through the centre of the archipelago are considered to be the eastern expression of the Blake Spur fracture zone identified by many workers in the western North Atlantic.

3) The 'M' sequence observed here compares very well, in terms of both spreading rate and spreading direction changes, with the western Atlantic described by Schouten & Klitgord (1982).

4) How well the existing structures of the oceanic crust relate to the distribution of the Cape Verde Islands has not been fully resolved. The possibility still exists that the northern most east-west limb of the archipelago has formed along a fracture zone trace. However more work is necessary to both study basement structures to the west of the archipelago and to obtain magnetic data closer to the islands.

CHAPTER 4 (SEISMIC INVESTIGATION)

4.1 INTRODUCTION

The age of the oceanic crust comprising the Cape Verde Rise can be estimated to range from 105 Ma, in the West, to 145 Ma, in the East, from seafloor spreading magnetic anomaly studies (Hayes & Rabinowitz (1975) and Chapter 3). Using the relationship between depth to oceanic crust and age, determined empirically by Parsons & Sclater (1977) for all the world's oceans, the expected depth to oceanic crust can be calculated. The Cape Verde Rise forms the largest anomalous oceanic bathymetric swell (Crough (1982)) with a depth anomaly (expected-observed) of ~2 km. To observe the actual anomaly amplitude of the oceanic crust it is necessary to penetrate any overlying sediments, and make corrections for the load of these overlying sediments.

Most useful in this respect is the seismic reflection profiling method. A high repetition sound source is used to transmit energy into the seafloor and sensitive detectors (hydrophones) record the energy reflected off interfaces along the ray path. Sufficient detail is usually present within the sediment layer that a crude seismic stratigraphy can be formed.

This type of study typically uses only vertical reflection ray-paths so no information can be gathered on the velocities of the material through which the energy is propagating. Velocity information, an essential part of any seismic interpretation, can, however, be obtained from wide angle reflection and refraction studies using disposable radio sonobuoys, Hill (1963).

The main objectives of the seismic investigation of the Cape Verde Rise are:-

1) To map the depth to oceanic layer 2 and compare this with the

expected depth for crust of the same age, after accounting for the isostatic load of the overlying sediments.

2) To study the seismic stratigraphy of the sediments on the Cape Verde Rise and try to relate these to uplift and formation of the Cape Verde Archipelago.

3) To calculate the velocity structure of the sediments and basement and where possible use these velocities to aid the interpretation in 2).

The study naturally divides into 2 parts; firstly, the seismic reflection interpretation and secondly, the seismic refraction experiments.

4.2 SEISMIC REFLECTION

The Cape Verde Rise was originally thought to be an accumulation of sediments only. It is now recognised, from seismic profiling, that oceanic basement is actually elevated over the rise. Seismic reflection work by Uchupi et al (1976), during a regional study of the West African coast, outlined reflections from the sediment/layer2 interface on profiles approaching the Cape Verde Archipelago. An attempt was also made to identify some of the sediment horizons. Later work by Goldflam et al (1980) showed a strong intersediment reflector that was identified as a basalt sill during drilling at D.S.D.P. hole 368 (Lancelot & Seibold et al (1977)).

The seismic reflection profiles described here were collected by scientists from Leicester University during December 1982 and January 1983. The equipment used is outlined in section 2.7 of Chapter 2. Figure 4.1 shows the positions of the profiles superimposed on a bathymetric map of the Cape Verde Rise. The profiles are numbered chronologically from Line 1 to Line 6. Figures 4.2 to 4.7 illustrate

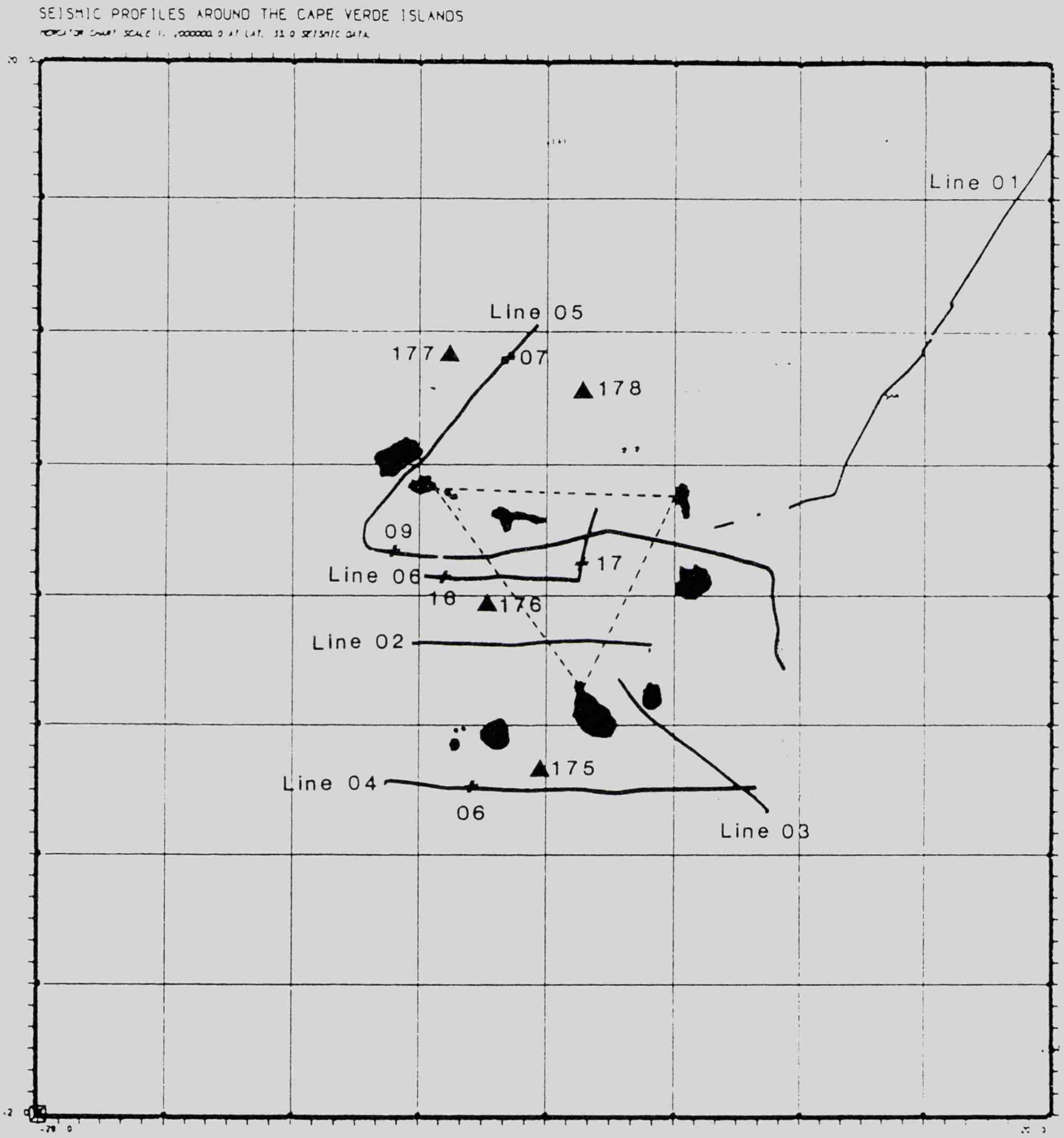

Figure 4.1 Chart of the Cape Verde Archipelago showing locations of seismic profile lines and positions of sonobuoy experiments. Sonobuoys deployed and interpreted by Hoskins et al (1974) are indicated by triangles. The dashed lines show the refraction profiles shot by King (1974).

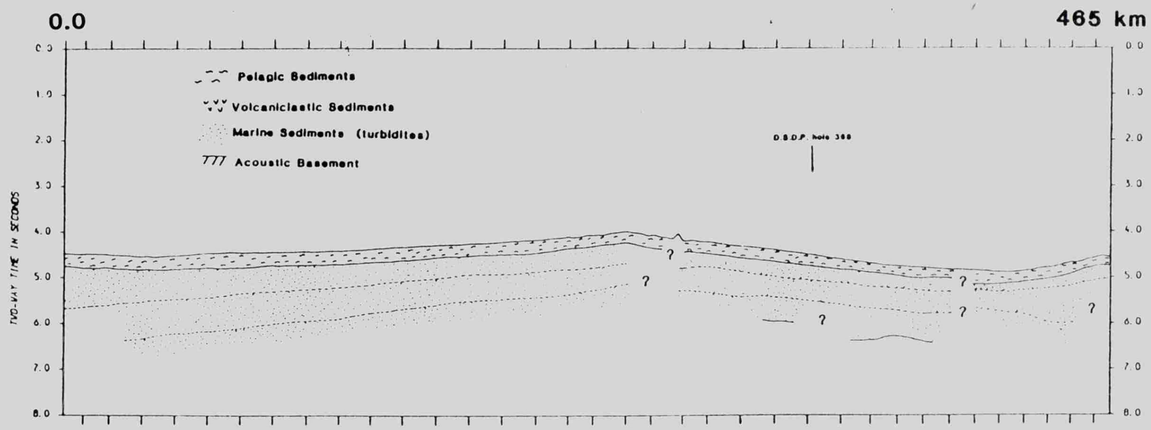

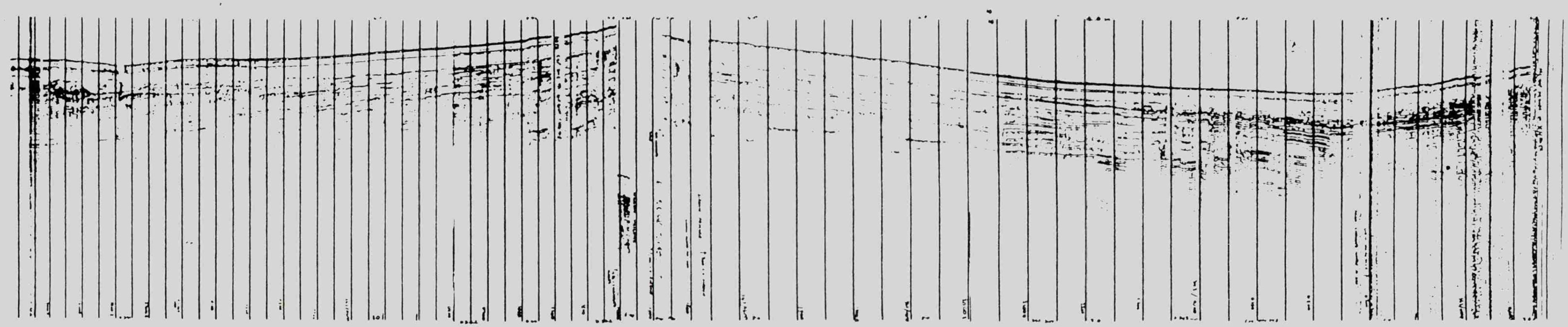

Figure 4.2 Seismic profile LINE 01. Hard copy seismic record, lower diagram, with corresponding interpreted line drawing, upper diagram. This particular profile record is of very poor quality due to problems with the receiver. The position of D.S.D.P. hole 368 is indicated. Vertical lines on the hard copy record are timing marks relating the record to ship's time. The horizontal axis of the line drawing is in kilometres along ship's track.

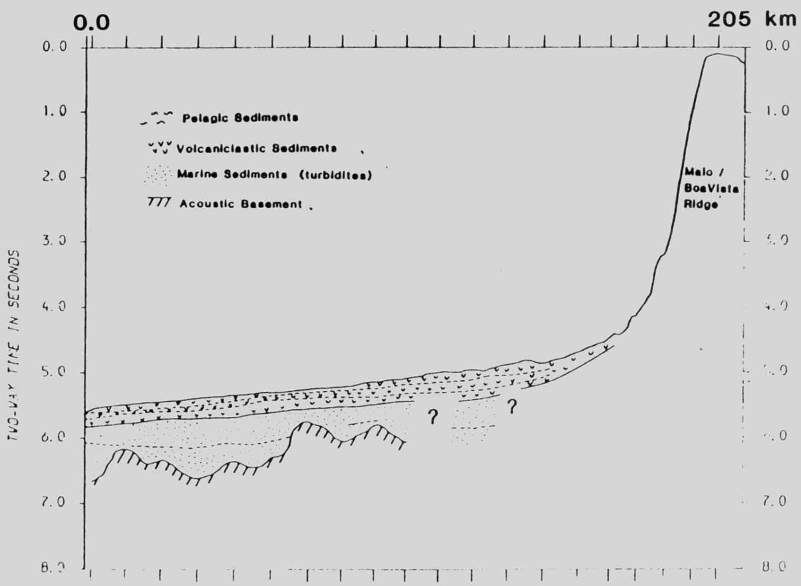

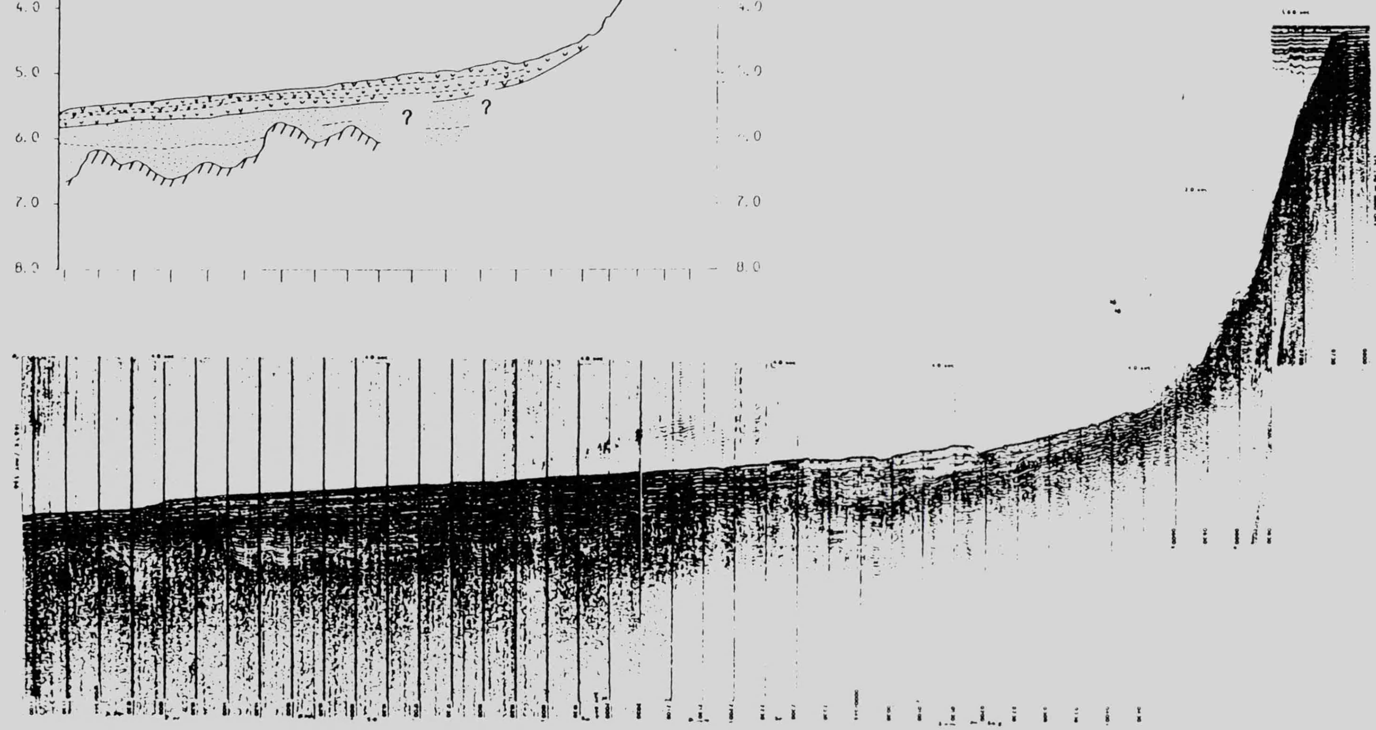

Figure 4.3 Seismic profile LINE 02. Profile collected heading east within the archipelago. Resolution of deep structures diminishes rapidly on approaching the islands.

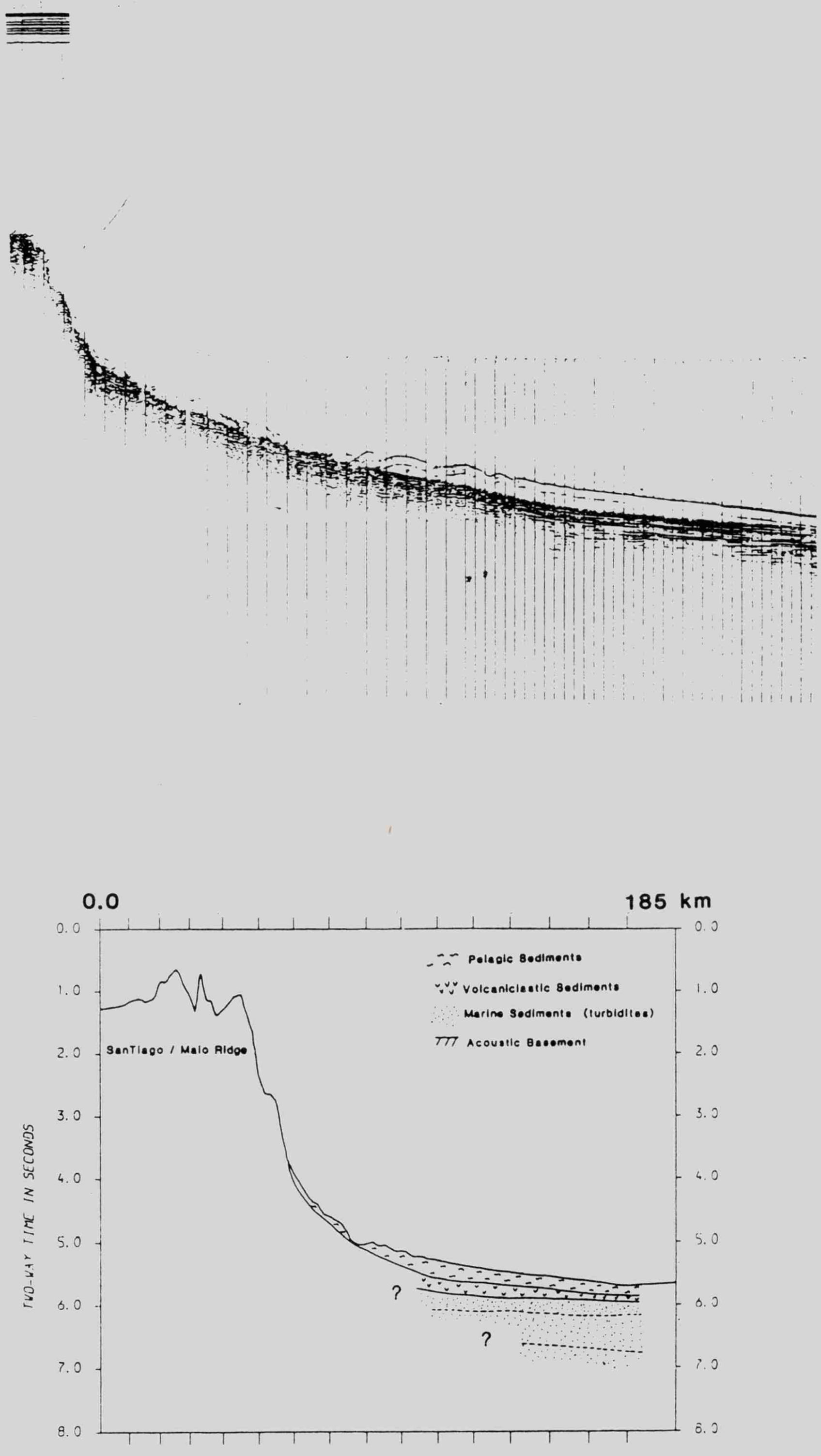

Figure 4.4 Seismic profile LINE 03. Ship's track heads south-east from the San Tiago/Maio ridge. Upper diagram is the actual hard copy record interpreted to get the line drawing shown in the lower diagram. Question marks indicate the limit to which the lower reflecting horizons could be followed.

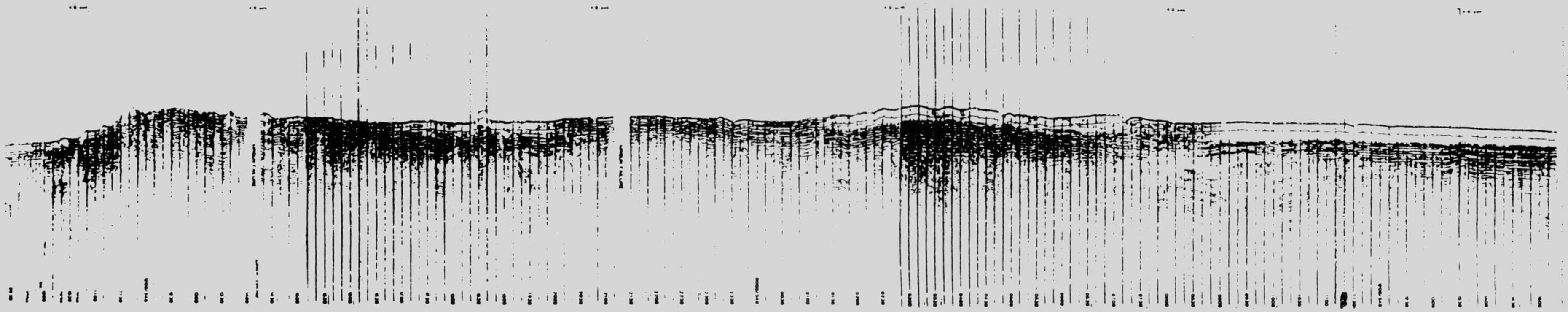

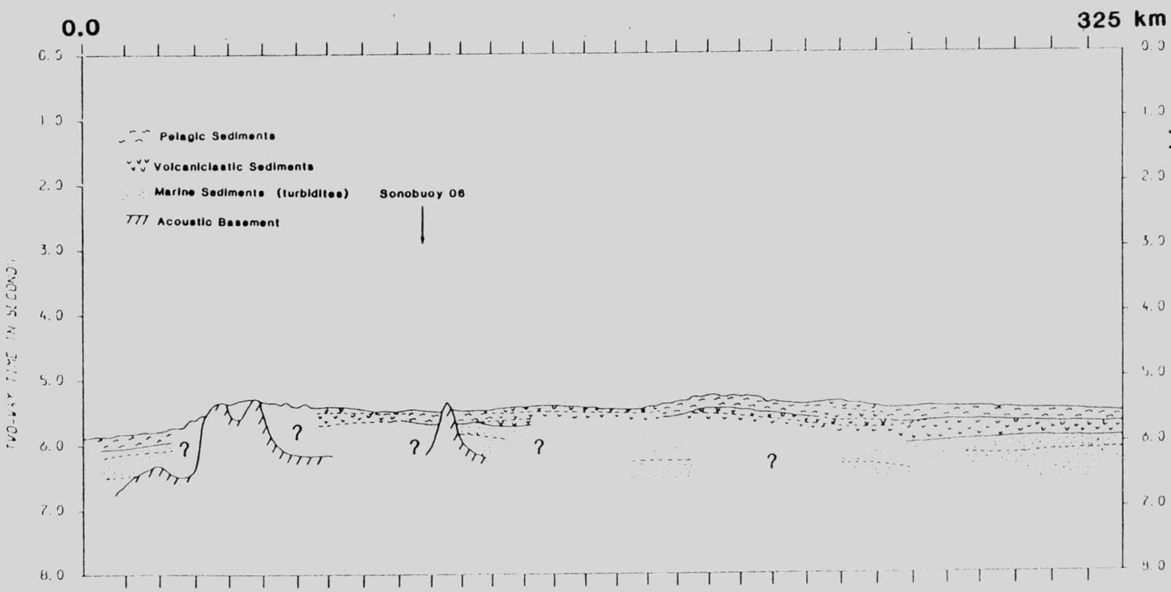

Figure 4.5 Seismic profile LINE 04. This profile was collected heading east on a track south of the archipelago. It illustrates well the alternating light and dark patches associated with pelagic and volcaniclastic reflectors. The rough topography to the west is due to a basement feature that outcrops on the seabed.

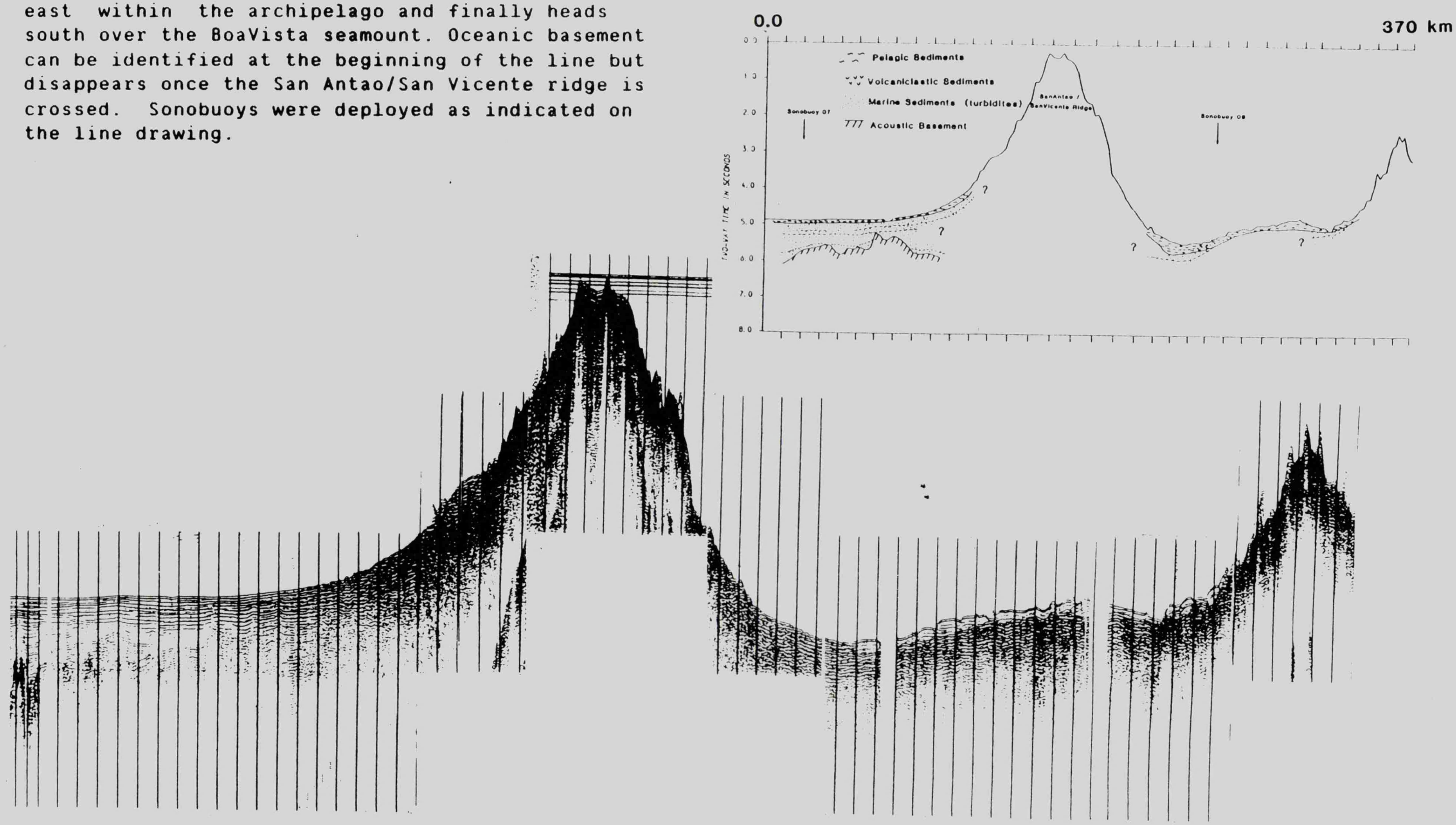

Figure 4.6 Seismic profile LINE 05. This profile starts to the north of San Antao and then heads east within the archipelago and finally heads south over the BoaVista seamount. Oceanic basement can be identified at the beginning of the line but disappears once the San Antao/San Vicente ridge is crossed. Sonobuoys were deployed as indicated on the line drawing.

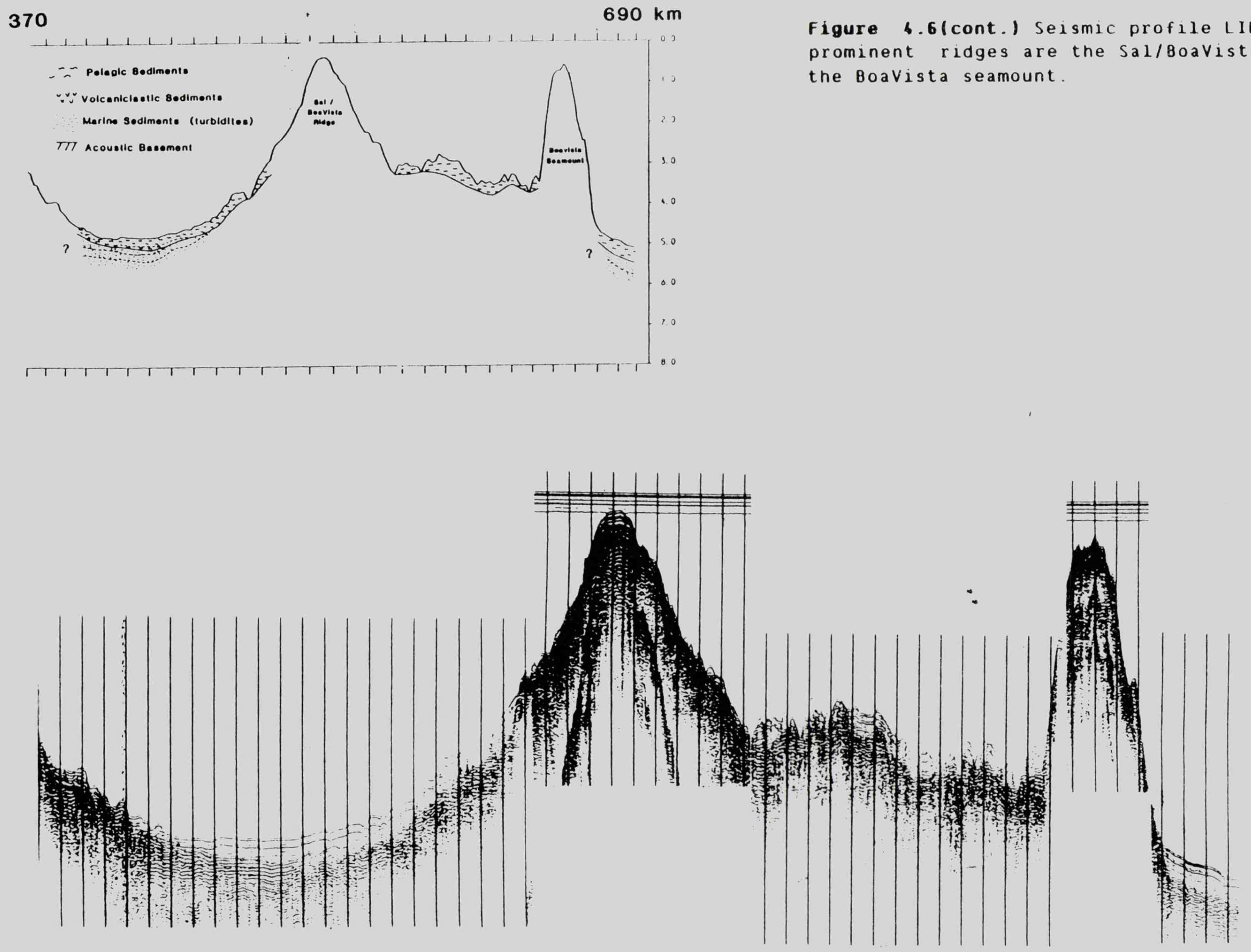

Figure 4.6(cont.) Seismic profile LINE 05. The 2 prominent ridges are the Sal/BoaVista ridge and the BoaVista seamount.

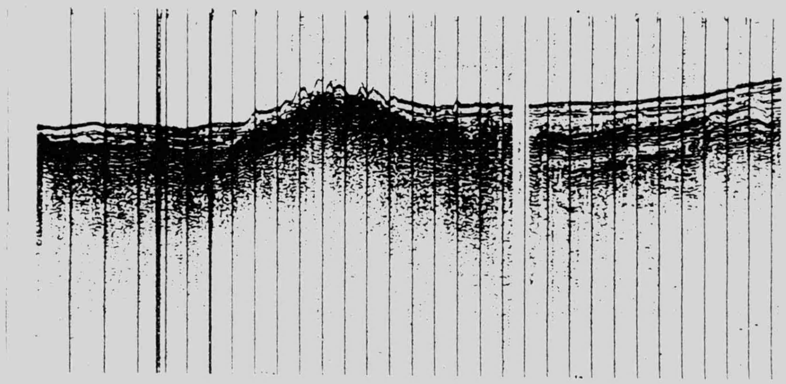

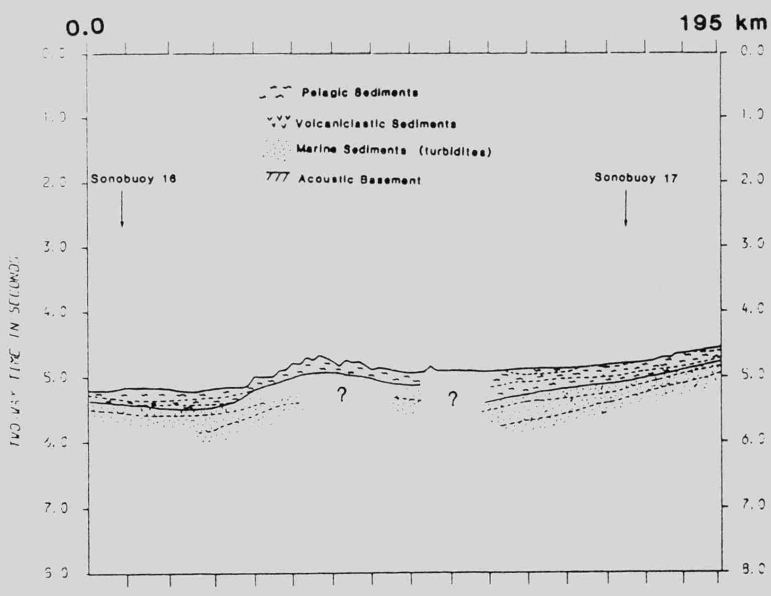

Figure 4.7 Seismic profile LINE 06. Ship's track heads east initially then turns to head north just before deploying Sonobuoy 17. The rough bottom topography is associated with a ridge extending south from the island of San Nicolua.

the hard copy records interpreted to produce the corresponding line drawings also shown in Figures 4.2 to 4.7. The horizontal scales are different between the line drawings and the actual records since the records are dependent on ship's time and the line drawings are plotted against distance along ship's track

The records were interpreted by tracing prominent horizons on the sections that corresponded to significant changes in seismic character or to angular unconformities that showed up as the gradual dissappearance of a group of reflectors. Problems that became apparent during the interpretation include; (1) the bubble pulse of the source signature, (2) the dominant frequency of the source, (3) the lack of penetration in parts of the survey, (4) there is a distinct lack of cross-over links between individual profiles which means the correlation of horizons between profiles is rather subjective.

The source signature of the airguns is degraded by oscillations of the bubble of air as it passes to the surface. This produces several cycles of energy instead of just the ideal single spike. Reflectors therefore tend to appear as parallel lines rather than single horizons. The dominant frequency of the source was 14 Hz and in a medium where the sound velocity is ~2 km/sec this means that horizons less than ~30 m thick will not produce a discrete reflection. Lastly, the penetration is proportional to the total energy output from the airguns and also to the acoustic characteristics, particularily attenuation, of the medium through which the energy must travel. The energy output from the airguns was sufficient to penetrate the sediment layers in some parts of the sections but not in others. Since the energy output was uniform, this serves to highlight the variability of the material comprising the sediments around the archipelago.

4.3 VERTICAL REFLECTION PROFILING INTERPRETATION

The seismic character of the various horizons identified can be summarised as follows.

1) The lowermost identifiable horizon is a series of diffraction hyperbolae. This horizon has variable topography and can appear at the surface in some profiles. No coherent reflections can be identified beneath this interface. It is typically found at approximately 1.0 second of two way travel time (TWT) beneath the seafloor and can be most easily identified when >50 km from the islands.

2) The next unit infills the topography of horizon (1) and forms a series of generally horizontal reflectors. Some of these reflectors can be traced easily over distances of up to 70 km whereas other parts of the records have a very broken and discontinuous appearance. This unit is bounded beneath by the diffraction hyperbolae and above by an angular unconformity. In contrast to the overlaying unit, (3), this layer appears relatively acoustically transparent in seismic character.

3) The third layer contrasts markedly with that beneath in that it contains many reflecting interfaces and is acoustically rather opaque. The reflectors are difficult to follow and have a diffuse nature. Where they are not bounded by an unconformity below they tend to be the lowest identifiable horizon in that part of the section. This horizon tends to merge laterally with the uppermost unit in a series of interfingering wedges. In other cases, however, this unit is bounded above and below by unconformities.

4) The uppermost unit is generally acoustically transparent and

for this reason is easily identifiable. In deep water it tends to be uniform and flat lying, but on the slopes of the interisland ridges slump structures are apparent.

4.4 GEOLOGICAL INTERPRETATION

Assigning lithologies to these seismic units is rather subjective as only one line, Line 1, has any geological control in the form of D.S.D.P. hole 368 (Lancelot & Seibold et al (1977)). Unfortunately the hydrophone streamer gave very poor signal to noise ratios during the initial phase of the experiment and the subsequent record for Line 1 (Figure 4.2) was of very poor quality. No attempt was made therefore to tie the seismic interpretation to the lithological log from D.S.D.P. site 368. However, the units outlined above are only broad divisions and therefore only a crude geological interpretation will be applied.

1) The lowermost unit with its rough contact with the unit above, as indicated by the diffraction hyperbolae, is certainly volcanic basement and may be either layer 2 or later intrusives. No coherent reflectors can be seen within this igneous layer. This reflector has been identified frequently by such workers as Mutter & Detrick (1984).

2) The next unit, lying on top of volcanic basement, is likely to be a series of limestones and cherts of normal marine origin. At least one of the prominent reflectors within this unit could correspond to the top of the black shales as indentified by Lancelot & Seibold et al (1977). Outcrops of mid ocean ridge basalts (MORB) have been reported on the island of Maio by Stillnan et al (1982). They also mapped an overlying sequence of

marine limestones, the Morro formation, which is considered to be equivalent to unit (2) identified here.

3) The acoustically opaque layer is suggested here as a volcaniclastic layer lying unconformably on top of a sequence of normal marine sediments. The scattering nature of the reflectors could be explained by poor sorting of angular fragments deposited by mass flows or turbidity currents from the volcanic islands. This interpretation is strengthened by the increase in thickness of this layer on approaching the islands.

4) The uppermost layer has been interpreted here as recent pelagic sediments consisting mainly of nanno marls and oozes. This is based on their seismically transparent character and also on the results of a study by Rothe (1973), who investigated the near surface sediments by studying core sections at various sites around the archipelago.

4.5 WIDE ANGLE REFLECTION/REFRACTION EXPERIMENTS

Velocity information is an essential criterion for characterising the different layers that make up the oceanic crust. Several models (Raitt (1963) and Kozminskaya & Kapustyan (1975)) have been proposed as an average seismic model for oceanic crust and Houtz & Ewing (1976) related changes in seismic structure to plate age. Seismic studies have also been made of marine sediments and velocity has been related to density, Nafe & Drake (1963). Determinations of velocity in the deep sea are best made by studying wide angle reflections and refractions, Hill (1963). Many workers have used this technique successfully, amongst the more recent publications are White (1979) and Houtz et al (1981).

The main problems that it is hoped a knowledge of the velocity structure will help solve, arise from continuous seismic profile (CSP) sections crossing the archipelago (section 4.3). The acoustic basement recognised as the deepest coherent reflection on the CSP may not correspond to oceanic basement, but may, in fact, be an acoustically opaque sedimentary horizon (White (1979)). Particularily strong reflectors within the sediments may be due to igneous intrusions; one such reflector was drilled on DSDP leg 41 and proved to be an igneous sill (Lancelot & Seibold et al (1977)). The sharp velocity contrast of intrusions into low velocity marine sediments should be detectable and hence any further occurences can be located. Finally, the normal marine sediments around and within the archipelago are interrupted periodically by horizons of volcaniclastic material (Grunau et al (1975)). This has also been noted earlier in this chapter on the basis of the character of the seismic reflection signal and by Robertson (1984) from sediment analysis on the island of Maio. The present day sedimentary regime around the islands was investigated by Rothe (1973) using coring techniques who concluded that the uppermost sediments are composed mainly of autochthonous marine organisms with a small component of volcanic material and that terrigenous material was scarce.

4.6 RADIO SONOBUOY TECHNIQUE

A hydrophone and transmitter unit (the sonobuoy) is dropped from the moving vessel and continuously transmits the signal from the hydrophone to a receiver on the ship. The ship, meanwhile, steams away from the sonobuoy firing shots at regular intervals. The shot instant is controlled and recorded on the ship.

A total of 17 sonobuoys were deployed during the refraction experiments. Of these, only 5 have been successfully recorded, digitised and interpreted and these are discussed below. The remainder were not utilised due to 2 sinking after gain modifications were attempted, 4 were deployed over the interisland ridge between Maio and San Tiago (and are reported elsewhere), 1 was used for test purposes only and 5 were deployed over areas of rough seabed topography. Table 4.1 lists the positions, durations and ranges of the 5 sonobuoys deployed during this experiment and subsequently interpreted. Figure 4.1 shows the positions of these sonobuoys and they are also indicated on the relevant figures for the concurrent CSP.

Picking of arrivals was hampered at small source/receiver offsets by overloading of the sonobuoy hydrophone amplifier. This resulted in a 'clipped' waveform being transmitted back to the ship and recorded on magnetic tape. Attempts to alter the gain of the amplifiers failed when the modified sonobuoys sank immediately on deployment.

TABLE 4.1 Positions, durations and ranges of Sonobuoys used in this study.

Sonobuoy	Latitude	Longitude	Duration	
No.	Deg Min	Deg Min	Hrs	n.ml
6	14 30.56	24 25.06	2.8	22.8
7	17 54.5	24 11.1	2.7	16.0
9	16 20.3	25 18.5	2.5	13.5
16	16 8.8	24 51.8	2.3	15.8
17	16 25.0	23 40.6	2.2	12.7

4.7 DETERMINATION OF VELOCITIES

The calculation of seismic velocities from wide angle reflections and refractions is well documented in such works as Houtz et al (1968), LePichon et al (1968), Knott & Hoskins (1975) and

Limond & Patriat (1975). Two problems particular to the radio sonobuoy technique are the calculation of source to receiver distances and the time shift caused by having the receiving hydrophone at some depth beneath the sea surface. The former can be overcome by fitting the seabed reflection times observed on the records to the expected times for a model in which the seabed reflection time is dependent on the source to receiver separation. This is prefered to using the direct wave arrival since the seabed reflection can be seen out to greater ranges. The second problem can also be overcome in the same manner as the first by including a constant time term to account for the hydrophone depth and using the seabed depth information from the precision echo sounder.

The relationship between the reflection times and the source/receiver distance is given by:-

$$T_{sb}^2=(T_v-T_o)^2+(dfact+vfact.X)^2/V_{wat}^2 \qquad \text{(E4.1)}$$

where T_{sb}=time for reflection off the seabed

T_v=normal incidence travel time to the seabed from the P.E.S.

T_o=static term to account for the hydrophone and gun depths

V_{wat}=mean velocity for that water depth from Carter (1980)

X=initial source/receiver separation assuming that X=0 represents normal incidence and that the ship's speed was a constant 5 knts and finally that there was no drift of the sonobuoy.

dfact=distance correction for the initial reflection not being normal incidence

vfact=correction to initial assumption of ship's velocity of 5 knts.

By minimising:-

$$F=\sqrt{[((\Sigma(T_{sb}-T_{obs})^2)/(n-1)]} \qquad (F4.2)$$

where T_{sb}=calculated time from E4.1

T_{obs}=observed time from the record

n=number of times used in the analysis

with respect to T_o, dfact and vfact, the necessary correction terms can be calculated. T_o, dfact and vfact were incremented over small intervals and a value for F from E4.2 calculated at each increment. The values of T_o, dfact and vfact finally chosen were those that gave the smallest F.

The best fitting values of T_o, dfact and vfact can be found by assuming V_{wat} is constant and can be calculated from Carter (1980).

Wide angle reflections can be described using simple geometry and assuming that interfaces are (i) planar and horizontal and (ii) that energy is not refracted when crossing them. The first assumption can be justified by examination of the continuous reflection profile but the second assumption is a simplification that means results will only be a first approximation. Stoffa et al (1982) examined the differences between interval velocities obtained from ray tracing and from using the above assumptions for a deep water sonobuoy record. The difference was less than 6% at offsets less than 7 km between source and receiver. Stoffa et al (1982) also state that the point at which the simple assumptions outlined above become unacceptable is very model dependent. However, taking into account the fact that only Sonobuoy 17 uses source receiver offsets up to 9 km for the calculation of average velocities, it is further assumed that the hyperbolic approximation is sufficient for this study.

Times for wide angle reflections can be obtained from:-

$$T_{rf}^2 = T_d^2 + X_m^2 / V_r^2 \qquad \text{(F4.3)}$$

where T_{rf}=time for reflection

T_d=delay time for the hydrophone and gun depths determined from E4.1

X_m=modified distance from F4.1 (X_m=(dfact+vfact.X))

V_r=average velocity to the interface

The velocity from E4.3 is an average velocity for the energy to travel to the reflecting interface and back. Limond & Patriat (1975) point out that velocities calculated from E4.3 are dependent on the square of distance and time. Due to concentrations of data points at small offsets the results can be biased. To overcome this it was decided to model the expected travel times using E4.3 for a variety of velocities and compare the expected to the observed times using the r.m.s. difference (F4.2). The error on the average velocity is calculated using the r.m.s. differences between the expected and observed travel times. The F-Ratio test was applied (Davis (1986)) to get the 95% confidence limits for the average velocity. The velocity of the individual layers can be calculated using Dix's interval velocity formula (Dix (1955)):-

$$V_{int}^2 = (V_{rn}^2 t_n - V_{r(n-1)}^2 t_{(n-1)}) / (t_n - t_{(n-1)}) \qquad \text{(F4.4)}$$

where V_{int}=interval velocity for a layer bounded by 2 reflecting interfaces

V_{rn}=V_r from E4.3 for lower interface

$V_{r(n-1)}$=" " " " upper "

t_n=normal incidence time for the lower interface

$t_{(n-1)}$= " " " " " upper "

Velocities and normal incidence times can be combined to get the depth to and thickness of the layers. The errors on these calculations can be obtained by combining the absolute and relative errors from the average velocities.

The time distance relationship for refractions is simpler:-

$$T_a = X_m / V_a + T_{int} \qquad (E4.5)$$

where T_a=time for the refracted arrival from the record

T_{int}=intercept time of the refracted arrival plot

X_m=modified source/receiver seperation

V_a=refraction velocity

The same assumptions apply to E4.5 as did to E4.3 and the calculated velocity is the velocity of energy travelling horizontally along an interface.

'Wiggly' trace plots of the sonobuoy signals were obtained by digitising the recorded anologue signals and replaying on suitable hardware. The necessary processing to get the digitised records is outlined in Appendix I. Figure 4.8 shows an example of the 'wiggly' trace plot for sonobuoy 07 and the corresponding plots for sonobuoys 06, 09, 16 and 17 are shown in Appendix I. The arrival times and distances for recognised reflection and refraction arrivals were picked using a digitising table. Figures 4.9 to 4.13 show the picked arrivals plotted against corrected source/receiver distance with the corresponding velocity depth profiles also shown. Table 4.2 lists the velocity/depth information and corresponding error estimates for the 5 sonobuoys interpreted here.

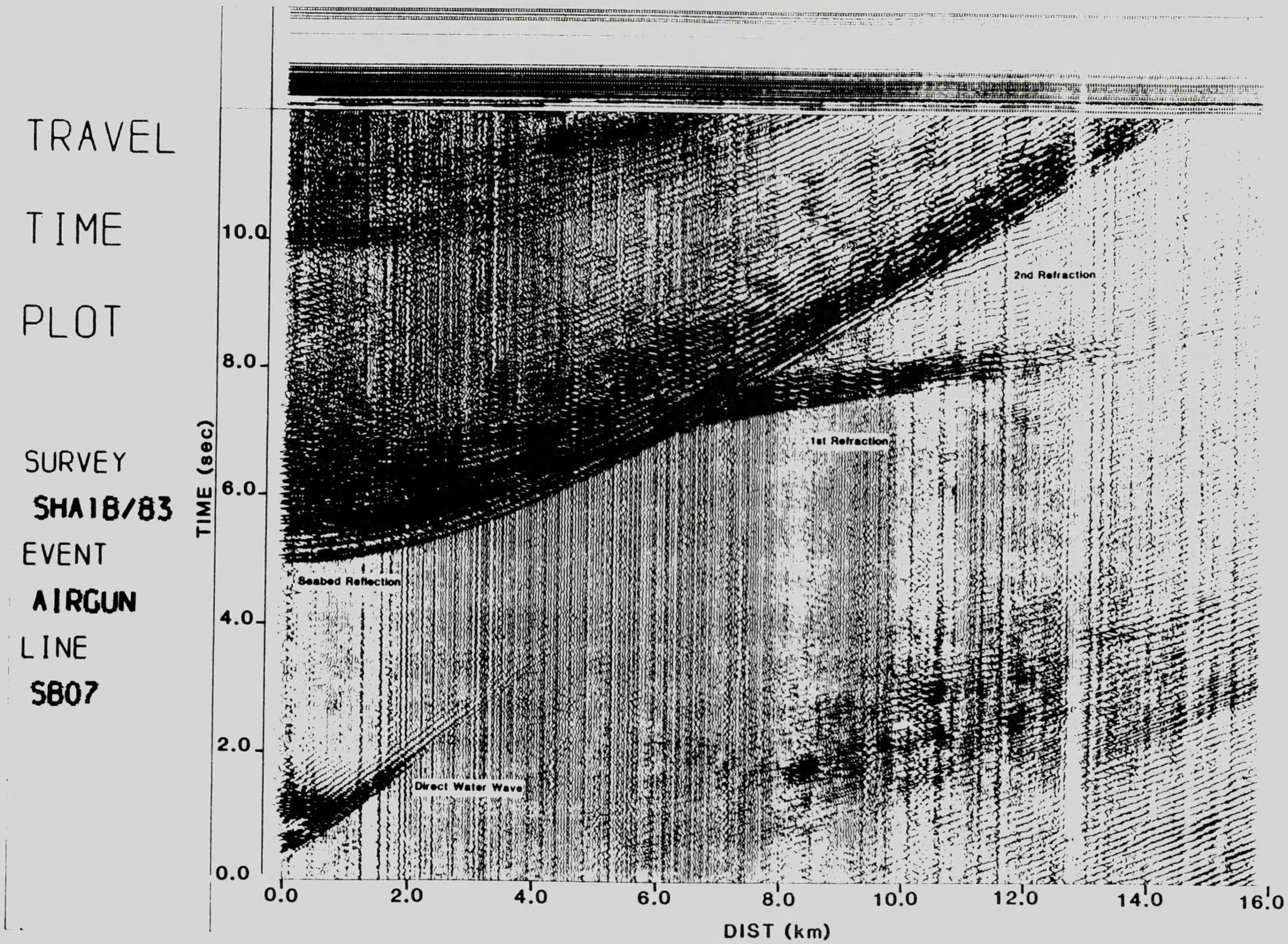

Figure 4.8 'Wiggly' trace plot of data from Sonobuoy 07. This has been produced after digitization. Digitization is fully described in Appendix I. The arrivals identified have been shaded and were subsequently 'picked' using a digitising table to get values of distance and time.

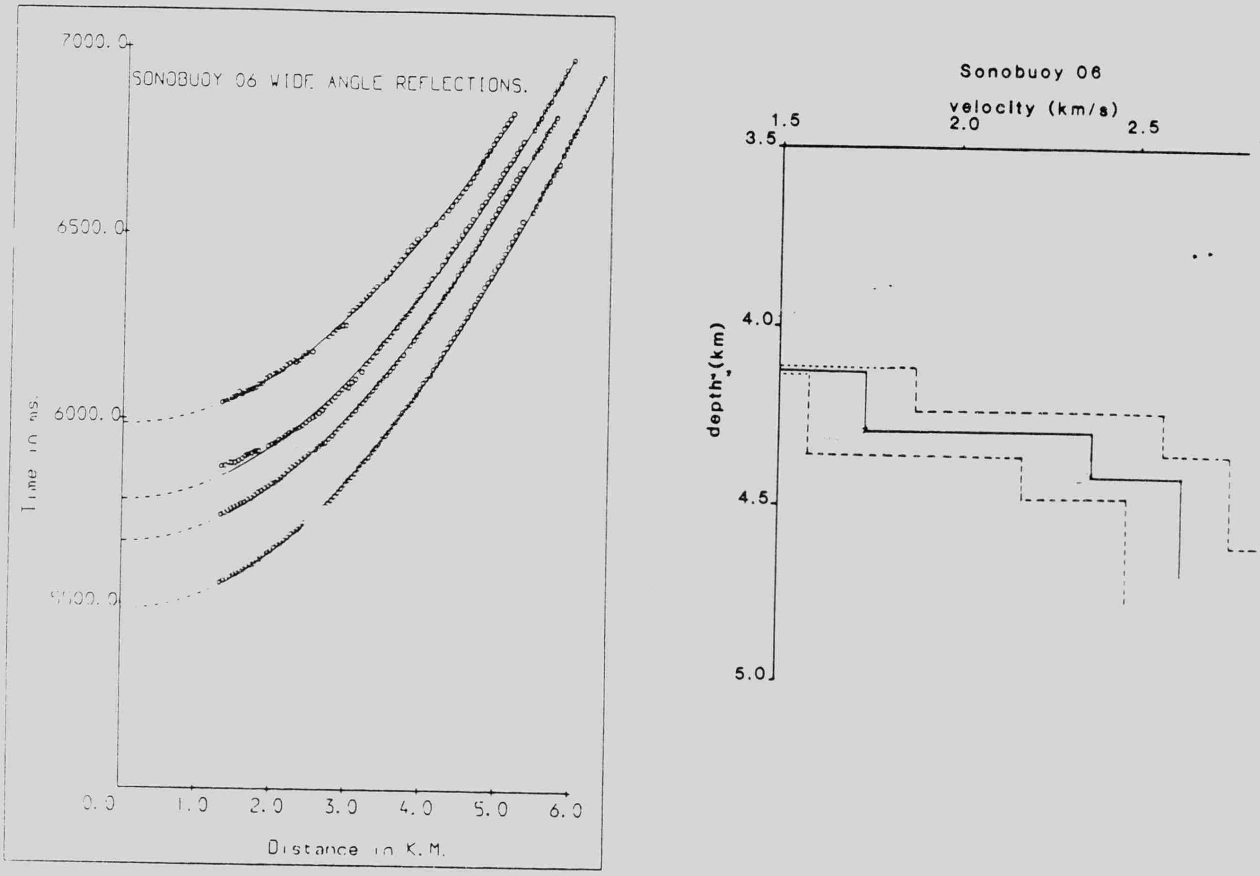

Figure 4.9 Corrected time distance plot for Sonobuoy 06. Only reflections were recognised for this experiment. The offset between normal incidence, zero on the distance axis, and the start of the data is due to initial poor tuning of the radio receiver and to overloading of the hydrophone distorting the signals. The resulting velocity depth profile is also shown. The general increase in velocity with depth is typical of oceanic sediments (Houtz et al (1968)).

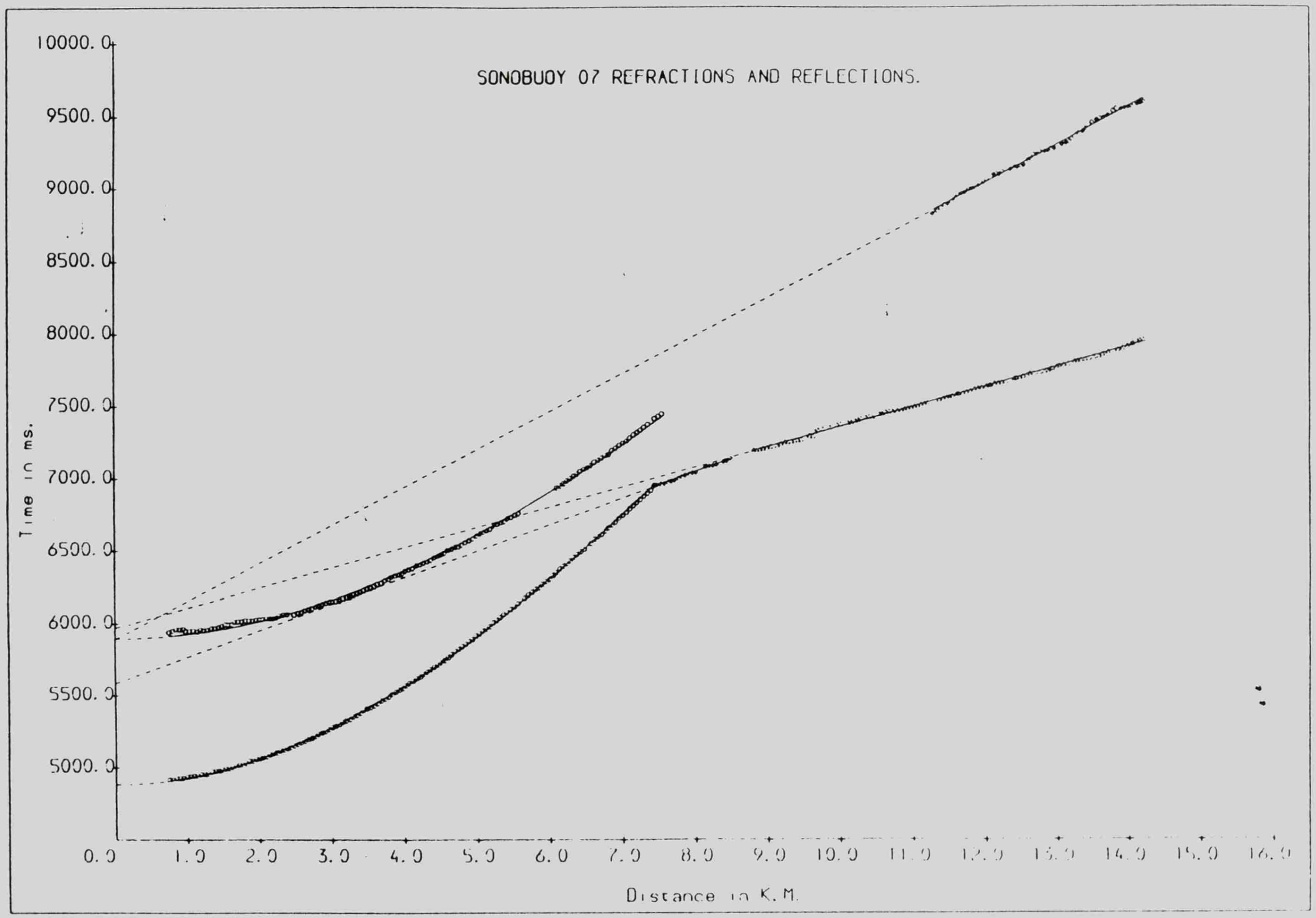

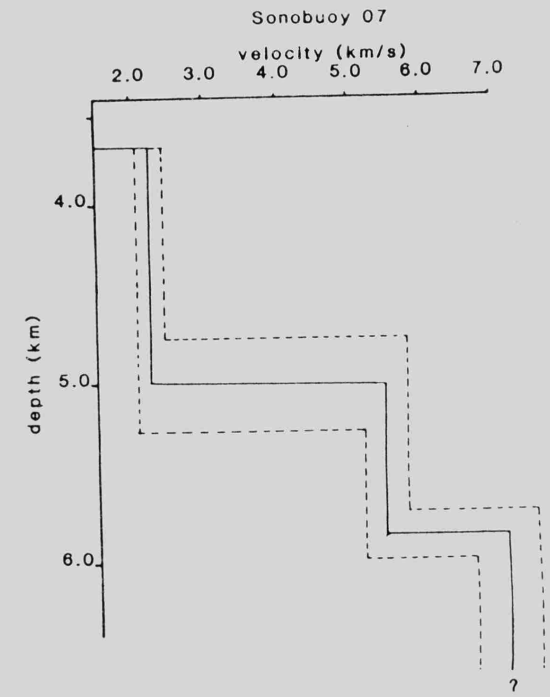

Figure 4.10 Corrected time distance plot for Sonobuoy 07. A total of two reflections, one being from the seabed, and three refractions were recognised on this record (see Figure 4.8). The first refraction can be traced back to the subseabed reflector which is considered to be oceanic layer 2. The second refraction appears to come from a deeper horizon. The last refraction is considered to be an S-wave refraction with conversion from P-wave at the sediment/layer 2 interface. The corresponding velocity depth profile is also shown.

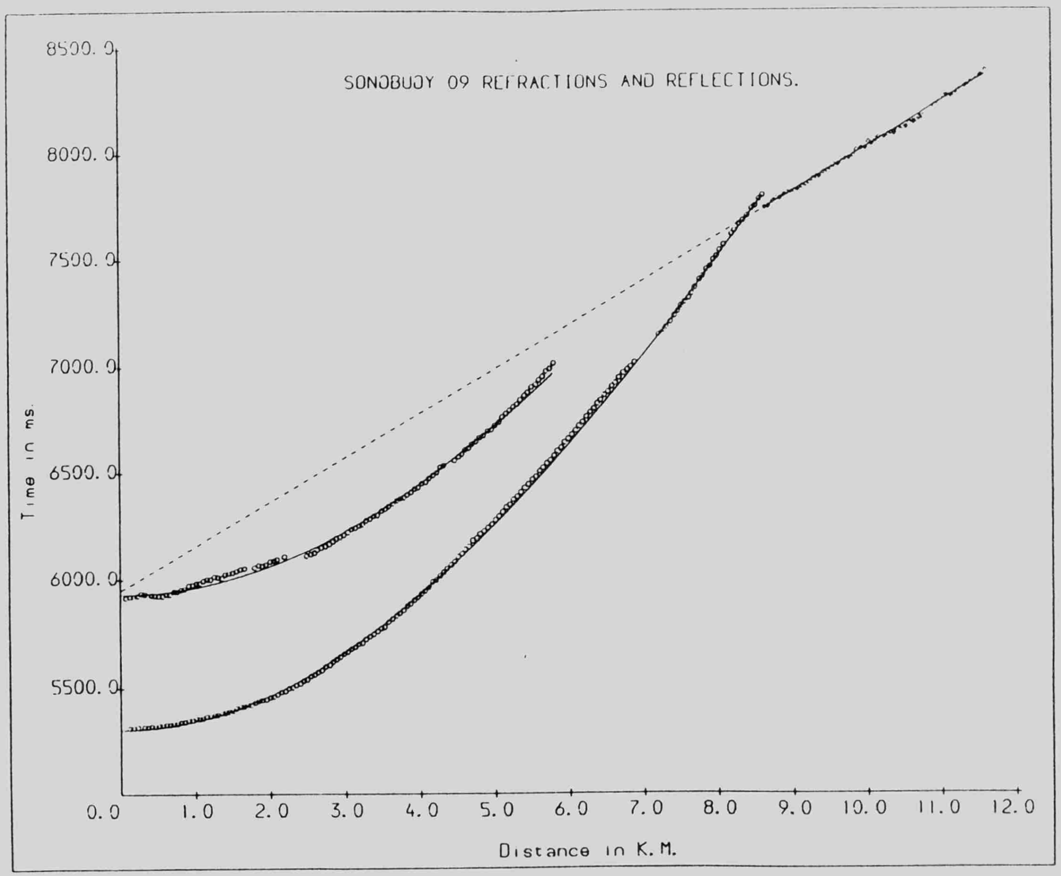

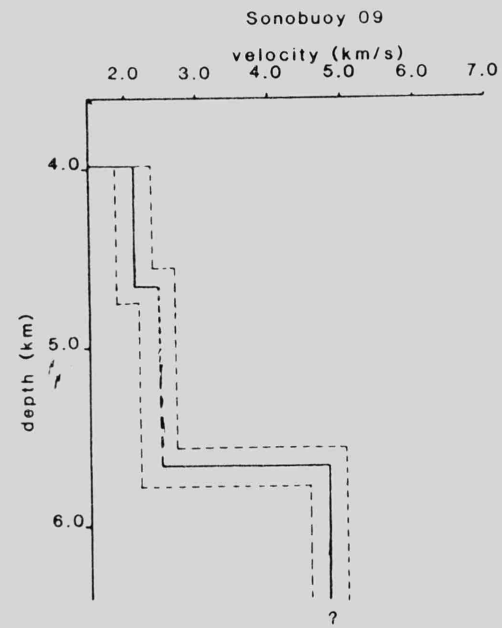

Figure 4.11 Corrected time distance plot for Sonobuoy 09. A single subseabed reflector and a single refractor were all that could be recognised from the record. The reflection and refraction do not occur from the same horizon. The corresponding velocity depth profile is also shown. The thick dashed line indicates an estimated velocity.

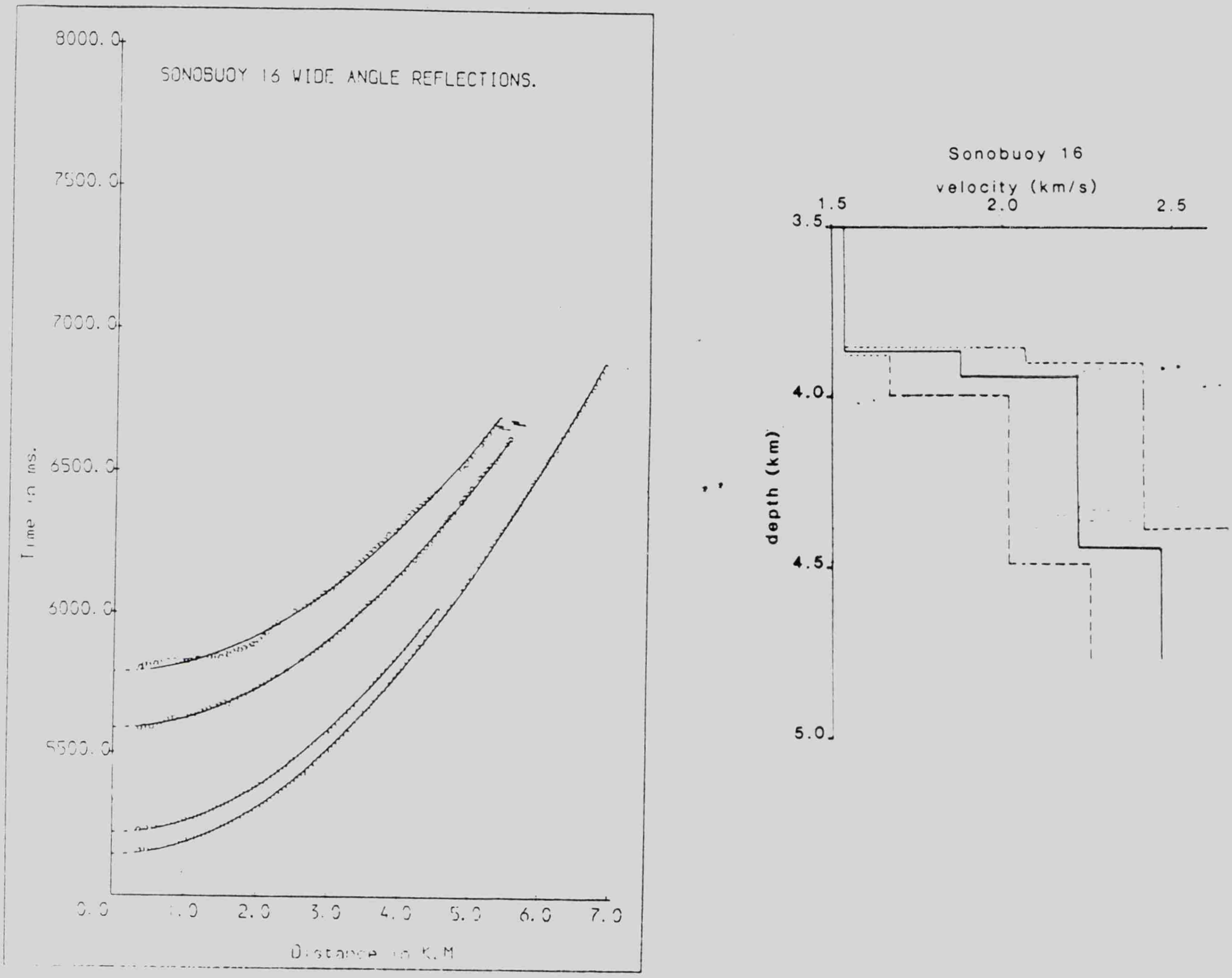

Figure 4.12 Corrected time distance plot for Sonobuoy 16. No refractions could be identified, but 4 reflecting horizons, including the seabed, were recognised. The corresponding velocity depth profile is shown and illustrates a large velocity increase relatively near the seabed.

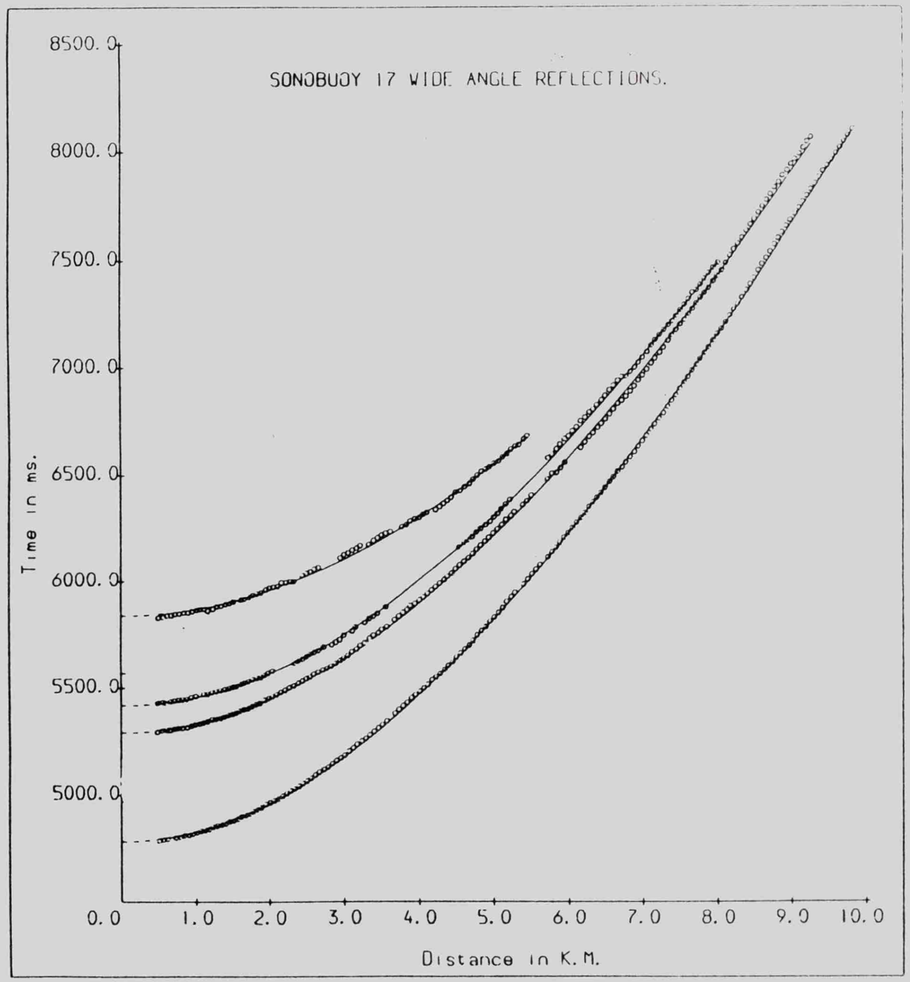

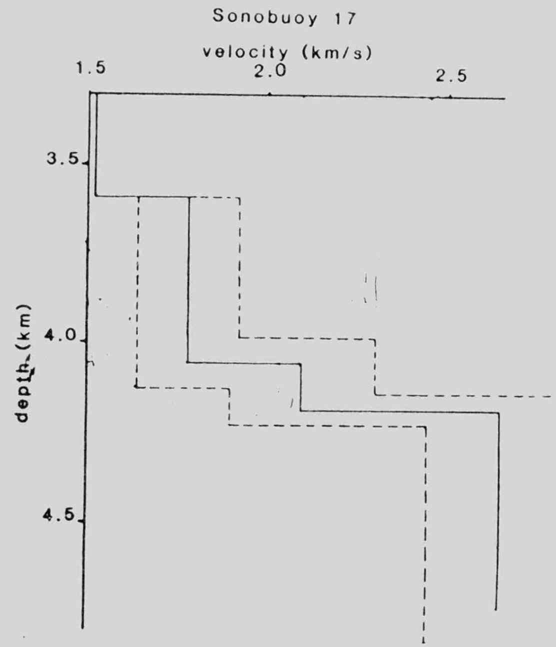

Figure 4.13 Corrected time distance plot for Sonobuoy 17. This plot is very similar to Figure 4.12, no refractions were seen. The corresponding velocity depth profile shows an unusually large velocity increase relatively near the seabed.

TABLE 4.2 Results of velocity analysis for Sonobuoys deployed during the RRS Shackleton cruise 1982/83.

SNB No	INTERVAL VELOCITY (km/sec)	ERROR IN VELOCITY (km/sec)	THICKNESS OF HORIZON (metres)	ERROR IN THICKNESS (metres)	
06	1.501	0.01	4127	4	(water layer)
	1.747	0.14	168	60	
	2.374	0.20	111	65	
	2.628	0.14	289	84	
07	1.503	0.01	3671	3	(water layer)
	2.316	0.16	1320	170	
	5.47**	0.30	850	140	
	7.19**	0.45	-	-	
09	1.498	0.013	3988	4	(water layer)
	2.118	0.125	680	100	
	2.475*	0.125	1000	100	
	4.81**	0.125	-	-	
16	1.503	0.005	3864	3	(water layer)
	1.871	0.20	71	50	
	2.222	0.20	500	50	
	2.460	0.21	320	88	
17	1.499	0.006	3590	4	(water layer)
	1.785	0.14	465	70	
	2.087	0.205	130	40	
	2.654	0.20	550	70	

KEY **velocity from refraction
*velocity estimated by assuming layer between the lowest reflector and the refracting horizon has constant velocity

n.b. i) All interval velocities calculated using Dix's formula and assuming plane horizontal layering.

ii) The interval velocities and associated errors for the water layers are an indication of the goodness of fit of the seabed reflection times from the observed records to the modelled reflection times using E4.3.

iii) The thicknesses of the water layers and their associated errors are obtained from the Precision Echo Sounder.

iv) The error estimates for the sub seabed horizon thicknesses include the error estimate for the interval travel time within that layer and are therefore necessarily larger than the errors from the interval velocities alone.

4.8 RESULTS OF VELOCITY ANALYSIS

Sonobuoy 06 was deployed, south of the islands of Fogo and Brava, on the seismic profile Line 04, and no refracted arrivals were observed on the digitised replay. A total of 5 reflectors, including the seabed, were recognised and measured. The time/distance plot is shown in Figure 4.9, with both the time and distance scales corrected as outlined above. The interval velocities and depths are shown in Table 4.2 and these results are summarised in Figure 4.9 as a velocity depth profile. The increase in velocity with depth has a slightly greater gradient (2.204 sec^{-1}) than the average gradient from Houtz et al (1968) (1.783 sec^{-1}). The lowermost layer has an apparent velocity, from the reflection analysis, of 2.63 km/s at a depth of 0.568 km below the seabed.

Sonobuoy 07, deployed just to the north of San Vicente, on Line 06, and shown in Figure 4.8, produced the strongest refracted arrivals of all the sonobuoys described here. Unfortunately only one reflecting horizon could be identified below the seabed. Figure 4.10 shows the corrected time distance plot of the picked arrivals and also shows the resulting velocity/depth profile. A total of 3 refracted arrivals were observed with the most obvious refraction producing a velocity of 7.19 km/s and a less prominent refraction occuring, over a limited range, before the faster arrival giving a velocity of 5.5 km/s. Both these apparent velocities may be rather higher than the true velocity since the concurrent CSP suggests that the acoustic basement slopes up from sonobuoy (receiver) to the ship (source). Assuming a slope of ~2 degrees, measured from the CSP, the velocities reduce to 6.95 and 5.1 km/s respectively. A second refracted arrival was picked, occuring over a similar range as the high velocity refractor, but at a later time.

The arrivals on Figure 4.8 marked as 2nd refraction give a velocity (3.813 ±0.13 km/s) and intercept time (5893 ±30 ms) which is incompatible with a P-wave interpretation. It is therefore proposed that this arrival is a doubly converted S-wave refracted along the layer 2/layer 3 interface. Double conversion from compressional to shear and back to compressional is necessary since the hydrophone is in a liquid environment. Calculation of possible Poisson's ratios gives 0.038 if the S-wave propagates in layer 2 and 0.305 if it is in layer 3. The Poisson's ratio of 0.038 indicates that the refractor is too fast to be due S-waves in layer 2. The 0.305 value is nearer to 0.28, from work by Purdy (1983) in the Western North Atlantic and to 0.25, used by White (1979) to calculate S-wave velocities in oceanic basement from P-wave velocities and this suggests that the S-wave is more likely to be associated with travel in layer 3. However, by considering that it is necessary to have a constant increase of velocity with depth to obtain refractions, the original conversion from compressional to shear must have occured at the sediment/layer 2 interface. The S-wave velocity can be estimated in layer 2 as 3.04 km/sec by using a Poisson's ratio of 0.28, Purdy (1983). Using this information the expected intercept time can be calculated for a simple 4 layer model where the energy travels as a P-wave in the water and sediments but as an S-wave in layer 2 and is critcally refracted at the layer 2/layer 3 interface. The calculated intercept time of 5723 ms compares reasonably well with the observed travel time of 5893 ±30 ms considering the simplifying assumptions made.

Sonobuoy 09, also on Line 06, but to the south of San Vicente, within the archipelago, gave a single sub-seabed reflection and a rather weak refracted arrival. The time/distance plot is shown in Figure 4.11 along with the resulting velocity/depth profile. The refraction and reflection do not appear to arise from the same horizon so the velocity of the intervening layer is estimated by assuming that the medium through which the energy is propagated is completely isotropic.

Sonobuoy 16 was deployed at the begining of Line 07, roughly south east of sonobuoy 09. No refractions could be observed but a total of 4 sub-seabed reflectors were observed and measured. The time/distance plot is shown in Figure 4.12.

Sonobuoy 17 was also deployed on Line 07, but as the profile headed north between San Luzia and Sal. This sonobuoy, like the sonobuoy 16, produced no refracted arrivals and only reflections. Again 4 reflecting horizons were picked and the resulting velocity/depth profile is shown in Figure 4.13 with the corrected time/distance plot.

The information from the velocity analysis outlined above can be supplemented by the results of previous studies by Hoskins et al (1974), who analysised 4 sonobuoy refraction profiles within the area of interest, and King (1974), who undertook 3 reversed refraction lines using the islands as recording stations. The positions of the previous sonobuoys are shown as triangles and the refraction lines shot by King (1974) are shown as dotted lines in Figure 4.1. Figure 4.14 shows the velocity depth profiles from Hoskins et al (1974).

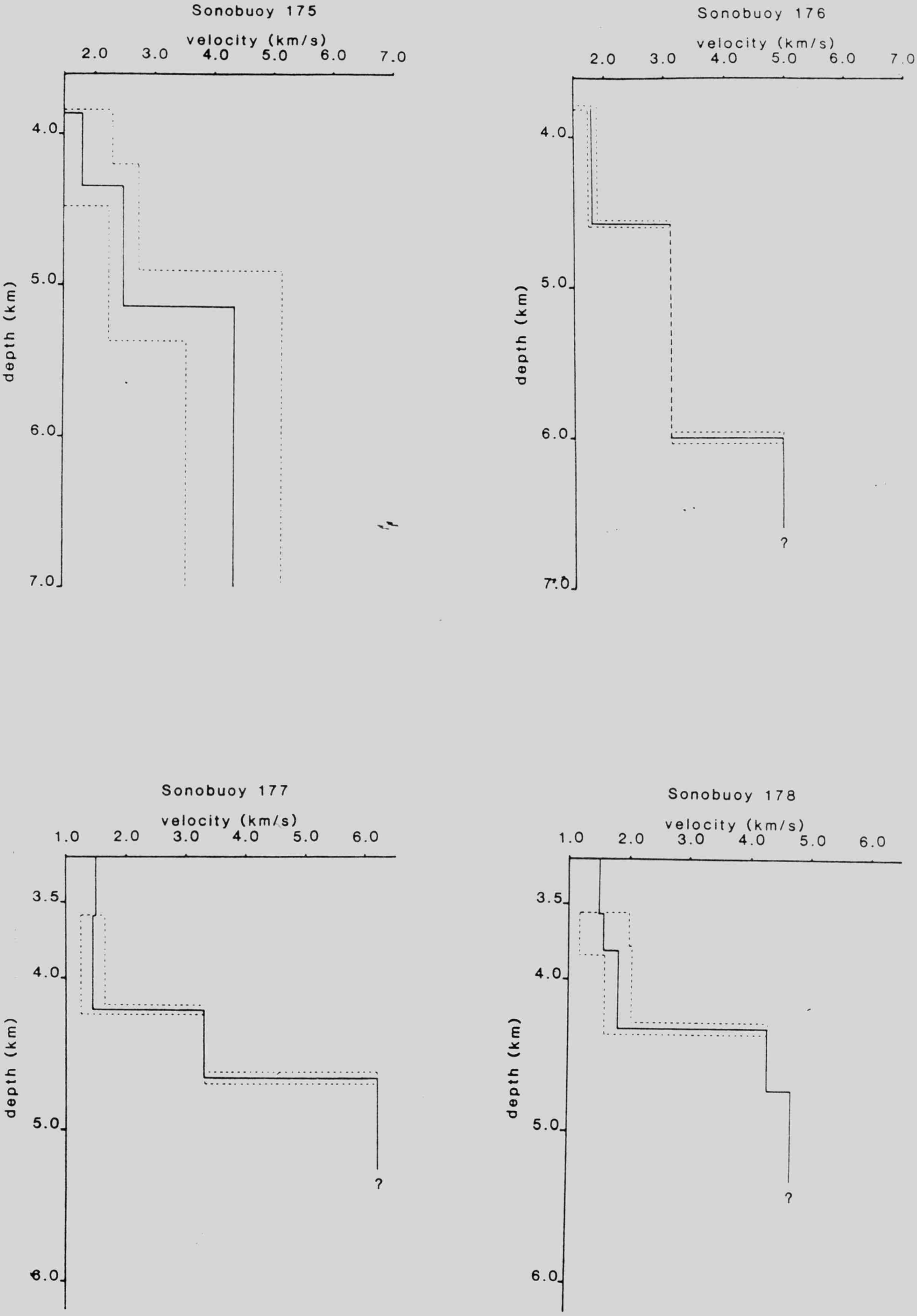

Figure 4.14 Velocity/depth profiles for Sonobuoys 175,176,177 & 178 from Hoskins et al (1974). The positions of these sonobuoy stations are indicated by triangles on Figure 4.1.

4.9 DISCUSSION

Recognition of oceanic layer 2 is very much dependent on the transmission characteristics of the overlying sediments. During this study, reflection hyperbolae indicative of volcanic basement were only seen on Line 2, when >50 km from the Maio/BoaVista ridge, on Line 4, to the extreme west, and on Line 5, to the north of the island of San Vicente. The limited area over which volcanic basement could be recognised is due to the masking effect of the overlying volcaniclastic sediments which increase towards the islands. This limiting factor is considered later in Chapter 5, section 5.5, when considering the relationship between bathymetry and free air gravity, or geoid, anomalies.

The shallowest recognisable occurence of volcanic basement is on Line 5 where it has an average depth of 6 seconds of two way travel time (TWT). This average takes into account the topography of the basement. There is a thickness of approximately 1 second of TWT of sediments on top of the basement at this location. Sonobuoy 07 was deployed in this area and recorded a velocity of ~5.1 km/s for the volcanic basement which suggests that it corresponds here to oceanic layer 2B from Houtz & Ewing (1976). The sediment velocity from the same sonobuoy was 2.32 km/s. The age of the lithosphere is ~110 Ma, from the magnetic anomaly study in Chapter 3. The expected depth for crust of this age assuming a cooling plate model, is, from Parsons & Sclater (1977), ~5800 m. The depth recorded by this study for oceanic layer 2 must be corrected for the isostatic loading of the overlaying sediments. The assumption here is that the sediments form a uniform thickness. Le Douaran & Parsons (1982) and Crough (1983) both studied the variation of sediment correction against TWT in D.S.D.P. holes in the North Atlantic for sediment densities varying from 1590 kg/m^3 to 2480 kg/m^3 and velocities from 1.65 km/s to 4.17 km/s.

Summary map showing velocity and lithology interpretations

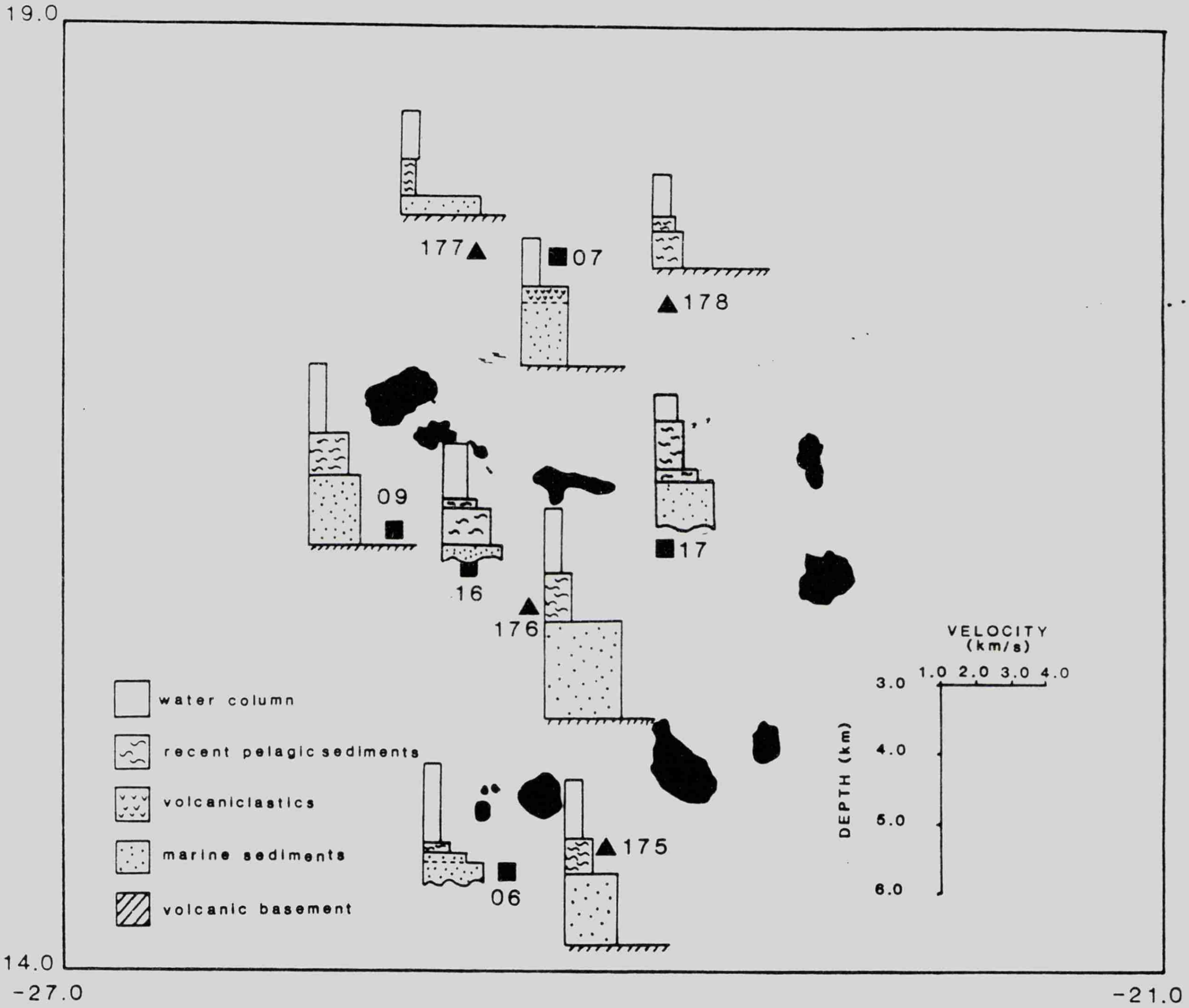

Figure 4.15 Summary diagram showing the velocity depth profiles for Sonobuoys 06, 07, 09, 16 & 17, from this study, and 175, 176, 177 & 178 from Hoskins et al (1972). The velocities have been assigned to lithologies as discussed in the text. The key for the lithologies is the same as that used for the seismic reflection line drawings. The width of the blocks indicates the velocity of that horizon. Scales are shown by the axis on the bottom right.

Crough (1983) estimates that the correction is accurate to within 10%. Using the corrections from Le Douaran & Parsons (1982) and Crough (1983) the observed depth to oceanic basement in the vicinity of Sonobuoy 07 is ~4200 m or ~4000 m respectively. Either of these two values is sufficient to demonstrate the observation made by Crough (1982) that the Cape Verde Rise has a depth anomaly of ~2 km. The oceanic swell is now at a depth equivalent to 25 Ma crust and Crough (1982) suggests this is evidence of thermal rejuvenation.

The crude seismic stratigraphy outlined in sections 4.3 and 4.4 can be used to infer a history of sedimentation for the Cape Verde Rise. The lithosphere was created at a mid ocean ridge in Late Jurassic times and thereafter followed a period of cooling and subsidence with deposition of normal marine limestones, black shales and cherts. Robertson (1984) suggests that the most likely time for uplift is around the late Palaeogene to early Miocene and it is suggested here that a certain amount of erosion took place at this time to form a regional unconformity. With the commencement of island building volcanism at ~20 Ma, Mitchell et al (1983), volcaniclastic sediments were deposited on this regional unconformity. Cessation of the major igneous activity resulted in a return to a more pelagic type of sedimentary regime with volcaniclastic material being limited to the areas close to the islands.

The velocity information does not contradict the seismic reflection interpretation. Figure 4.15 illustrates an interpretation of the velocity information from this study and Hoskins et al (1974) in terms of the seismic stratigraphy from the seismic reflection investigation. Those horizons detected using the sonobuoy refraction study that have velocities around 2.0 km/s are attributed to recent pelagic sediments. These occur on Sonobuoys 06, 16 & 17. A similar lithology has been given to a layer with velocity 2.13 km/s on

Sonobuoy 09 but this is more due to the reflection character; the velocity may be too high due to the reflector dipping up from receiver to source (see Figure 4.6).

The volcanic basement indicated in Figure 4.15 may be either oceanic layer 2 or volcanism associated with the Cape Verde Islands. No velocities were observed within the archipelago that have high enough values, >5.0 km/s for layer 2B from Houtz & Ewing (1976), to be attributable to oceanic basement. To the north of the archipelago, Sonobuoy 07 gives velocities of ~5.1 km/s and ~6.9 km/s. These velocities are comparable with a study of oceanic crust of the same age, in the Western North Atlantic, by Purdy & Rohr (1979) and Purdy (1983) and with velocities obtained by King (1974) and they are attributed to oceanic layers 2 and 3 respectively. The King (1974) study was a refraction experiment within the Cape Verde Archipelago and apart from the velocity mentioned above the results bear little similarity to the present study. Average sediment thickness was calculated, by King, to be 2-3 km using a combination of seismic refraction and gravity analysis, whereas this study suggests sediment thicknesses of only ~1.2 km. Comparison of this study with the results from Hoskins et al (1974) is good for Sonobuoys 175 and 176 but poor for Sonobuoys 177 and 178, to the north of the archipelago, and lithologies have been assigned on the basis of velocity information alone. No explanation can be given for the differences between Sonobuoy 07 and Sonobuoys 177 and 178 without recourse to the original data and the concurrent seismic reflection profiles.

4.10 CONCLUSIONS

1) The present study confirms, by observation of the oceanic basement and an isostatic correction for a uniform sediment layer, that layer 2 on the Cape Verde Rise is ~2 km higher than expected for crust of this age. Due to the masking nature of the overlying sediments volcanic basement could only be seen when >50 km from the islands. It is not possible, therefore, to accurately map the depth to volcanic basement around the archipelago.

2) The crude seismic stratigraphy derived from reflection analysis is compatible with a history of uplift around Miocene times, deposition of volcaniclastics during island building and a later return to a more pelagic type of sedimentation.

3) Velocities observed by radio sonobuoy wide angle reflection and refraction methods do not contradict the reflection profiling interpretations. Refraction velocities are compatible with an interpretation that the acoustic basement is layer 2 (~5.0 km/s). Wide angle reflection velocities suggest a complex history of sedimentation within the archipelago with lower velocities (~2.0 km/s) attributed to recent pelagic sediments and higher velocities (~2.5-~3.5 km/s) attributed to pre-volcanic marine sediments.

CHAPTER 5 (GRAVITY & GEOID MODELS)

5.1 INTRODUCTION

Observations of free air gravity anomalies and bathymetry taken by surface ships can be used to examine the state of compensation of bathymetric features in the worlds oceans. The general relationship between free air gravity anomalies, geoid anomalies and bathymetry is shown in Figure 5.1. The relationship appears, from simple observation, to be dependent on the wavelength being considered. At short wavelengths (<50 km) the bathymetry and gravity look similar but at long wavelengths the bathymetry and gravity look dissimilar.

The similarity in shape between the signals corresponding to free air gravity and bathymetry can be easily explained by considering the first order approximation that the gravity anomaly is due to the density contrast between sea-water and the material comprising the bathymetric feature. The value of the free air gravity anomaly, however, depends not only on the size, shape and density of the bathymetric feature, but also on its state of compensation.

When studying the gravity/bathymetry relationship at long wavelengths (>100km) the situation is not quite as simple as that outlined above. As water depth increases away from the bathymetric high the free air gravity anomalies typically decrease to values below zero and then gradually rise to settle at values close to zero. These negative side lobes to the gravity and local geoid anomalies are shown shaded in Figure 5.1. Their importance is that they indicate the state of compensation of the bathymetric feature. Two different models are described below and equations for the admittance, or response function, are given for each. The models are uncompensated topography and regionally compensated topography. Lambeck (1981), McNutt & Menard (1978) and Walcott (1970) used similar types of models but their, space domain, analysis required several stages. Firstly,

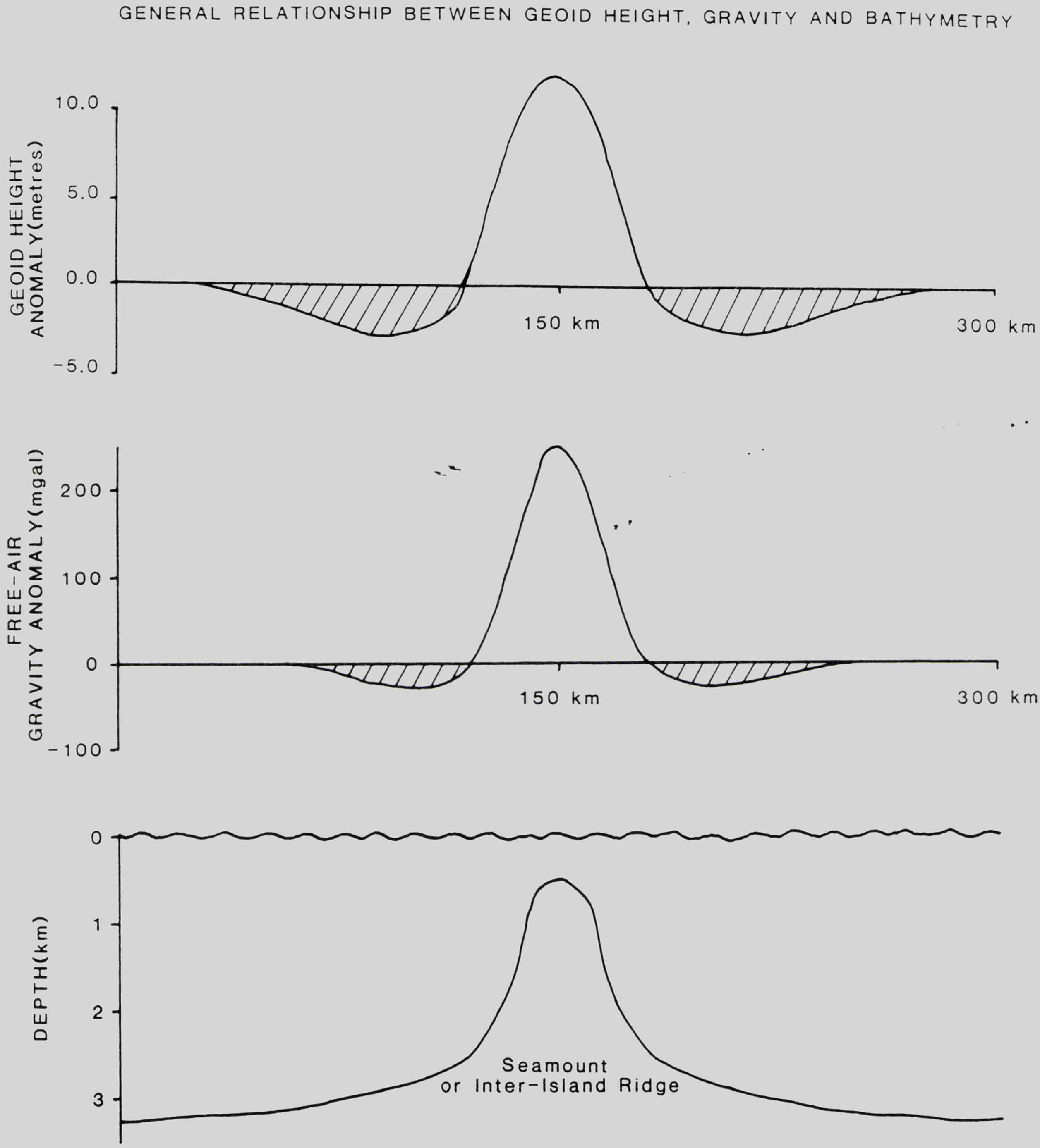

Figure 5.1 Diagramatic general relationship between free air gravity anomalies, geoid height anomalies and bathymetry. The signals appear similar at short (<50 km) wavelengths but dissimilar at longer (>100 km) wavelengths. Part of the dissimilarity can be attributed to the negative side lobes, shown shaded, which represent the gravity and geoid anomaly due to the compensation.

the load had to be calculated. This was normally done by modelling the bathymetric feature by prisms, the heights of which were defined above a certain depth, considered to be normal depth for that area. A density must also be assumed for the topography. Secondly, in the case of the regionally compensated model, the compensation due to this load was calculated. Finally, the free air gravity, or marine geoid, anomaly was calculated for the combination of the load and its compensation. Comparison of the calculated gravity, or geoid, with the observed values was used to determine if the model was satisfactory or not. This method, although having the advantages of accuracy and avoiding the problems inherent in using Fourier analysis, is considered clumsy and time consuming. The approach favoured here is to perform the calculations in the spatial frequency domain. In this method the relationship between gravity, or geoid, and bathymetry is calculated as a function of wavenumber ($\underline{k}_n$), or inverse wavelength (λ^{-1}). Watts (1979) reached a similar conclusion and opted to use linear transfer function techniques (Lewis & Dorman (1970) and McKenzie & Bowin (1976)) when modelling the geoid anomaly over the Hawaiian Ridge.

The advantages of using linear transfer function techniques are that the models can be compared directly with the observed relationship in the spatial frequency domain and that calculating the gravity, or geoid, effect of the models becomes greatly simplified. It is necessary, however, to constrain the relationship to being linear by ignoring orders higher than the first in the topography. The former is called, here, inversion and is the main subject of Chapter 7. The latter is called, here, forward modelling and comprises the second half of Chapter 8 and is also touched on briefly in the later stages of Chapter 7.

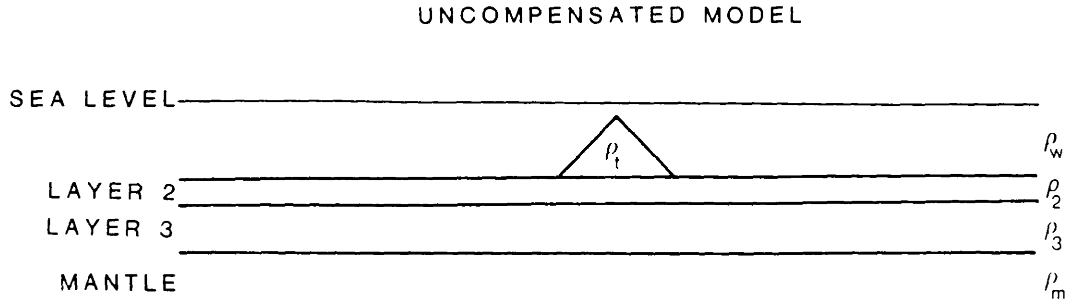

Figure 5.2 Simple uncompensated topography model of the oceanic lithosphere. The free air gravity anomaly is due to the density contrast between the bathymetric feature (ϱ_t) and sea water (ϱ_w).

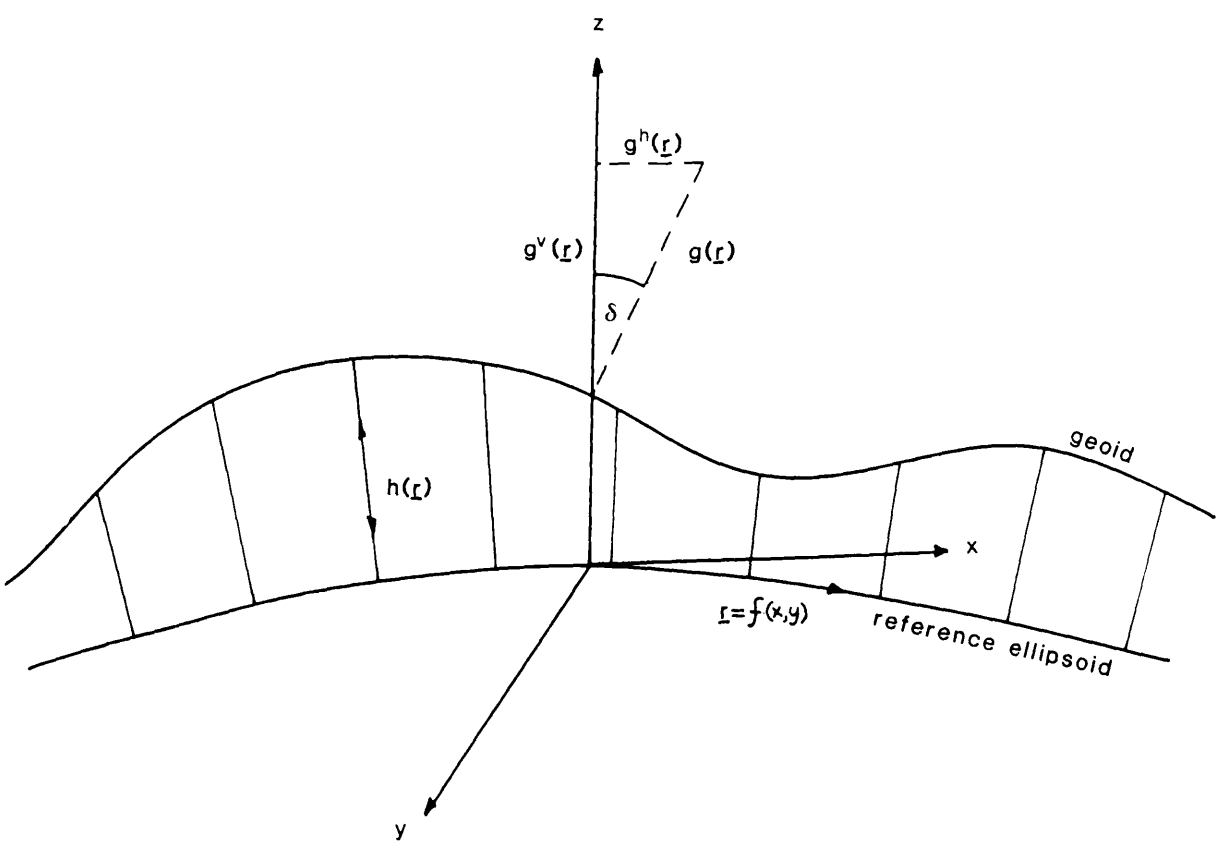

Figure 5.3 Relationship of a coordinate system with the z-axis perpendicular to the reference ellipsoid. Gravity is everywhere normal to the geoid and can be divided into horizontal and vertical components. The deflection of the vertical can be related to the geoid ($h(\underline{r})$).

5.2 UNCOMPENSATED TOPOGRAPHY

The simplest model for the relationship between gravity and bathymetry is one where the bathymetric load is uncompensated. This is illustrated in Figure 5.2. In this case the gravity anomaly will be due to the density contrast between the bathymetric feature and seawater. This has been used previously by such workers as McKenzie & Bowin (1976), Watts (1978) and McNutt (1979).

The following is modified from Parker (1972). Using a coordinate system with z vertically upwards and $\underline{r}$ representing a horizontal vector in the x-y plane, such that $\mathbf{r}=(\underline{r},z)$ (see Figure 5.3), then the Fourier transform of a function $f(\underline{r})$ can be obtained from:-

$$F(\underline{k}_n)={}_x\int f(\underline{r})\exp(-i\underline{k}_n.\underline{r})\ dS \qquad \text{(F5.1)}$$

where $F(\underline{k}_n)$=Fourier transform of $f(\underline{r})$

$\underline{k}_n$=wavenumber

$i=\surd(-1)$

dS=integration over the x-y plane

x=area of integration

The gravitational potential of a layer of material, density ρ, bounded below by z=0 and above by $z=b(\underline{r})$, is given by:-

$$U(\mathbf{r}_o)=G\rho\ {}_V\int 1/(|\mathbf{r}_o-\mathbf{r}|)\ dV \qquad \text{(F5.2)}$$

where $U(\mathbf{r}_o)$=gravitational potential measured at $\mathbf{r}_o$

G=gravitational constant

ρ=density of the anomalous material

dV=volume integral

F5.2 can be changed from a volume integral to the product of a surface integral and depth integral.

$$U(\mathbf{r}_o)=G\varrho \;{}_0\!\int^{b(\underline{r})} {}_D\!\int 1/(|\mathbf{r}_o-\mathbf{r}|)\; dS\; dz \qquad (F5.3)$$

where $b(\underline{r})$=bathymetry, or topography

$|\mathbf{r}_o-\mathbf{r}|$=distance from the measurement point to the element of anomalous material

D=domain of integration in the x-y plane

The second integral is taken over a finite domain, D, in the x-y plane and assumes that $b(\underline{r})=0$ for $|\underline{r}|>R$, where R is the limit of the domain. This is necessary to ensure convergence and is considered valid since the potential due the topography will diminish rapidly at distances far from the measurement point. If it is further assumed that measurements are all made on a plane lying above all the topography, $z_o>\text{maximum}(b(\underline{r}))$, then the Fourier transform of F5.3 is:-

$$\Omega(\underline{k}_n)=G\varrho \;{}_x\!\int {}_0\!\int^{b(\underline{r})} {}_D\!\int \exp(-i\underline{k}_n.\mathbf{r}_o)\; 1/(|\mathbf{r}_o-\mathbf{r}|)\; dS\; dz\; dS_o \qquad (E5.4)$$

where $\Omega(\underline{k}_n)$=Fourier transform of the potential

$\underline{k}_n$=wavenumber, or spatial frequency

By changing the order of integration the integral dependent on $\mathbf{r}_o$ can be solved using polar coordinates so that:-

$$\Omega(\underline{k}_n)=G\varrho \;{}_0\!\int^{b(\underline{r})} {}_D\!\int [2\pi\exp(-i\underline{k}_n.\underline{r}-|\underline{k}_n|(z_0-z))](1/|\underline{k}_n|)\; dSdz \qquad (E5.5)$$

The integral in dz can now be performed explicitly using the limits of $0\rightarrow b(\underline{r})$, to give:-

$$\Omega(\underline{k}_n)=2\pi G\rho \,_0\!\int \exp(-i\underline{k}_n.\underline{r}-|\underline{k}_n|z_0)[\exp(|\underline{k}_n|b(\underline{r}))-1](1/|\underline{k}_n|^2)\ dS \quad (F5.6)$$

The exponential term, $\exp(|\underline{k}_n|b(\underline{r}))$, can be expanded in a Maclaurin series to give:-

$$\exp(|\underline{k}_n|b(\underline{r}))=1+\Sigma(|\underline{k}_n|^m/m!)\ b^m(\underline{r}) \quad \text{summed over } m=0\rightarrow\infty \qquad (F5.7)$$

Only the first 2 terms of this series will be used and the analysis will be restricted to be linear. Dorman & Lewis (1970) calculated that the quadratic term for the relationship between gravity and topography is less than 10% of the linear term. McNutt & Menard (1978) also state that the linear approximation is satisfactory provided that the maximum deformation is less than 10% of the elastic plate thickness and show that in the case of the Cook-Society island range the linear approximation is justified. Banks et al (1977) also state that only using the linear term in the relationship is a reasonable approximation. Substituting only the first 2 terms of E5.7 back into F5.6 then the Fourier transform of the potential can be described by the Fourier transform of the topography after modification by a $2\pi G\rho$ constant and an exponential term. Thus:-

$$\Omega(\underline{k}_n)=2\pi G\rho \,_0\!\int \exp(-i\underline{k}_n.\underline{r})\ \exp(-|\underline{k}_n|z_0)\ b(\underline{r})\ 1/|\underline{k}_n|\ dS$$

$$=2\pi G\rho\ \exp(-|\underline{k}_n|z_0)\ B(\underline{k}_n)\ 1/|\underline{k}_n| \qquad (F5.8)$$

where $B(\underline{k}_n)$=Fourier transform of the topography, $b(\underline{r})$

z_0=plane of observation relative to the topography

The expression E5.8 is for the potential, but we wish to find the corresponding relationships for the gravity and geoid. The vertical attraction Δg is by definition of the potential:-

$$\Delta g=-\partial U/\partial z_o \quad (z_o \text{ positive upwards}) \tag{E5.9}$$

It follows that:-

$$G(\underline{k}_n)=-|\underline{k}_n|\Omega(\underline{k}_n) \tag{E5.10}$$

where $G(\underline{k}_n)$=Fourier transform of the gravity

The relationship between gravity and bathymetry in the spatial frequency domain is given by combining E5.10 & E5.8 so that:-

$$G(\underline{k}_n)/B(\underline{k}_n)=-2\pi G\varrho \exp(-|\underline{k}_n|z_o) \tag{E5.11}$$

The gravity/bathymetry relationship is called the admittance or response and is denoted by $Z(\underline{k}_n)$. If the bathymetry is measured downwards then the negative sign disappears from E5.11. The density ϱ can be replaced by the density contrast of the bathymetric feature causing the gravity anomaly and seawater. The expression E5.11 then looks like:-

$$Z(\underline{k}_n)=2\pi G(\varrho_t-\varrho_w)\exp(-|\underline{k}_n|d_t) \tag{E5.12}$$

where $Z(\underline{k}_n)$=the gravity admittance, or response

$\underline{k}_n$=wavenumber, or inverse wavelength

G=gravitational constant

ϱ_t=density of the topography

ϱ_w=density of seawater

d_t=depth of the topography relative to the observation plane

This is the linear term of a series expansion from Parker (1972). That just using the linear terms from E5.7 is a good approximation was shown by Watts (1978) by comparison with the line integral method of calculating gravity anomalies. The response for this model is similar to a Bouguer slab when $|k_n|=0$. This is to be expected since a $|k_n|=0$ term represents the mean, or DC shift, and can be approximated by a simple slab. As $|k_n|$ increases, the exponential term means that the smaller wavelength features of the bathymetry contribute less to the total gravity effect. The exponential term is modified by the depth to the topography since the shallower the topography the greater will be the gravity effect.

The relationship between the marine geoid and bathymetry can be calculated in a similar way by using a transfer function to get from the gravity to the geoid in the spatial frequency domain. The geoid height can be defined as (Garland 1979, p161):-

$$h(\underline{r}_o)=U(\underline{r}_o)/g \qquad \text{(E5.13)}$$

where $h(\underline{r}_o)$=geoid height

$U(\underline{r}_o)$=gravitational potential (as in equation E5.2)

g=gravitational gradient

Taking the Fourier transform equivalent of E5.13 gives:-

$$H(\underline{k}_n)=\Omega(\underline{k}_n)/g \qquad \text{(E5.14)}$$

where $H(\underline{k}_n)$=Fourier transform of the geoid height

$\Omega(\underline{k}_n)$=Fourier transform of the gravitational potential

The Fourier transform of the gravitational potential has been given earlier in E5.8 and the linear approximation is:-

$$\Omega(\underline{k}_n)=2\pi G\varrho\exp(-|\underline{k}_n|z_o)B(\underline{k}_n)/|\underline{k}_n| \qquad (F5.15)$$

The Fourier transform of the gravitational potential can be expressed in terms of the Fourier transform of the gravity.

$$\Omega(\underline{k}_n)=G(\underline{k}_n)/|\underline{k}_n| \qquad (E5.16)$$

where $G(\underline{k}_n)$=Fourier transform of the gravity

Combining E5.14 and E5.16 gives an expression for the Fourier transform of the geoid in terms of the Fourier transform of the gravity, thus:-

$$H(\underline{k}_n)=1/g|\underline{k}_n|\ G(\underline{k}_n) \qquad (F5.17)$$

The geoid response is denoted by $Z'(\underline{k}_n)$ to distinguish it from the gravity response $Z(\underline{k}_n)$.

$$Z'(\underline{k}_n)=1/g|k_n|\ 2\pi G(\varrho_t-\varrho_w)\exp(-|\underline{k}_n|d_t) \qquad (F5.18)$$

The main effect of the transfer function is to reduce the short wavelength terms of the geoid (large $|\underline{k}_n|$) relative to the long wavelength terms (small $|\underline{k}_n|$). This results in geoid anomalies being 'wider' than the corresponding gravity anomalies.

Anomalies from the uncompensated model are typified by having a high degree of correlation between the bathymetry and gravity, or geoid, at all wavelengths.

5.3 REGIONAL COMPENSATION

The regional compensation mechanism used in this study is an elastic thin plate model that flexes under an applied load. This model is illustrated in Figure 5.4. The theory that the earth's crust responds to loading by bending is not new. Hertz (1884) suggested that the loading effect of glaciers could be described by flexure of a thin plate. Further application of this work to a geological situation was taken up by Vening Meinesz (1931) and later by Gunn (1943), who examined the gravity anomalies over mountain chains. Of particular relevance to this study was the conclusion by Vening Meinesz (1948) that the Cape Verde Islands are regionally compensated on a scale of several hundred kilometres.

The basic assumptions of the thin plate model are:-

1) The earth's crust can be modelled as an elastic plate overlying a fluid substratum.

2) The plate's thickness is small relative to the wavelength of the bending.

These assumptions are considered to be geologically realistic since the lower lithosphere can be expected to behave as a fluid (Banks et al (1977)) over time periods measured in millions of years and the crust maintains its rigidity over similar periods. The rigidity of the thin plate can be expressed as a parameter termed the effective elastic thickness. Previous studies by McNutt (1979), Cochran (1979) and Watts (1978), amongst others, have shown that the oceanic crust has values of effective elastic thickness of between 5 km and 30 km. The wavelength of bending has typical values of $\sim$200 km, from Watts & Cochran (1974).

The equation to be solved is adapted from mechanical engineering and can be found in texts such as Sneddon (1969). The equation for equilibrium of the thin plate model is given here from McNutt & Menard (1978) for a load, $p(\underline{r})$.

$$D\nabla^4 w(\underline{r})=p(\underline{r}) \tag{F5.19}$$

where D=flexural rigidity of the plate

$w(\underline{r})$=deflection of the plate

$p(\underline{r})$=forces acting on the plate

$\nabla=\underline{x}\ \partial/\partial x+\underline{y}\ \partial/\partial y$

The flexural rigidity of the plate can be expressed in terms of an effective elastic thickness, as already mentioned above.

$$D=ET^3/12(1-\sigma^2) \tag{F5.20}$$

where E=Young's modulus

σ=Poisson's ratio

T=effective elastic thickness

The forces acting on the plate comprise the downward force due to the load, of density contrast $(\rho_t-\rho_w)$, and the buoyancy force set up by the displaced fluid, density contrast $(\rho_m-\rho_w)$.

$$p(\underline{r})=-(\rho_t-\rho_w)gb_o(\underline{r})-(\rho_m-\rho_w)gw(\underline{r}) \tag{F5.21}$$

where g=normal gravity

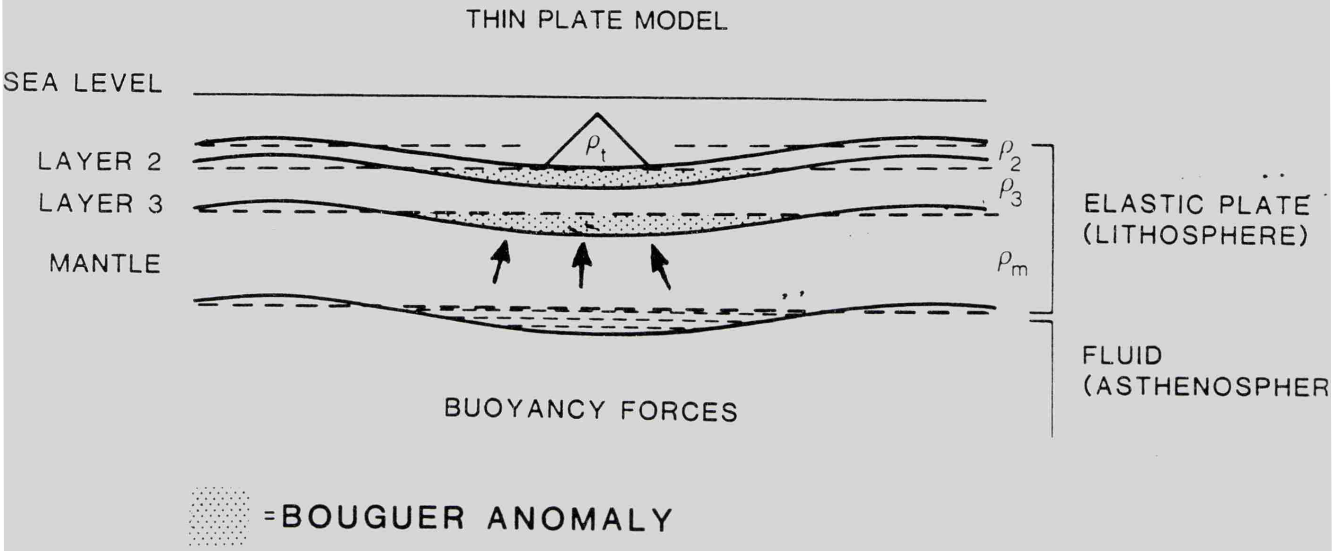

Figure 5.4 Thin plate model that flexes under an applied load. The amount of bending is dependent on the flexural rigidity of the plate which can be expressed as an effective elastic thickness. The contributions to the compensation anomaly are shown shaded and correspond to the layer2/layer3 and layer3/moho interfaces. The bouyancy forces are assumed to act at the interface between the elastic plate and the fluid substratum. This model can be contrasted with the simple uncompensated model shown in Figure5.2.

The measured bathymetry $b(\underline{r})$, also comprises two parts; the bathymetry of the load, $b_o(\underline{r})$, and the deflection topography, $w(\underline{r})$.

$$b(\underline{r})=b_o(\underline{r})+w(\underline{r}) \tag{F5.22}$$

As pointed out by <u>Banks et al (1977)</u> the solution to the above system of equations can be greatly simplified by taking the two-dimensional Fourier transforms of (E5.19),(E5.21) and (F5.22). This means the solution will be in the spatial frequency domain and can thus be compared directly with observed admittance estimates. Combining (E5.19) and (E5.21) we find:

$$|\underline{k}_n|^4 DW(\underline{k}_n)=-(\rho_t-\rho_w)gB_o(\underline{k}_n)-(\rho_m-\rho_w)gW(\underline{k}_n) \tag{E5.23}$$

where $W(\underline{k}_n)={}_x\int w(\underline{r})\exp(-i\underline{k}_n.r)\ dS$
and dS=surface integral over the x-y plane

combining (E5.23) and the Fourier transform of (F5.22) gives:

$$W(\underline{k}_n)=-((\rho_t-\rho_w)/(\rho_m-\rho_t))(1+|\underline{k}|^4 D/(\rho_m-\rho_t)g)^{-1}B(\underline{k}_n) \tag{E5.24}$$

Equation (E5.24) can be related to the gravity anomaly due to the deflection, $w(\underline{r})$, using, <u>Parker (1972)</u>. This is a modification of equation (E5.8) where density varies with depth and there are an infinite number of layers.

$$G(\underline{k}_n)=2\pi GW(\underline{k}_n)\int(\partial\rho/\partial z)\exp(-|\underline{k}_n|z)dz \tag{F5.25}$$

However, this more general expression can be simplified since it is assumed the gravity anomaly is due to density contrasts at known depths; i.e. the layer2/layer3 interface and the moho.

$$G(\underline{k}_n)=2\pi GW(\underline{k}_n)\{(\rho_3-\rho_2)\exp(-|\underline{k}_n|z_1)+(\rho_m-\rho_3)\exp(-|\underline{k}_n|z_2)\} \quad (E5.26)$$

Hence:-

$$Z(\underline{k}_n)=-2\pi G((\rho_t-\rho_w)/(\rho_m-\rho_t))(1+|\underline{k}_n|^4 D/(\rho_m-\rho_t)g)^{-1}[(\rho_3-\rho_t)\exp(-|\underline{k}_n|z_1)+(\rho_m-\rho_3)\exp(-|\underline{k}_n|z_2)] \quad (E5.27)$$

To the above must be added the response of the bathymetry alone. This is simply the response of the uncompensated topography model used in section 5.2.

$$Z(\underline{k}_n)=2\pi G(\rho_t-\rho_w)\exp(-|\underline{k}_n|d_t) \quad (E5.28)$$

The final response in the spatial frequency domain as calculated using the thin plate approximation is thus:

$$Z(\underline{k}_n)=2\pi G(\rho_t-\rho_w)\{\exp(-|\underline{k}_n|d_t)-(1+|\underline{k}_n|^4 D/(\rho_m-\rho_t)g)^{-1}[((\rho_3-\rho_t)/(\rho_m-\rho_t))\exp(-|\underline{k}_n|z_1)+((\rho_m-\rho_3)/(\rho_m-\rho_t))\exp(-|\underline{k}_n|z_2)]\} \quad (E5.29)$$

where $Z(\underline{k}_n)$=the response of the model at wavenumber k_n

ρ_w=the density of sea water

ρ_t=the density of the topography (=density of layer 2)

ρ_3= " " " layer 3

ρ_m= " " " the upper mantle

d_t=the depth of the topography relative to the plane of observation

z_1=depth to the layer 2/layer 3 interface

z_2=depth to the layer 2/moho interface

The modification of the above, gravity response, to geoid response is done in exactly the same manner as for the uncompensated model. That is:-

$$Z'(\underline{k}_n)=1/g|\underline{k}_n|\ Z(\underline{k}_n) \qquad \text{(E5.30)}$$

As the flexural rigidity in the above model tends to very high values ($D\rightarrow\infty$) the response becomes similar to that of the uncompensated model. This is to be expected since the load will become supported by the strength of the lithosphere alone and the buoyancy term becomes negligable. As the flexural rigidity tends to very low values ($D\rightarrow 0$) the response approaches something similar to simple isostatic compensation, where the load is supported by buoyancy terms alone.

5.4 MORE COMPLEX FLEXURAL MODELS

The thin plate model outlined above is very simple in terms of its assumed density distribution and its linear response to loading with respect to time. Also no account is taken of any sediments that may overlay the oceanic basement. Figure 5.5 shows a slightly more realistic geological model and can be compared with the simple thin plate model of Figure 5.4.

The density of the load is considered, here, to be constant and equal to the density of the material that infills the flexural moat. This is a considerable simplification since Robertson (1967) showed from a study of the Southern Cook Islands that islands can have a high density inner core associated with them. The material that infills the flexural moat is likely to be a mixture of high density volcanic material plus relatively lower density marine sediments, or

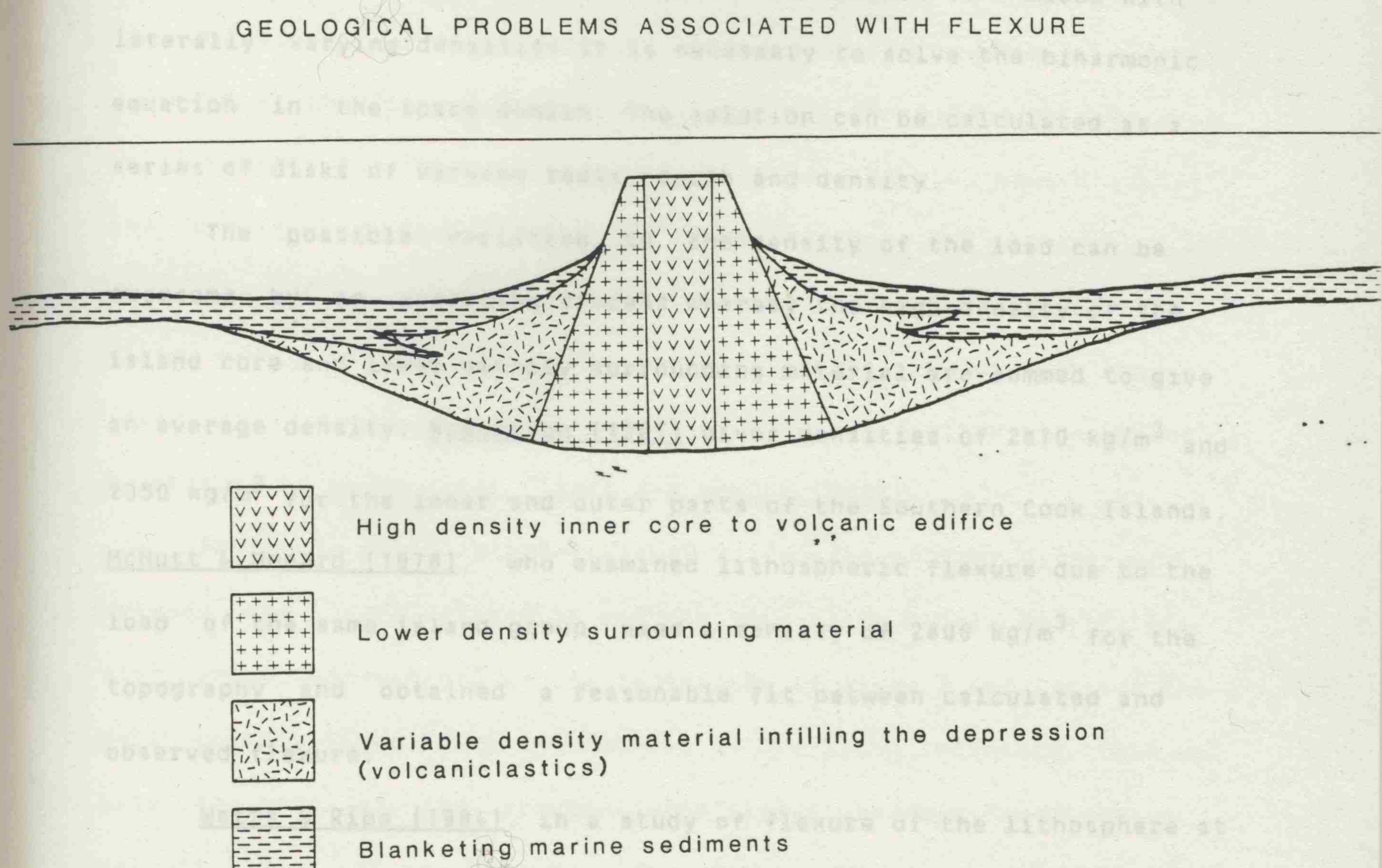

Figure 5.5 Additional geological factors that complicate the simple thin plate model are outlined in this diagram and are discussed in the text. The main features are the laterally varying density of the load, the inclusion of a sediment layer and variable density infill of the depression around the load.

volcaniclastics, and will not necessarily have the same density as that assumed for the topography. This was termed the 'archipelagic apron' by Menard (1956). To calculate the flexure of a model with laterally varying densities it is necessary to solve the biharmonic equation in the space domain. The solution can be calculated as a series of disks of varying radii, depth and density.

The possible variation in the density of the load can be overcome by an averaging process whereby the high density of the island core and lower density surrounding material are summed to give an average density. Robertson (1967) gives densities of 2870 kg/m^3 and 2350 kg/m^3 for the inner and outer parts of the Southern Cook Islands. McNutt & Menard (1978), who examined lithospheric flexure due to the load of the same island group, used a density of 2800 kg/m^3 for the topography and obtained a reasonable fit between calculated and observed flexure.

Watts & Ribe (1984), in a study of flexure of the lithosphere at seamounts, examined 4 different models, including the thin plate model shown above and a similar model with variable density sediment infill. The techniques described by Bodine et al (1981) were used to calculate the gravity and geoid anomalies due to each of the models. The amplitudes of both the gravity and geoid anomalies for the sediment infill model were higher than the anomalies for the constant density thin plate model. This suggests that using the constant density model will result in overestimating the effective elastic thickness. Therefore the model used in Chapters 7 & 8 will give estimates of the effective elastic thickness that can be considered to be a maximum. A similar conclusion was reached from a study by Lambeck & Nakiboglu (1980).

The response of the lithosphere to an applied load is, in the model outlined above, assumed to be linear with respect to time. The possibility that this is not the case was investigated by Watts (1978) and Watts & Cochran (1974) while studying the Hawaiian-Emperor seamount chain. A viscoelastic model was used to try and account for the variation in effective elastic thickness from the Hawaiian Ridge (~30 km) to the Emperor Seamounts (10-30 km). The time constants were so different for the two parts of the seamount chain, however, that the simple viscoelastic model had to be rejected. The alternative is that the effective elastic thickness, measured by the simple thin plate model, is acquired at the time of loading and does not change appreciably with time. This suggestion has been further strengthened by studies by Watts et al (1980) and McNutt (1984).

Sediments that blanket layer 2 are also another difference between the 'real' situation and the thin plate model. Ideally the study should concentrate on the topography of layer 2 and correct the depth to this layer for the thickness of overlying sediments. This was used as part of the argument for flexure beneath Hawaii by Walcott (1970). It is, however, impractical to use such an argument in the case of the Cape Verde Rise since the seismic evidence is not as detailed as in the Hawaiian case (Chapter 4 outlines the available seismic data for the Cape Verde Rise). The sediments will serve to smooth out the rough topography of layer 2 and since the sediments form a more or less uniform blanket over the rise they can be accounted for by a D.C. shift, or constant offset term in the bathymetric signal. The spatial frequencies that could be affected are therefore either very high (λ^{-1}>0.05 km^{-1}) or very low (λ^{-1}<0.002 km^{-1}). Ribe (1982) suggests that the diagnostic waveband for examining lithospheric flexure is between 0.003 km^{-1} and 0.02 km^{-1}. It is considered therefore that the overlying sediments will not seriously affect the observed relationship between the bathymetry and gravity, or geoid.

CHAPTER 6 (DATA PROCESSING)

6.1 INTRODUCTION

Using the thin plate model outlined in Chapter 5 it is possible to attribute the negative gravity anomalies to lower density material displacing higher density material. The layered model proposed in Chapter 5 provides for contributions to this negative anomaly from the topography/layer2, layer2/layer3 and layer3/upper mantle interfaces. The total free air gravity anomaly observed by a surface ship will be the sum of the anomaly due to the bathymetric feature and the anomaly due to the compensation. The size of the contribution from the compensation will depend on the density contrast across the interfaces and the wavelength at which the compensation will contribute will depend on the rigidity of the oceanic crust.

As was outlined in Chapter 5, a very rigid crust, that is one with a high effective elastic thickness (>40 km), will support a load with little bending and hence the negative gravity anomaly due to the compensation will be very small and distributed over long wavelengths (>200 km). A very weak crust, that is one with a low effective elastic thickness (<5km), on the other hand, will bend easily and produce a large compensation anomaly over relatively short wavelengths (50-100km). The extremes of this type of simple model are:-

1) The crust is infinitely strong and the load is supported by the strength of the crust alone. The gravity anomaly is due to the bathymetric feature and no contribution from the compensation occurs.

2) The crust has no strength and the load is supported by bouyancy forces from below. This would produce a maximum compensation anomaly and the load would be in local isostatic equilibrium.

Watts et al (1985) show examples of these two extremes from observation of bathymetry and free air gravity in the pacific. Figure 6.1 shows data collected over the Necker Ridge and an unnamed seamount

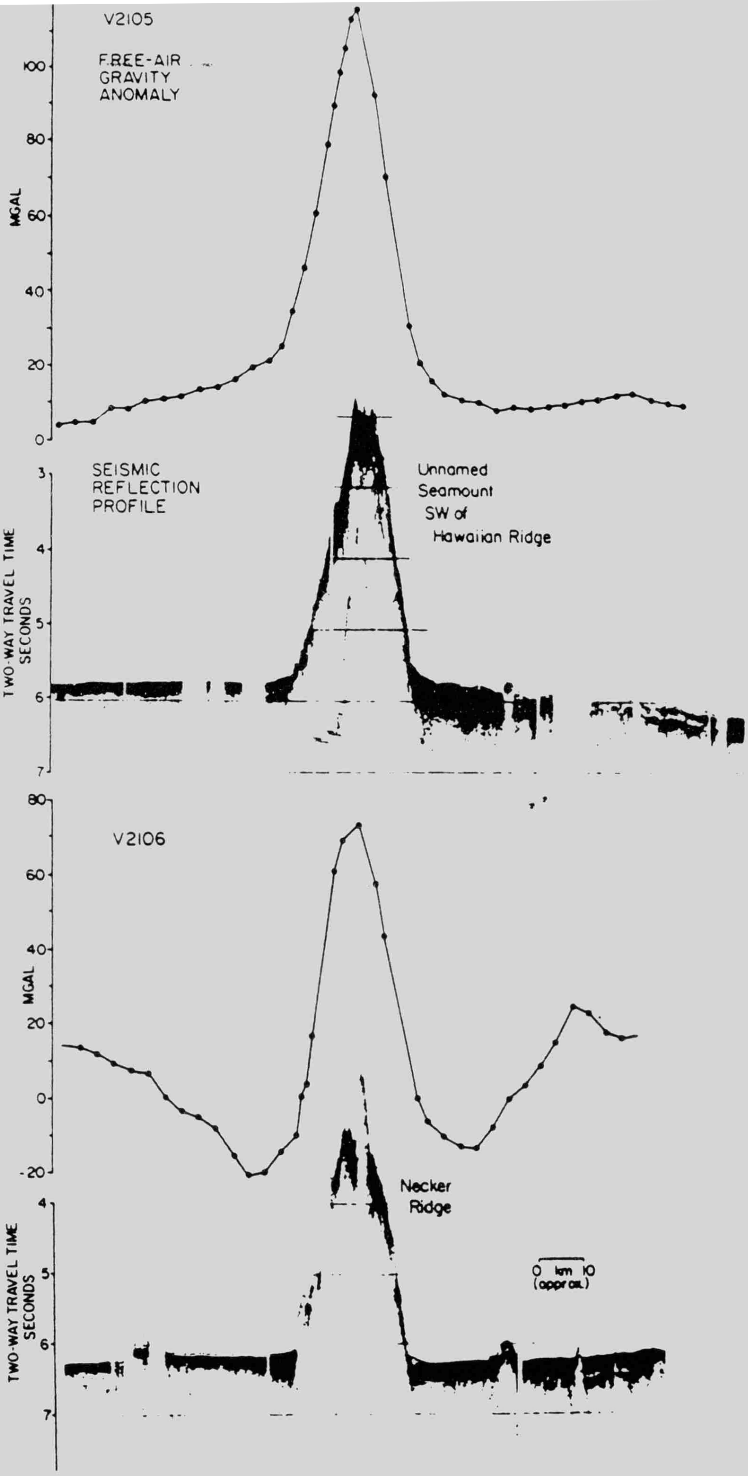

Figure 6.1 Observed variation of free air gravity and bathymetry over two bathymetric features, of similar horizontal and vertical dimensions, in the Pacific ocean, taken from <u>Watts et al (1985)</u>. The upper profile is over an unnamed seamount south-west of the Hawaiian Ridge and shows relatively small, or absent, negative side lobes. This feature is considered to be formed on crust with a high (>30 km) effective elastic thickness and thus the topography is supported by the rigidity of the lithosphere. The lower profile over the Necker Ridge shows pronounced negative side lobes. This indicates that the topography is not wholly supported by the rigidity of the crust and some regional compensation has occured.

south west of the Hawaiian Ridge. Both features are of similar cross sectional area. The Necker Ridge is characterised by a relatively small amplitude (80mgal) high over the ridge, flanked by relatively small amplitude lows (-20 mgal) on either side. This situation corresponds to the low flexural rigidity case. In contrast the unnamed seamount has a high amplitude (120 mgal) anomaly over the bathymetric high and very small amplitude, or absent, flanking lows. This would correspond to a case where the effective elastic thickness, and hence flexural rigidity, was high.

6.2 FOURIER TRANSFORMATION

The purpose of processing the bathymetry and free air gravity anomaly data is to try and parameterize their relationship and to show how this varies with wavelength. The observed relationship can then be compared with calculated relationships using the simple model shown in Chapter 5. It is necessary to break down the complex signals of gravity and bathymetry into their constituent wavelength components.

The same techniques that are used in time sequence analysis can be applied to signals in the space domain. Fourier series are a convenient way of describing a complex signal as a sum of sine and cosine terms of varying amplitude and wavelength.

A function f(t) can be described, over the period $-T/2 \leq t \leq T/2$, by the infinite series (Kreyzig (1979) p479):-

$$f(t)=a_0+\Sigma(a_n\cos(2\pi nt/T)+b_n\sin(2\pi nt/T)) \qquad (E6.1)$$

where $a_0=1/T\int f(t)dt$

$a_n=2/T\int f(t)\cos(2\pi nt/T)\,dt$

$b_n=2/T\int f(t)\sin(2\pi nt/T)\,dt$

and the interval of integration is over the period $-T/2 \leq t \leq T/2$.

The coefficients a_n and b_n give the amplitudes of the cosine and sine functions respectively at wavelengths from T, the period of the function, to an infinitely small wavelength. The a_0 term can be considered as a constant, or D.C. shift, term.

The series can be split into two parts: the even coefficients comprised of cosine terms and the odd coefficients comprised of the sine terms. The cosine terms are considered even since they are symmetric about zero. That is:-

$$\cos(x)=\cos(-x) \qquad (E6.2)$$

Similarily the sine terms are considered odd since sine functions are asymmetric about zero. That is:-

$$\sin(x)=-\sin(-x) \qquad (E6.3)$$

Using Euler's formula it is possible to rewrite the Fourier series in terms of complex arithmetic.

$$\exp(ix)=\cos(x)+i\sin(x) \quad \text{Euler's formula.} \qquad (E6.4)$$

$$f(t)=\Sigma F_n \exp(i2\pi nt/T) \qquad (E6.5)$$

where $F_n=1/T\int f(t)\exp(-i2\pi nt/T)\,dt$

$i=\sqrt{(-1)}$

This introduces the concept of a signal being composed of real and imaginary parts. The real part corresponds to the even cosine terms, whereas the imaginary part corresponds to the odd, sine terms.

Figure 6.2 shows how a complicated signal, that could represent

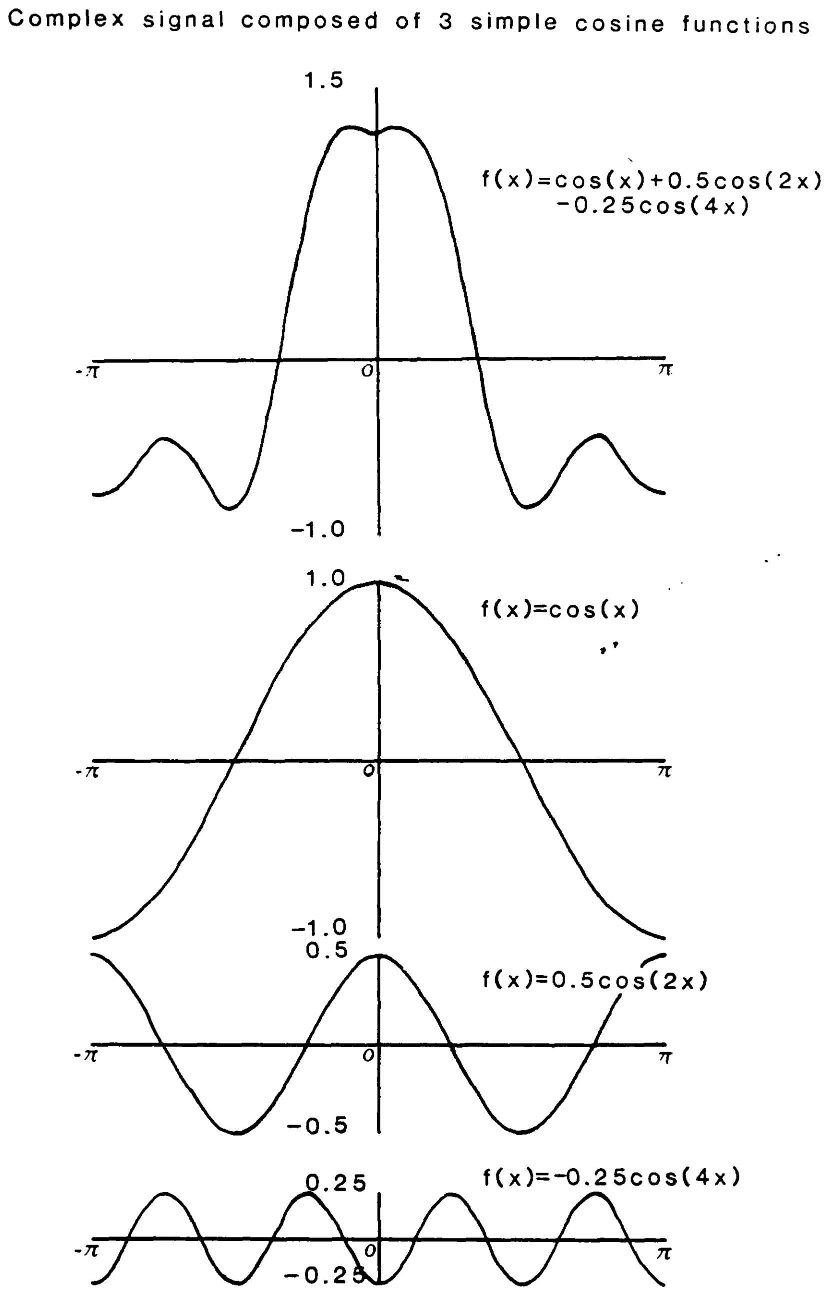

Figure 6.2 Example of how a complex signal (upper curve) can be broken down into a series of simple cosines (lower curves). This is the principle of Fourier analysis and is a limited application of equation E6.1.

a seamount or inter-island ridge, be decomposed into a simple sum of cosine terms. The original signal is symmetric so only real, cosine terms are necessary to describe it. The amplitude coefficients can be either negative or positive.

The algorithm (E6.5) given above is only suitable to describe continuous functions and must be modified for use with functions sampled at discrete intervals. Figure 6.3 illustrates the difference between continuous and discrete functions. The discrete form of the Fourier tranform is:-

$$F(t_k)=\Sigma f(x_j)\exp(-i2\pi kj/N) \qquad (E6.6)$$

where $k=0,1,2,......,(N/2)$

It is possible to get the original space domain data series from the Fourier coefficients by application of the inverse Fourier transformation.

$$f(x_j)=1/N\Sigma F(x_k)\exp(i2\pi kj/N) \qquad (E6.7)$$

where $j=1,2,3,......,N$

The transformation from space domain to spatial frequency domain is completely analogous to transforming from time to frequency. If the original series has wavelength (λ) units of km then the transformed series has spatial frequency units of km^{-1}, or inverse wavelength (λ^{-1}). Again, as in the time series analogy, the higher the spatial frequency the shorter the wavelength and vice versa.

Computation using equation E6.7 can be slow in terms of computer time since it requires N^2 generations of addition and multiplication.

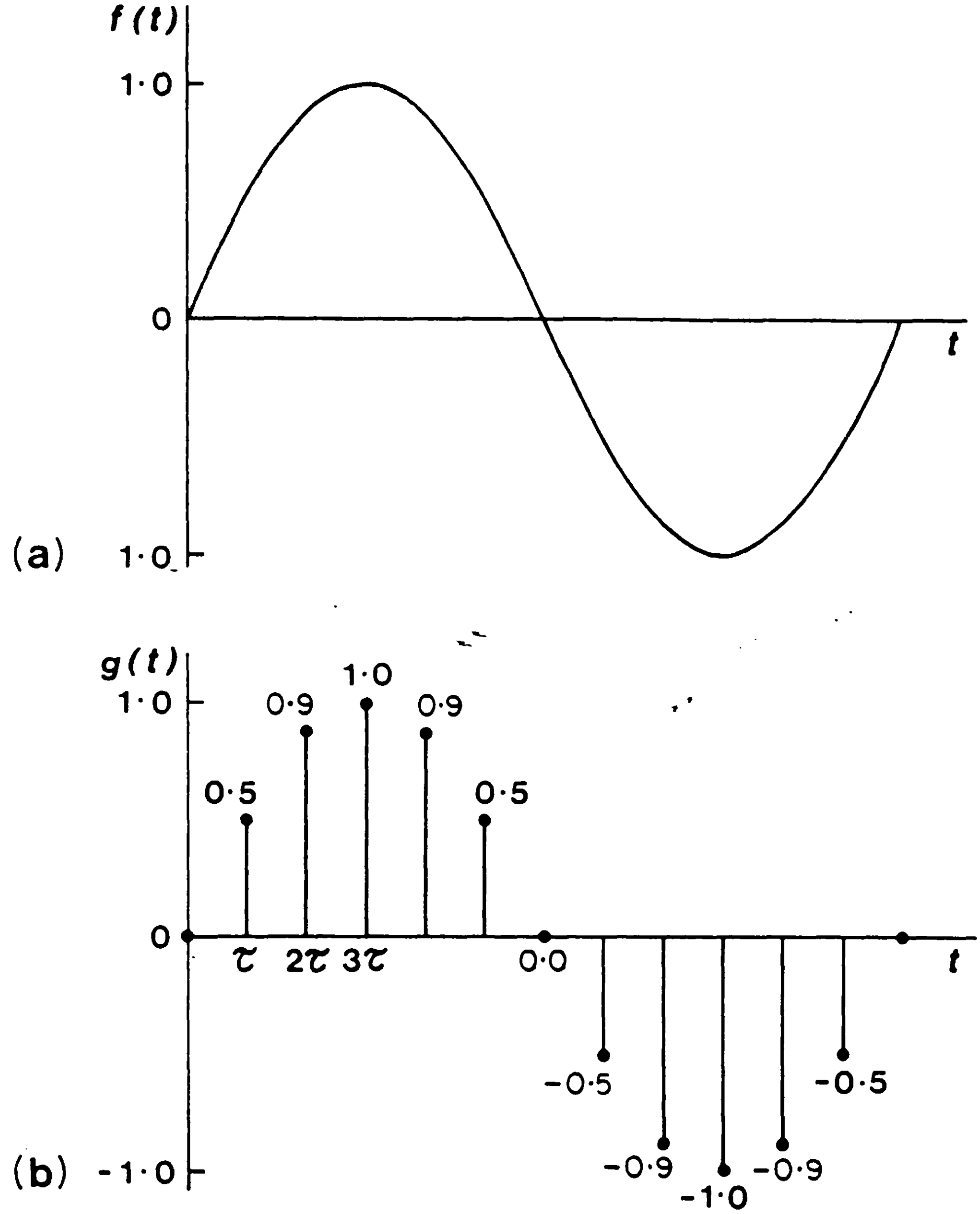

Figure 6.3 Illustration of discrete sampling of a continuous function. a) represents the continuous, in this case sine, function varying as a function of (t). b) represents the sampled function with the sample rate at 6/π. Sampling reduces the smallest resolvable frequency to the Nyquist frequency, in this case 3/π.

By using an algorithm known as the Fast Fourier Transform (FFT) it is possible to reduce the number of operations to $N\log_2 N$ and thus make transformation of large series more efficient. A major requirement, however, is that the data series is an integer power of 2 long. The algorithm used throughout this work is by Cooley and Tukey (1966).

Several important constraints must be satisfied before data can be passed into the Fast Fourier Algorithm.

1) The data points should be regularly spaced; the data series should have a constant sample interval. The minimum data spacing required to define a sinusoidal wave is 2 samples/wavelength. Therefore the maximum spatial frequency that can be resolved will be half the sampling frequency. This maximum frequency is known as the Nyquist fequency.

2) As has already been noted, a requirement for the FFT is that the data series has length equivalent to an integer power of 2. The total length of the data series represents the lowest resolvable frequency that the transformed data series will contain. This frequency is known as the first harmonic, $1/(N\Delta x)$, and the series increases up to the Nyquist frequency, $(N/2)/(N\Delta x)=1/2\Delta x$.

3) The final constraint is that the first and last data point should be equal. This is a circular universe requirement whereby a finite series can be considered infinite by joining up the first and last points to form a continuous loop. This assumes that the data series is periodic over the range sampled.

The original data series is passed into the FFT algorithm as a complex array with the data values in the real part and the imaginary part set to zero. After transformation the complex series contains the cosine coefficients in the real part and the sine coefficients in the imaginary part. The symmetry of the transformed series is important, especially if the inverse Fourier transform is to be applied at some later stage.

For an input series of:-

$$f(x_n)=(a_n+ib_n) \tag{F6.8}$$

where $n=0,1,2,3.....(N-1)$

N=integer power of 2

$b_n=0$

$a_n=f(x_n)$

The transformed series is $F(k_n)$:-

$$F(k_n)=(c_n+id_n) \tag{F6.9}$$

where $n=0,1,2,3.....(N-1)$ as before

c_n=real, cosine coefficients

d_n=imaginary, sine coefficients

The symmetry is as follows:-

$d0=0=dN/2$

$d1=-d(N-1)$

. .

. .

$d(N/2-1)=-d(N/2+1)$

The above theory has been outlined for a simple 1-dimensional system where $f(x)$ is dependent only on x. This can, however, be easily extended for the case where $f(x,y)$ is dependent on 2 variables, x and y. The same algorithm can be used but care must be taken when rearranging the coefficients that the correct symmetry is maintained. Kanasewich (1975), shows that for 2-dimensional data the symmetry should be of the form:-

a0	a1	a2	a3	a4	a3	a2	a1
b0	b1	b2	b3	b4	b3	b2	b1
c0	c1	c2	c3	c4	c3	c2	c1
d0	d1	d2	d3	d4	d3	d2	d1
e0	e1	e2	e3	e4	e3	e2	e1
d0	d1	d2	d3	d4	d3	d2	d1
c0	c1	c2	c3	c4	c3	c2	c1
b0	b1	b2	b3	b4	b3	b2	b1

The data are passed into the FFT algorithm as a 1-dimensional series by reading the 2-dimensional series by columns or rows.

6.3 ADMITTANCE (OR RESPONSE FUNCTION)

The relationship of bathymetry to free air gravity anomaly in the spatial frequency domain is known as the admittance or response function. This relationship can also be described in the space domain, as pointed out by McKenzie & Bowin (1976), as a convolution of the bathymetry with a filter, the result of which is the gravity. By using the convolution theorum, it is simple to show that the convolution in the space domain is equivalent to multiplication in the spatial frequency domain. Many workers, such as McNutt (1979), Watts & Ribe (1984) and Ribe & Watts (1982), have used this relationship. The admittance is the cross spectrum of gravity and bathymetry divided by the power of the bathymetry at a particular spatial frequency, $\underline{k}_n$. That is:-

$$Z(\underline{k}_n)=\langle G(\underline{k}_n)*B(\underline{k}_n)^*\rangle/\langle B(\underline{k}_n)*B(\underline{k}_n)^*\rangle \qquad (E6.10)$$

where $Z(\underline{k}_n)$=the admittance, or response

$G(\underline{k}_n)$=fourier transformed gravity series

$B(\underline{k}_n)$=fourier transformed bathymetry series

*=the complex conjugate

$\langle\ \rangle$=averaging over several estimates

Averaging can be performed by using several 1-dimensional profiles over the same geological feature as was done by Tamsett (1984), Watts (1979) and Cochran (1979). The admittance estimates are made at equal arithmetic intervals of Δk, where $\Delta k=2\pi/T$ km^{-1} and T=the total length of the data series, and $k_n=n\Delta k$, with n=1,2,3....etc. This arrangement gives a strong concentration of data values at the short wavelength end of the spectrum. Logarithmically spaced estimates, as shown by Dorman & Lewis (1972), each contribute approximately the same amount of information so the admittance estimates are further averaged over logarithmically increasing bandwidths. This is the technique that has been applied, in the analysis of free air gravity and bathymetry over the Cape Verde Rise, in Chapter 7. Alternatively if the data is 2-dimensional, averaging can be done by summing the Fourier coefficients within set limits of $|\underline{k}_n|$, where $|\underline{k}_n|=\surd(k_{xn}{}^2+k_{yn}{}^2)$. This type of azimuthal averaging was used by McNutt (1979), Dorman & Lewis (1972) and Banks & Swain (1978) and was utilised in Chapter 8 for analysis of the relationship between the marine geoid and bathymetry, in 2-dimensions, over the Cape Verde Rise.

The observed admittance is a complex series with both real and imaginary parts. McKenzie & Bowin (1976), pointed out that theoretically the admittance should be real for all values of $\underline{k}_n$. This is easily understood by considering that a constant density bathymetric feature that is roughly symmetric should produce a free air gravity anomaly that has the same symmetry; there should be no phase shift between the gravity anomaly and the bathymetry.

The phase of the admittance, $Z(\underline{k}_n)$, can be calculated simply from:-

$$\phi(\underline{k}_n)=\tan^{-1}(Im(Z(\underline{k}_n))/Rl(Z(\underline{k}_n))) \quad (E6.11)$$

where Im=the imaginary part

Rl=the real part

This calculated phase can be used as a measure of how close the observed admittance approaches the theoretical admittance. The observed admittance should have low phase values at all wavelengths.

Another useful measure of the similarity of bathymetry and gravity in the spatial frequency domain is the coherence. This is the measure of the portion of the observed gravity that can be attributed to the bathymetry at the same spatial frequency. It is calculated from:-

$$\gamma^2=(N(CC^*/E1E2)-1)/(N-1) \quad (E6.12)$$

where C=the cross spectrum of bathymetry and gravity

E1=the power of the gravity

E2=the power of the bathymetry

N=the number of values used in the averaging.

The coherence should vary from 1, for a good correlation of gravity and bathymetry, to zero, for a very poor correlation of gravity and bathymetry.

An estimate of the error associated with observed values of admittance can be calculated from the coherence by assuming that the observed values have zero mean and are normally distributed with a variance given by, Munk & Cartwright (1966):-

$$\sigma'^2(\underline{k}_n)=Z^2(\underline{k}_n)(\gamma^{-2}-1)/2(N-1) \qquad (E6.13)$$

The available bathymetry, free air gravity and marine geoid data, over the Cape Verde Rise has been outlined in Chapter 2, section 2.5. The analysis can be split into two quite separate parts with the free air gravity anomalies and bathymetry along ship's tracks forming a 1-dimensional analysis and the gridded bathymetry and marine geoid data forming a 2-dimensional analysis.

6.4 1-DIMENSIONAL DATA FOR THE CAPE VERDE RISE

Watts (1978), analysed ship's track profiles crossing the Hawaiian-Emperor seamount chain and assumed that since this feature is essentially a long continuous ridge it could be treated as a 1-dimensional problem. The same type of analysis will be applied to the data for the Cape Verde Islands, but the particular profiles must be chosen carefully. The Cape Verde Islands, as can be seen in Figure 6.4, are disposed along two prominent ridges. The strike length of these ridges is much smaller than the strike length of the Hawaiian Emperor ridge of seamounts and this problem is dealt with in Chapter 7, in the interpretation section. Of more immediate importance is the lack of suitable profiles that run directly perpendicular to the island ridges and continue some distance on either side. To overcome this problem it was decided to select profiles that approached the island ridges as near to perpendicular as possible and then project them onto a truly perpendicular track. Also, these tracks typically altered course dramatically at, or near, the top of the island ridges and then ran parallel to them. To overcome this the projected tracks were reflected about their midpoints. This forced the condition of perfect symmetry. Of the 10 tracks used in the analysis of Chapter 7 only 1 was non-reflected.

BATHYMETRIC & TRACK CHART OF THE CAPE VERDE ARCHIPELAGO

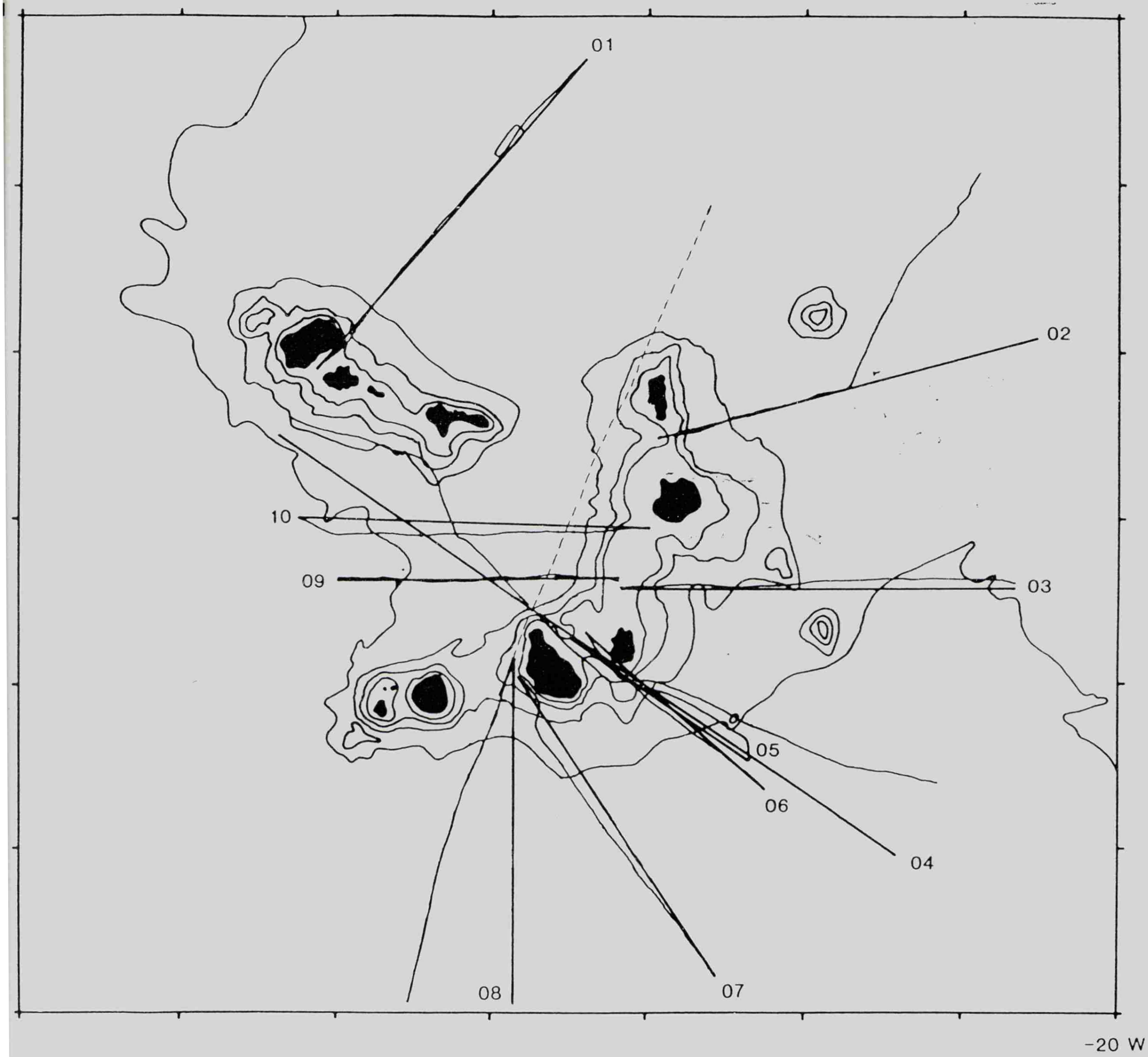

Figure 6.4 Bathymetric map of the Cape Verde Rise with the available gravity and bathymetry track density shown. The islands appear to be disposed along two prominent ridges of limited lateral extent. The ridges are from San Antao to San Nicolau and from Sal to Brava.

The purpose of the study is to try and estimate the effective elastic thickness of the Cape Verde Rise using the response of the oceanic lithosphere to the load of the Cape Verde Islands and a simple thin plate model, outlined in Chapter 5. The profiles, therefore had to be selected that ran towards the islands but remained over the Cape Verde Rise. This limited the size of the data series to ~500 km. In fact, to satisfy one of the constraints of the FFT algorithm the maximum size of the data series was taken as 512 km. For the reflected profiles this meant that only 256 km of data were necessary. The Nyquist frequency was taken as 0.125 km^{-1}, which represents a wavelength of 8 km. This value was chosen as a compromise between the close data point spacing of the Leicester data set, ~0.3 km, and the rather larger data point spacing on some of the World Data Centre tracks, up to 2.8 km.

Linear interpolation was used to get from the irregular spacing of the ship's track data to a regular spacing of 4 km, necessary for the FFT algorithm.

The data processing sequence for the gravity and bathymetry profiles along ship's tracks was as follows:-

1) The irregularly spaced data along the ship's tracks was projected onto a profile perpendicular to the island ridge.

2) The data were then interpolated onto a constant sample interval of 4 km.

3) A mean and trend was removed from this interpolated data set.

4) The ends of the data set were tapered by half-cosine bell ends to remove any discontinuities between the first and last data values.

5) The data series was padded out with zeros, where necessary, to make the total length 512 km.

Averages were obtained of the power of the bathymetry and the cross-spectrum of bathymetry and gravity by averaging all the wavelengths over the 10 profiles analysed. In addition averaging was also performed using a logarithmically increasing bandwidth to preferentially smooth the short wavelength end of the spectrum. Averaging was centred about $k_n=2\pi n\Delta k$, where $\Delta k=1/512\ km^{-1}$ and $n=1,2,3,5,9,15,25,60$. Details and results of the 1-dimensional analysis, of gravity and bathymetry, are given in Chapter 7.

6.5 2-DIMENSIONAL DATA FOR CAPE VERDE RISE

As was pointed out in the previous section, the Cape Verde Islands can only be approximated as a 1-dimensional, or line load, and then only by careful selection of ship's tracks. The horseshoe shape of the archipelago really requires a full 2-dimensional analysis to examine the relationship between bathymetry and gravity. Unfortunately insufficient gravity data coverage is available to form a gridded data set over the Cape Verde Rise. The bathymetry is, however, sufficiently well known and, as was shown in Chapter 2, a 5'x5' gridded data set is available.

Instead of using gravity, measurements of the marine geoid could be substituted, and the relationship between the geoid and the bathymetry examined. Geoid height data are available over the Cape Verde Rise on a 7.5'x7.5' grid from combined SEASAT and GEOS3 satellite passes.

Since the aim of the study is to estimate the effective elastic thickness of the Cape Verde Rise, a suitable array size must be chosen that sits over the rise and includes the bathymetry of the islands and inter-island ridges. The grid size is decided by the geoid data and is 7.5'x7.5'. The bathymetry was, therefore, linearly interpolated onto the same grid size. For the analysis several simplifying assumptions were made. Firstly, it was approximated that a minute of latitude be equal to 1.844 km. Secondly, it was assumed that a minute of latitude was equal to a minute of longitude. At the latitude of the Cape Verde Islands this introduces an error of only 4%. Thus the Nyquist frequency is, for the 2-dimensional study, 0.0362 km^{-1}; or, in other terms, the smallest resolvable wavelength will be 27.66 km.

The data are to be processed using the FFT algorithm so the constraint that the data series be of length equal to an integer power of 2 still applies. An array of size 64x64 was chosen, which gives a 1^{st} harmonic at a frequency of 0.001129 km^{-1}, or a maximum wavelength of 885.12 km. A simple square array was used so that azimuthal averaging could be applied.

The data processing sequence for the 2-dimensional data is similar to that outlined above for the 1-dimensional data with a few alterations.

1) No resolving onto perpendicular profiles is necessary.

2) No interpolation is required since the data is already on a regular grid.

3) A least squares best fitting plane was removed which, it is assumed, corresponds to any mean and trend in the data.

4) The edges of the data array were cosine tapered.

5) The 64x64 element array needed no padding with zeros and the data was read into a 1-dimensional array, of length 4096, by columns before passing into the FFT algorithm.

Before computation of the response function, or admittance, it is necessary to perform some averaging to smooth the spectral estimates of the bathymetric power and cross-spectrum of bathymetry and geoid. For gridded data, azimuthal averaging is used with a logarithmically increasing bandwidth. In this case, where $|k_n| = \sqrt{(k_{xn}^2 + k_{yn}^2)}$, estimates were obtained at n=1,2,3,5,9,15,25. Results and details of this 2-dimensional analysis of geoid and bathymetry data are given in Chapter 8.

6.6 FORWARD MODELLING

Using the simple thin plate model outlined in Chapter 5 it is possible to combine the observed bathymetry and the calculated model admittance to produce the calculated, or predicted, gravity or geoid due to the observed bathymetry. This has been called, here, forward modelling to distiguish it from the inversion of the observed relationship between gravity, or the marine geoid, and bathymetry.

The predicted, or calculated, gravity and geoid values are on similar grids to the bathymetry used in the computation. To compare the observed variation of gravity and geoid it is necessary to interpolate the calculated values to the same latitude and longitude as the observed values. This is done using a Nag library subroutine based on quadratic interpolation.

By using gridded 2-dimensional bathymetry data, it is possible to account for the complicated shape of the Cape Verde Archipelago. After forward modelling the resulting 2-dimensional geoid, or gravity, can be compared with the observed geoid, or gravity, along sub-satellite tracks, or ship's tracks. This analysis can be performed for many models at varying effective elastic thicknesses until a best fit is obtained between the 2-dimensional calculated values and the 1-dimensional observed values.

The results of forward modelling of the gravity over the Cape Verde Rise are described towards the end of Chapter 7. Similarly results for the marine geoid are described in the latter half of Chapter 8.

CHAPTER 7 (GRAVITY/BATHYMETRY RELATIONSHIP)

The following chapter has been written as a paper that has been accepted for publication in the Journal of Geophysical Research. The work involved in this paper was initiated and carried out by R. Young and the contribution from Dr. I.A. Hill was limited to corrections of grammar and style suitable for publication. The chapter is presented here in a slightly modified form than that which was finally accepted by the editors of the journal.

AN ESTIMATE OF THE EFFECTIVE ELASTIC THICKNESS OF THE CAPE VERDE RISE

Robert Young and Ian A. Hill

Department of Geology, Leicester University, Leicester, U.K.

7.1 ABSTRACT

Application of the response function technique to the load of the Cape Verde Archipelago on the Cape Verde Rise suggests the effective elastic thickness of the rise is only ≈15 ±3 km. This is thinner than would be expected, for 130 Ma crust, from previous observations worldwide which suggest a value of ≈30 ±10 km. This thinning is considered to be substantial evidence that the lithosphere of the Cape Verde Rise has undergone thermal rejuvenation. Comparison of this study with previous work at Hawaii suggests that reduction of the effective elastic thickness over swells with large depth anomalies is related to plate motion over the mantle heat source.

7.2 INTRODUCTION

The Cape Verde Islands lie to the south-west of the crest of the Cape Verde Rise 500 km west of the Senegalese coast of Africa. The rise forms a broad (≈800 km) bathymetric swell on oceanic crust dated by marine magnetic anomalies at between 105 & 155 Ma, (Hayes & Rabinowitz 1975). Comparison of observed depths to oceanic basement with calculated depths using an empirical age:depth relationship, (Parsons & Sclater 1977), suggest the rise is 2 km higher than normal crust of that age. Crough (1978) compared the depth anomalies of 10 oceanic swells with the above age:depth relationship and concluded that hot-spot swells rise to a depth equivalent to 25 Ma crust regardless of the age of the oceanic lithosphere at that position. One of the possible mechanisms for formation of the swell is reheating and thinning of the lithosphere. If this is really the case then the thermal properties of the lithosphere would also be expected to change. A technique for examining the thermal state of the crust is to calculate the effective elastic thickness of the lithosphere and compare it with that predicted by a cooling plate model. The effective elastic thickness can be obtained by examining the response of the lithosphere to an imposed load and by assuming that the crust behaves like an elastic plate overlying a fluid. In this study the variation of gravity and bathymetry on the Cape Verde Rise is used to calculate the response of the lithosphere to the load of the Cape Verde Islands.

7.3 THEORY

The isostatic response method simply involves the derivation of a filter which, convolved with the bathymetry in the space domain, produces a series which resembles the observed gravity, again in the space domain. This is similar to previous studies by such workers as McKenzie & Bowin (1976), Watts (1978), Cochran (1979) and McNutt (1979). This process can be represented in the 1-dimensional space domain by:

$$g_c(x)=f(x)*b(x) \qquad (E7.1)$$

where $b(x)$= series representing bathymetry

$f(x)$= series representing the filter

$g_c(x)$= the calculated free-air gravity series

$*$= the convolution operator

By use of the convolution theorem, (Kanasewich 1975), and the assumption of a linear relationship between gravity and bathymetry the above convolution in the space domain is equivalent to multiplication in the spatial frequency domain.

$$G_c(k_n)=Z(k_n)B(k_n) \qquad \text{(E7.2)}$$

where $B(k_n)$, $Z(k_n)$ and $G_c(k_n)$ are the discrete Fourier tranforms of $b(x)$, $f(x)$ and $g_c(x)$ respectively.

$Z(k_n)$ is known as the admittance. The wavenumber is given by the reciprocal of the wavelength ($k_n=2\pi/\lambda$). The above can be rearranged to give:

$$Z(k_n)=G_c(k_n)/B(k_n) \qquad \text{(E7.3)}$$

It should be possible to obtain $Z(k_n)$ by replacing G_c by G_o, the discrete Fourier transform of the observed gravity series $g_o(x)$. However, $Z(k_n)$ obtained in this way is influenced by noise in the gravity field particularly at short wavelengths. A better estimate of $Z(k_n)$ acccording to Munk & Cartwright (1966) and McKenzie & Bowen (1976) can be obtained from:

$$Z(k_n)=\{G_o(k_n)B(k_n)^*\}/\{B(k_n)B(k_n)^*\} \qquad \text{(E7.4)}$$

where *=complex conjugate

Now the admittance is given by the cross-power of the gravity and bathymetry divided by the power of the bathymetry. The filter $(f(x))$ can be obtained in the space domain by inverse Fourier transforming the admittance estimate. The estimate still contains noise and some form of spectral smoothing must be applied. McKenzie & Bowen (1976) subdivided their profiles into a number of smaller segments and obtained admittance estimates for each segment. They then averaged over all the segments. A problem with this approach to smoothing is that each segment will contain a slightly different geological signal and these cannot be isolated after averaging. Another approach was adopted by Dorman & Lewis (1970), McNutt (1979) and Banks & Swain (1978) who applied smoothing in the spatial frequency domain by averaging about particular wavelengths. The method used in this study is that of Watts (1978) where many profiles, all crossing the particular feature of geological interest, are examined and many independent estimates of the cross-spectrum and bathymetric power obtained. The results are averaged and the smoothed spectra used to calculate the admittance.

The filter $(f(x))$ calculated from the real admittance is symmetric (i.e there should be no phase shift between the Fourier transform of the bathymetry and the Fourier transform of the corresponding gravity anomaly). The effect of this in the spatial frequency domain will be that the admittance should have zero phase $(Im(Z(k_n))=0)$ since the Fourier transform of $f(x)$ will consist principally of a series of even (cosine) functions. This can be examined by calculating the phase of $Z(k_n)$ from:

$$\phi(k_n)=\tan^{-1}(Im(Z(k_n))/Rl(Z(k_n))) \qquad (E7.5)$$

Another useful parameter is the coherence; this is the measure of the portion of the observed gravity that can be attributed to the bathymetry. The coherence is given by:

$$\gamma^2=(N(CC^*/E1E2)-1)/(N-1) \qquad (E7.6)$$

where C=the cross-spectrum of bathymetry and gravity

E1= power of the gravity

E2=power of the bathymetry

N=number of profiles

Spectral estimates are obtained at equal arithmetic intervals of Δk, where $\Delta k=1/512\ km^{-1}$, and $k_n=2\pi n\Delta k$, where n=1,2,3...etc. This means that there is a strong concentration of data points at the short wavelength end of the spectrum. Dorman & Lewis (1972) point out that logarithmically spaced estimates each contribute approximately the same amount of information. By averaging over logarithmically increasing bandwidths it is possible to reduce the errors in the admittance at the short wavelengths. The increase in error at these wavelengths is due to the decrease in signal:noise of the gravity. Estimates of the admittance have therefore been made at n=1,2,3,5,9,15,25,60. This is similar to previous work by Banks & Swain (1978) and McNutt (1979) who used bandwidth averaging on gridded data.

The errors associated with the admittance estimates can be calculated, according to Munk & Cartwright (1966), by assuming that they have zero mean and are normally distributed with variance given by:

$$\sigma'^2(k_n)=Z^2(k_n)(\gamma^{-2}-1)/2(N-1) \quad (F7.7)$$

where N=total number of profiles used in estimate

γ^2=coherence

They also show that the estimate is positively biased for an error function defined as:

$$\sigma=\sigma'/Z(k_n) \quad (F7.8)$$

if it's value exceeds 0.25, i.e. for $\sigma<0.25$ the admittance estimate is a good approximation to the true admittance and for $\sigma>0.25$ the estimate is slightly larger than the true admittance.

The resulting admittance estimate is based entirely on the observed relationship between the gravity and the bathymetry. Also, since the estimate is obtained using relatively short profiles concentrated over a particular feature then the admittance is relevant only to that feature. This can then be compared with different models to examine the isostatic compensation.

7.4 DATA ANALYSIS

The islands comprising the Cape Verde Archipelago are located along three distinct ridges which form a westward opening 'horseshoe' shape (see Figure 7.1). The computational method outlined above assumes that the bathymetry is two-dimensional and this requires that profiles run perpendicular to any geological strike and that the strike has infinite extent. Profiles were therefore chosen that approached the islands in as near a normal direction as possible. All the profiles were also limited to 512 km length to ensure that the admittance calculated was applicable to the Cape Verde Rise and not to

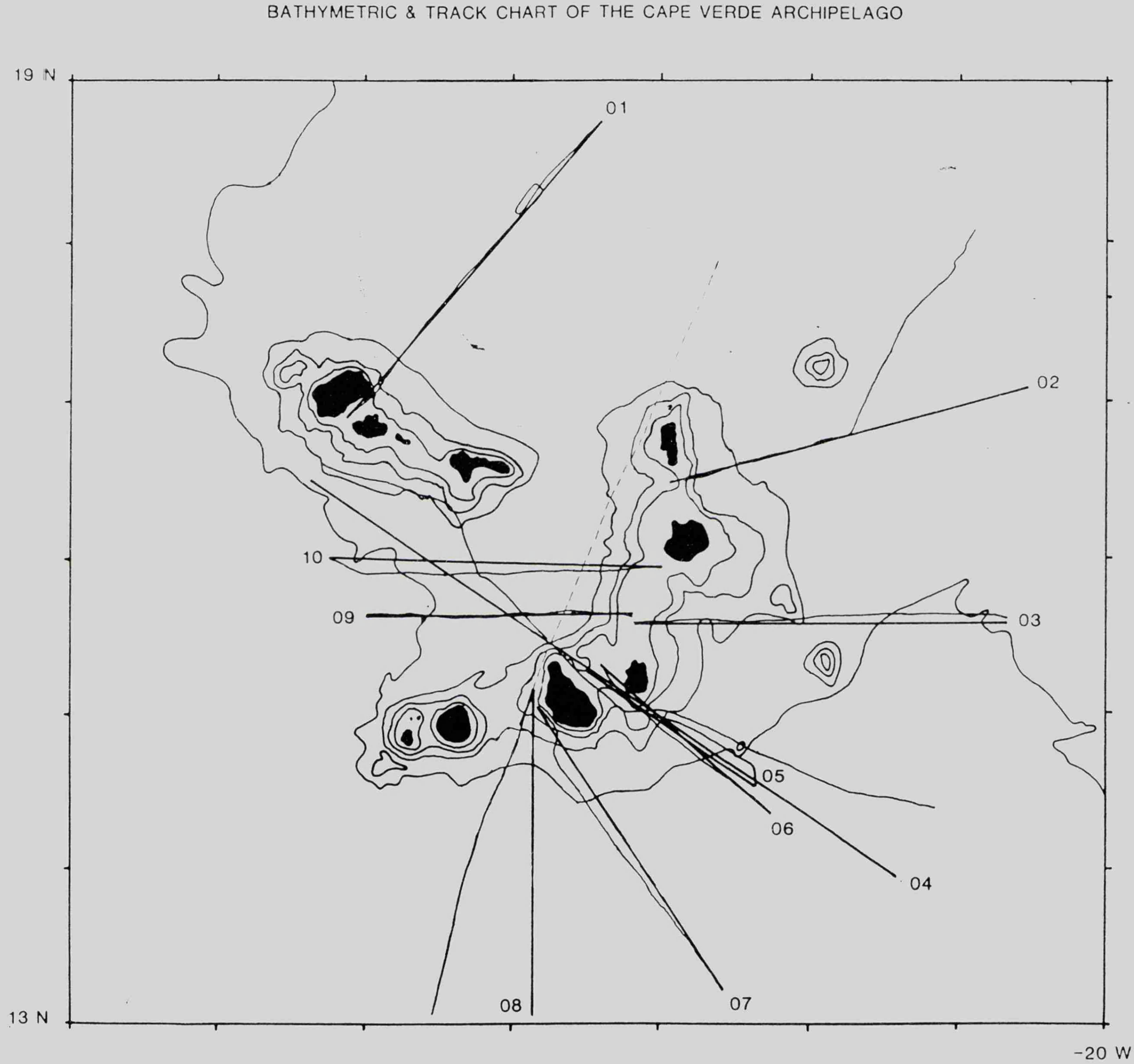

Figure 7.1 Bathymetry map of the Cape Verde Archipelago. Contour interval 1000m. Actual tracks (light lines) and projected tracks (heavy lines) shown with profile numbers.

the surrounding 'normal' oceanic crust. The limited lateral extent of the ridges is considered later (see section 7.5).

A total of 10 profiles with free air gravity anomaly and bathymetric data, up to 512 km long, were projected onto straight line tracks either approaching the Cape Verde Islands or traversing the archipelago (see Figure 7.1). Of the 10, 6 were obtained during the 1982/83 cruise of the RRS Shackleton to investigate the islands and their relation to the Cape Verde Rise. The rest of the profiles were obtained from the World Data Centre. An analysis of 23 track cross-overs gives an rms error, for the measured free air gravity, of 2.6 mgals. A large proportion of this error can be attributed to profile 04, cruise V2207, which used sextant/dead reckoning for navigation. The cross-over mis-tie is considered to be positional, rather than due to large differences in gravimeter performance. The other profiles used satellite/dead reckoning navigation. A problem with the majority (9) of the profiles is that they either terminate on reaching the islands or change course upon reaching them and run parallel to the geological strike (i.e. the ridges of Maio-Sal, San Antao-San Nicolau and San Tiago-Brava).

Before applying the discrete Fourier transform to the data series each had to be linearly interpolated on to an even spacing (4 km spacing used), a mean and trend removed, cosine tapered at the ends of the data to avoid discontinuities and finally zeros added to make the series length an integer power of 2. The latter was necessary so that the fast Fourier transform algorithm, (Cooley & Tukey 1966), could be used. To avoid loss of data when cosine tapering, the profiles that terminated on bathymetric highs were reflected about their mid-points and the new symmetric series processed as before. By reflecting the profiles, however, this forced the condition of perfect symmetry and thus the admittance was real for these profiles. Previous studies have shown that in general the admittance has low phase angles at long (>20 km) wavelengths so the reflected profiles are still considered valid approximations.

Table 7.1 Details of tracks used in this analysis. Profile marked (*) was not reflected about it's midpoint and therefore had double the weighting of the other profiles during averaging.

PROFILE NUMBER	PROFILE LENGTH	CRUISE NAME	MEAN DEPTH	MEAN F.A.A.	R.M.S. MISFIT
01	254km	SHA1B/83	3.22km	37.2mgal	0.5mgal
02	254	SHA1A/83	2.96	22.4	0.7
03	254	DISC/143	3.33	12.0	1.4
04	*510	V2207	4.22	-22.6	1.0
05	154	SHA1A/83	2.42	62.2	1.2
06	176	SHA1A/83	3.22	37.2	1.3
07	246	V2713	3.92	-2.3	0.9
08	230	73003121	4.20	-3.0	1.8
09	255	SHA1A/83	3.48	-2.6	1.5
10	235	SHA1B/83	3.49	-1.5	1.4

The mean free air anomaly is plotted against mean depth for each profile and is shown in Figure 7.2. The least squares best fit line for this data, using the bathymetry as the independent variable, gives a slope of -39 $\pm$ 6 mgal/km. This relationship can be used to infer that the Cape Verde Islands are compensated on a regional scale since the mean free air anomaly decreases as the depth increases.

The cross-spectrum of gravity and bathymetry was calculated for each of the 10 profiles. The sample interval of 4 km gives a maximum spatial frequency of 0.125 km^{-1} and a minimum, equivalent to the track length, of 0.001953 km^{-1}. The 10 independent estimates of

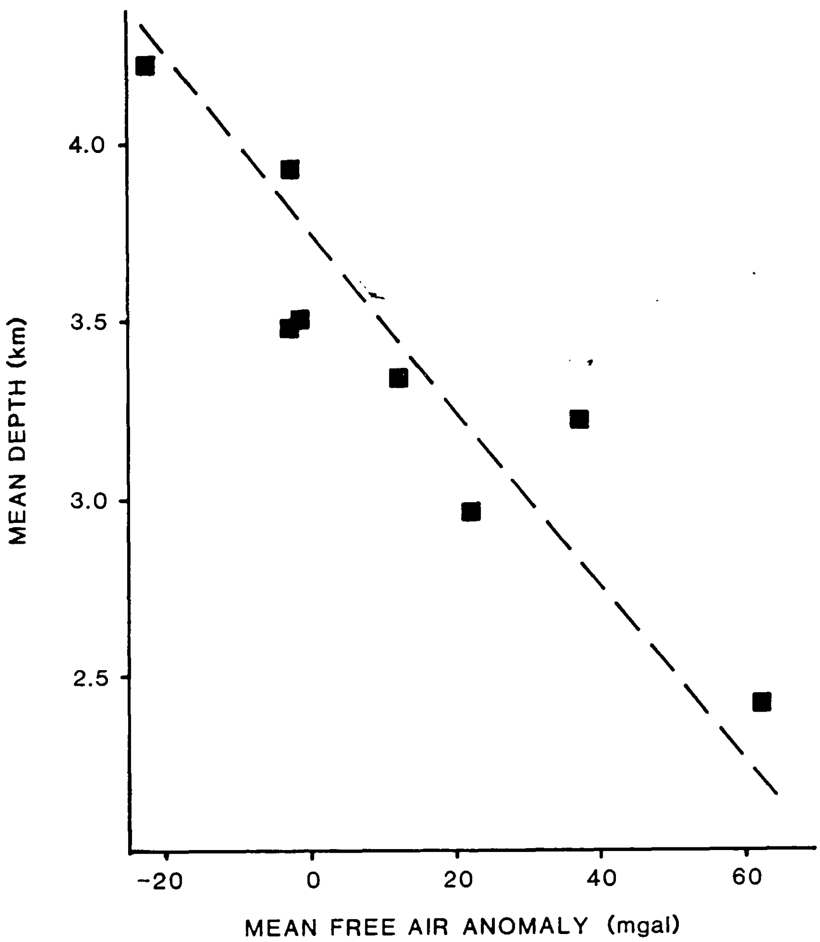

Figure 7.2 Plot of mean Free Air Anomaly against mean Depth for the 10 profiles of Figure 7.1. Dashed line is least squares best fit assuming bathymetry is the independent variable.

cross-spectrum and bathymetric power have been combined, with the reflected profiles given only half the weighting of the non-reflected profile, to produce a smoothed estimate of the admittance. Figure 7.3a shows a plot of Log_{10} of the amplitude of the admittance plotted against inverse wavelength and also shows the coherence, Figure 7.3b. The phase has been calculated for the single non-reflected profile and is also shown in Figure 7.3c. Finally the admittance estimate is used to produce the gravity, $g_c(x)$, from the bathymetry, $b(x)$, and this is compared with the observed gravity in Figure 7.4, for profiles 01 & 04. The calculated gravity is obtained from $G_c(k_n)$ by simple inverse Fourier transformation. The space domain representation of $Z(k_n)$, $z(x)$, is shown in Figure 7.3d.

The coherence plot has values above 0.5 for wavelengths greater than 20 km (λ^{-1}<0.05) suggesting that more than half the power of the gravity can be attributed to the bathymetry at these wavelengths. At shorter wavelengths (λ^{-1}>0.05) the coherence plot is rather noisy which suggests the assumption of a simple one-dimensional relationship between gravity and bathymetry breaks down at these wavelengths. The plot of Log_{10} Admittance amplitude also exhibits a simple form for wavelengths greater than 20 km with increased noise at shorter wavelengths. The phase plot for the single non-reflected profile is rather noisy over all the wavelengths examined and does not exhibit the same smoothness as the other plots. The values obtained do appear to oscillate about zero for wavelengths > 20 km (λ^{-1}<0.05). Final confirmation of how good the admittance estimate is can be obtained from a comparison of the observed and calculated free air gravity anomalies. Table 7.1 shows the rms misfit of the observed gravity and the gravity calculated from the observed admittance and these misfits, all below 2 mgals, are comparable with the cross-over analysis misfit of 2.6 mgals.

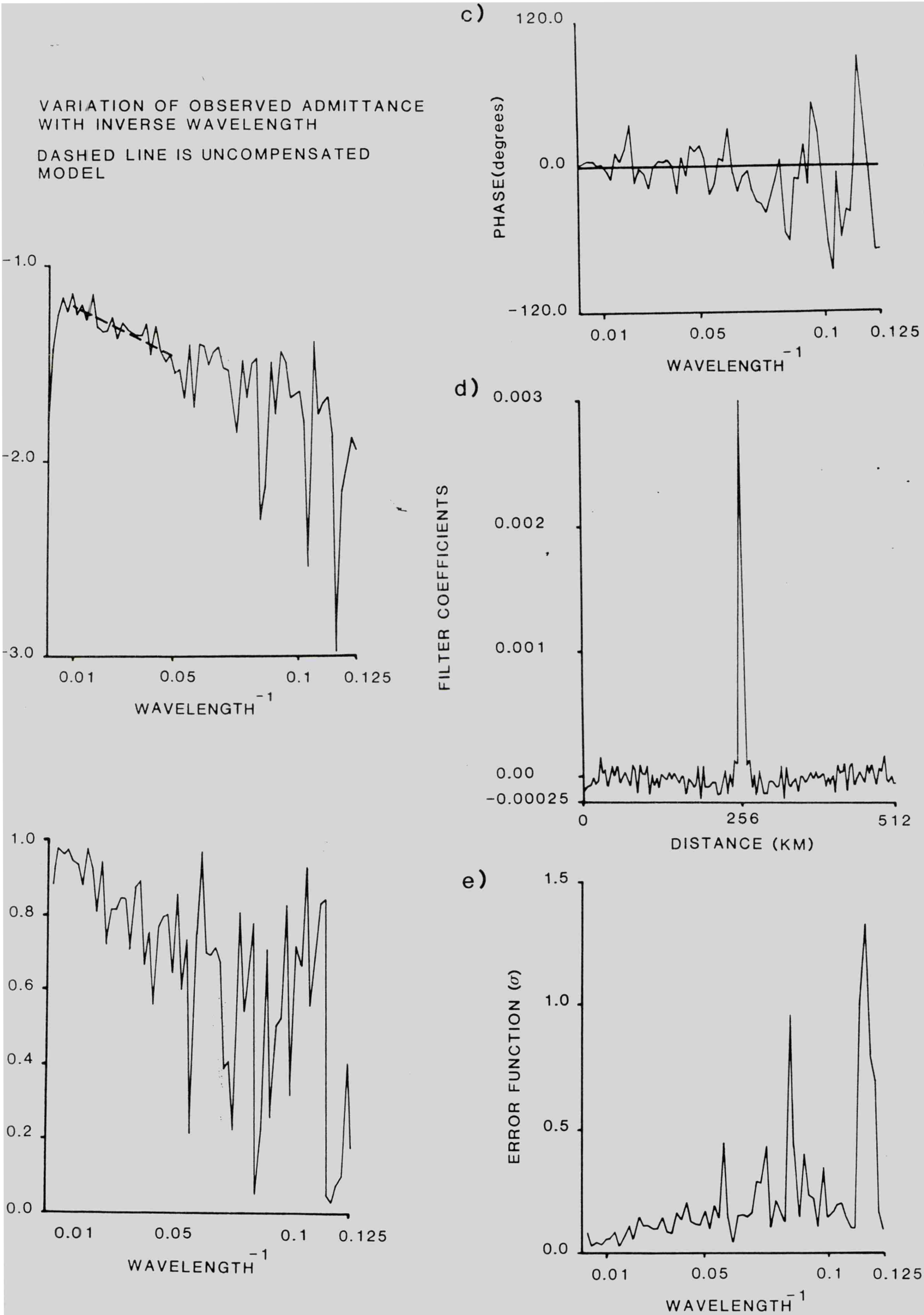

Figure 7.3 a) Plot of Log10 amplitude of the admittance. Dashed line is least squares best fit to the portion $0.01 > \lambda^{-1} > 0.05$ b) Coherence c) Phase d) Space domain representation of admittance e) Error function. All, except d), plotted against λ^{-1}.

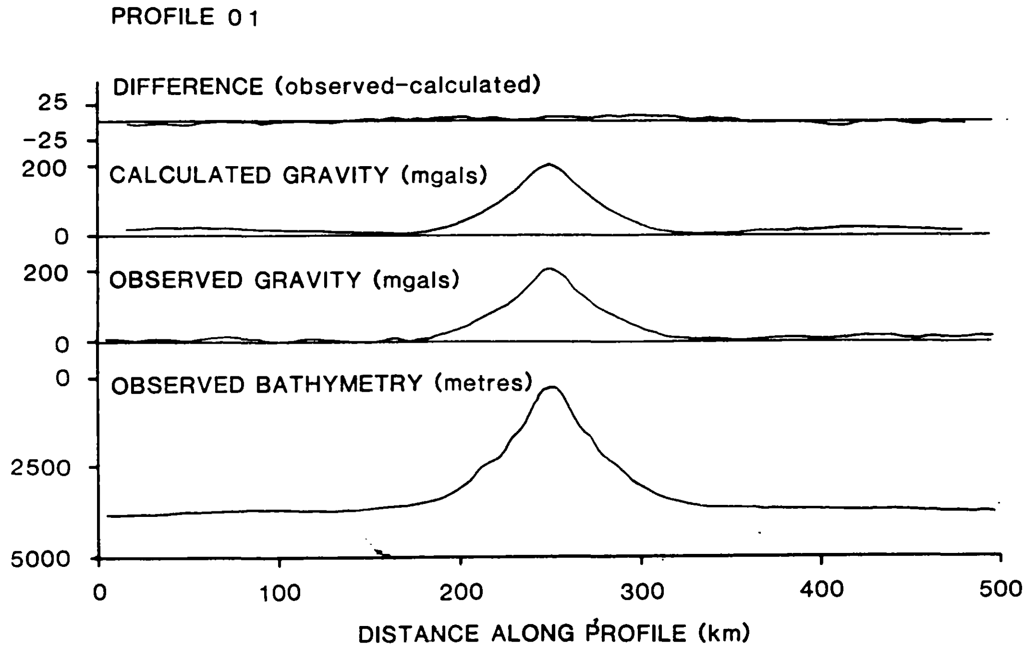

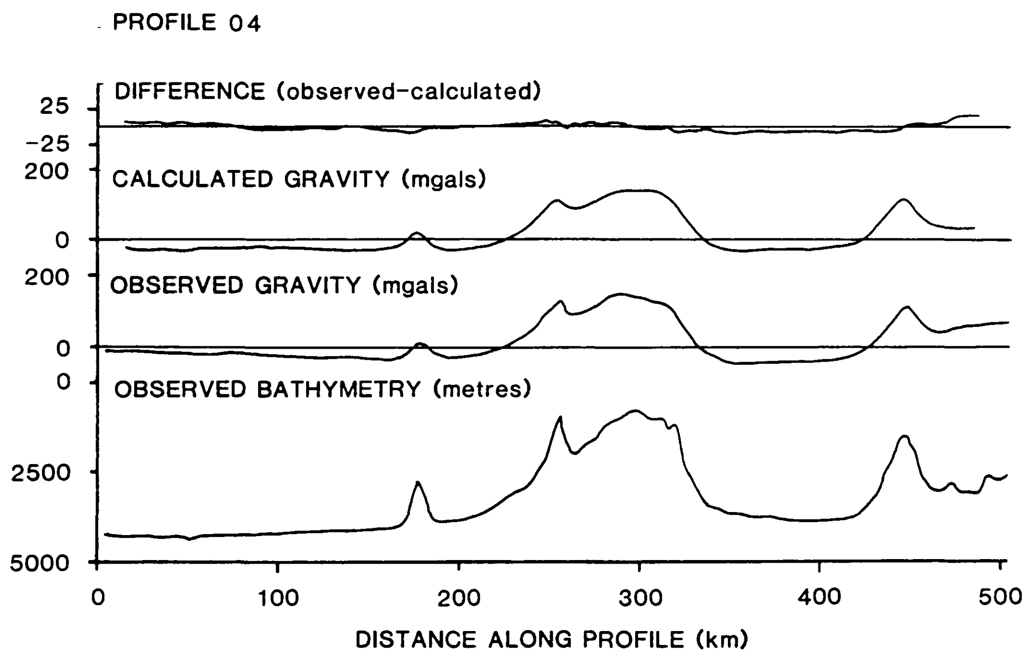

Figure 7.4 Profiles 01 & 04 showing, from bottom to top, bathymetry in metres, observed gravity in mgals, gravity calculated using the observed admittance in mgals and difference between observed and calculated in mgals.

7.5 INTERPRETATION

The initial model used to explain the observed admittance assumes that the gravity is due to the bathymetry alone and there is no compensation mechanism. McKenzie & Bowin (1976), Watts (1978) and McNutt (1979) show that this relationship can be calculated, assuming 1-dimensionality, from:

$$Z(k_n)=2\pi G(\rho_t-\rho_w)\exp(-k_n d_t) \quad \text{(E7.9)}$$

all quantities are defined in Table 7.2.

This is the 1-dimensional equivalent of E5.12 in Chapter 5.

This represents the linear term of a series expansion, Parker (1972), that describes the gravity effect of a two dimensional sinusoidal body of density ρ_t at a depth below sea level of d_t. Watts (1978) has shown that this first term is a good approximation to the line integral method of calculating gravity anomalies. The above equation represents a straight line on a plot of $\mathrm{Log}_{10}\, Z(k_n)$ against inverse wavelength. The slope of the line is given by $-2\pi d_t$ and the intercept by $\log_{10}[2\pi G(\rho_t-\rho_w)]$. Fitting a least squares straight line to the admittance plot in Figure 7.3a gives values of 2790 $\pm$125 kg/m^3 and 3.17 $\pm$0.38 km for ρ_t and d_t respectively. The best fit line is shown dashed in Figure 7.3a. The density estimated for the topography agrees well with Watts (1978) (2800 kg/m^3) and Lambeck (1981) (2700 kg/m^3), and with an independent estimate of the density of the Maio-Sal ridge (Brown (1984)), but is slighty higher than the values of 2600 kg/m^3 and 2400 kg/m^3 obtained by McKenzie & Bowin (1976) and McNutt (1979) respectively. A possible explanation is that the latter studies were applied over large areas whereas this study and those of Watts (1978) and Lambeck (1981) are concentrated over specific geological features. The depth estimate is lower than the true mean depth of 3.50 km, for the 10 profiles analysed here, but the true value lies within the upper error bound of the estimate. The similarity of ρ_t and d_t to independently obtained values is an indication that the admittance between 20 & 100 km can be related to the real geological situation.

The uncompensated topography model does not fit the observed admittance values at very long wavelengths. It would be expected that the admittance would continue to increase as the wavelength increases, whereas the admittance is observed to decrease as the wavelength increases. This suggests that the bathymetry is compensated on a regional scale. This can be seen on the profiles as the gravity and bathymetry appear related at short wavelengths but the free air gravity anomaly disappears at longer wavelengths, which implies that the ocean floor topography is compensated at longer wavelengths.

A more complex compensation model can be calculated by assuming that the oceanic lithosphere is an elastic plate overlying a fluid. Many workers have used this type of model (eg. Watts et al 1980, Lambeck 1981) where the deflection due to the load must be calculated as part of the gravity effect. The basic elements of the model are outlined in Figure 7.5. McKenzie & Bowin (1976) give an expression for the admittance of this model, using finite-plate theory, but the equation used here subdivides the oceanic crust into layers 2 and 3 and uses the thin plate approximation modified from Banks et al (1977).

The one-dimensional admittance of an elastic plate can be calculated using a simplified version of E5.29 from Chapter 5, thus:

$$Z(k_n)=2\pi G(\rho_t-\rho_w)\{\exp(-k_nd_t)-(1+k^4D/(\rho_m-\rho_t)g)^{-1}[((\rho_3-\rho_t)/(\rho_m-\rho_t))$$
$$\exp(-k_nz_1)+((\rho_m-\rho_3)/(\rho_m-\rho_t))\exp(-k_nz_2)]\} \qquad (E7.10)$$

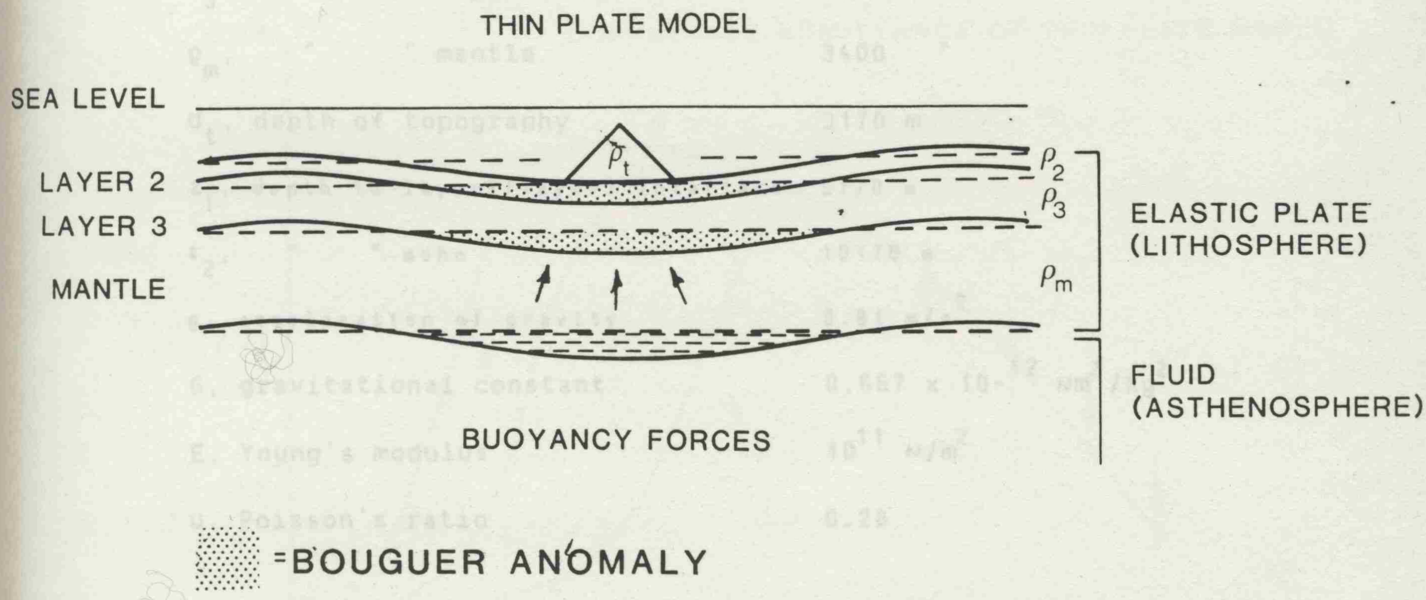

Figure 7.5 Diagram of thin plate model used to calculate theoretical admittance. Gravity anomaly has three parts, topographic attraction, low density topography displacing higher density layer 3 and layer 3 displacing higher density mantle.

where all quantities are as defined in Table 7.2 and the density of layer 2 is assumed to be the same as the density of the topography.

Table 7.2 Summary of parameters used in model calculations.

Parameter	Value
ρ_w, density of seawater	1020 kg/m^3
ρ_t, " " topography (=layer 2)	2790 "
ρ_3, " " layer 3	2900 "
ρ_m, " " mantle	3400 "
d_t, depth of topography	3170 m
z_1, depth to layer2/layer3 interface	5170 m
z_2, " " moho	10170 m
g, accelaration of gravity	9.81 m/s^2
G, gravitational constant	0.667×10^{-12} Nm^2/kg^2
E, Young's modulus	10^{11} N/m^2
υ, Poisson's ratio	0.28

The effective elastic thickness, T_e, is related to the rigidity of the elastic plate by:

$$D=ET_e^3/12(1-\upsilon^2) \quad \text{(equation E5.20 in Chapter 5)} \qquad \text{(E7.11)}$$

The depth to the layer 2/layer 3 interface is taken from Houtz & Ewing (1976) for oceanic crust approximately 100 Ma. The depth to the moho is estimated from a wide-aperture seismic reflection study in the Western North Atlantic by Mutter & Detrick (1984). Poisson's ratio is taken from Purdy (1983) and the value for Young's modulus is the same as used by previous workers such as McNutt (1979) and Watts (1978). Poisson's ratio and Young's modulus are necessary in equation E7.11 to relate the rigidity (D) to the effective elastic

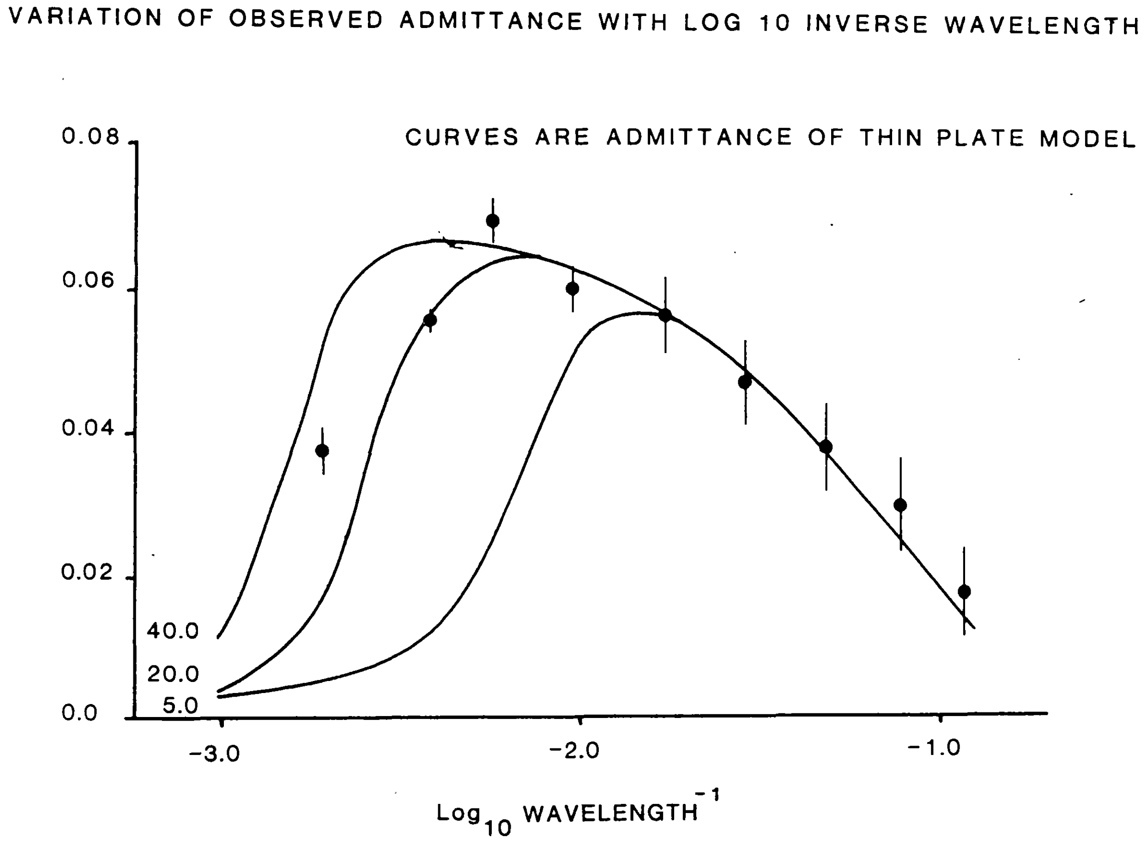

Figure 7.6 Observed admittance estimates plotted against $Log_{10}\lambda^{-1}$ with bars indicating + 1 standard error. Curves represent admittance of plate model for various values of effective elastic thickness.

thickness T_e. The values used here are similar to values used in other flexural studies since the estimate of the effective elastic thickness calculated here will be compared with T_e from these other studies which used a similar rheological model for the lithosphere.

Figure 7.6 shows various curves of admittance plotted against $\mathrm{Log}_{10}\ \lambda^{-1}$ for different values of T_e. Also shown are the observed admittance estimates with their associated errors (bars=$\pm$1 standard error).

The observed data fit both the uncompensated and thin plate models well at the short wavelength end of the spectrum. This is to be expected since the models approximate uncompensated topography at these wavelengths and the values of ρ_t and d_t used in the models were obtained directly from the data. The poor fit at λ^{-1}>0.05 is most likely due to lateral density variations over the ridges, but may also be due in part to a positive bias since the error function (σ), plotted against λ^{-1} in Figure 7.3e, becomes large (>0.25) for this part of the data.

The best fit to the elastic plate model appears to be at $T_e \approx 20$ km and this is consistent with previous estimates for oceanic lithosphere away from spreading centres such as Watts & Cochran (1974), Watts et al (1975) and Watts (1978). As has already been pointed out, the limitation of this study is that in using profiles it is assumed that the bathymetry is two dimensional and that the data are collected perpendicular to the geological strike. This is only a first approximation to the real case. McKenzie & Bowin (1976) examined this problem and proposed modifying k_n as the solution. When applying the response function technique to gridded data $|\underline{k}_n| = \sqrt{(k_{xn}^2 + k_{yn}^2)}$, where k_{xn} and k_{yn} are the wavenumbers in the x and y directions respectively; x and y being orthogonal coordinates. Examination of a bathymetric map of the Cape Verde Archipelago,

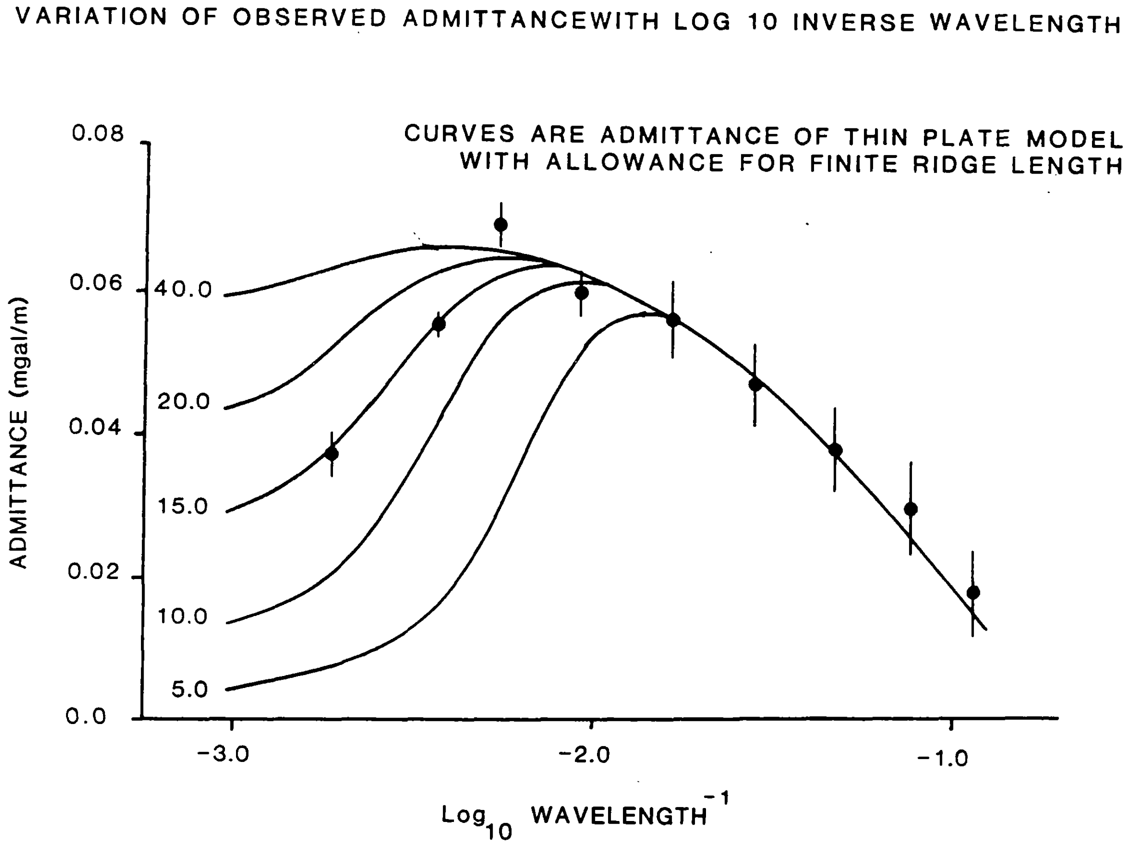

Figure 7.7 As for Figure 7.6 but curves represent admittance of plate model after inclusion of an estimate of the finite extent of the ridges.

(Brown 1984), gives a wavelength $\lambda_y \approx 350$ km ($k_y \approx 0.018$). The modified plate model curves are shown in Figure 7.7 along with the observed admittance estimates. The calculated admittance is still plotted as a function of k_x and not a function of $\underline{k}_n$. The effect of including an estimate of k_y is to alter the long wavelength response. This result is confirmed by Ribe (1982) who showed in a more rigorous study that the admittance of a feature of finite strike length on an elastic plate is greater than that of its two-dimensional counterpart.

The observed admittance estimates now give a least squares best fit to the curve for $T_e = 15 \pm 3$ km as shown in Figure 7.7. The error estimate for the best fit is obtained from the width of the least squares minimum.

The model proposed here, of a thin plate with an effective elastic thickness of 15 km, can be tested using 2-dimensional analysis rather than the 1-dimensional analysis performed on the profiles. Bathymetric data is available, via the World Data Centre, as 5'x5' gridded data points over the area of the Cape Verde Rise. A subset of this data was selected between latitudes 13.25°N to 18.50°N and longitudes -26.00°W to -20.75°W. This represents a 64 x 64 array of 5'x5' bathymetry values. A 2-dimensional Fourier analysis can be applied to this data set, after removal of a mean and trend and cosine tapering at the edges to remove discontinuities. An isometric plot of this gridded data set is shown in Figure 8.8.

The constraint of an integer power of 2, for the number of data points, has already been dealt with by selecting a 64 x 64 subset of the data.The inverse wavelengths, obtained by inverting this data, range from $k_{x2}=k_{y2}=0.001695$ km^{-1} to $k_{x65}=k_{y65}=0.054230$ km^{-1} (the Nyquist frequency), assuming that 1 minute of latitude is equivalent to 1.844 km at the latitude of the Cape Verde Islands. The data after application of the 2-dimensional Fourier transform consist of a 64 x

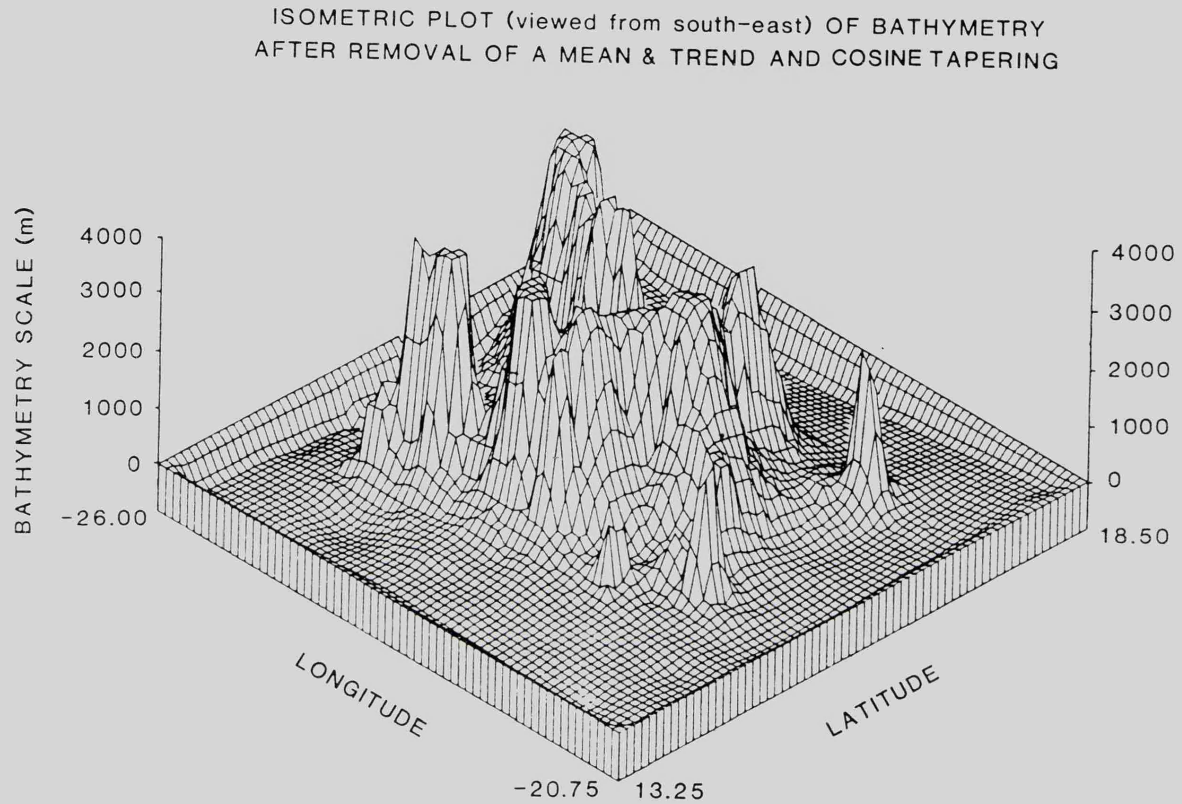

Figure 7.8 Isometric plot, viewed from south-east corner, of gridded bathymetry data. A mean and trend have been removed and the data at the edges of the grid have been cosine tapered to minimise discontinuities.

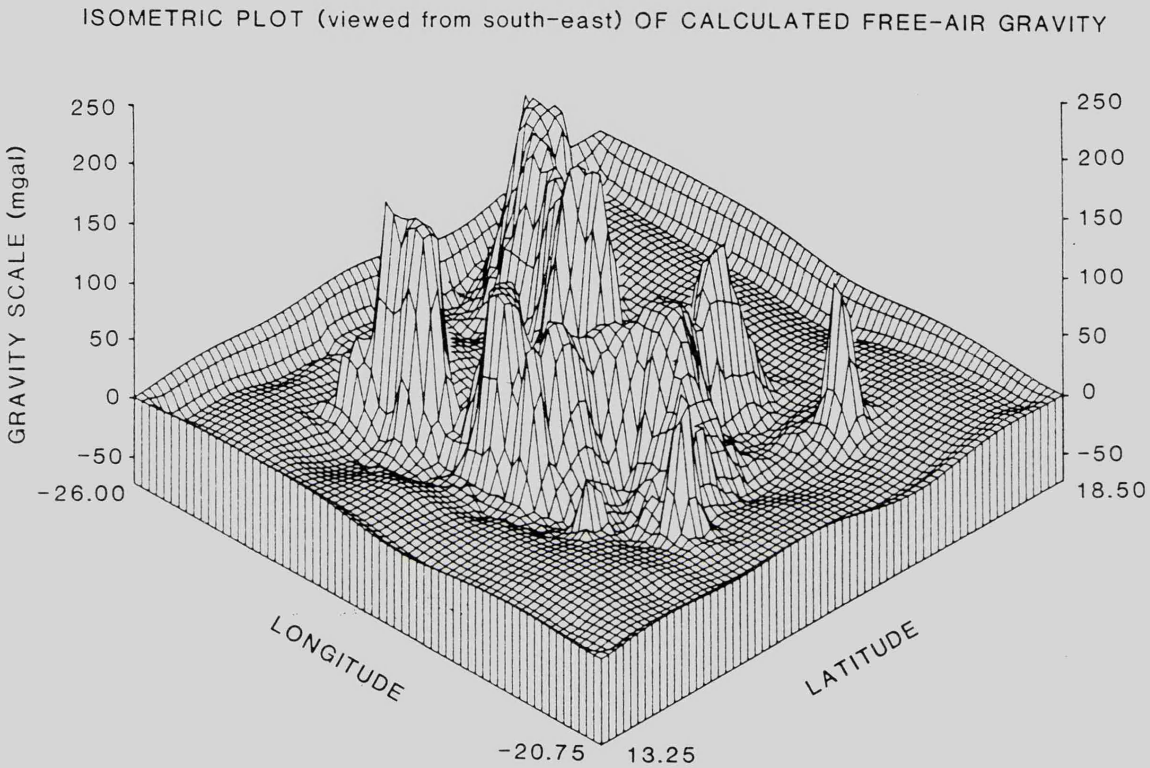

Figure 7.9 Isometric plot of the calculated gravity using a thin plate model with an EET of 15 km and assuming that admittance is independent of azimuth.

64 grid of both real (cosine) and imaginary (sine) coefficients. The 2-dimensional Fourier transform of the calculated free air gravity anomaly can be obtained in exactly the same manner as for the 1-dimensional case. The 2-dimensional Fourier transform of the bathymetry is multiplied, in the spatial frequency domain, by a 2-dimensional response function. The response, or admittance, in 2-dimensions can be calculated from (E7.10) by using:

$$|\underline{k}_n| = \sqrt{(k_{xn}^{2} + k_{yn}^{2})} \qquad \text{(E7.11)}$$

The calculated free air gravity anomaly can be obtained by taking the inverse 2-dimensional Fourier transform of the product of bathymetry and admittance. The result is a 64x64 grid of 5'x5' calculated gravity values. The calculated gravity obtained by using a model with an EET of 15 km is shown in Figure 7.9.

Calculated gravity can be compared with observed free air gravity anomalies along profiles used in the original analysis. Data values are obtained by linear interpolation of the calculated gravity on the grid at each observed gravity position. Figure 7.10 shows just such a comparison for profiles 02, 08 and 09. Profile 09, has been extended into the archipelago to show how well the calculated gravity predicts the observed gravity outwith the area covered by the original, inverted data set. The constant offset between the observed and calculated gravity anomalies can be accounted for since the relationship between mean gravity and mean bathymetry (as shown in Figure 7.2) is not included in the calculated gravity anomaly.

Comparison of observed and calculated profiles indicates that the model, suggested by this study, for the response of the Cape Verde Rise to the load of the Cape Verde Islands, predicts the free air gravity anomaly well. The comparison is particularly good at

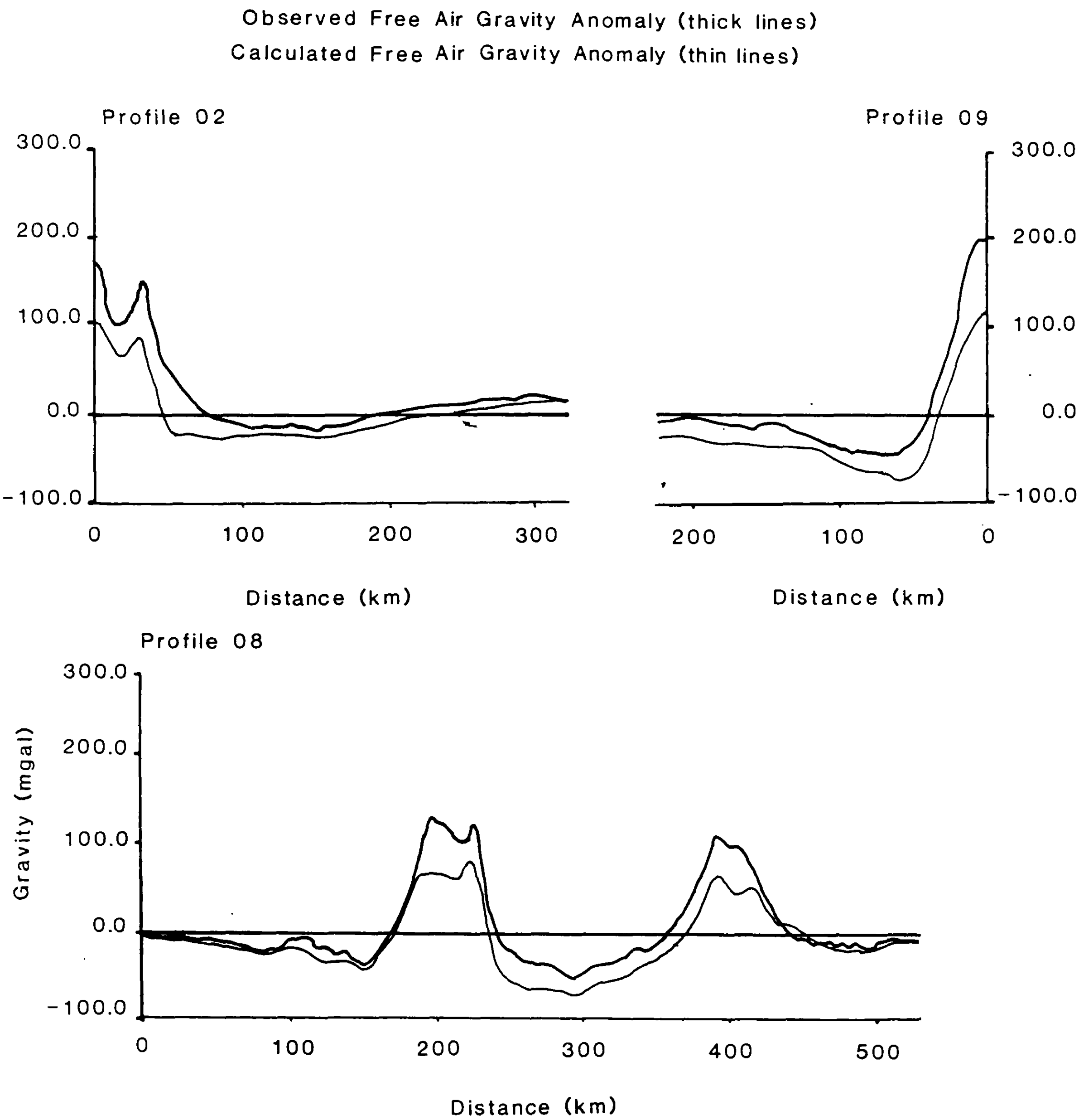

Figure 7.10 Profiles of calculated (thin lines) and observed (thick lines) free air gravity from tracks 02, 08 and 09. The calculated gravity is obtained from the gridded values, shown in Figure 7.9, by linear interpolation. The constant offset between calculated and observed is due to not including the relationship between mean bathymetry and mean gravity (as shown in Figure 7.2) in the calculated gravity.

wavelengths greater than 50 km. At shorter wavelengths (<20 km) the observed gravity is generally greater than the calculated gravity. This can be accounted for, however, by variations in density of material comprising the islands, or inter island ridges. This possibility has already been discussed in the 1-dimensional analysis.

7.6 DISCUSSION

The Cape Verde Archipelago is situated to the south-west of the crest of a large bathymetric swell; the Cape Verde Rise. This swell rises to approximately 3.5 km depth and is thus 2 km shallower (after accounting for sediment loading) than the empirical age:depth relationship (Parsons & Sclater 1977) would suggest. The effective elastic thickness (EET) of the swell has been calculated by this study to be $\approx 15 \pm 3$ km. This value compares favourably with an independent estimate made by McNutt (1984), who studied the uplift of the other islands in the archipelago due to the loading effect of Fogo, and calculated a value for the EET of between 7-12 km. Mitchell et al (1983) showed, from a geological and geochronological study, that there is little evidence for extensive volcanism, on Maio, before 20 Ma. Assuming island building, and hence elastic deformation, was started at around this time, then the EET calculated by this study must represent the value for the lithosphere within the last 20 Ma. This value of EET must also correspond to the maximum reheating since any elastic deformation would be 'frozen in' during cooling. Figure 7.11a is modified from Watts et al (1980) and shows the EET plotted against age of the crust at the time of loading for several recent studies. The curves show the variation of depth to the 300^{o} and 600^{o} isotherms assuming a cooling plate model (Parsons and Sclater 1977). The calculated EET is thinner than the value predicted by the relationship in Figure 7.11a which suggests that the EET should be ≈ 30

a) GLOBAL COMPILATION OF E.E.T. vs AGE AT TIME OF LOADING

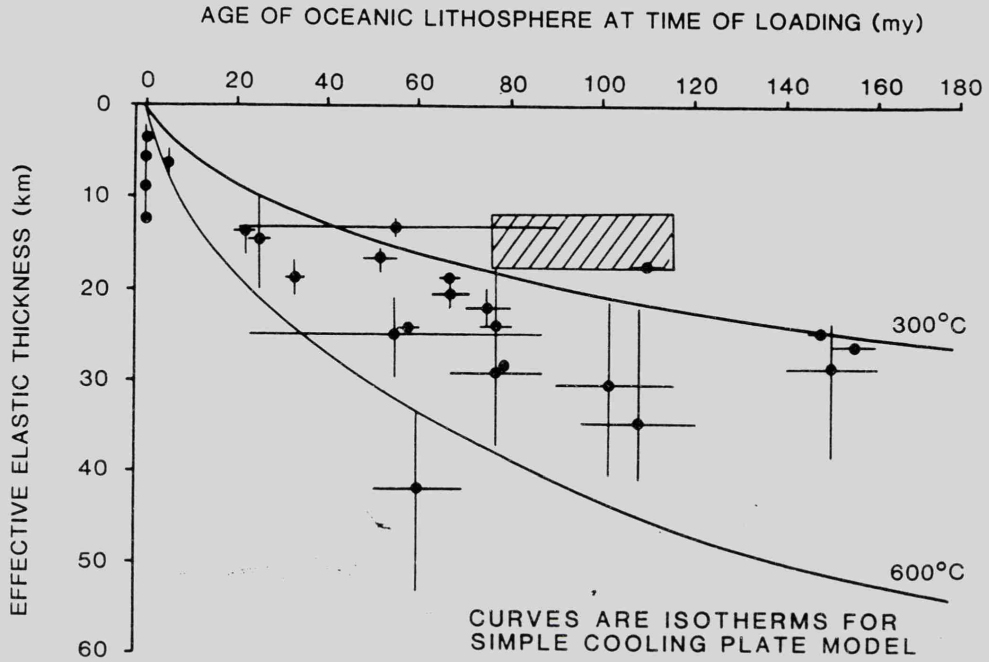

b) GLOBAL COMPILATION OF OCEANIC SWELL DEPTH vs AGE OF CRUST

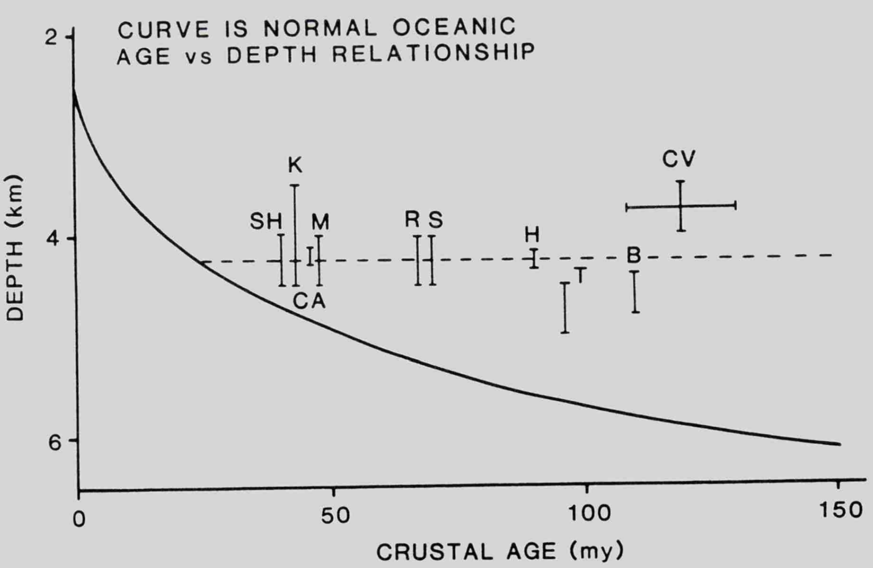

Figure 7.11 a) Effective elastic thickness against age of plate at time of loading. Curves show variation of depth to the 300° and 600° isotherms with age for a cooling plate model (<u>Parsons & Scalter (1977)</u>). Data from this study (shaded area) and <u>Watts et al (1980)</u> (filled circles). b) Depth anomaly against age of crust. Data from this study (CV=Cape Verde Rise) and <u>Crough (1978)</u> (H=Hawaii, CA=Cook-Austral, S=Society, M=Marquesas, R=Reunion, K=Kerguelen, B=Bermuda, SH=St Helena and T=Trindade).

± 10 km for the age of the crust around the Cape Verde Archipelago.

The EET thus appears to be related to the thermal state of the crust. The crust of the Cape Verde Rise has been thermally rejuvenated and now has a thermal age equivalent to ≈25 Ma crust. Crough (1978) plotted the depth of 10 hotspots against crustal age and suggested that all oceanic swells rise to a height equivalent to 25 Ma crust; a similar plot is shown in Figure 7.11b. This suggests that all oceanic rises should have EET's corresponding to similarily young crust. That is, the thermal effect that causes the depth anomaly should also cause a thermal rejuvenation and reduction of the EET. However, the effective elastic thickness for Hawaii, as calculated by Watts (1978), is not significantly lower (Te≈30 km) than normal lithosphere of the same age. Menard & McNutt (1982) considered this situation whereby lithospheric reheating could produce a large depth anomaly and a negligible change in the EET. They suggest that by confining the initial reheating to greater than 45 km depth the depth anomaly can be accounted for by thermal expansion in the lower half of the lithosphere but the upper half of the plate is not immediately affected due to the slow conductive time constant of the upper lithosphere. If this model is realistic then the difference between the elastic thicknesses of the Cape Verde Rise and the Hawaiian swell can be related to the velocity of the plate over the heat source.

McNutt (1984) suggests two possible models for thermal rejuvenation. The first is a model of the type proposed here for the Cape Verde Rise, whereby the entire lithospheric column is reheated, causing both a depth anomaly and a reduction in the EET. The second model has reheating confined to the lower lithosphere only and this causes a depth anomaly but no observable reduction in the EET.

Hawaii is less vulnerable to mid-plate volcanism than the Cape Verde Rise principally because the Pacific plate is moving at 10 cm/yr and this results in incomplete thermal rejuvenation. Heating may be insufficient to change the effective elastic thickness from the value associated with normal crust of that age. The Cape Verde Rise, however, has been very slow moving over its 'hotspot' for at least 30 Ma, Minster & Jordan (1978), and the effective elastic thickness is therefore much less than the expected value for 130 Ma crust.

7.7 CONCLUSIONS

1)The observed admittance estimates, obtained from profiles crossing the Cape Verde Archipelago, can be compared with a thin plate model, assuming the ridges which form the archipelago have a finite strike length (≈350 km), to give an effective elastic thickness ≈15 ±3 km. This model, although initially calculated using 1-dimensional analysis, predicts the observed gravity well when using 2-dimensional analysis.

2)The value of the EET from this study is thinner than expected for 130 Ma crust (T_e≈30±10 km) and this is considered to be due to thermal rejuvenation. The lithosphere now has an effective thermal age of ≈25 Ma which is observed as both a depth anomaly and a reduced EET.

3)This study indicates that substantial re-heating of the lithosphere underlying the Cape Verde Rise has occurred. A similar conclusion was reached by Crough (1978) from a study of the bathymetric anomaly and McNutt (1984) from a study of Fogo. However, neither this study, nor others, can preclude a component of uplift due to the existence of minor density variations, in the underlying upper mantle, of non-thermal origin.

4)The difference between this study (T_e≈15 km) and Hawaii (T_e≈30 km) is related to plate velocity over the heat source. The effect of the low velocity of the African plate at the Cape Verde Rise overcomes the thermal resistance of the thick lithosphere and the result of this is dramatic reduction of the EFT.

CHAPTER 8 (GEOID/BATHYMETRY RELATIONSHIP)

8.1 INTRODUCTION

The relationship between the marine geoid and bathymetry can be used to examine the state of compensation of bathymetric features in the world's oceans. The accuracy and coverage of geoid height measurements has increased dramatically since the release of data obtained by the SEASAT satellite mission. This mission was sponsored by the National Aeronautics and Space Administration (NASA) of the U.S.A. to measure the height of the sea surface, by radar altimetry, to an accuracy of 10 cm. Combination of the SEASAT coverage with an earlier satellite mission, GEOS3, provides suitable data density to interpolate the geoid heights onto a regular (7.5'x7.5') grid, Rapp (in press). The gridded geoid data set provides an opportunity to examine the relationship between geoid height and bathymetry in 2-dimensions over the Cape Verde Rise. The results of this analysis can be compared with the results of a 1-dimensional gravity/bathymetry analysis carried out over the same area and reported in Chapter 7. Lame & Borne (1982) give an excellent overview of the SEASAT mission and details of the acquisition techniques can be found in section 2.8 of Chapter 2.

The marine geoid is an equipotential surface whose 1st vertical derivative is gravity. Geoid measurements have been used in the past, by such workers as Watts et al (1985), Cazenave et al (1980) and Watts (1979), to examine the state of compensation of bathymetric features. An advantage of geoid measurements over gravity measurements is that the geoid is more sensitive to deep seated density variations and should, therefore, better detect the anomaly due to regional compensation. Another advantage of geoid measurements is that the satellite coverage is more uniform than the shipborne gravimeter coverage. Dixon et al (1983) made use of the satellite coverage, linear transfer function techniques and the accuracy of the SFASAT radar altimeter to predict bathymetry in the Pacific ocean. To check how well satellite altimetry measurements correlated with gravity and bathymetry, Vogt et al (1984) undertook ground truth surveys by ship along two sub-satellite tracks in the North Atlantic. Their results suggest that free air gravity anomalies and seafloor topography correlate well with geoid anomalies in the space domain between wavelengths of ~400 km to ~50 km. The main difference between gravity anomalies and geoid anomalies is that the gravity field has a higher frequency cutoff and is thus better at resolving shallow, short wavelength features. The $1/r$ dependence of geoid anomalies (versus $1/r^2$ dependence for gravity) averages the density anomalies out to longer wavelengths and produces a smoother signal. This last point was also noted by Chapman (1979) who studied techniques for investigating geoid anomalies.

Previous workers who have used geoid anomaly and bathymetry relationships, such as Watts (1979) and Dixon et al (1983), have restricted their analysis to individual tracks so that their results are strictly 1-dimensional. Cazenave et al (1980) used gridded GEOS3 data to investigate the response of the lithosphere to seamount loading but did not apply linear transfer function techniques to their 2-dimensional data. Rather they computed the geoid anomalies over the bathymetric features using numerical integration and compared this with the observed geoid. A previous study by Crough (1982) is more directly applicable to the Cape Verde Rise in that it compares observed geoid heights and bathymetry over an area of the Atlantic that includes the rise. The result was the suggestion that the Cape Verde Rise was supported by an isostatic root at an average depth of 40 km.

This does not help, however, to determine the state of compensation of the load of the Cape Verde Islands on the lithosphere of the Cape Verde Rise. The purpose of the present study is to use the available 2-dimensional data, of geoid heights and bathymetry, to calculate the effective elastic thickness (EET) of the lithosphere of the Cape Verde Rise. This will utilise the same thin plate model of flexure outlined in Chapter 5, section 5.3, and used previously in Chapter 7.

8.2 2-DIMENSIONAL DATA

The 2-dimensional data used in this study is a combined data set of GEOS3 and SEASAT values interpolated onto a 7.5'x7.5' grid. This data was made available by R. Rapp from Ohio State University in the U.S.A., Rapp (pers. comm.). Figure 8.1 shows the sub-satellite track density for the area of the Cape Verde Rise. Breaks in the track coverage can be due to excessive noise, pre-programmed switching off of the sensor or "blunder point" editing of the data set. Figure 8.2 shows an isometric view of the whole geoid height data set available for analysis at Leicester University. This data was provided by R. Rapp from Ohio State University and details of the interpolation are given in Rapp (in press). The horizontal and vertical scales are as shown and the arrows indicate the 64x64 element subset of the data used in the later analysis. The data shown in Figure 8.2 are dominated by a very large (>50 m) long wavelength (>1000 km) component that increases from West to East and from South to North. Despite this, however, it is still possible to pick out the geoid anomaly due to the Cape Verde Islands and Rise.

Watts et al (1985) and Dixon et al (1983) suggest that long wavelength (>1000 km) geoid anomalies are due to density variations deep in the mantle. It is necessary to remove this long wavelength component from the geoid signal before an adequate comparison between

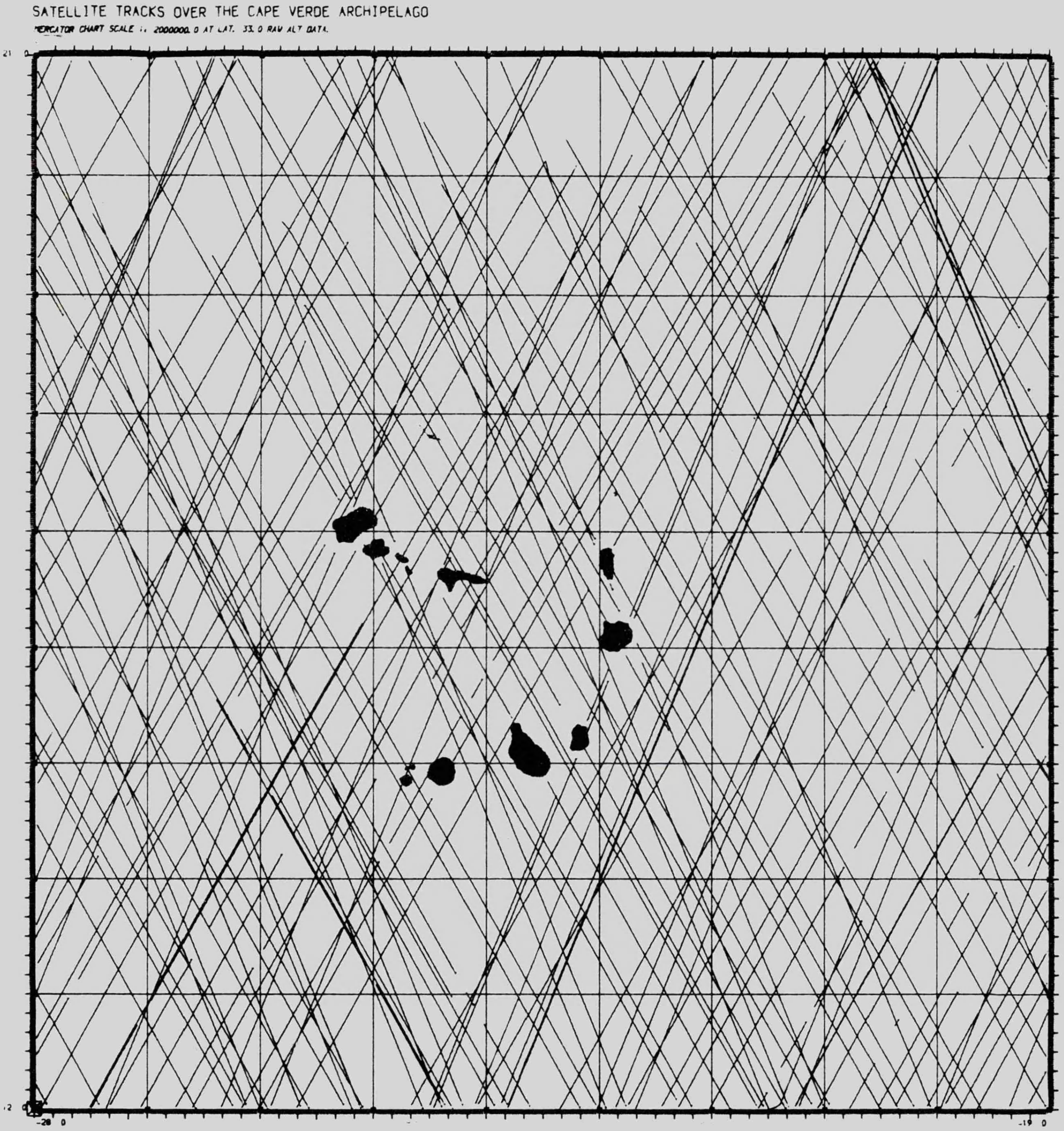

Figure 8.1 Satellite tracks for the combined GEOS3 and SEASAT data sets. The track density shown here is considered suitable for interpolation onto a 7.5'x7.5' grid. The gridded geoid height data is shown in Figure 8.2.

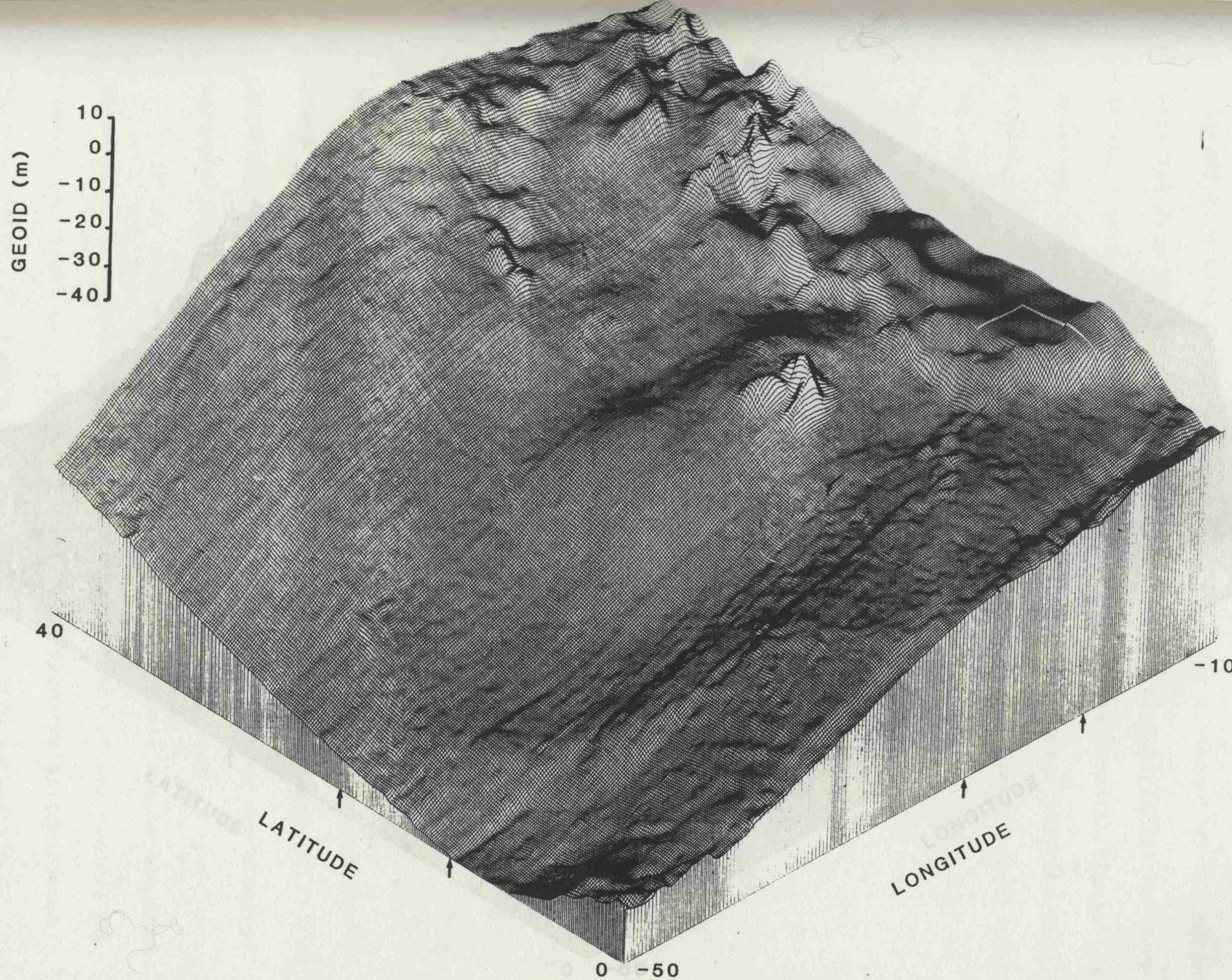

Figure 8.2 Isometric plot, viewed from the south-west, of the total gridded (7.5'x7.5') geoid data available for analysis at Leicester University. The area covered is from 0^{0} N to 40^{0} N and -10^{0} W to -50^{0} W. A large regional geoid signal is present in this diagram that slopes up from west to east and from south to north. The arrows indicate the 64x64 subset of the data used in the later analysis.

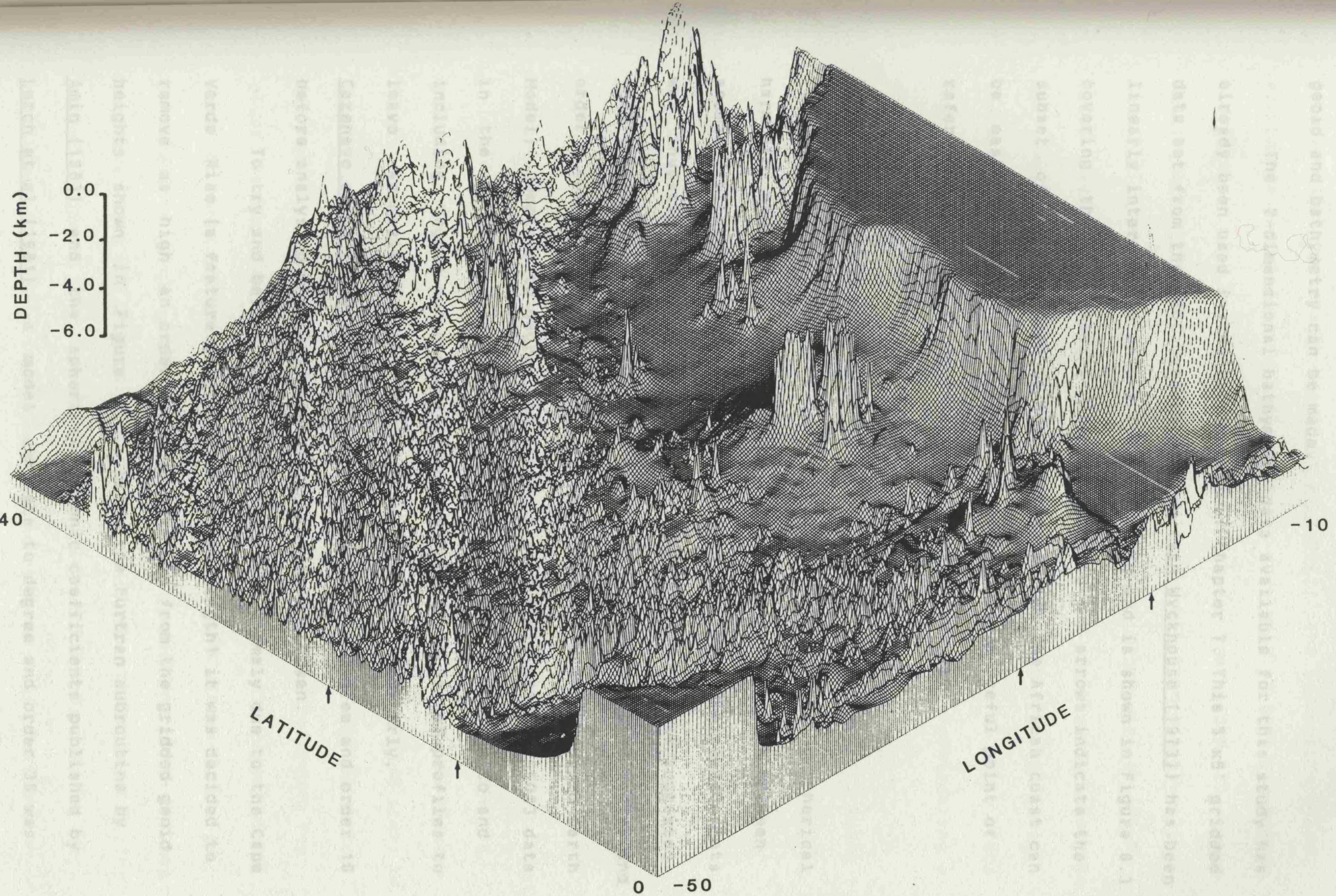

Figure 8.3 Isometric plot, viewed from the south-west, of the bathymetry data covering the same area as Figure 8.2 and also gridded at 7.5'x7.5'. The continental areas of South America and Africa have constant values of -10 m and act as useful points of reference. The arrows indicate the 64x64 subset of the data used in the later analysis

geoid and bathymetry can be made.

The 2-dimensional bathymetry data available for this study has already been used in the latter part of Chapter 7. This 5'x5' gridded data set from the NGDC Synbaps program (van Wyckhouse (1973)) has been linearly interpolated onto a 7.5'x7.5' grid and is shown in Figure 8.3 covering the same area as Figure 8.2. Again the arrows indicate the subset of the data used in the later analysis. The African coast can be easily seen in this isometric plot and is a useful point of reference. The Cape Verde Islands also stand out well.

8.3 REGIONAL GEOID ANOMALY

The geoid of the earth as a whole can be described by spherical harmonic expansion terms, Jacobs (1974). The relationship between anomaly block size and the number of spherical harmonic coefficients was investigated by, amongst others, Rapp (1977). It was suggested that the mean anomaly block size described by expansions to degree and order N was $180^{o}/N$. Watts et al (1985) removed a GEM10 (Goddard Earth Model) complete to degree and order 10 from their gridded GEOS3 data in the Pacific. Vogt et al (1984) subtracted the GEM9 up to and including degree and order 14 from their observed SEASAT profiles to leave anomalies ~1000 km in wavelength. Similarly, Cazenave et al (1980) removed a model complete to degree and order 10 before analysing the geoid anomaly in the Indian ocean.

To try and better distinguish the geoid anomaly due to the Cape Verde Rise (a feature only ~800 km in wavelength) it was decided to remove as high an order model as possible from the gridded geoid heights shown in Figure 8.2. Using the Fortran subroutine by Amin (1983) and the spherical harmonic coefficients published by Lerch et al (1981), a model complete to degree and order 36 was calculated. This model is called a PGS-S3 (Preliminary Gravity

Solution-SEASAT) model (Lerch et al (1982)) and is considered to provide an improvement in orbit accuracy over that of GEM9 and GEM10B. A solution has been calculated to degree and order 180 (Lerch et al (1981)) which would, using the relationship given in Rapp (1977), define geoid anomalies down to a block size of $1^{o}x1^{o}$. These coefficients, termed the GEM10C model, are not readily available but would provide a simple method of removing the regional geoid anomaly due to the Cape Verde Rise. It is necessary to do a two stage regional removal using the PGS-S3[36,36] model and then subtracting a calculated local regional geoid anomaly.

Figure 8.4 shows a computer contoured map of the PGS-S3 model bounded by latitudes -80^{o} S to $+80^{o}$ N and longitudes -90^{o} W to $+90^{o}$ E. The contour interval is 5m and the dashed box shows the area over which the gridded geoid data is available. Figure 8.5 shows an isometric plot of the PGS-S3 data in this area of interest. It can be seen by comparison with Figure 8.2 that the the regional geoid is well described. Also, the [36,36] solution does not pick out features as small as the Cape Verde Rise.

The PGS-S3[36,36] model has been removed from the observed gridded geoid data and is shown in Figure 8.6. The comparison between Figures 8.6 and 8.3 is quite striking. In Figure 8.6 the land areas of Africa and South America have been given a constant value of 5m for the geoid. These continental areas provide a useful reference for other features in the isometric plot. The mid-Atlantic ridge can be seen on both the geoid and bathymetry plots as a sinuous spine of intermediate values going from south to north. The Cape Verde Islands and Rise stand out well on the residual geoid plot of Figure 8.6. The arrows indicate the 64x64 element subset of the data used in the subsequent analysis. Little more will be said about the correlation of bathymetric features and residual geoid anomalies outside the area of

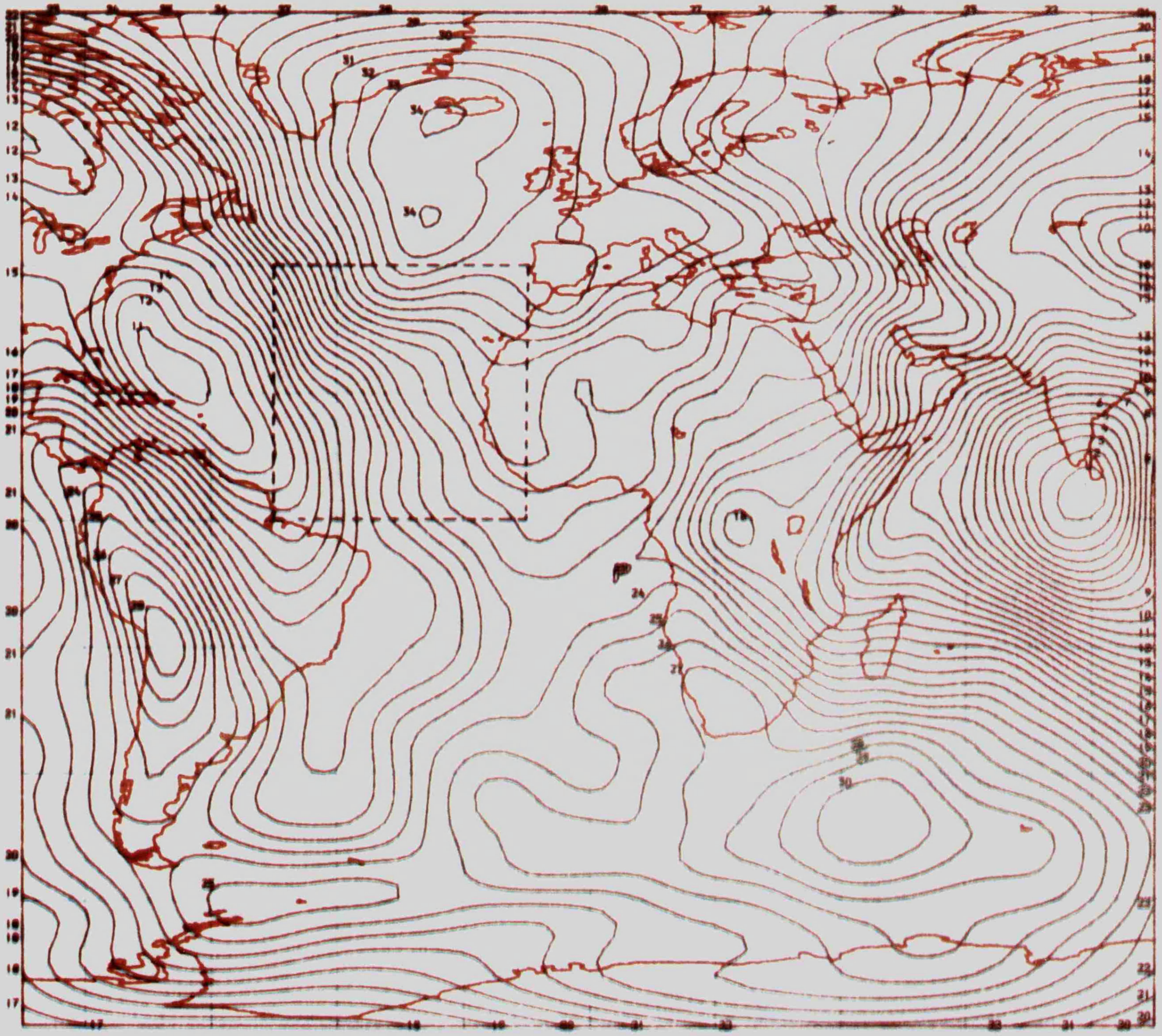

Figure 8.4 Computer contoured map of the PGS-S3[36,36] model. The area is bounded by latitudes $-80^{\circ}N$ to $+80^{\circ}N$ and longitudes $-90^{\circ}W$ to $+90^{\circ}E$. The projection is simple cylindrical with the outline of the continents shown in red. The green grid is at 20° intervals. The contour interval is 5m and the numbered contours start at 1=-100m and continue up to 34=+70m. The dashed box indicates the area for which gridded bathymetry and geoid data are available.

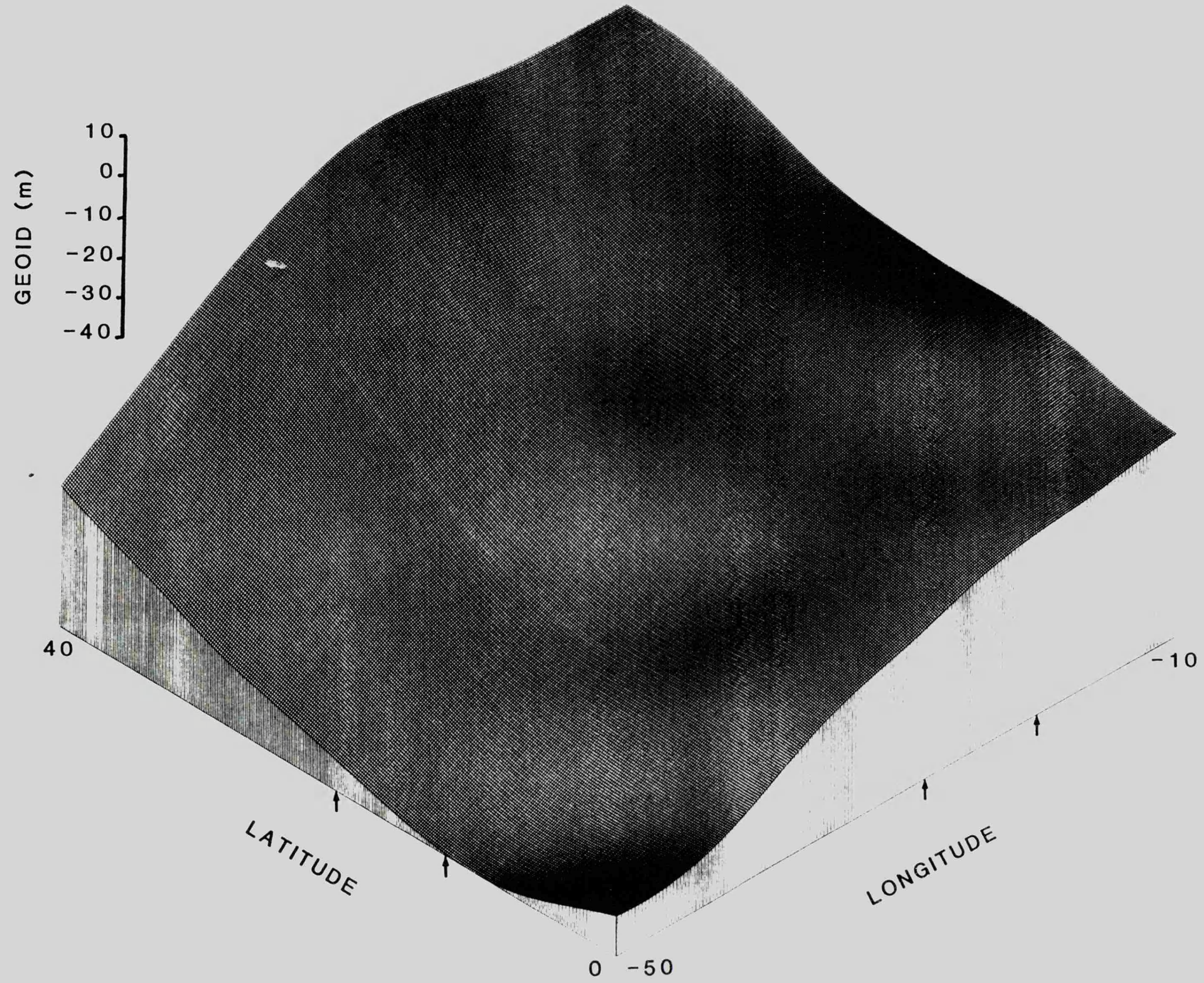

Figure 8.5 Isometric plot, viewed from the south-west, of the PGS-S3[36,36] model geoid variation for the area of the dashed box in Figure 8.4. This plot corresponds well to the long wavelength behaviour of the gridded geoid data shown in Figure 8.2.

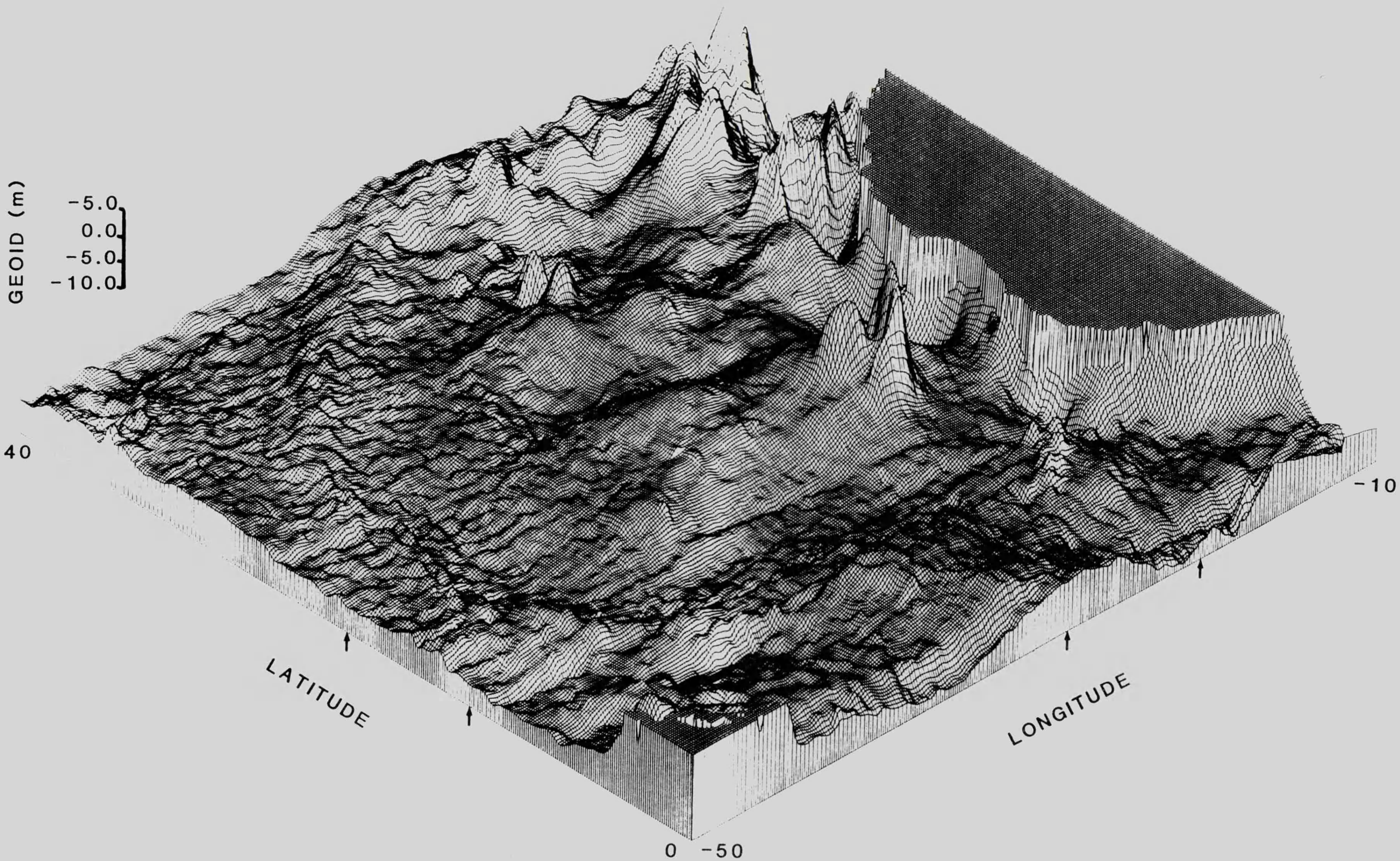

Figure 8.6 Isometric plot, viewed from the south-west, of the gridded geoid height data after removal of the PGS-S3[36,36] model. The continental areas of South America and Africa have been assigned constant values of +5 m and serve as useful points of reference. The arrows indicate the 64x64 subset of the data used in the later analysis. This figure should be compared to the bathymetric plot in Figure 8.3.

the Cape Verde Rise as it is outside the scope of this study.

8.4 RESIDUAL GEOID ANOMALY

Figure 8.7 shows the 64x64 element subset of the data selected for analysis of the relationship between geoid heights and bathymetry over the Cape Verde Rise. This particular size of subset was chosen to satisfy one of the constraints of the Fast Fourier Transform (FFT) algorithm; the size of the input array must be an integer power of 2 in length (see Chapter 6). It can be seen in the isometric plot of Figure 8.7 that the rise forms a major part of the signal. This is only to be expected since the removal of a [36,36] spherical harmonic expansion regional will still leave wavelengths of $5^o x 5^o$ unaffected. The local mean geoid due to the rise must be removed. Crough (1982) removed a quadratic surface from the anomaly due to the rise, but this did not alter the anomaly shape of the rise itself.

It was decided to calculate a mean geoid over the rise by a simple running mean procedure. An area of 25x25 elements was averaged to give a mean geoid value at the centre of the 25x25 grid. The mean geoid is shown in Figure 8.8. To check that this mean geoid is a reasonable approximation to the local geoid anomaly as calculated in the GDR (Geophysical Data Record), Lorell et al (1980), a comparison was made between the data in Figure 8.8 and the GEM10B $1^o x 1^o$ gravimetric geoid. The results of this comparison are shown in Figure 8.9 and indicate that the 25x25 point average is a good approximation to the GEM10B gravimetric geoid.

Figure 8.10a shows the local geoid anomaly after removal of both the PGS-S3[36,36] regional and the 25x25 point local geoids. The main contrast between Figure 8.10a and Figure 8.8 is the appearance of the flanking geoid lows that will indicate the state of compensation of the lithosphere of the Cape Verde Rise.

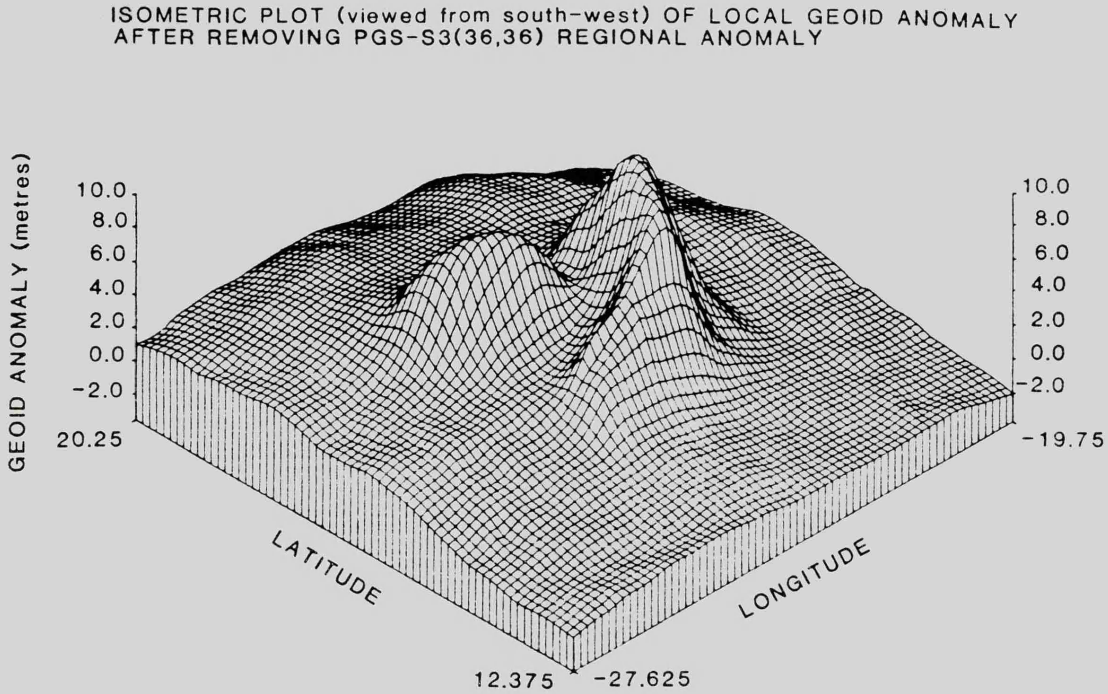

Figure 8.7 Isometric plot, viewed from the south-west, of the 64x64 element subset of the gridded geoid data shown in Figure 8.6. The geoid anomaly of the Cape Verde Rise and Cape Verde Archipelago are very prominent in this plot.

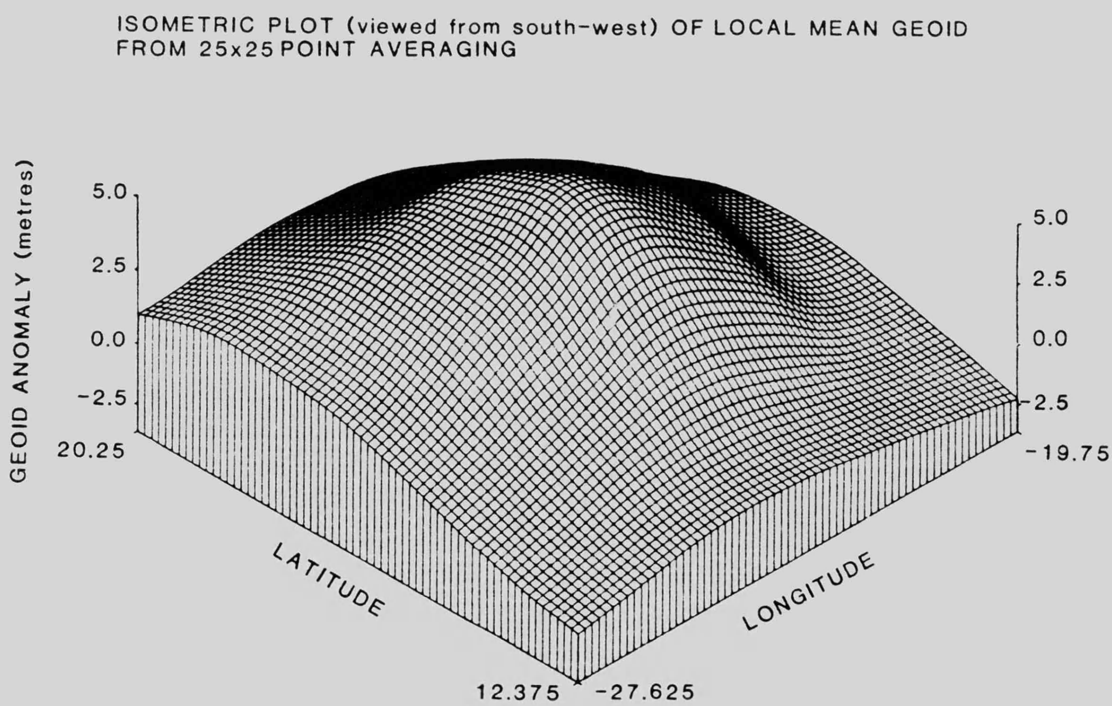

Figure 8.8 Isometric plot, viewed from the south-west, of a 25x25 point running mean of the data shown in Figure 8.7. This plot illustrates the local geoid anomaly due to the Cape Verde Rise.

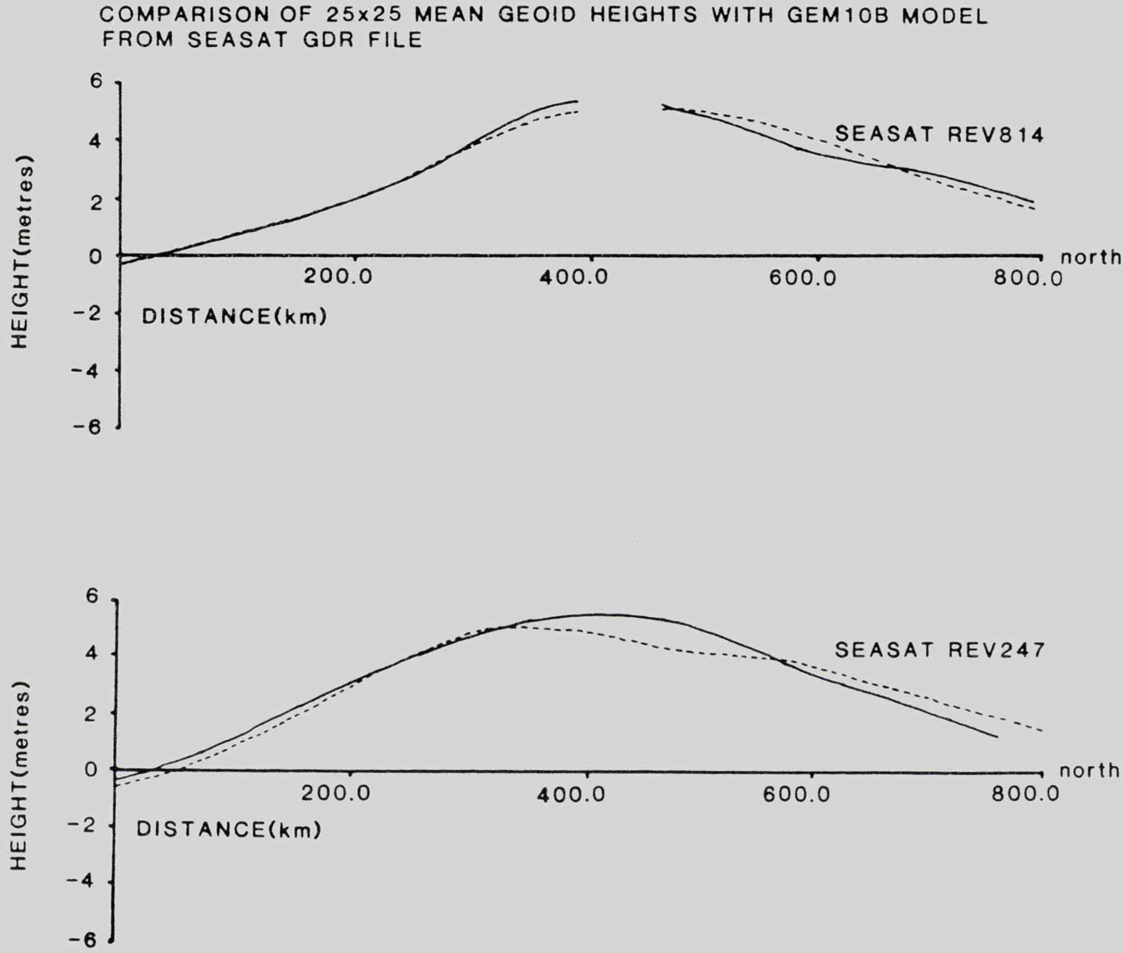

Figure 8.9 Comparison of the 25x25 point running mean, shown in Figure 8.8, with the GEM10B $1^{o}\times1^{o}$ gravimetric geoid from the SEASAT GDR data file for two satellite passes over the Cape Verde Rise. In both cases shown here the 25x25 point gridded mean is the dashed line and the observed SEASAT geoid hieght is the full line.

a)

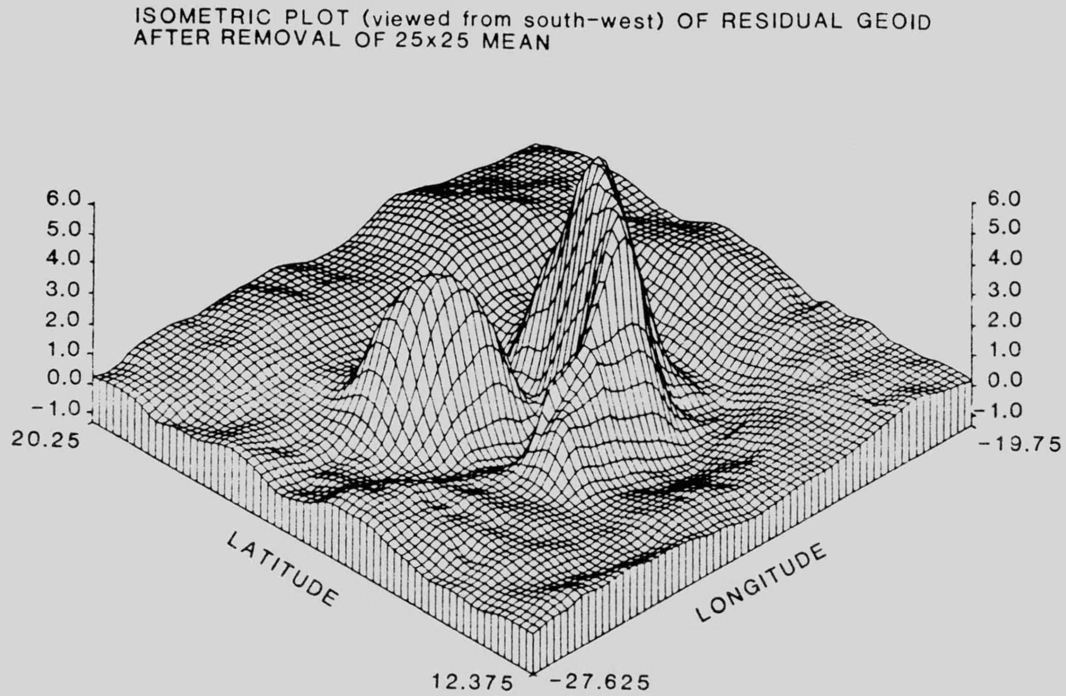

b)

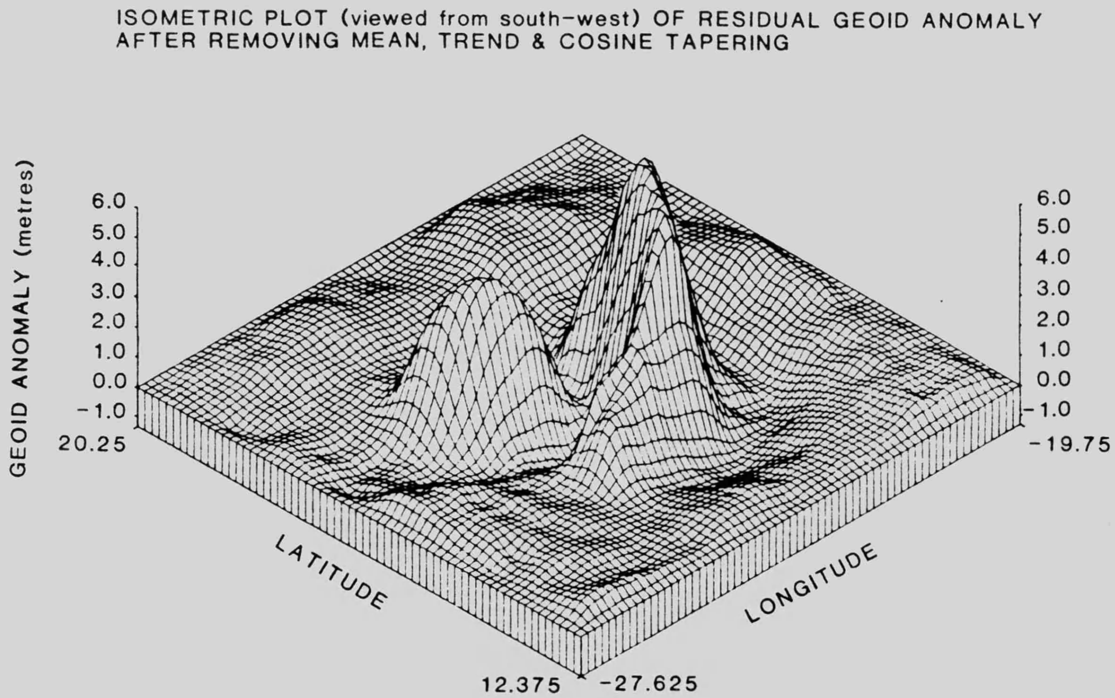

Figure 8.10 a)Isometric plot, viewed from the south-west, of the geoid anomaly after removal of both the PGS-S3[36,36] model and the local 25x25 point running mean. The main difference between this and the plot in Figure 8.7 is the flanking geoid low around the geoid high due to the Cape Verde Islands. b) Isometric plot of the same data as in the upper plot, but after removal of a mean, trend and cosine tapering

a)

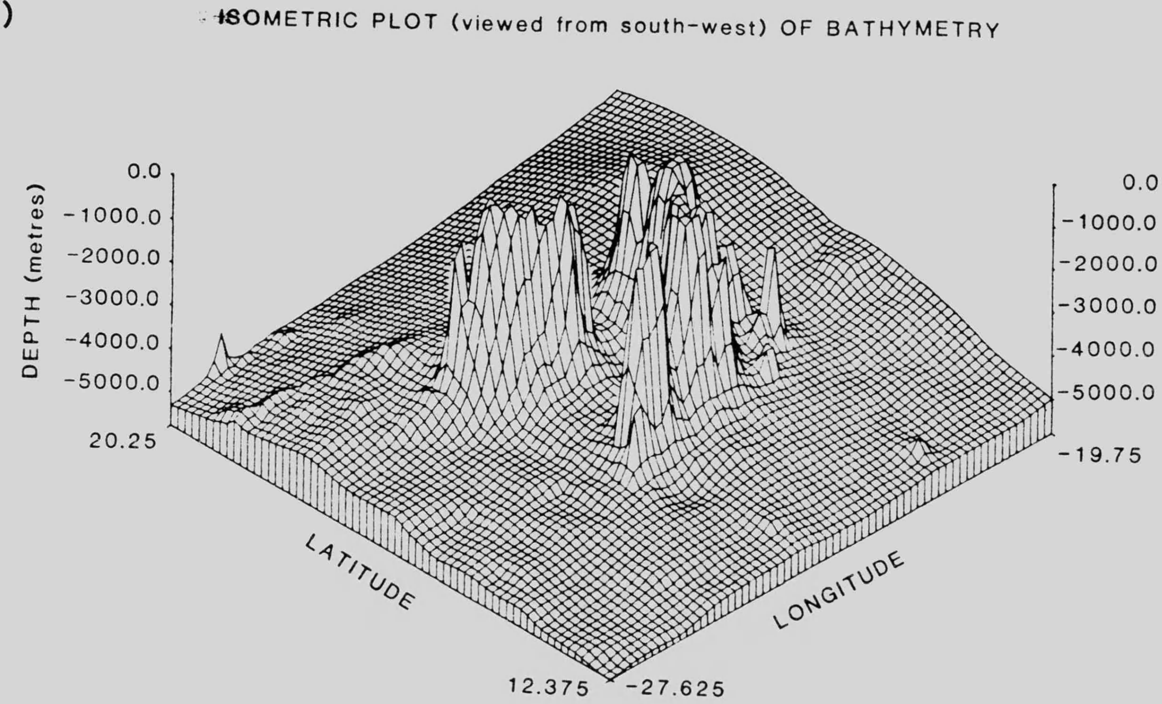

b)

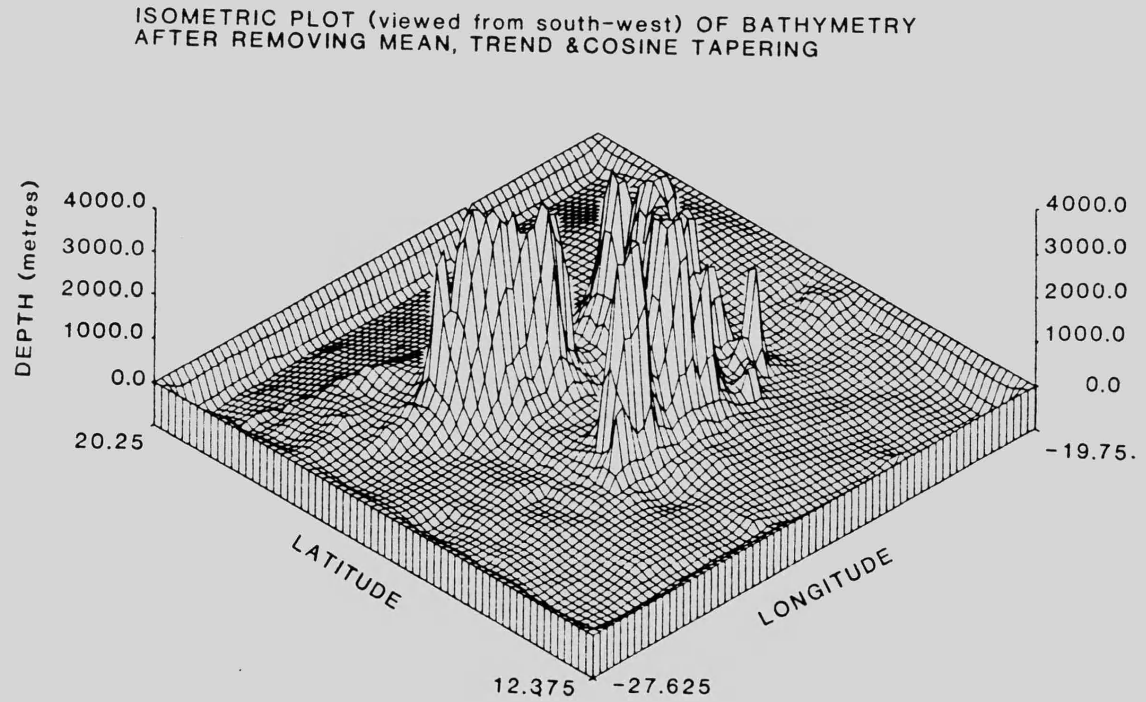

Figure 8.11 a) Isometric plot of the 64×64 element subset of the bathymetry data for the same area as the data in Figure 8.10. b) Bathymetric data after removal of a mean, trend and cosine tapering.

Before Fourier analysis it is necessary to remove a mean, trend and cosine taper the edges of the data. This has been done for the local geoid anomaly and is shown in Figure 8.10b. Figure 8.11a shows that subset of the bathymetry data before removal of a mean, trend and cosine tapering and Figure 8.11b shows the same data afterwards.

8.5 GEOID RESPONSE FUNCTION

Calculation of the relationship between geoid and bathymetry in the spatial frequency domain is exactly analogous to the response function, or admittance, calculated using free air gravity in Chapter 7. The response of the geoid is denoted by $Z'(\underline{k}_n)$ to distinguish it from $Z(\underline{k}_n)$ used for the gravity.

If $h(x,y)$ is the gridded geoid data and $b(x,y)$ is the gridded bathymetry data, then after Fourier transformation we will have two series $H(k_{nx},k_{ny})$ and $B(k_{nx},k_{ny})$.

The response function is given by:-

$$Z'(\underline{k}_n)=\langle H(\underline{k}_n)B^*(\underline{k}_n)\rangle/\langle B(\underline{k}_n)B^*(\underline{k}_n)\rangle \qquad \text{(E8.1)}$$

where $|\underline{k}_n|=\sqrt{(k_{nx}{}^2+k_{ny}{}^2)}$

$\langle\rangle$=an averaging process

When calculating $Z(\underline{k}_n)$ for the gravity considerable smoothing in the spatial frequency domain was achieved by averaging over many estimates of $G(\underline{k}_n)$ and $B(\underline{k}_n)$ obtained from 10 independent one-dimensional profiles of $g(x)$ and $b(x)$. In the case of the gridded data, however, this type of smoothing cannot be achieved. Azimuthal averaging can be applied by assuming that the admittance is independent of azimuth. The result will be the equivalent 1-dimensional admittance. It is also possible to average over bandwidths and sum all the Fourier coefficients that lie between bound of $|\underline{k}_n|$, where $|\underline{k}_n| = \surd(k_{nx}^2 + k_{ny}^2)$ and n=1,2,3,5,9,15,23,30. Both types of averaging will be used in this study. A similar scheme of averaging was adopted by Banks & Swain (1978) and McNutt (1982).

The response $Z'(\underline{k}_n)$ as calculated from the above equation will be a complex variable with real and imaginary parts. As with the gravity, the response of the geoid is expected to be real. The phase of the response function can be calculated simply from:-

$$\phi'(\underline{k}_n) = \tan^{-1}(Rl(Z'(\underline{k}_n))/Imag(Z'(\underline{k}_n))) \qquad (E8.2)$$

The phase should be close to zero for those wavelengths where the response of the geoid to bathymetry has a simple relationship. The coherence can also be calculated and should indicate how much of the power in the geoid is due to the power in the bathymetry at particular wavelengths. The coherence is given by:-

$$\gamma'^2(\underline{k}_n) = (N(CC^*/E1E2)-1)/(N-1) \qquad (E8.3)$$

where C=cross power of geoid and bathymetry

E1=power in the geoid

E2=power in the bathymetry

*=complex conjugate

N=number of values averaged

Lastly, the coherence can be used to estimate the error in the observed response value, according to Munk & Cartwright (1966), by assuming the errors in observed values have zero mean and are normally distributed with variance given by:-

$$\sigma''^2(\underline{k}_n)=Z'^2(\underline{k}_n)(\gamma^{-2}-1)/2(N-1) \qquad (E8.4)$$

8.6 RESULTS OF OBSERVED ADMITTANCE

Application of the FFT algorithm to the data shown in Figures 8.10b and 8.11b results in a series of complex Fourier coefficients for the geoid anomaly and bathymetry respectively. These were combined to form the cross-power spectrum of geoid and bathymetry, the power of the bathymetry and the power of the geoid. These quantities were then averaged over azimuth to get the 1-dimensional equivalent variation in admittance with inverse wavelength. The original data series was a 64x64 element grid with each element having length ~13.83 km. The Nyquist spatial frequency will be 0.0362 km^{-1} and the 1st harmonic will occur at 0.00113 km^{-1}. However, during azimuthal averaging it is assumed that $|\underline{k}_n|=\sqrt{(k_{nx}^2+k_{ny}^2)}$ and this alters the Nyquist frequency to 0.0512 km^{-1} (~19.53 km) and the 1st harmonic to 0.00160 km^{-1} (~625.86 km). Application of equations E8.1, E8.2 and E8.3 to the averaged cross-power spectrum and power spectra of geoid and bathymetry results in the admittance, coherence and phase estimates shown in Figure 8.12.

The $\log_{10}$ admittance, coherence and phase are plotted against inverse wavelength (λ^{-1}). The $\log_{10}$ admittance plot shows a linear trend between inverse wavelengths 0.004 km^{-1} to 0.016 km^{-1}. At inverse wavelengths greater than 0.016 km^{-1} (λ<62.5 km) there does not appear to be any simple relationship between geoid anomaly and bathymetry. This conclusion is supported by evidence from the plots of coherence and phase.

The coherence plot (Figure 8.12b) shows high values (>0.7) for inverse wavelengths less than 0.008 km^{-1} (λ>125 km). This suggests that at wavelengths less than 125 km little of the power in the geoid can be attributed to the power in the bathymetry. Watts (1979) found a similar result when analysing GEOS3 profiles over the Hawaiian ridge

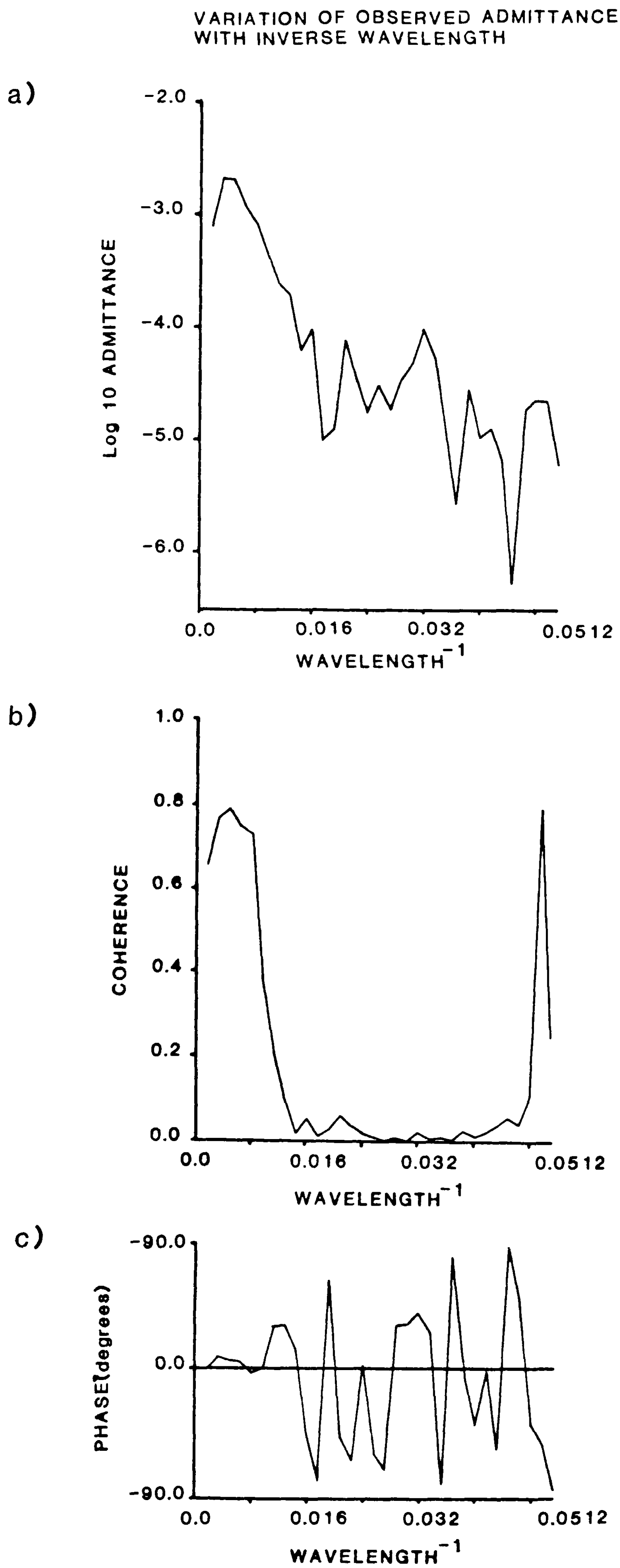

Figure 8.12 a)Plot of Log_{10} observed admittance against inverse wavelength. b)Plot of coherence against inverse wavelength. c)Plot of phase against inverse wavelength.

and stated that coherence dropped considerably at wavelengths less than 130 km. Similarly the plot of phase against inverse wavelength (Figure 8.12c) has low phase angles for wavelengths greater than 125 km. The plots in Figure 8.12 all suggest that the relationship between geoid heights and bathymetry may be relatively simple for inverse wavelengths less than 0.016 km^{-1}.

The averaging that has been applied so far is only azimuthal averaging and a logarithmically spaced bandwidth average can also be applied. Estimates of admittance are obtained at equal arithmetic intervals of Δk, where Δk=0.00160 km^{-1}, and $k_n = 2\pi n \Delta k$, where n=1,2,3,4,5......etc. This means there is a strong concentration of data points at the short wavelength end of the spectrum. Dorman & Lewis (1972) point out that logarithmically spaced estimates each contribute approximately the same amount of information. The admittance values displayed in Figure 8.12a were further averaged about wavenumbers n=1,2,3,5,9,15,23,30. A similar scheme was used by Banks & Swain (1978) and McNutt (1979) on gridded data.

Figure 8.13 shows the azimuthal and logarithmically bandwidth averaged admittance data plotted against $\log_{10}$ inverse wavelength. The change to a log scale for the abscissa is to provide a better picture of the long to intermediate wavelength behaviour. The error bars indicate ±1 standard error and are calculated using E8.4. The geoid admittance values in Figure 8.13 display a similar variation to the gravity admittance calculated in Chapter 7. The geoid admittance has low values (<0.0005 m/m) for wavelengths less than 100 km. At intermediate wavelengths (400>λ>100 km)the admittance values increase to a maximum of ~0.002 m/m. The admittance does not continue to increase, however, with increasing wavelength.

8.7 INTERPRETATION

The behaviour exhibited by the geoid response in Figure 8.13 is very similar to the behaviour of the gravity response in Chapter 7 (see Figure 7.6). The thin plate model that was used successfully to describe the gravity response, and which is described in Chapter 5, will also be used here. The two-dimensional geoid response of a thin plate flexing under an applied load can be calculated from:-

$$Z'(\underline{k}_n)=(1/g|\underline{k}_n|)2\pi G(\varrho_t-\varrho_w)\{\exp(-|\underline{k}_n|d_t)-(1+|\underline{k}_n|^4D/(\varrho_m-\varrho_t)g)^{-1}$$
$$[((\varrho_3-\varrho_t)/(\varrho_m-\varrho_t))\exp(-|\underline{k}_n|z_1)+((\varrho_m-\varrho_3)/(\varrho_m-\varrho_t))$$
$$\exp(-|\underline{k}_n|z_2)]\} \qquad (E8.5)$$

as derived in Chapter 5, E5.29 and E5.30.

where $Z'(\underline{k}_n)$=the response of the model at wavenumber $\underline{k}_n$

ϱ_w=the density of sea water

ϱ_t=the density of the topography (=density of layer 2)

ϱ_3= " " " layer 3

ϱ_m= " " " the upper mantle

d_t=depth of the topography

z_1=depth to the layer 2/layer 3 interface

z_2= " " " moho

g=normal gravity

and where $D=ET_e^3/12(1-\upsilon^2)$

with υ=Poisson's ratio

T_e=effective elastic thickness (EET)

Table 8.1 shows the values of the various parameters assumed for the model. The only difference between this model and the one used for the gravity is the mean depth to the topography. In this case the mean depth was calculated to be 3.99 km from the mean and trend removed

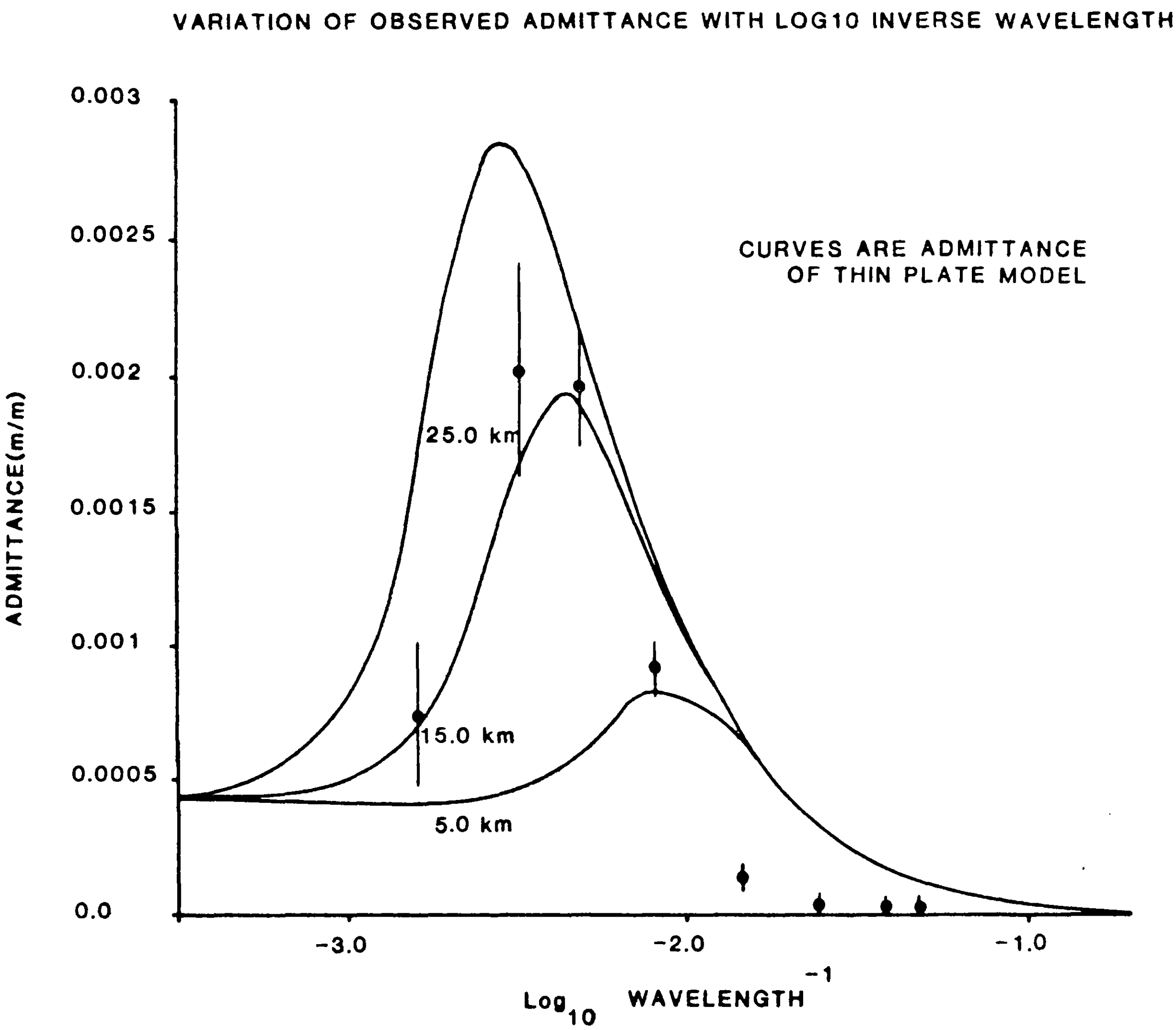

Figure 8.13 Plot of observed admittance against Log_{10} inverse wavelength. The admittance data have been averaged over azimuth and then bandwidth averaged. The curves illustrate the variation of admittance with Log_{10} inverse wavelength for the thin plate flexure model for effective elastic thicknesses of 5km, 15km and 25km.

from the gridded bathymetry data before entering the FFT.

Table 8.1 Summary of parameters used in model calculations.

Parameter	Value
ρ_w, density of seawater	1020 kg/m^3
ρ_t, " " topography (=layer 2)	2790 "
ρ_3, " " layer 3	2900 "
ρ_m, " " mantle	3400 "
d_t, depth of topography	3990 m
z_1, depth to layer2/layer3 interface	5990 m
z_2, " " moho	10990 m
g, accelaration of gravity	9.81 m/s^2
G, gravitational constant	0.667×10^{-12} Nm^2/kg^2
E, Young's modulus	10^{11} N/m^2
υ, Poisson's ratio	0.28

By repeated application of equation E8.5 with different values of the flexural ridigity, or effective elastic thickness, the variation of calculated response with wavelength can be computed for a host of different models. This approach has been applied to geoid analysis before by Dixon et al (1983), who used a single layered model with a density of 2600 kg/m^3, and by Watts (1979), who used a two layered elastic lithosphere with densities of 2800 kg/m^3 and 2900 kg/m^3 for the topography and layer 3 respectively. Cazenave et al (1980) also used a flexural model to calculate the expected geoid for an assumed flexural rigidity. The densities of the model used here are the same as those used in the gravity study. This model, if it is a good approximation to the geological situation, should work equally well for both the gravity and geoid response.

The variation of admittance with wavelength for the thin plate model at three different values of the EET are shown as curves, along with the observed admittance, in Figure 8.13. The observed admittance values are considerably lower than those predicted by the thin plate model at wavelengths less than ~70 km. The 4 estimates of admittance obtained from the gridded geoid and bathymetry data, for wavelengths longer than ~100 km, suggest the most appropriate EET for the thin plate model is ~15 km.

The low coherence values in Figure 8.12b and the highly variable phase in Figure 8.12c, at wavelengths shorter than ~100 km, combined with the poor fit of the model to the observed admittance, suggests that the gridded geoid data values are poor at measuring short wavelength geoid behaviour. Okal & Cazenave (1985) examined SEASAT profiles in the Pacific and suggested that the horizontal resolution of this data was 10-50 km. White et al (1983), while studying detection of seamount signatures using SEASAT passes, noted that the SEASAT data has a noise floor at wavelengths from ~13 km to ~50 km. From these previous works it would be expected that the minimum wavelength containing any information on the relationship between geoid and bathymetry would be ~50 km and not ~100 km as is evident from the present study. Figure 8.14 shows a comparison of the observed geoid height variation for 2 passes of the SEASAT radar altimeter and the gridded geoid height data using a combination of SEASAT and GEOS3 information. The comparison for REV814 is very good in that the curves match in terms of both amplitude and wavelength. In REV814, however, the radar altimeter has not recorded any geoid heights close to the island of San Nicolau. REV247, the lower set of curves in Figure 8.14, show that the gridded geoid data, dashed curve, does not match the SEASAT data, full curve, over the short wavelength (~60 km) anomaly in the vicinity of the island of St. Luzia. Rapp (in press) estimates that the resolution limit of the gridded data set is ~26 km but also

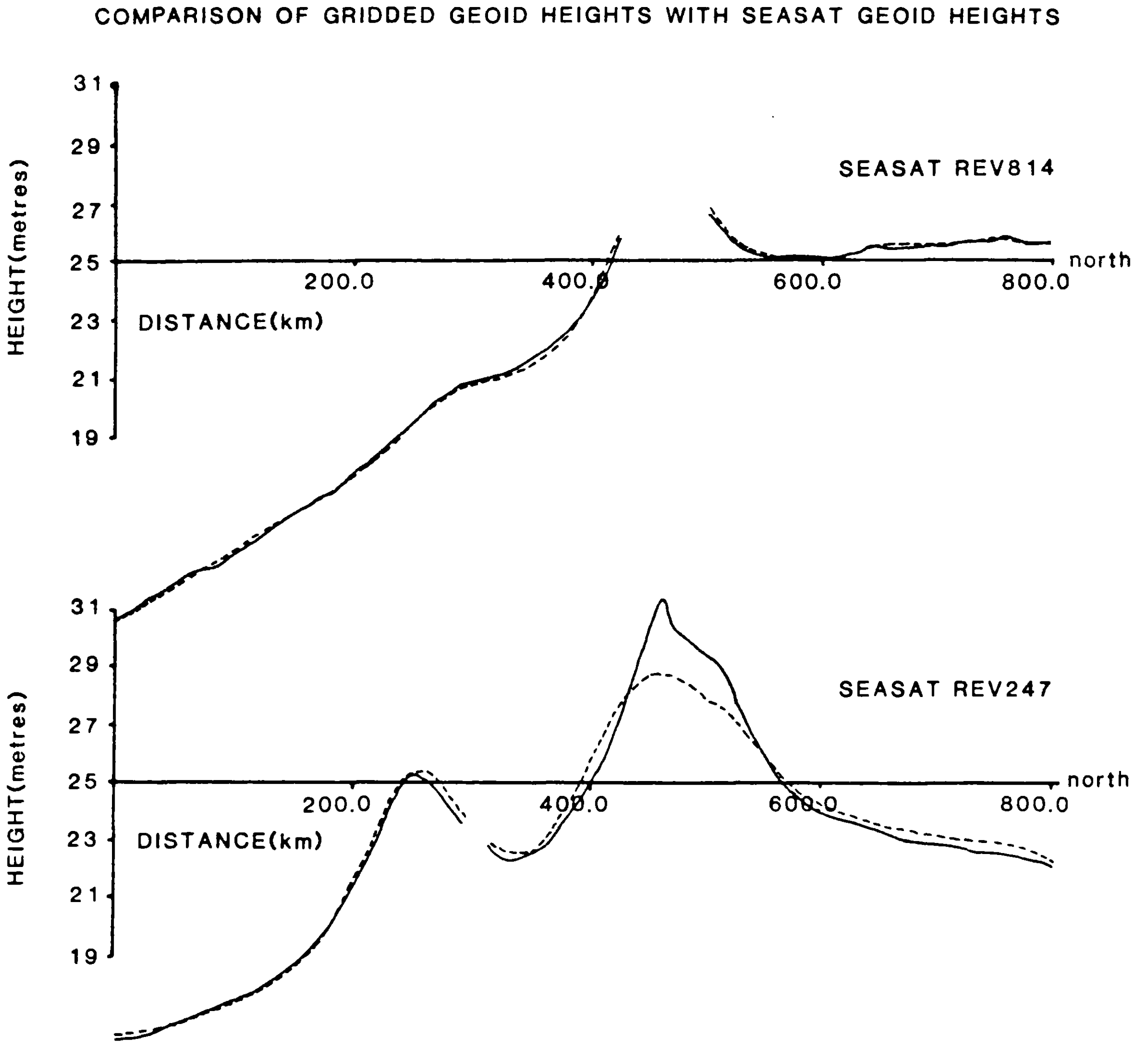

Figure 8.14 Comparison of observed SEASAT geoid heights with the gridded geoid data set for two satellite passes over the Cape Verde Rise. The observed SFASAT data has a higher frequency data cutoff than the gridded geoid data set.

states that high frequency signals may be lost if the appropriate data points are not selected during the interpolation process. It is suggested here that the interpolation in the area of the Cape Verde Islands has reduced the resolution of the gridded geoid data set to ~75-100 km and this accounts for the poor fit of the observed admittance to the model admittance in Figure 8.13. This low pass filtering does not interfere, however, with the waveband of between 100-300 km suggested by Ribe (1982) to be diagnostic for flexural rigidity studies. The data obtained in this study are considered adequate to distinguish between EET's of 5-40 km expected for oceanic lithosphere from previous work by McKenzie & Bowin (1976), Cochran (1979), Watts (1978) and Tamsett (1984).

8.8 FORWARD MODELING

The response function, or admittance, that can be calculated from models, such as the thin plate flexure model used here, is the spatial frequency representation of a space domain filter that, when convolved with the bathymetry, produces a close approximation to the geoid, or gravity. The reasons for working in the spatial frequency domain are given in Chapter 5 and will not be repeated here. Using the convolution theorem, Kanasewich (1975), whereby multiplication in the spatial frequency domain is equivalent to convolution in the space domain, the expected geoid can be calculated for a variety of different models relatively easily. The complex Fourier transform of the bathymetric data (shown in Figure 8.11b) can be multiplied by the 2-dimensional admittance from the thin plate model (E8.5) for a variety of different EET's. By taking the inverse Fourier transform of the resulting complex series, the expected, or calculated, 2-dimensional geoid will be obtained.

The expected geoid can be compared to the observed SEASAT geoid and this will circumvent the low pass filtering problems of the gridded geoid height data. A best fit can be calculated by taking the standard deviation of the observed from the calculated geoids. This is similar to a method used by Cazenave & Dominh (1984), who examined 30'x30' gridded geoid height data in the South Pacific.

8.9 SEASAT DATA

Figure 8.15 shows a chart of the area of the Cape Verde Rise with 8 SEASAT sub-satellite tracks superimposed. Tracks were selected that crossed, or passed close to the Cape Verde Islands. A similar problem of removing the regional and local variations, as was encountered with the gridded geoid heights, arises when dealing with isolated satellite tracks.

It was decided to use the GEM10B $1^{o}x1^{o}$ gravimetric geoid contained in the GDR and calculated for every observed SEASAT data point. This was shown in Figure 8.9 to be very similar to the 25x25 point mean subtracted from the gridded data over the Cape Verde Rise. This will maintain consistency between both aspects of this investigation. The geoid anomaly that will be compared with the expected geoid will be the observed SEASAT geoid height minus the GEM10B $1^{o}x1^{o}$ gravimetric geoid.

The resolution of the SEASAT data is, from Okal & Cazenave (1985), 10-30 cm for geoid heights and 10-50 km for wavelengths. It will be useful to see if the calculated geoid height data have a similar horizontal resolution to the observed.

8.10 CALCULATED GEOID

The thin plate model from Chapter 5 will be utilised again here. Equation E8.5 can be used to calculate the 2-dimensional admittance of this model. The values of the various parameters are given in Table

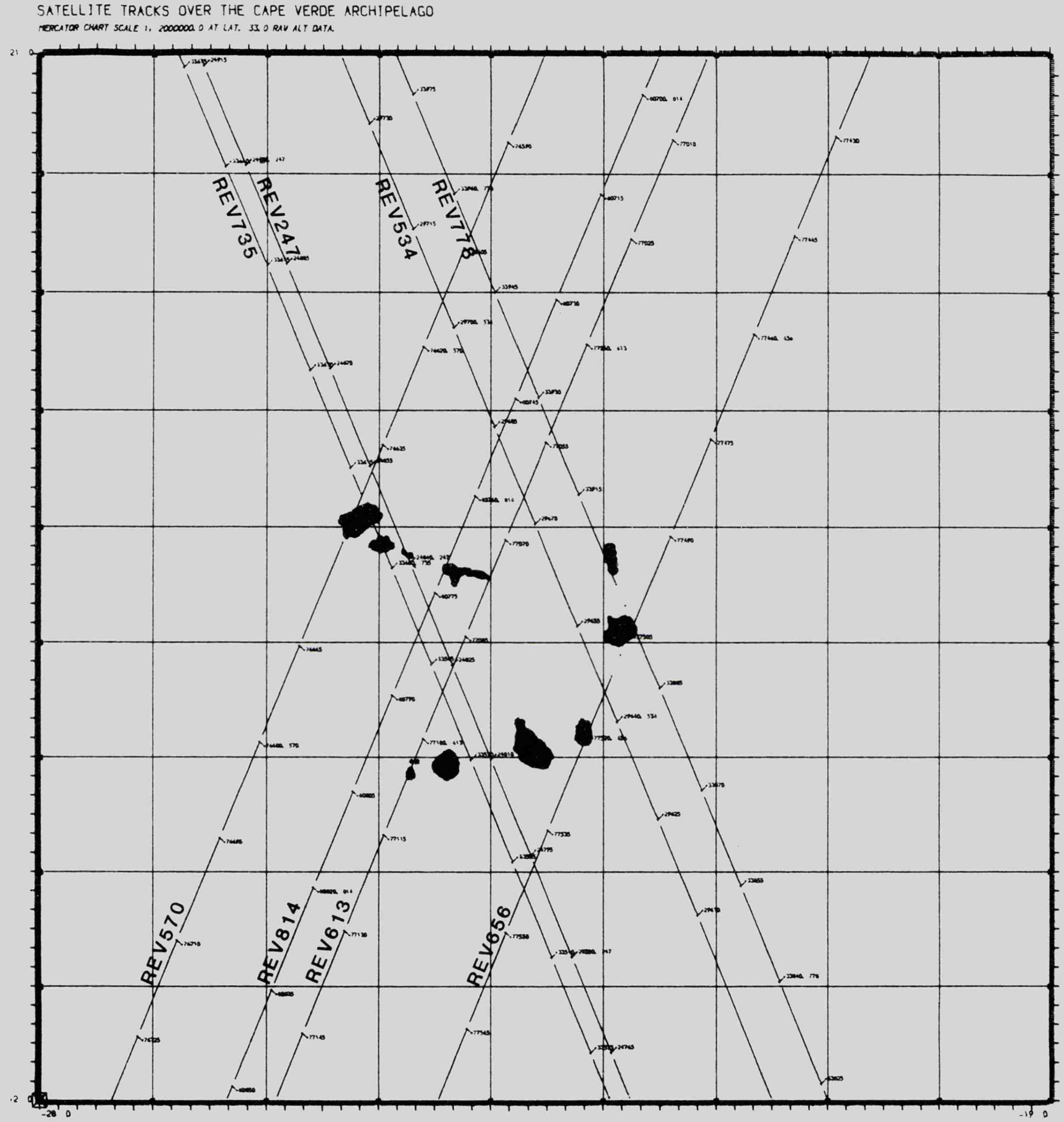

Figure 8.15 Chart of the area of the Cape Verde Rise with 8 subsatellite SEASAT tracks superimposed. The tracks were chosen to cross, or pass close to, the Cape Verde Islands.

8.1. An isometric plot of the expected geoid variation for an EFT of 15 km is given in Figure 8.16. A total of 18 models were created from an EFT of 10 km to an EFT of 27 km, inclusive, at 1 km intervals. This range of values was chosen to bracket the expected best fitting model of ~15 km from the observed admittance study reported earlier.

Comparison of these calculated values with observed values was done by linearly interpolating the calculated gridded geoid heights along the sub-satellite track. The goodness of fit between observed and calculated was obtained from the standard deviation detween the 2 curves. The standard deviation is given by:-

$$\sigma=\sqrt{((1/(N-1))\Sigma(X_i-Y_i)^2)}$$

where X_i=observed geoid height after removal of the GEM10B gravimetric geoid regional

Y_i=calculated geoid height

N=number of observations

It has been noted by several workers, Marsh & Williamson (1982) and Tapley et al (1982), that the observed SEASAT geoid heights in the GDR file have a time dependent error that can be approximated by an offset and linear trend. This has been introduced, it is thought, by radial orbit error terms and as such the wavelength of this phenomenon is greater than 5000-10000 km. Such errors were removed from the gridded geoid data set by extensive cross-over analyses. Prior to calculation of the standard deviation of the expected and observed geoids, a time dependent constant offset and slope was removed, by least squares, from the observed geoid heights. Thus the standard deviation values are not biased by any differences between radial orbit errors from track to track.

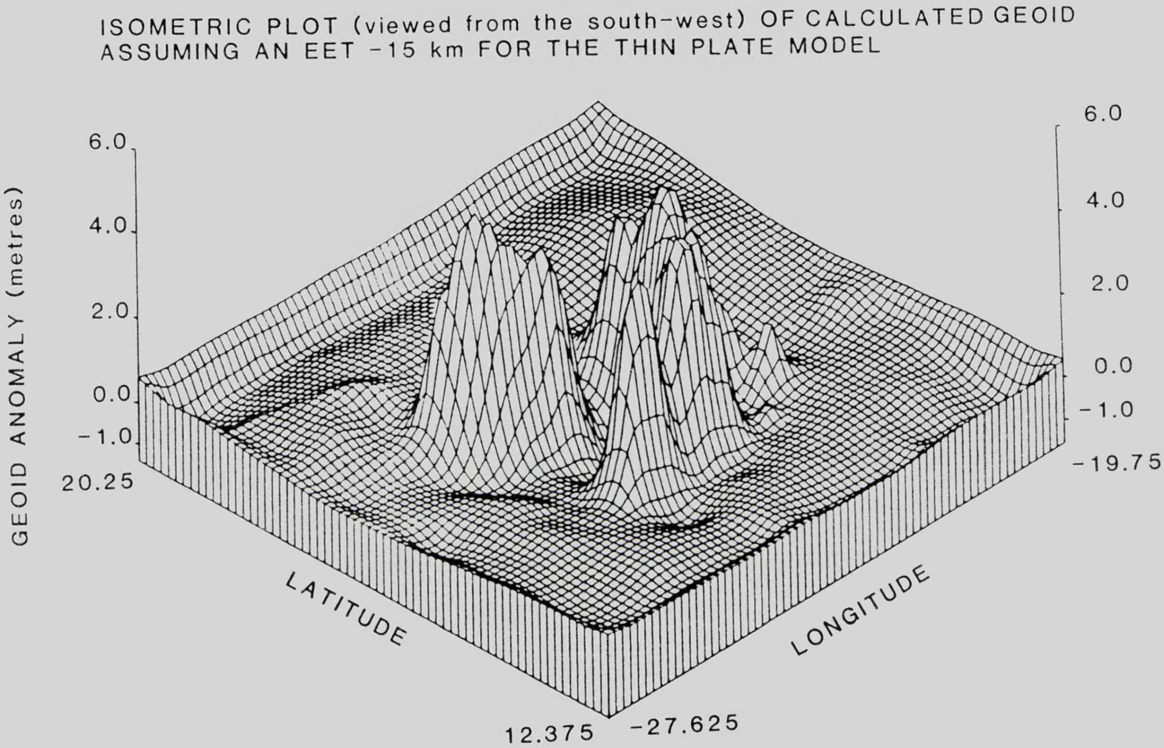

Figure 8.16 Isometric plot, viewed from the south-west, of the expected geoid height variation over the Cape Verde Rise assuming an effective elastic thickness of 15 km for the thin plate flexure model.

The differences between observed and calculated geoids are illustrated in Figure 8.17 for REV613 against models with EET's of 10, 15 and 25 km. The standard deviations for each model are shown beside the relevant profile. It can be seen from this figure that the best fit is for a model with an EET of around 15 km. By using models in steps of only 1 km it is hoped to determine the best fitting models for each of the 8 sub-satellite tracks shown in Figure 8.15.

Figure 8.18 shows the observed geoid height variation for the 4 descending tracks REVS 570, 613, 656 and 814 with the best fitting model curves. Figure 8.19 shows the same as Figure 8.18, but for the 4 ascending tracks, REVS 247, 534, 735 and 778. The smaller inset graphs for each profile show the variation of standard deviation with EET and the minimum on this graph corresponds to the best fitting model. The width of the minimum gives an idea of how quickly the observed and calculated curves converge to the best fitting model.

Table 8.2 lists the orbit numbers and the corresponding best fitting EET for the thin plate model. The values vary from a low of 14 km, for REV613, to a high of 22 km, for REV534. The mean best fitting EET from the 8 SEASAT sub-satellite passes used here is 18.4 km with a standard deviation of 2.6 km. This value is somewhat higher than that expected from the preferred fit of the observed admittance to the model admittance for an EET of 15 km shown in Figure 8.13. However, the fit of the calculated to the observed geoid in Figures 8.18 and 8.19 is very good indeed and this, combined with the small incremental step size in the models used to produce Figures 8.18 and 8.19, suggests that a value of 18$\pm$3 km for the EET is quite realistic.

Table 8.2 Best fit models for 8 SEASAT sub-satellite passes.

REVOLUTION NUMBER	BEST FIT MODEL (km)	STANDARD DEVIATION (m)
247	18	0.3171
534	22	0.2902
570	19	0.3050
613	14	0.3228
656	21	0.3340
735	18	0.3552
778	20	0.3146
814	16	0.2123

8.11 DISCUSSION

The study of the relationship between gridded geoid anomaly heights and gridded bathymetry, when examined in the spatial frequency domain suggests that the effective elastic thickness of the lithosphere of the Cape Verde Rise is ~15 km. Only 3 model curves were produced for comparison with the observed admittance; at 5, 15 and 25 km. Using a smaller increment (1 km) for the models and comparing the calculated, or expected, geoid with that observed along 8 separate SEASAT sub-satellite profiles, a value of 18±3 km can be deduced for the EET. The results from the inversion and forward modeling are not incompatible but do reflect differences in the 2 methods used in this study.

As was pointed out in Chapter 5, certain simplifying assumptions have been made in using the thin plate model. The nett result of these assumptions is that the EET calculated from the thin plate model can be considered to be a maximum (Watts & Ribe (1984)).

The value of the EET for the Cape Verde Rise obtained here from

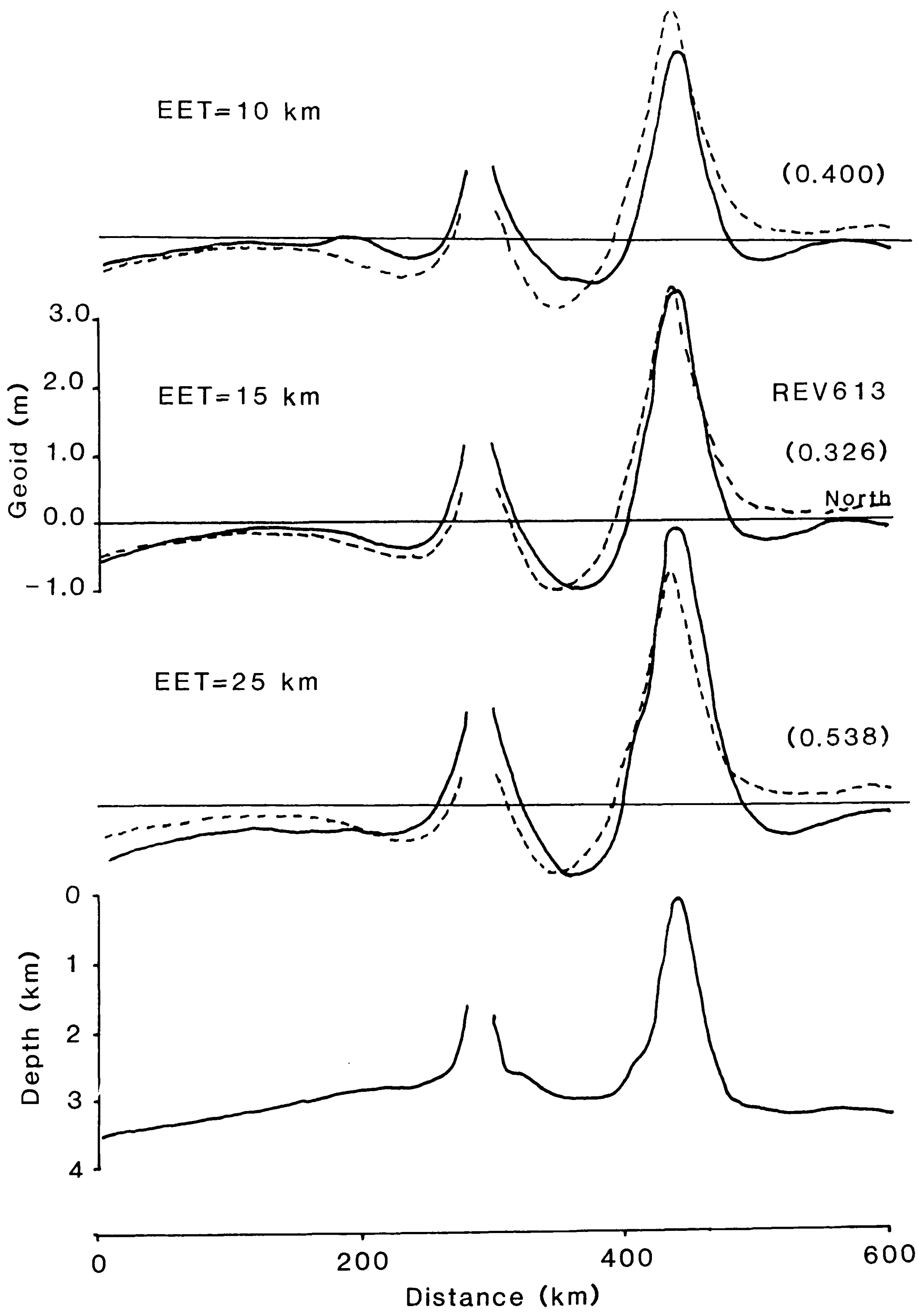

Figure 8.17 Variation of observed and calculated geoid heights for three different effective elastic thickness models. The calculated data are compared with the observed data for REV613. The curves are, from top to bottom, 10km, 15km, and 25km. The standard deviation for each model is shown, in brackets, beside the curves. The observed data are shown as a dashed line with the calculated data shown as a full line. The best fit occurs around the 15 km model.

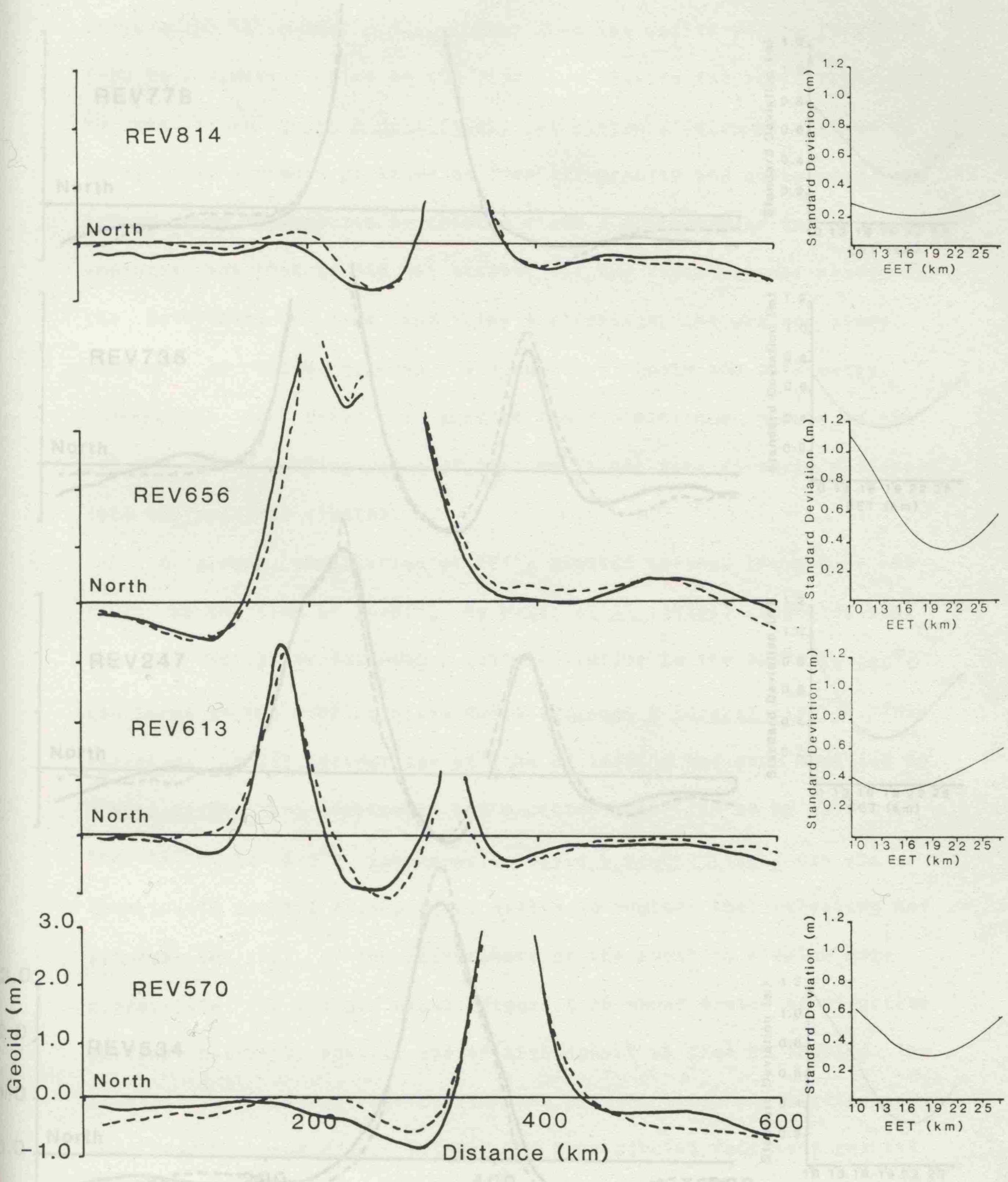

Figure 8.18 Observed geoid height variation from the SEASAT GDR file (dashed lines) for descending tracks REVS 570, 613, 656 and 814. The full lines are the best fitting model geoid heights (see Table 8.2). The inset box in each case shows the variation of standard deviation against EET. The minimum for the curve indicates the best fitting model.

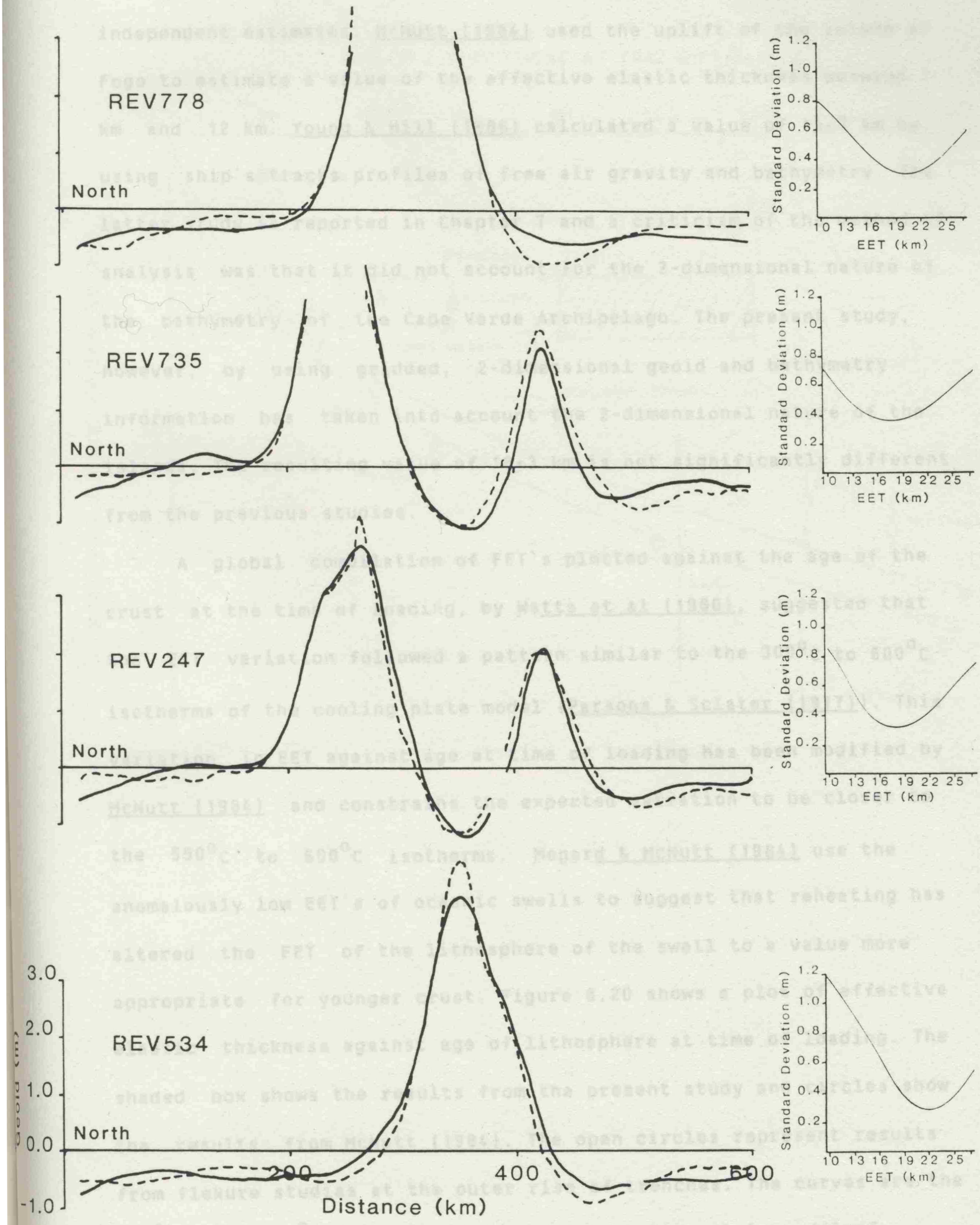

Figure 8.19 As for Figure 8.18 but in this case showing the comparison of observed geoid heights to best fitting model geoid heights for ascending REVS 247, 534, 735 and 778.

the geoid/bathymetry relationship can be compared with 2 other independent estimates. McNutt (1984) used the uplift of the island of Fogo to estimate a value of the effective elastic thickness between 7 km and 12 km. Young & Hill (1986) calculated a value of 15±3 km by using ship's tracks profiles of free air gravity and bathymetry. The latter study is reported in Chapter 7 and a criticism of the method of analysis was that it did not account for the 2-dimensional nature of the bathymetry of the Cape Verde Archipelago. The present study, however, by using gridded, 2-dimensional geoid and bathymetry information has taken into account the 2-dimensional nature of the islands. The resulting value of 18±3 km is not significantly different from the previous studies.

A global compilation of EET's plotted against the age of the crust at the time of loading, by Watts et al (1980), suggested that the EET variation followed a pattern similar to the 300°C to 600°C isotherms of the cooling plate model (Parsons & Sclater (1977)). This variation in EET against age at time of loading has been modified by McNutt (1984) and constrains the expected variation to be closer to the 550°C to 600°C isotherms. Menard & McNutt (1984) use the anomalously low EET's of oceanic swells to suggest that reheating has altered the EET of the lithosphere of the swell to a value more appropriate for younger crust. Figure 8.20 shows a plot of effective elastic thickness against age of lithosphere at time of loading. The shaded box shows the results from the present study and circles show the results from McNutt (1984). The open circles represent results from flexure studies at the outer rise of trenches. The curves are the 550°C and 600°C isotherms from the cooling plate model of Parsons & Sclater (1977).

The age of the lithosphere of the Cape Verde Rise varies from 105 Ma to 140 Ma in the vicinity of the Cape Verde Islands, from

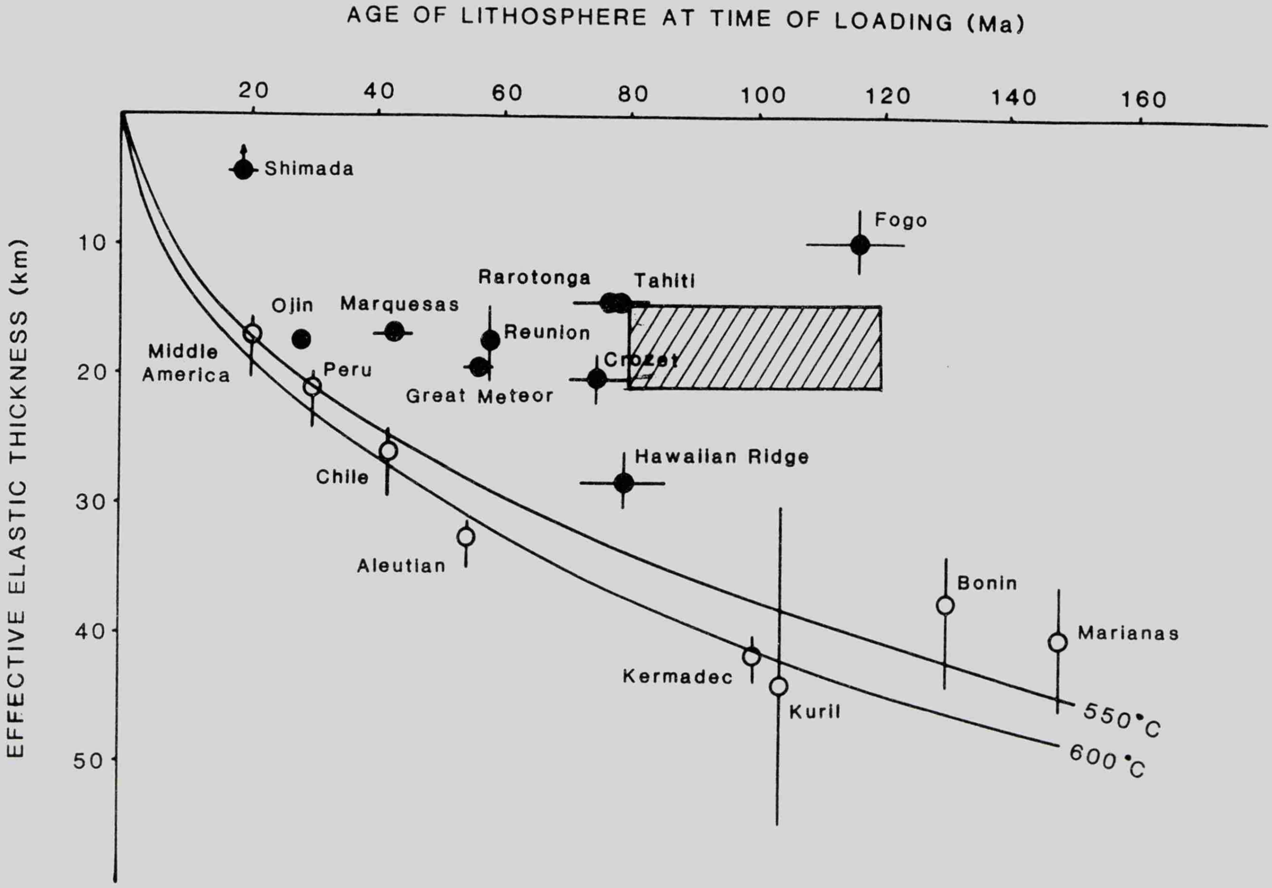

Figure 8.20 Variation of EET against age of lithosphere at the time of loading. This is modified from McNutt (1984) to include the results from this study. The shaded box indicates the results from the present geoid analysis, the filled circles are results from previous ocean island and seamount studies and the open circles are results from flexure studies at the outer rise of trenches. The curves are isotherms from the cooling plate model of Parsons & Sclater (1977).

Hayes & Rabinowitz (1975) and Chapter 3, and extensive volcanism did not start until 20 Ma ago, Mitchell et al (1983). The age at the time of loading must be around 85-135 Ma. From Figure 8.20 the expected EET should be 30-40 km. The above value for the observed EET of 18±3 km still represents a considerable reduction in the EET.

This result agrees with those of Young & Hill (1986) and McNutt (1984) that the lithosphere of the Cape Verde Rise has undergone thermal rejuvenation and now has an effective elastic thickness more appropriate to younger (25 Ma?) oceanic crust.

8.12 CONCLUSIONS

1) Gridded geoid height values can be combined with gridded bathymetry values in the spatial frequency domain to estimate the observed admittance of the Cape Verde Rise. Comparison of this observed admittance with calculated admittance values for a thin plate flexure model suggest the effective elastic thickness of the Cape Verde Rise is ≈15 km.

2) Forward modeling using the gridded bathymetry to predict the geoid values, assuming the thin plate model is correct, suggest, by comparison with SEASAT sub-satellite passes, that the effective elastic thickness is 18±3 km. The difference between this and the value obtained from inversion is not considered significant and probably reflects differences in the 2 methods of analysis.

3) The values for the EET from this study agree well with values from Young & Hill (1986), who used 1-dimensional analysis of gravity/bathymetry profiles to estimate the EET as 15±3 km.

4) The value of the EET for the lithosphere of the Cape Verde Rise is less than that predicted by a global compilation of EET's against age at time of loading. This is considered to be evidence of thermal rejuvenation possibly due to a hot-spot beneath the Cape Verde Rise.

CHAPTER 9 (SUMMARY OF CONCLUSIONS)

9.1 INTRODUCTION

The purpose of this study has been to conduct a geophysical investigation of the lithosphere of the Cape Verde Rise. The Cape Verde Rise is considered to be the result of 'Hot Spot' activity. The techniques employed in this work have been total field magnetic anomalies, free air gravity anomalies, seismic reflection and refraction, bathymetry and geoid height anomalies.

Measurements of these quantities over the rise can be compared with values expected from either simple mathematical models, or from similar measurements in areas not thought to be affected by 'Hot Spot' activity. The seafloor spreading magnetic anomalies in the area are an indication of the regional structures over the rise. The free air gravity anomalies associated with the islands are indicative of the state of compensation of the lithosphere. Seismic reflection techniques show the crude seismic stratigraphy of the sediments over the rise and can be compared with proposed uplift histories. Velocity information aids the reflection interpretation. The geoid height anomalies also indicate the state of compensation of bathymetric features on the Cape Verde Rise.

9.2 MAIN RESULTS OF THIS STUDY

The magnetic study looked at the variation of total field magnetic anomalies in and around the Cape Verde Archipelago and compared these with a Mesozoic sea floor spreading reversal model. Seafloor spreading magnetic anomalies have been identified within the archipelago; a result that was not previously known. The previous work in this area by Hayes & Rabinowitz (1975) has been refined to show that a total of 4 fracture zone traces are present around the Cape Verde Archipelago. Offsets along these fracture zones vary from zero to ~30 km at the youngest end of the 'M' sequence. Comparison of the present study with work in the Western North Atlantic shows that the spreading rate history is very similar, indicating that the Mid-Atlantic Ridge was spreading symmetrically from 105 to 145 Ma. The islands forming the archipelago do not appear to be related to the fracture zone traces but the position of the northern fracture zone could be altered, within the constraints of the available data, to pass through the northern limb of the archipelago.

The seismic reflection investigation erected a crude seismic stratigraphy over the Cape Verde Rise. The units outlined were, (i) the diffraction hyperbolae from the volcanic basement, (ii) a series of horizontal reflectors comprising pre-volcanism marine sediments, (iii) a unit of scattering reflectors attributed to volcaniclastic material and, finally, (iv) a layer characterised by relative acoustic transparency which is considered to be post-volcanism pelagic sediments. It was not possible to penetrate the overlying sediments and see reflectors indicative of volcanic basement when <50 km away from the islands. Thus, the depth of layer 2 could not be continuously mapped. However, the depth to layer 2 could be observed and measured at several locations. The observed depth at the centre of the rise is ~2 km less than that expected from the variation of oceanic depth with age derived empirically for all the world's oceans. A global compilation of oceanic swell depth with age of oceanic crust suggests that all swells are at a depth equivalent to 25 Ma crust. This figure is derived from comparison with a cooling plate model.

The seismic refraction experiments did not contradict the reflection interpretation with volcanic basement having high velocities (4.0 to 5.0 km/s), lithified Mesozoic sediments having velocities in the range 2.0 to 3.5 km/s and pelagic sediments having velocities less than ~2.0 km/s.

The relationship between free air gravity and bathymetry has been examined using linear transfer function techniques and the results compared with a thin plate flexure model. The model has a variable rigidity which is expressed as an effective elastic thickness (EET) where high values ($\sim$40 km) represent rigid crust and low values ($\sim$5 km) represent relatively soft crust. The observed variation of admittance, which relates the gravity and bathymetry in the spatial frequency domain, suggests the EET of the lithosphere of the Cape Verde Rise is 15 $\pm$3 km. A global compilation of EET against age of the lithosphere at the time of loading suggests the EET most appropriate for lithosphere loaded at 80 to 120 Ma is $\sim$30 $\pm$10 km. The variation of EET with age is similar to the variation of the 500^o to 600^o isotherms from a cooling plate model. This is important since it provides a link between the variation of EET, an observable quantity, and the thermal properties of the lithosphere. The reduced value of EET for the Cape Verde Rise is considered to be evidence for thermal rejuvenation. The lithosphere of the Cape Verde Rise now has a thermal age equivalent to 25 Ma crust. This is observed as both a reduction in the EFT and as a depth anomaly.

The relationship between geoid height and bathymetry can also be examined in a similar manner to the gravity. The advantage of using the geoid is that the data coverage is 2-dimensional, whereas the gravity along ship's tracks is only 1-dimensional. The same thin plate flexure model is used here as was utilised for the gravity study. The simple relationship between geoid anomalies and gravity anomalies is outlined in Chapter 5. The observed geoid admittance compares well with a thin plate flexure model having an EET of $\sim$15 km. The frequency content of the gridded geoid height data is less than that of individual sub-satellite profiles. A forward modeling process is accomplished by predicting the geoid height anomaly due to the bathymetry and assuming values for the EFT. The predicted, or calculated, anomaly is compared with the observed anomaly until a best fit is found. The result for the Cape Verde Archipelago is a best fitting model with an EET of 18$\pm$3 km. This result is comparable with the result from the observed gravity admittance that the lithosphere of the Cape Verde Rise has been thermally rejuvenated.

9.3 LIMITATIONS OF THIS STUDY

The study undertaken here has had several limiting factors. The magnetic anomaly track coverage still contains large gaps. In particular there is a lack of magnetic data just to the north of the northern limb of the archipelago. This results in poor resolution of the position of the northern fracture zone.

The seismic reflection profiling failed to penetrate the sediments when close to the islands. This means that no direct evidence is available for the flexure trough expected around the bathymetric load of the islands from the thin plate model. The seismic refraction experiments, although giving reasonable results, could have been distributed more uniformly around the archipelago.

The gravity profiles examined along ship's tracks had to be truncated and reflected about their maximum bathymetric values to be processed using Fourier analysis. A larger number of suitable free air gravity anomalies would have prevented this necessity.

9.4 DISCUSSION

This examination of the lithosphere of the Cape Verde Rise has been conducted to look at the variation of geophysical properties that may provide evidence for 'Hot Spot' activity. The main link between the measurement of EET and the thermal properties of the lithosphere are the global compilations of Watts et al (1980) and McNutt (1984).

These in turn are based on the assumption of a simple cooling plate model by Parsons & Sclater (1977). The results from this study can be compared with similar studies undertaken around Hawaii, in the Pacific.

The obvious physical parameter that has not been measured is the heat flow. A recent study by Courtney & White (1986) undertook measurements of heat flow across the Cape Verde Rise along a south to north isochron. Their results suggest a heat flow anomaly exists which is centred on the bathymetric, and geoid height, highs of the rise. The value of the heat flow is only 62$\pm$4 mW/m^2 whereas normal heat flow values for crust of this age (125 Ma) are typically ~46 mW/m^2 (Parsons & Sclater (1977)). The expected heat flow for 25 Ma crust is ~120 mW/m^2. Courtney & White (1986) modelled their heat flow results in terms of lithospheric reheating. This gave poor prediction of the heat flow but good fits for both the predicted geoid height anomaly and the depth anomaly. The difference between the observed heat flow anomaly and that expected for crust reheated to have the equivalent thermal structure of 25 Ma crust can be explained in terms of the heating mechanism. Crust created at a Mid Ocean Ridge is heated throughout, cools from the top down and therefore will be associated with a particular heat flow anomaly as shown by Parsons & Sclater (1977). The reheating mechanism proposed in this thesis involves heating from below and the extent to which the thermal anomaly perturbates through the crust determines whether a depth anomaly (Hawaii) or a depth anomaly plus a reduction in effective elastic thickness (Cape Verde Archipelago) is observed. The heat flow anomaly associated with this type of reheating is unlikely to be as large as when the whole of the crust is involved.

The model preferred by Courtney & White (1987) is one where the uplift of the rise is caused by dynamic upwelling of a mantle plume and this results in a better fit to the observed heat flow. However, constraining the model to fit the heat flow means that the geoid height and bathymetry data are not well predicted. The conclusion from the work presented in this thesis, that the Cape Verde Rise is the result of thermal rejuvenation and that it now has a thermal age equivalent to 25 Ma, does not try and predict the heat flow anomaly. McKenzie (1984) suggests that the energy required to melt material in the lithosphere will restrict the heat flow anomaly measured at the surface to $\sim$20 mW/m^2 regardless of the heating mechanism. Work on the relationship of topography and gravity to thermal structure has also been carried out by Parsons & Daly (1983), who state that comparison of observations with models is relatively insensitive to the mode of heating. The thin plate flexure model used for modelling the gravity and geoid anomalies over the Cape Verde Rise cannot rule out the possibility that a small component of dynamic support exists. The present study has been limited to the lithosphere of the rise itself and has not tried to constrain the mechanism of support of the rise as a whole.

The global compilations of EET against age of the crust at the time of loading have used results from a variety of different studies. These include linear transfer function techniques using both gravity and geoid data, uplift of atolls on the periferal bulge of the flexure trough and the bulge seaward of oceanic trenches. The assumption is that all these techniques are measuring the same quantity of the elastic properties of the lithosphere. The original compilation by Watts et al (1980) has been updated and corrected by McNutt (1984). The latter study assumed that the misfit between observed EET's and those expected from the cooling plate model was due to thermal rejuvenation and suggested that the EET was an indicator of the depth to the 550^o isotherm. The thermal age of the lithosphere can be estimated from the size of its depth anomaly (Crough (1978)) and when the observed EET's are plotted against the corrected thermal age of the lithosphere then a much better fit is obtained for all the data points.

Comparison of this study of the Cape Verde Rise with similar work over the Hawaiian Ridge suggests there may exist important differences between the reheating mechanisms of these two 'Hot Spots'. The Cape Verde Rise is characterised by both a reduction in the observed EET and by a large (~2 km) depth anomaly. The Hawaiian ridge has a depth anomaly but not a significant reduction in the observed EET. Detrick et al (1981) explain the depth anomaly over the Hawaiian Ridge in terms of reheating at a depth below the 550^o isotherm. This produces uplift, but since the 550^o isotherm is not raised above that normal for lithosphere of that age then no reduction of the EET can occur. The Cape Verde Rise has had both heating of the lower lithosphere, to produce the depth anomaly, and raising of the 550^o isotherm to cause a reduction in the EET. This hypothesis is not dependent on the mode of heat injection into the lithosphere. The difference between the two expressions of thermal rejuvenation can be explained by considering the motion of the plates with respect to the 'Hot Spot' reference frame. Minster & Jordan (1978) have shown that the Cape Verde Rise is moving slowly (<1 cm/yr) over its mantle heat source and this suggests that the heat anomaly has had time to perturbate to high in the lithosphere and therefore effect the observed EET. Hawaii, however, is moving, with the Pacific plate, at ~10 cm/yr over its heat source and thus the heat anomaly has not had time to raise the 550^o isotherm, therefore no significant reduction of the EET is observed.

9.5 SUGGESTIONS FOR FURTHER WORK

Based on the present study it is suggested that further work be undertaken in 3 areas.

1) Magnetic anomaly profile data should be collected to the north of the islands of San Antao, San Vicente, San Luzia and San Nicolau. This will better define the northern fracture zone trace identified by this study. In addition, data should also be collected to the east of the Maio/BoaVista ridge where there there are several unsurveyed areas. Direct observation of topographic features on oceanic layer 2 could also be attempted using seismic reflection profiles orientated roughly north-south. A sufficiently powerful source should be utilised to penetrate the sediments particularily near the islands.

2) Seismic reflection profiles should be collected approaching the islands to try and observe the flexural trough predicted from the gravity and geoid observations. The amplitude and wavelength of the trough can be used to further constrain the EET most appropriate for the Cape Verde Rise. The seismic stratigraphy of the material infilling the trough can indicate the history of developement of the rise. This type of work has been used by Brink & Watts (1985) to investigate Hawaii.

3) Further modeling of the thermal structure of the rise could be carried out to try and define the nature of the mantle 'Hot Spot'. The type of questions that can be addressed are the time delay between input of a heating event at the base of the lithosphere and observations of the resulting gravity, geoid and depth anomalies at the surface, the effects of injecting molten material at high levels in the lithosphere and the buffering effect of melting on any subsequent heat flow anomalies.

APPENDIX I (DIGITISATION)

A.1 INTRODUCTION

To display sonobuoy wide angle reflection/refraction seismic data as 'wiggly' trace plots, using hardware available at Leicester University, it is necessary to have the data in digital form. The data were originally recorded as continuous analogue signals on magnetic tape along with the 'shot' instant. Analogue to digital conversion was carried out at Leicester using a facility attached to the CDC Cyber 73 mainframe computer.

The handling and display of large amounts of digital seismic data requires an efficient storage system and suitable software for easy access to specific parts of the whole data set. The SDPS system was created to handle digital earthquake seismic data and software had to be written to link the data handling and display facilities already available with the particular requirements of this study. The requirement is that the digitised sonobuoy seismic signal be split into a number of separate channels for each 'shot' using the 'shot' instant, or keypulse, recorded on magnetic tape alongside the sonobuoy signal.

A.2 ANALOGUE SEISMIC DATA

The sonobuoy wide angle reflection/refraction seismic data digitised at Leicester was recorded on analogue magnetic tape during a cruise to the Cape Verde Archipelago onboard the RRS Shackleton. The signal from the hydrophone suspended beneath the sonobuoy was frequency modulated and transmitted back to the ship by a radio link. A receiver onboard demodulated the signal and transfered it to magnetic tape recording at either 15/16 ths, or 15/8 ths inchs/second. Also recorded were the shot instant; usually a 5 volt TTL pulse of around 20 ms duration, an event mark; acting as a crude time code and,

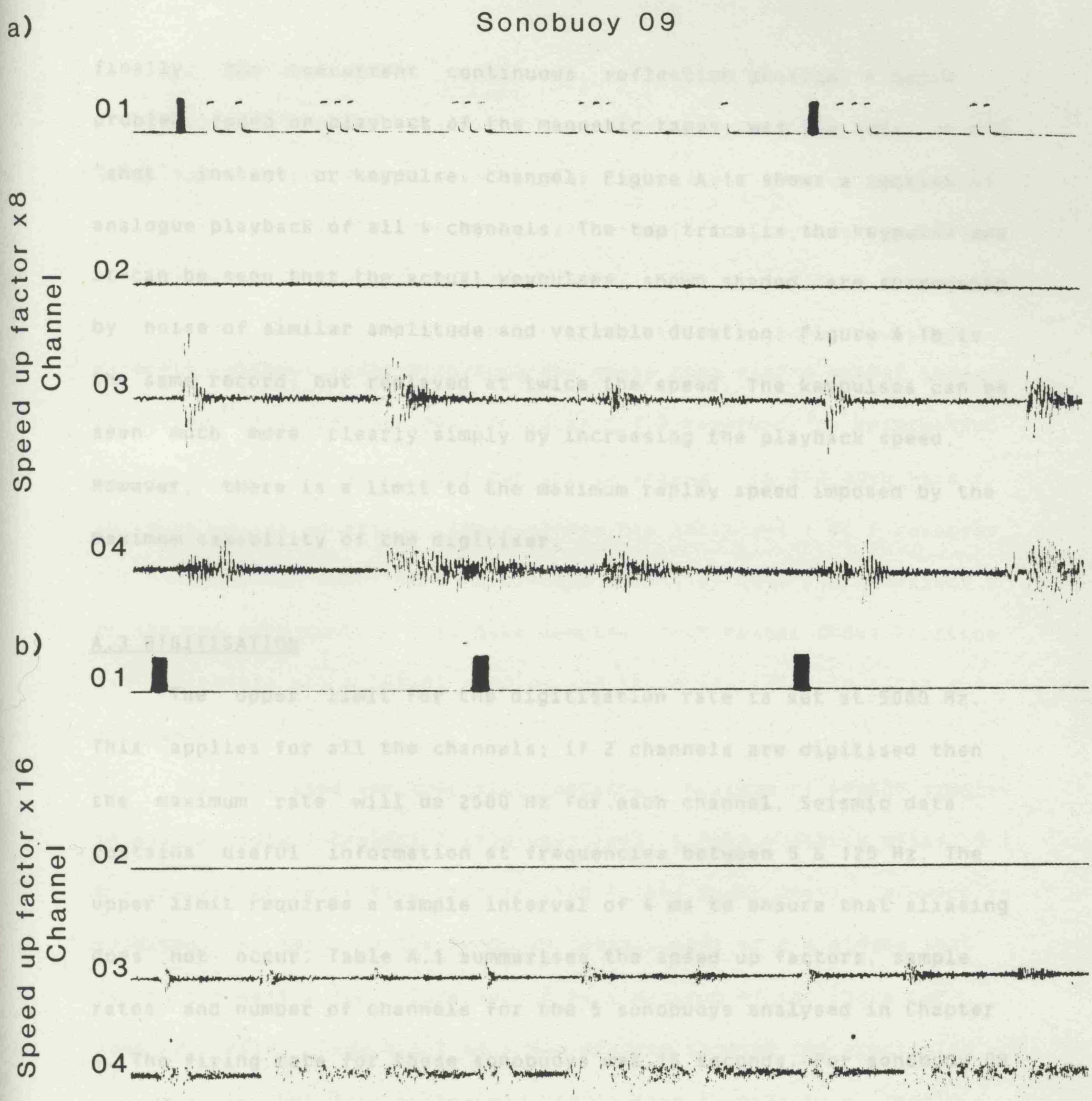

Figure A.1 Analogue playbacks of sonobuoy data to show noise on the 'keypulse' channel. a) Speed up factor of only x8. Channel 01 is the keypulse with actual positions of true pulses shaded. The other square waves on this channel are due to noise. Channels 02, 03 and 04 represent the event mark, sonobuoy seismic data and continuous reflection data respectively. b) Speed up factor of x16 gives a better 'keypulse' signal bu tmay require digitising at a lower frequency, or a reduction in the number of channels digitised.

finally, the concurrent continuous reflection profile. A major problem, found on playback of the magnetic tapes, was the noise on the 'shot' instant, or keypulse, channel. Figure A.1a shows a section of analogue playback of all 4 channels. The top trace is the keypulse and it can be seen that the actual keypulses, shown shaded, are surrounded by noise of similar amplitude and variable duration. Figure A.1b is the same record, but replayed at twice the speed. The keypulses can be seen much more clearly simply by increasing the playback speed. However, there is a limit to the maximum replay speed imposed by the maximum capability of the digitiser.

A.3 DIGITISATION

The upper limit for the digitisation rate is set at 5000 Hz. This applies for all the channels; if 2 channels are digitised then the maximum rate will be 2500 Hz for each channel. Seismic data contains useful information at frequencies between 5 & 125 Hz. The upper limit requires a sample interval of 4 ms to ensure that aliasing does not occur. Table A.1 summarises the speed up factors, sample rates and number of channels for the 5 sonobuoys analysed in Chapter 4. The firing rate for these sonobuoys was 16 seconds. For sonobuoy 09 the sampling rate and number of channels was halved and the speed up factor doubled to increase the signal to noise ratio.

Table A.1 Details of digitisation parameters for sonobuoys reported in Chapter 4.

SONOBUOY NUMBER	SAMPLE RATE	SPEED-UP FACTOR	NUMBER OF CHANNELS	FILTER Lo	FILTER Hi
06	0.004	x 4	4	8	125
07	0.008	x 16	2	5	62.5
09	0.008	x 16	2	5	62.5
16	0.004	x 8	2	5	125
17	0.004	x 8	2	5	125

The result of digitisation was a computer file containing a maximum of 409600 samples/channel of data sampled at either 4 or 8 ms.

A.4 SDPS SYSTEM

Digitisation of seismic data generates very large volumes of data and a method storage and display is required that is both quick and easily accessable. The system at Leicester University is called the Seismic Data Processing System (SDPS). SDPS is based on the series of indices whereby a particular subset of data can be accessed directly without reading through the whole data set. A master index totalling 403 locations has locations 1 & 2 reserved for information pertinent to the whole data set and locations 3 to 403 each have a subindex of 109 locations. The subindex has locations 1 to 8 reserved for information about that particular subset of data and locations 9 to 109 can each contain 4096 data samples. Each master index location can therefore store 409600 samples and there are 400 such locations available.

The digitised sonobuoy file contains a maximum of 409600 samples in master index locations 3 (the keypulse), 4 (the sonobuoy data), 5 (the concurrent reflection profile) and 6 (the event mark). Software is required to split up the sonobuoy seismic data into a single shot record per master index location up to a maximum of 400 shots per sonobuoy file. Figure A.2 is a flo-diagram showing the processing sequence to get from analogue magnetic tape records to a 'wiggly' trace plot.

A.5 FORTRAN PROGRAM FCSNDG

Program FCSNDG was written in Fortran 77 to split up a digitised sonobuoy file, using the keypulse channel, and put each shot record onto a separate master index location. The program finds the location of the first lo-hi edge of the keypulse and writes the next 'n' number of samples from the sonobuoy data channel into the master index of a new file, starting at index location 3. The distance between keypulses

FLO-DIAGRAM FOR PROCESSING SONOBUOY DATA

```
                ORIGINAL SIGNAL ON MAGNETIC TAPE
                               ↓
                               ↓
                       [AR11 DIGITIZER]
                               ↓
                         FILE ARSB***
                               ↓
                               ↓
                       [POST PROCESSOR]
                               ↓
                         FILE DSB***
                               ↓
                               ↓
HEADER INFORMATION → [DEMULTIPLEXER]
                               ↓
                         FILE HSB***
                               ↓
                               ↓
CONTROL PARAMETERS → {PROGRAM FCSNDG}
                               ↓
                         FILE RSB***  containing typically 90-100
                               ↓            shots
                               ↓
                     [MERGE WITH OTHER]
                  [FILES OF SAME SONOBUOY]
                               ↓
                         FILE SNB***  containing up to 400 shots
                               ↓
                               ↓
                     [DISPLAY PROGRAMS TO]
                 [GIVE FINAL GRAPHICAL OUTPUT]
```

Figure A.2 Flo-diagram for the processing sequence to get from an analogue magnetic tape to the final 'wiggly' trace plot.

should not vary and the program can jump to where the next keypulse is expected before starting its search. The program will keep a record of the average distance between keypulses and also the average length of each keypulse. This information is used to check that a keypulse has actually been identified.

The program input is listed below and the program is usually run in 'batch' mode. Figures A.3, A.4, A.5 and A.6 show the 'wiggly' trace records corresponding to Sonobuoys 06, 09, 16 and 17.

1st READ STATEMENT, FORMATTED (A6,2(A10))

NFILE= subfile name of the file being accessed. This will be the same as the demultiplexed filename.

NSHPT= 10 alphanumeric characters describing the shotpoint

NRCPT= " " " " " recordpoint

2nd READ STATEMENT, FREE FORMAT

SHTDST= distance in k.m. between successive shots. All the data at this juncture are assumed to have been collected at a constant 5 knts.

PERCNT= percentage error allowed for in the KeyPulse length before the average KeyPulse spacing is used.

3rd READ STATEMENT, FREE FORMAT

KEYSIZ= size of the KeyPulse in volts. An estimate of this can be obtained from the jet-pen records or from the demultiplexing program output.

KEYLON= length of the KeyPulse in number of samples. This is necessary only to trap the first KeyPulse as afterwards the average KeyPulse length is used.

KEYSPC= time in seconds between KeyPulses. This is simply the firing rate of the seismic source.

NF= number of data samples required after the KeyPulse.

SINT= sample interval in seconds.

KEYNUM= number of cycles the program is required to perform. This is useful if not all the data is wanted.

KEYST= start number for the shot point number header information.

ICHA= channel number from which data is to be read. The KeyPulse channel is number 0 and the first data channel is 1.

DSTST= the starting distance for the shot-receiver header information. This increases by SHTDT every time the program cycles.

KEYGES= the number of samples skipped before starting to look for the first KeyPulse. This is necessary to start the program in periods of noise.

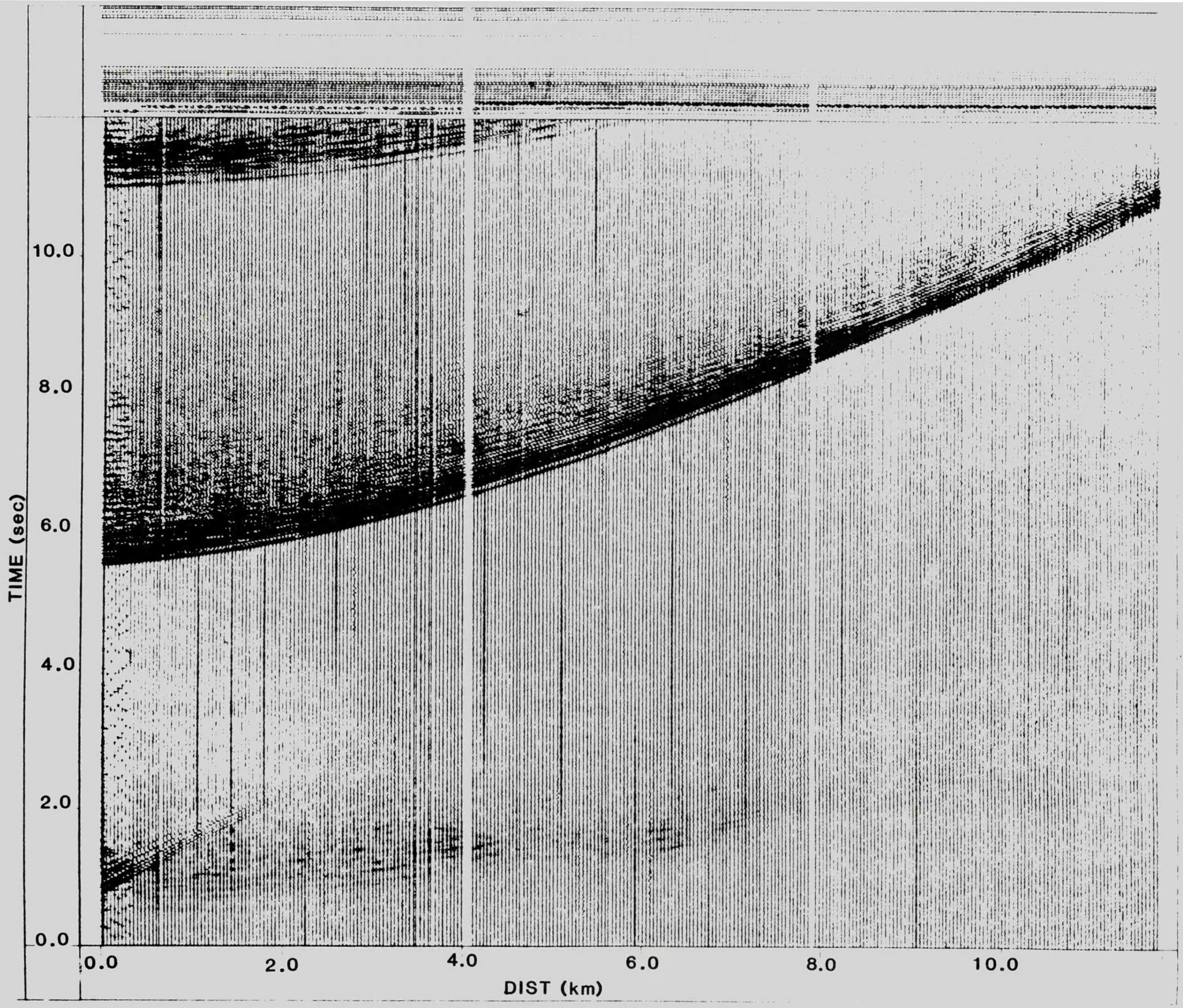

Figure A.3 'Wiggly' trace plot of digitised data for Sonobuoy 06. The y-axis is in milliseconds and the x-axis is in kilometres. Data gaps are due to dropouts on the analogue magnetic tape records. Only wide angle reflections can be seen on this record.

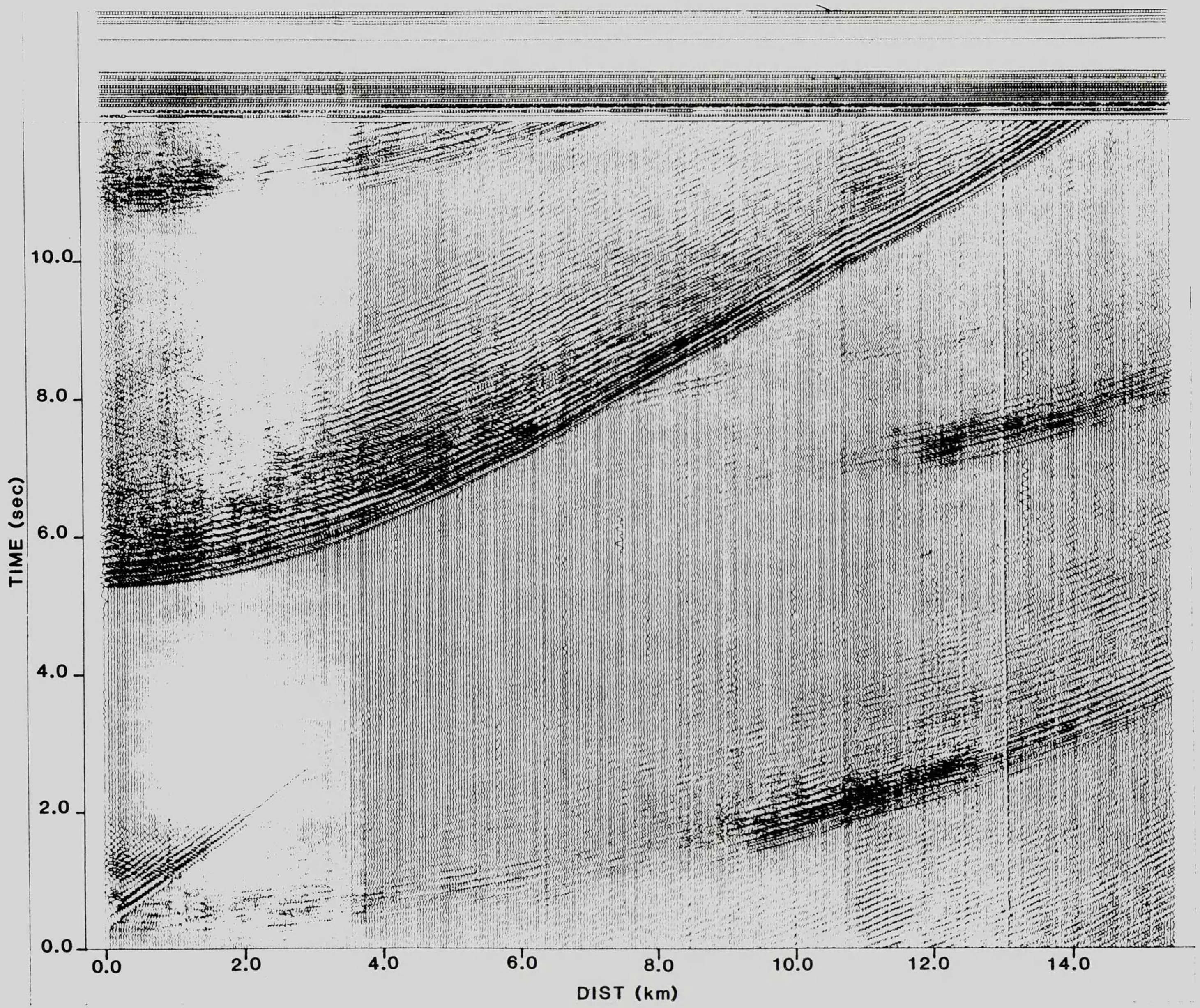

Figure A.4 'Wiggly' trace plot of digitised data for Sonobuoy 09. Axes are the same as for Figure A.3. Blank patches are due to glare during reproduction of this diagram from the original. A refracted arrival can be identified on this record.

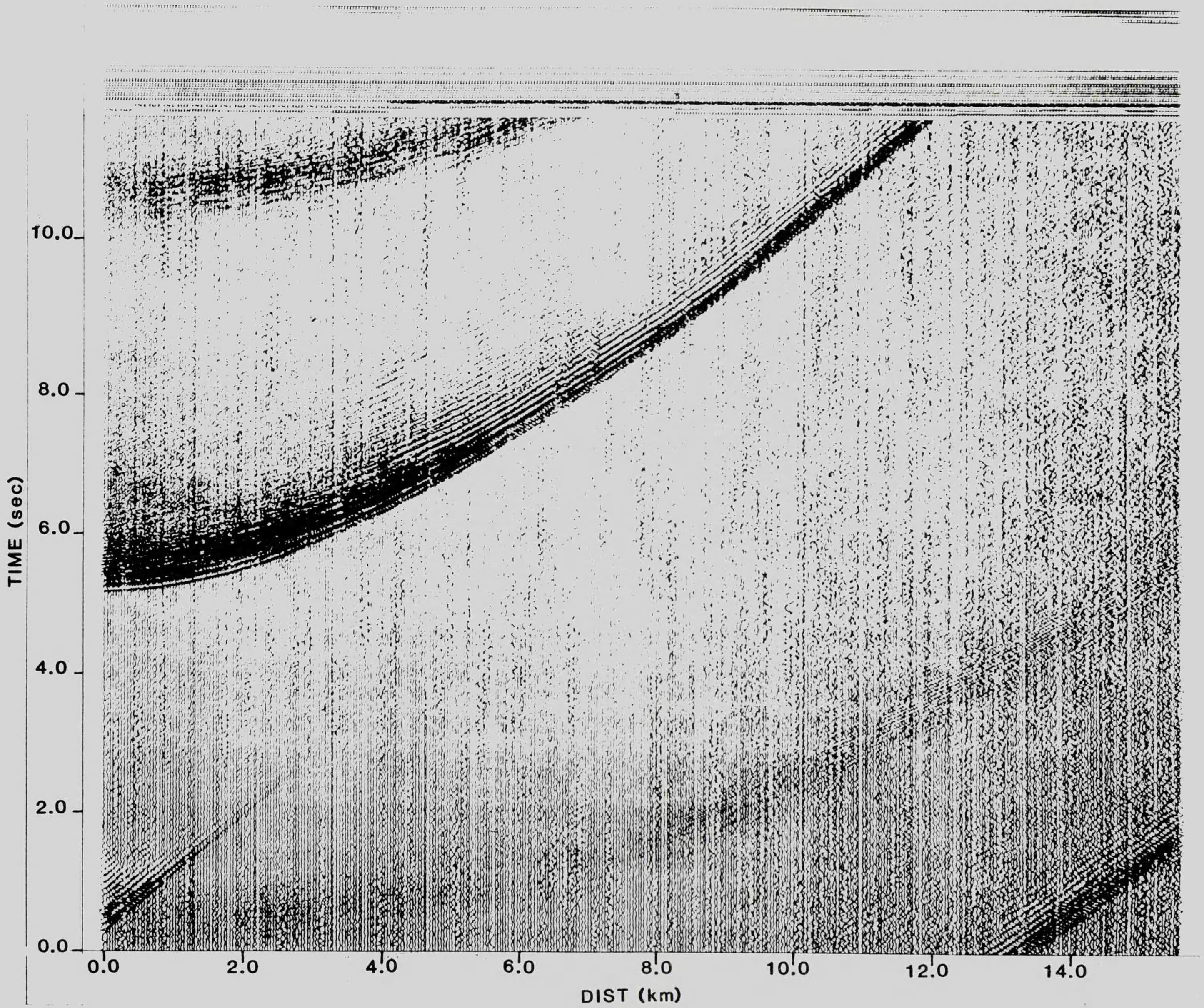

Figure A.5 'Wiggly' trace plot of digitised data for Sonobuoy 16. Only wide angle reflections can be identified on this record.

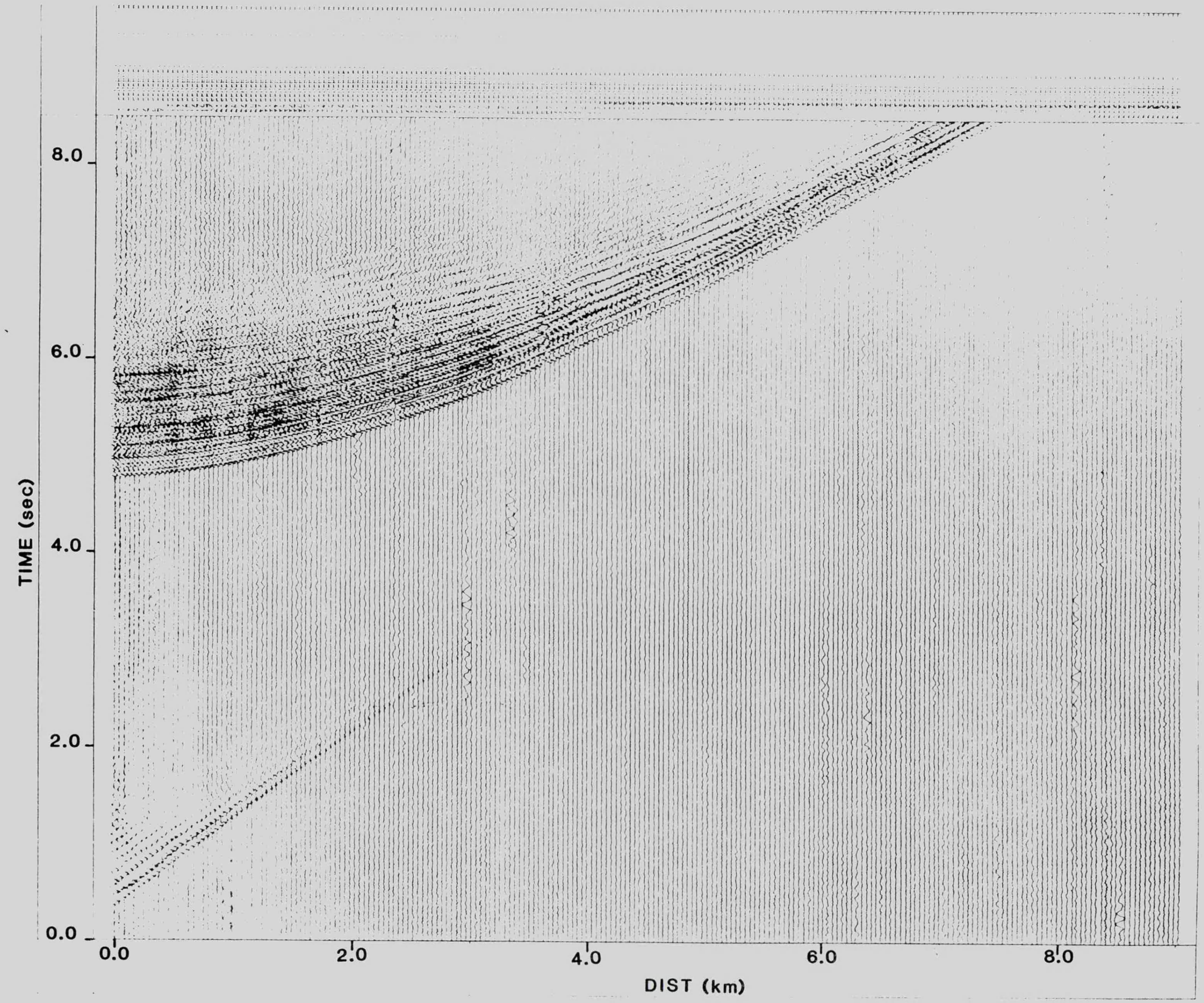

Figure A.6 'Wiggly' trace plot of digitised data for Sonobuoy 17. Again, only wide angle reflections can be identified on this record.

REFERENCES

Amin, M.,1983. An algorithm to compute the geoid surface, *Institute of Oceanographic Sciences, Report.*, 168: 18pp.

Banks, R.J., Parker, R.L. and Huestis, S.P.,1977. Isostatic compensation on a continental scale, *Geophys. J. Roy. Astron. Soc.*, 51: 431-452.

Banks, R.J. and Swain, C.J.,1978. The isostatic compensation of East Africa, *Proc. Roy. Soc. London Ser. A*, 364: 331-352.

Barret, D.L. and Keen, C.E. 1976. Mesozoic magnetic lineations, the magnetic quiet zone and sea floor spreading in the Northwest Atlantic, *J. Geophys. Res.*, 81: 4875-

Bebiano J.B., 1932. A geologia do Arquinpelago de Cabo Verde, *Comm. Serv. Geol. Port.*, *18: 1-275*

Bodine, J.H., Steckler, M.S. and Watts, A.B.,1981. Observations of flexure and the rheology of the oceanic lithosphere, J. Geophys. Res., 86: 3695-3707.

Brink, t.U.S. and Watts, A.B.,1985. Seismic stratigraphy of the flexural moat flanking the Hawaiian Islands, *Nature*, 317: 421-424.

Brown, S.J.,1984. PhD Thesis, Leicester University, *In preparation.*

Carter, D.J.T.,1980. Echo-sounding correction tables (formerly Matthew's tables), *Publ. Hydrographic Dept., Ministry of Defence, Taunton.* 3rd Ed.

Cazenave, A. and Dominh, K.,1984. Geoid heights over the Louisville Ridge, *J. Geophys. Res.*, 89: 11171-11179.

Cazenave, A., Lago, B., Dominh, K. and Lambeck, K.,1980. On the response of oceanic lithosphere to seamount loads from GEOS3 satellite radar altimetry observations, *Geophys. J. R. Astron. Soc.*, 63: 233-252.

Chapman, M.,1979. Techniques for interpretation of geoid anomalies, J.

Geophys. Res., 84: 3793-3801.

Cochran, J.R.,1979. An analysis of isostasy in the world's oceans, 2, Mid-ocean ridge crests, *J. Geophys. Res.*, 84: 4713-4729.

Cooley, J.W. and Tukey, S.W.,1966. An algorithm for the machine calculation of complex Fourier transforms, *Mathematics of Computation*, 19: 297-301.

Courtney, R.C. and White, R.S.,1986. Anomalous heat flow and geoid across the Cape Verde Rise: evidence for dynamic support from a thermal plume in the mantle, *Geophys. J. R. Astron. Soc.*, 87: 815-867.

Crough, S.T.,1983. The correction for sediment loading on the seafloor, *J. Geophys. Res.*, 88: 6449-6454.

Crough, S.T.,1978. Thermal origin of mid-plate hot-spot swells, *Geophys. J. Roy. Astron. Soc.*, 55: 451-469.

Crough, S.T.,1982. Geoid height anomalies over the Cape Verde Rise, *Marine Geophys. Res.*, 5: 263-271.

Dash, B.P., Ball, M.M., King, G.A., Butler, L.W. and Rona, P.A. 1976. Geophysical investigation of the Cape Verde Archipelago, *J. Geophys. Res.*, 81: 5249-5259

Davis, J.C., 1986. Statistics and data analysis in geology, *Publ. John Wiley & Sons.*

Detrick, R.S., von Herzen R.P., Crought, S.T., Epp, D. and Fehn, V.,1981. Heat flow on the Hawaiian swell and lithospheric reheating, *Nature*, 292: 142-143.

Dix, C.H.,1955. Seismic velocities from surface measurements, *Geophysics*, 20: 68-86.

Dixon, T.H., Naraghi, M., McNutt, M.K. and Smith, S.M.,1983. Bathymetric prediction from SEASAT altimeter data, *J. Geophys. Res.*, 88: 1563-1571.

Dorman, L.M. and Lewis, B.T.R.,1970. Experimental isostasy, 1, Theory of the determination of the earth's isostatic response to a concentrated load, *J. Geophys. Res.*, 75: 3357-3365.

Dorman, L.M. and Lewis, B.T.R.,1972. Experimental isostasy, 3, Inversion of the isostatic Green function and lateral density changes, *J. Geophys. Res.*, 77: 3068-3077.

Garland, G.D., 1979. Introduction to geophysics: Mantle, Core and Crust, *Publ. W.B. Saunders*.

Gass, I.G., Chapman, D.S., Pollack, H.N. and Thorpe, R.S.,1978. Geological and Geophysical parameters of mid-plate volcanism, *Phil. Trans. Roy. Soc. London Ser. A*, 288: 581-597.

Goldflam, P., Hinz, K., Weigel, W. and Wissman, G., 1980. Some features of the Northwest African margin and magnetic quiet zone, *Phil. Trans. Roy. Soc. Lond. Ser. A.*, 294: 87-96.

Grunau, H.R., Lehner, P., Cleintaur, M.R., Allenbach, P. and Bakker, G.,1975. New radiometric ages and seismic data from Fuerteventura (Canary Islands), Maio (Cape Verde Islands) and Sao Tome' (Gulf of Guinea), *Progress in Geodynamics: Amsterdam, Royal Netherland Academy of Science.*, 90-118.

Gunn, R.,1943. A quantitative evaluation of the influence of the lithosphere on the anomalies of gravity, *J. Franklin Inst.*, 236: 373-396.

Hayes, D.E. and Rabinowitz, P.D.,1975. Mesozoic magnetic lineations and the magnetic quiet zone off Northwest Africa, *Earth Planet. Sci. Lett.*, 28: 105-115.

Hertz, H.,1884. Uber das gleichgewicht schwimmender elstischer platten, *Weidemann's Annalen der Physik*, 22: 449-455.

Hess, H.H.,1962. History of the ocean basins, in *Petrologic Studies 599-620, Geol. Soc. Am.*

Hill, M.N.,1963. Single ship seismic refraction shooting, *The Sea, vol 3, New York-London Interscience Publ.*

Hittleman, A.M., Groman, R.C., Haworth, R.T., Holcombe, T.L., McHendrie, G. and Smith, S.M., 1981. The Marine Geophysical Data Exchange Format "MGD77" (Bathymetry, Magnetics and Gravity), Key to geophysical records documentation No 10 (revised), *N.O.A.A. National Geophysical and Solar Terrestrial Data Centre, Boulder Colorado, USA.*

Hoskins, H., Rogers, C.V. and Woo, A.O.,1974. Data report of oblique reflection-refraction radio sonobuoy profiles on the African continental margin (R/V Atlantis cruises 67 & 75), *Woods Hole Oceanographic Institution Tech. Rep. 74-34 (unpublished manuscript).*

Houtz, R.E.,1980. Crustal structure of the North Atlantic on the basis of large-airgun sonobuoy data, *Geol. Soc. Am. Bull.*, 91: 406-413.

Houtz, R.E., Eittreim, S. and Grantz, A.,1981. Acoustic properties of Northern Alaska shelves in relation to the regional geology, *J. Geophys. Res.*, 85: 3935-3943.

Houtz, R.E., Ewing, J. and LePichon, X.,1968. Velocity of deep sea sediments from Sonobuoy data, *J. Geophys. Res.*, 73: 2615-2641

Houtz, R.E. and Ewing, J.,1976. Upper crustal structure as a function of plate age, *J. Geophys. Res.*, 81: 2490-2498.

Jacobs, J.A.,1974. A textbook on Geonomy, *Publ. Adam Hilger, London.*

Jeffreys, H.,1970. *The Earth*, 5th edn., Cambridge University Press.

Kanasewich, E.R.,1975. *Time sequence analysis in geophysics*, 2nd edn., The University of Alberta Press.

King, G.A.,1974. Crustal studies on and around the Cape Verde Archipelago, *PhD Thesis, University of London.*

Knott, S.T. and Hoskins, H.,1975. Collection and analysis of seismic wide angle reflection and refraction data using radio sonobuoys, *Wood Hole Oceanographic Institution Tech. Rep. 75-33 (unpublished manuscript).*

Koelsch, D.E. and Hess, F.R.,1981. A high quality low cost receiver for military sonobuoys, *Marine Geophys. Res.*, 4: 479-483.

Kozminskaya, I.P. and Kapustyan, N.K.,1975. A generalised seismic model for an oceanic type of crust, *Izvestiya.*, 11: 37-49.

Kreyszig, E.,1979. Advanced engineering mathematics, *Publ. John Wiley & Sons.*

Lambeck, K.,1981. Flexure of the oceanic lithosphere from island uplift, bathymetry and geoid height observations: The Society Islands, *Geophys. J. Roy. Astron. Soc.*, 67: 91-114.

Lambeck, K. and Nakiboglu, S.M.,1980. Seamount loading and stress in the oceanic lithosphere, *J. Geophys. Res.*, 85: 6403-6418.

Lame, D.B. and Born, G.H.,1982. SEASAT measurement system evaluation: Achievements and limitations, *J. Geophys. Res.*, 87: 3175-3178.

Lancelot, Y., Seibold, E., et al, 1977. Initial reports of the deep sea drilling project 41: 233-326, *U.S. Government Printing Office, Washington, D.C.*

Larson, R.L. and Hilde, T.W.C., 1975. A revised timescale of magnetic reversals for the early Cretaceous and late Jurassic, *J. Geophys. Res.*, 80: 2586-2594.

LeDouaran and Parsons, B.,1982. A note on the correction of ocean floor depths for sediment loading, *J. Geophys. Res.*, 87: 4715-4722.

LePichon, X., Ewing, J. and Houtz, R.E.,1968. Deep-sea velocity determination made while reflection profiling, *J. Geophys. Res.*, 73: 2597-2614.

LePichon, X. and Fox, P.J., 1971. Marginal offsets, fracture zones and the early opening of the North Atlantic, *J. Geophys. Res.*, 76: 6294-

Lerch, F.J., Marsh, J.G, Klosko, S.M. and Williamson, R.G.,1982. Gravity model improvement for SEASAT, *J. Geophys. Res.*, 87: 3281-3296.

Lerch, F.J., Wagner, C.A., Klosko, S.M. and Putney, B.H.,1981. Goddard earth models for oceanographic applications (GEM10B and 10C), *Mar.*

Geod., 5: 2-43.

Lewis, B.T.R. and Dorman, M.L.,1970. Experimental isostasy II: An isostatic model for the U.S.A. derived from gravity and topographic data, *J. Geophys. Res.*, 75: 3367-3386.

Limond, W.Q. and Patriat, Ph.,1975. The accuracy of determination of seismic interval velocities from variable angle reflection (disposable sonobuoy) records, *Geophys. J. Roy. Astron. Soc.*, 43: 905-938.

Lorrel, J.,1980. SEASAT altimeter geophysical algorithm specifications, *J.P.L. Internal Rep. 622-226, Jet Propul. Lab., Pasedena, Calif. U.S.A.*

Lorrel, J., Parke, M.E. and Scott, J.F.,1980. SEASAT geophysical data record (GDR) user's handbook, *J.P.L. Internal Rep. 622-97, Jet Propul. Lab., Pasedena, Calif. U.S.A.*

Marsh, J.G. and Williamson, R.G.,1982. SEASAT altimeter timing bias estimation, *J. Geophys. Res.*, 87: 3232-3238.

Marsh, J.G., Williamson, R.G. and Martin, T.V.,1977. Tracking station coordinate investigation, *paper presented at the GEOS3 principal investigators meeting, NASA GEOS3 Project, New Orleans, U.S.A.*

McKenzie, D.P.,1984. The generation and compaction of partially molten rock, *J. Petrol.*, 25: 713-765.

McKenzie, D.P. and Bowin, C.,1976. The relationship between bathymetry and gravity in the Atlantic ocean, *J. Geophys. Res.*, 81: 1903-1915.

McQuillin, R. and Ardus, D.A.,1977. Exploring the geology of shelf seas, *Publ. Graham & Trotman Ltd.*

McNutt, M.K.,1984. Lithospheric flexure and thermal anomalies, *J. Geophys. Res.*, 89: 11,180-11,194.

McNutt, M.K.,1979. Compensation of oceanic topography: an application of the response function technique to the Surveyor area, *J. Geophys. Res.*, 84: 7589-7598.

McNutt, M.K. and Menard, H.W.,1978. Lithospheric flexure and uplifted atolls, *J. Geophys. Res.*, 83: 1206-1212.

Menard, H.W.,1956. Archipelagic aprons, *Bull. Amer. Asso. Petrol. Geol., 40: 2195-2210.*

Menard, H.W. and Atwater, T., 1968. Change in direction of seafloor spreading, *Nature*, 219: 463-467.

Menard, H.W. and McNutt, M.K.,1982. Evidence for and consequences of thermal rejuvenation, *J. Geophys. Res.*, 87: 8570-8580.

Mitchell, J.G., LeBas, M.J., Zielonka, J. and Furnes, H.,1983. On dating the magmatism of Maio, Cape Verde Islands, *Earth and Plan. Sci. Lett.*, 64: 61-76.

Minster, J. and Jordan, T.H.,1978. Present day plate motions, *J. Geophys. Res.*, 83: 5331-5354.

Munk, W.H. and Cartwright, D.E.,1966. Tidal spectroscopy and prediction, *Phil. Trans. Roy. Soc. London Ser. A*, 259: 533-581.

Mutter, J.C. and Detrick, R.S., 1984. Multichannel seismic evidence for anomalously thin crust at Blake Spur fracture zone, *Geology*, 12: 534-537.

Nafe, J.E. and Drake, C.L.,1963. Physical properties of marine sediments, *The Sea, vol 3, NewYork-London Interscience Publ.*

National Academy of Sciences.,1972. Formats for marine geophysical data exchange, *National Research Council, U.S.A.*

Okal, E.A. and Cazenave, A.,1985. A model for the plate tectonic evolution of the Fast-Central Pacific based on SFASAT investigations, *Earth and Plan. Sci. Lett.*, 72: 99-116.

Parker, R.L.,1972. The rapid calculation of potential anomalies, *Geophys. J. Roy. Astron. Soc.*, 31: 447-455.

Parsons, B. and Daly, S.,1983. The relationship between surface topography, gravity anomalies and temperature structure of convection, *J. Geophys. Res.*, 83: 1129-1144.

Parsons, B. and Sclater, J.G.,1977. An analysis of the variation of ocean floor bathymetry and heat flow with age, *J. Geophys. Res.*, 82: 803-827.

Purdy, G.M.,1983. The seismic structure of 140 Myr old crust in the Western Central Atlantic ocean, *Geophys. J. Roy. Astron. Soc.*, 72: 115-137.

Purdy, G.M. and Rohr, K., 1979. Geophysical survey within the Mesozoic magnetic anomaly sequence south of Bermuda, *J. Geophys. Res.*, 84: 5487-5496.

Raitt, R.W.,1963. The crustal rocks, *The Sea, vol 3, NewYork-London, Interscience Publ.*

Rapp, R.H.,1986. Gravity anomalies and sea surface heights derived from a combined GFOS3/SEASAT altimeter data set, *J. Geophys. Res.*, submitted.

Rapp, R.H.,1977. The relationship between mean anomaly block sizes and spherical harmonic representations, *J. Geophys. Res.*, 82: 5360-5364.

Ribe, N.M.,1982. On the interpretation of frequency response functions for oceanic gravity and bathymetry, *Geophys. J. Roy. Astron. Soc.*, 70: 273-294.

Ribe, N.M. and Watts, A.B.,1982. The distribution of intraplate volcanism in the Pacific ocean basin: A spectral approach, *Geophys. J. Roy. Astron. Soc.*, 71: 333-362.

Robertson, A.H.F., 1984. Mesozoic deep-water and Tertiary volcaniclastic deposition of Maio, Cape Verde Islands: implications for Atlantic palaeoenvironments and ocean island evolution, *Geol. Soc. Amer. Bull.*, 95: 433-453.

Robertson, E.I.,1967. Gravity effects of volcanic islands, *N.Z. J. Geophys.*, 10: 1466-

Rona, P.A., Brakl, J. and Heirtzler, J.R., 1970. Magnetic anomalies in the Northwest Atlantic between the Canary islands and Cape Verde islands, *J. Geophys. Res.*, 75: 7412-7420.

Rothe, P.,1973. Sedimentation in the deep-sea areas adjacent to the Canary and Cape Verde islands, *Marine Geology.*, 14: 191-206.

Schouten, H. and Klitgord, K.D., 1982. The memory of the accreting plate boundary and the continuity of fracture zones, *Earth Plan. Sci. Lett.*, 59: 255-266.

Schouten, H. and White, R.S., 1980. Zero offset fracture zones. *Geology*, 8: 175-179.

Schult, F.R. and Gordon, R.G., 1984. Root mean square velocities of the continents with respect to the hot-spots since the early Jurassic, *J. Geophys. Res.*, 89:1789-1800.

Smith, A.G., Hurley, A.M. and Briden, J.C.,1981. Phanerozoic paleocontinental world maps, *Publ. Cambridge University Press.*

Sneddon, I.A.,1969. Crack problems in the classical theory of elasticity, *Society for Industrial and Applied Mathematics: Series in applied mathematics, Publ. John Wiley & Sons.*

Stillman, C.J., Furnes, H., Le Bas, M.J., Robertson, A.H.F. and Zielonka, J., 1982. The geological history of Maio, Cape Verde Islands, *J. Geol. Soc. Lond.*, 139: 347-361.

Stoffa, P.L., Diebold, J.B. and Buhl, P., 1982. Velocity analysis for wide aperture seismic data, *Geophysical Prospecting*, 30: 25-57.

Tamsett, D.,1984. An application of the response function technique to profiles of bathymetry and gravity in the Gulf of Aden, Geophys. J. *Roy. Astron. Soc.*, 78: 349-369.

Tapley, B.D., Born, G.H. and Parke, M.E.,1982. The SEASAT altimeter data and its accuracy assessment, *J. Geophys. Res.*, 87: 3179-3188.

Tulcholke, B.E. and Ludwig, W.J., 1982. Structure and origin of the J-Anomaly ridge Western North Atlantic ocean, *J. Geophys. Res.*, 87: 9389-9407.

Uchupi, E., Emery, K.O., Bowin, C.O. and Phillips, J.D.,1976.

Continental margin off western Africa: Senegal to Portugal, *A.A.P.G.*, 60: 809-878.

Van der Linden, W.J.M., 1981. The crustal structure and evolution of the continental margin off Senegal and the Gambia, from total-intensity magnetic anomalies, *Geol. Mijnbouw*, 60: 257-266.

Van Wyckhouse, R.J.,1973. Synthetic bathymetric profiling system (SYNBAPS), *Tech. Rep. TR233, U.S. Naval Oceanogr. Office, Washington D.C.*

Vening Meinesz, F.A.,1931. Une nouvelle method pour la reduction isostatique regionale de l'intensite de la pesanteur, *Bull. Geod.*, 29.

Vening Meinesz, F.A.,1948. Gravity expeditions at sea 1923-1938, vol 4, *Neth. Geod. Comm. Delft*.

Vine, F.J., 1966. Spreading of the ocean floor: new evidence, *Science*, 154: 1405-1415.

Vogt, P.R., Anderson, C.N. and Bracey, D.R., 1971. Mesozoic magnetic anomalies, seafloor spreading and geomagnetic reversals in the southwestern North Atlantic, *J. Geophys. Res.*, 76: 4796-4823.

Vogt, P.R., Zondek, B., Fell, P.W., Cherkis, N.Z. and Perry, R.K.,1984. SEASAT altimetry, the North Atlantic Geoid, and evaluation by shipborne subsatellite profiles, *J. Geophys. Res.*, 89: 9885-9903.

Walcott, R.I.,1970. Flexure of the lithosphere at Hawaii, *Tectonophysics*, 9: 435-466.

Watts, A.B.,1978. An analysis of isostasy in the world's oceans 1. Hawaiian-Emperor seamount chain, *J. Geophys. Res.*, 83: 5989-6004.

Watts, A.B.,1979. On geoid heights derived from GEOS3 altimeter data along the Hawaiian-Emperor seamount chain, *J. Geophys. Res.*, 84: 3817-3826.

Watts, A.B. and Cochran, J.R.,1974. Gravity anomalies and flexure of the lithosphere along the Hawaiian-Emperor seamount chain, *Geophys. J. Roy. Astron. Soc.*, 39: 119-141.

Watts, A.B., Bodine, J.H. and Steckler, M.S.,1980. Observations of flexure and the state of stress in the ocean lithosphere, *J. Geophys. Res.*, 85: 6369-6376.

Watts, A.B., Cochran, J.R. and Selzer, G.,1975. Gravity anomalies and flexure of the lithosphere: A three-dimensional study of the Great Meteor Seamount, Northeast Atlantic, *J. Geophys. Res.*, 80: 1391-1398.

Watts, A.B., McKenzie, D.P., Parsons, B.E. and Roufosse, M.,1985. The relationship between gravity and bathymetry in the Pacific ocean, *Geophys. J. Roy. Astron. Soc.*, 83: 263-298.

Watts, A.B., Ten Brink, U.S., Buhl, P. and Brocher, T.M.,1985. A multichannel seismic study of lithospheric flexure across the Hawaiian-Emperor seamount chain, *Nature*, 315: 105-111.

Watts, A.B. and Ribe, N.M.,1984. On geoid heights and flexure of the lithosphere at seamounts, *J. Geophys. Res.*, 89: 11152-11170.

White J.V., Sailor, R.V., Lazarewicz, A.R. and LeShack. A.R.,1983. Detection of seamount signatures in SFASAT altimeter data using matched filters, *J. Geophys. Res.*, 88: 1541-1551.

White, R.S.,1979. Oceanic upper crustal structure from variable angle seismic reflection-refraction profiles, *Geophys. J. Roy. Astron. Soc.*, 57: 683-726.

Young, R. and Hill, I.A.,1986. An estimate of the effective elastic thickness of the Cape Verde Rise, *J. Geophys. Res.*, 91: 4854-4866.